ISBN 978-82-326-5380-5 (printed ver.)
ISBN 978-82-326-6768-0 (electronic ver.)
ISSN 1503-8181 (printed ver.)
ISSN 2703-8084 (electronic ver.)

NTNU
Norwegian University of
Science and Technology

Mikkel Eske Nørgaard Sørensen

Doctoral thesis

Doctoral theses at NTNU, 2021:401

NTNU
Norwegian University of
Science and Technology
Thesis for the degree of
Philosophiae Doctor
Faculty of Information Technology
and Electrical Engineering
Department of Engineering Cybernetics

NTNU

Doctoral theses at NTNU, 2021:401

Mikkel Eske Nørgaard Sørensen

Topics in Nonlinear and Model-based Control of Ships

NTNU
Norwegian University of
Science and Technology

Mikkel Eske Nørgaard Sørensen

Topics in Nonlinear and Model-based Control of Ships

Thesis for the degree of Philosophiae Doctor

Trondheim, December 2021

Norwegian University of Science and Technology
Faculty of Information Technology
and Electrical Engineering
Department of Engineering Cybernetics

NTNU
Norwegian University of
Science and Technology

NTNU
Norwegian University of Science and Technology

Thesis for the degree of Philosophiae Doctor

Faculty of Information Technology
and Electrical Engineering
Department of Engineering Cybernetics

ISBN 978-82-326-5380-5 (printed ver.)
ISBN 978-82-326-6768-0 (electronic ver.)
ISSN 1503-8181 (printed ver.)
ISSN 2703-8084 (electronic ver.)

ITK-report: 2021-8-W

Doctoral theses at NTNU, 2021:401

PRINTED IN
NORWAY
NO - 1598

NORDIC SWAN ECOLABEL
Printed matter
2041 0731

Printed by Skipnes Kommunikasjon AS

To my dearly departed grandmother (1932-2017)
"You can achieve anything you want by working hard for it"

Summary

This PhD thesis considers topics within automatic motion control of ships, which has been an active research topic since the early 20th century. Specifically, the thesis aims at designing controllers to achieve a good tracking performance by handling actuator constraints, internal uncertainties and external disturbances of the ship's inner-loop control e.g. controlling the velocity loops in order to achieve robust manoeuvrability.

The thesis proposes improvements to two existing ship models, which have been found by evaluating the steady state velocities for uniformly distributed control inputs. Through this evaluation it is shown that the original ship models give rise to physically impossible motions. It is suggested to add extra terms to the damping matrices in order to overcome the issues with the existing ship models.

An overview of existing performance metrics is given. Subsequently, three novel performance metrics are suggested. These performance metrics evaluate the overall energy consumption, wear and tear of the actuators and a combination of these. The proposed performance metrics are used as a tool to compare and evaluate the performance of various controllers.

In addition, the use of purely nonlinear feedback strategies and combinations of linear-nonlinear feedback strategies are investigated for pose and velocity control of ships. The nonlinear feedback terms are based on a sigmoid function which limits the effects of the error term. A modification to the nonlinear feedback terms concepts is suggested by changing them from symmetric to asymmetric nonlinear feedback terms. This results in a stepping stone to handle actuator constraints.

A novel motion control method is suggested in order to handle magnitude constraints of the actuator. This is based on a simplified version of the collision avoidance algorithm called dynamic window. The dynamic window algorithm was originally developed for collision avoidance for mobile robots. This control method is suggested for 2 and 3 degrees-of-freedom motion control. Here, the benefits and limitations of both the design and results are discussed.

Some state-of-the-art adaptive control algorithms have been applied to a mathematical model of a ship to see if it is possible to accommodate for internal uncertainties and external disturbances. The performance of the considered adaptive control algorithms have been checked both in a numeral simulation and experimental environment.

Finally, experimental work in the Marine Cybernetics laboratory and onboard the research vessel Gunnerus is described. Here, the equipment and software of the laboratory and ship are presented and discussed. Additionally, all the experimental results from the publications in Appendix A are summarised here.

The thesis is organized as a mix between a monograph and an article collection. It includes eight conference papers, two published journal paper. One additional paper is mentioned, but is outside the scope of this thesis.

Preface

This thesis is submitted in partial fulfillment of the requirements for the degree of philosophiae doctor (PhD) at the Norwegian University of Science and Technology (NTNU). The work was mainly carried out from August 2014 to September 2018 at the Department of Engineering Cybernetics under the supervision of Morten Breivik and Roger Skjetne. The project has been funded by NTNU through a strategic SO scholarship, while additional operating funds have been given from the Research Council of Norway through the Centre for Autonomous Marine Operations and Systems, project number 223254.

Acknowledgments

During the last years, the work for this thesis was carried out. These years have gone incredibly fast, but I have gained a tremendous amount of knowledge and have had the opportunity to work together with inspiring people.

First of all, I would like to thank Morten Breivik for giving me the opportunity to pursue the PhD degree on a topic of great personal interest. He has managed to keep a good balance between giving me constructive input and guidance, and leaving me the freedom to proceed with my own ideas. His input and discussions between us have been invaluable throughout this period and he has always been able to find time for me and my problems. Additionally, I want to thank my co-supervisor Roger Skjetne for setting up full scale experiments in collaboration with Kongsberg Maritime and for the feedbacks on the publications we have done together.

To my office mate Jonatan Ralf Axel Klemets thank you for our discussions and for making me look forward to going to the office every day. I also want to thank Kristian Klausen, Konstanze Kölle, Anna Magdalena Kohl, Bjørn-Olav Holtung Eriksen, João Fortuna, Lorenzo Fusini and Christoph Josef Backi for all the technical discussions we had over the years. I will always remember the coffee breaks at ITK, weekly cageball games and all the time I have spent travelling around the world with so many of you working at ITK and AMOS.

I would like to express my gratitude to the administrative staff at ITK. I greatly appreciate the help of Tove Kristin Blomset Johnsen, Unni Johansen and Bente Seem Lindquist in relation to travels and my duty work at ITK. I am also greatly indebted to workshop and technical staff at both ITK and IMT. Without your assistance, the experiment in this thesis would not have happened. Thanks to Stefano Bertelli, Terje Haugen, Glenn Angell and Torgeir Wahl.

Second to last I want to thank my family and friends from Denmark for their support. A special thanks to my parents Tove and Markus for always being there for me, supporting me in every possible way and their sacrifices not only for me but also for my brother, in order to achieve the best possible education.

Finally, I want to thank Anette Borge for helping me through a hard year of mental stress and emotional problems. Coming home to your smile after a rough day meant the world to me. I would never have been able to complete this without you and for that I am truly grateful.

12/11-2021 Mikkel Eske Nørgaard Sørensen

Contents

List of Figures

List of Tables

Abbreviations

AUV	Autonomous underwater vehicle
CSAD	CyberShip Inocean Cat I Drillship
CLF	Control Lyapunov function
cRIO	CompactRIO
DOF	Degree of freedom
DP	Dynamic positioning
DWC	Dynamic window-based controller
IADC	Integral of absolute differentiated control
IAE	Integral of the absolute value of the error
IAEW	Integral of the absolute value of the error multiplied by the energy consumption
IAEW-WT	Integral of the absolute value of the error with work, wear and tear
ISE	Integral of the square of the error
ITAE	Integral of time multiplied by the absolute value of the error
LP-LV	Linear pose feedback and linear velocity feedback
MC-lab	Marine Cybernetics laboratory
MRS	Magnitude-rate saturation
MPC	Model predictive control
MRAC	Model reference adaptive control
NP-LV	Nonlinear pose feedback and linear velocity feedback
NP-NV	Nonlinear pose feedback and nonlinear velocity feedback
QTM	Qualisys track manager
RPM	Revolutions per minute
UES	Uniformly exponentially stable
UGAS	Uniformly globally asymptotically stable
UGES	Uniformly globally exponentially stable
USGES	Uniformly semiglobally exponentially stable

Chapter 1

Introduction

1.1 Motivation

One of the most important things you need as a control engineer is to have a good model of the system for which you want to design a controller. A good model is for example important when you want to simulate the behavior of a physical system such as a ship. If your model is inaccurate or lacking some important properties, you can experience that your simulation will show results that are not physically possible. In addition to having a good simulator for verification, a model that represents the physical system will make it easier to design a control algorithm that gives the desired performance. For a model-based control algorithm, it is crucial to have a model that represents the physical system, since a poorly designed model-based controller could in the worst case make the closed-loop system unstable. Prototype tests are useful to ensure that you have a good model and to make sure that a novel control design actually works before testing it in full-scale trials. Having done such a test before you do full-scale trials, you might only need to make small adjustments to the control parameters to get the best performance possible in the full-scale trials.

When testing a controller, whether in a simulation environment or in an experiment, it is important to verify and validate the closed-loop performance. The performance evaluation of the controller is often done by looking at the stability analysis, the control error plot and the control input plot. However, these can give an incomplete understanding of the behavior. As such, performance metrics can be used to tune and evaluate the performance of controllers. In this regard, one performance metric only shows one characteristic of the controller; you therefore need many different performance metrics to get an evaluation of all the important characteristics you require your controller to have.

The most used controllers reported in the literature have linear feedback terms. However, the world is not a linear environment and, therefore, the use of nonlinear feedback terms in the controllers could be beneficial. Another thing that is often not considered in the literature when designing a controller is magnitude and rate constraints. By not considering these constraints problems could occur when operating a ship, since the actuators can be worn down faster.

A good controller has the ability to handle both internal uncertainties and external disturbances to the system to be controlled. Examples of uncertainties can be wrongly estimated model parameters, or a difference between the commanded and actual control signal. Examples of disturbances can be wind, current and waves in the surrounding environment of the ship. Additionally, it can be difficult or impossible to measure the effect of the environment on the ship. All these factors can make the ship deviate from the desired path and in the worst case make the ship collide with surrounding traffic or other obstacles. It is therefore important to have a controller with a good performance.

Figure 1.1: The RV Gunnerus is the research ship of the Norwegian University of Science and Technology (NTNU). It is vital for the operational precision and safety of such ships to be equipped with well-performing motion control systems. This thesis proposes and investigates new ship controllers. Courtesy of Helge Sunde / Samfoto.

Having designed a controller, it is important to test if it works as intended. Here, it is not enough to just do simulations. Companies never deliver a product with a controller not thoroughly tested. After the controller has been verified to work as intended in the simulation environment, it is a good idea to verify that it has a similar behavior in a model-scale experiment, before validating the performance of the controller performance in a full-scale experiment.

Summing up, the objective of this thesis is to investigate topics in nonlinear and model-based control of ships, including ship modelling aspects; new control strategies; implementation and testing of controllers in numerical simulations, model-scale experiments and full-scale experiments; as well as metrics to evaluate and compare controller performance. The research focus is on control strategies which can handle model uncertainties and actuator constraints.

1.2 Main Contributions

The main contributions of this thesis are the following:

- Ship models: An investigation and modification of two existing models of scale-model ships are made in order to achieve a more physically realistic behavior. In Paper A.6, a steady-state analysis is made on the Cybership II, which shows that existing models in the literature give rise to physically unrealistic motion. Here, it is shown that an extension of the nonlinear damping matrix is needed to overcome the destabilising behavior which is introduced by the Munk moment. In Paper A.9, a modification to the model parameters for CyberShip Inocean Cat I Drillship in the damping matrix related to the yaw moment has been introduced to get a more physically realistic motion compared to the parameters previously reported in the literature.
- Performance evaluation: A novel performance metric named integral of the absolute value of the error multiplied by the energy consumption (IAEW) is used to compare controllers. The IAEW combines control accuracy and energy use in one single metric and is presented in Paper A.3. In addition, the two controllers are combined with a variation of a command governor to check if the transient performance is improved. Paper A.1 designs an adaptive controller, a robust controller and a standard PID controller for a nonlinear unmanned aerial vehicle (UAV) system, and evaluates their tracking performance and ability to accommodate uncertainties. The IAEW performance metric is used for the evaluation.
- Nonlinear feedback control: Variations of cascaded nonlinear feedback controllers are developed and compared with a cascaded linear feedback controller in papers A.4 and A.2. The motivation for the development is that linear feedback typically gives rise to nice exponential stability properties. However, considering that all actuators have saturation constraints, such stability properties are not feasible in practice. One approach to mitigate the effect such constraints is to introduce nonlinear feedback terms.
- Modified dynamic window-based control: In Paper A.4 it is shown that cascaded nonlinear feedback control is able to limit the control signal within the actuator constraints if the control error is large. By using a simplified version of the dynamic window algorithm [21], which is a constraint-handling algorithm, we are able to make the control signal stay within the actuator constraints in Paper A.6. Here, it is shown that the algorithm works for under-actuated ship. By mapping the set of possible velocities in 3 degrees-of-freedom, it is possible to extend the result of Paper A.6 to fully-actuated ship. These results are presented in Paper A.9.
- Experiments: Verification and validation of the performance of various control schemes through model-scale experiments in an ocean basin and full-scale trials on NTNU's research vessel R/V Gunnerus.

In addition, I have had the privilege of co-supervising three master students, which has resulted in the three conference publications A.5, A.8 and A.9, which are connected with [7], [28] and [33], respectively.

1.3 List of Publications

This thesis is based on the following publications in internationally recognized journals and conferences. A graphical overview of the relations between the publications is shown in Figure 1.2.

Journal Publications

- M. E. N. Sørensen, S. Hansen, M. Breivik and M. Blanke, Performance comparison of controllers with fault-dependent control allocation for UAVs, *Journal of Intelligent & Robotic Systems*, 87(1):187–207, 2017. Referred to as Paper A.1
- M. E. N. Sørensen, M. Breivik, and R. Skjetne, Comparing combinations of linear and nonlinear feedback terms for ship motion control, *IEEE Access*, vol. 8, pp. 193813-193826, 2020. Referred to as Paper A.2

Conference Publications

- M. E. N. Sørensen and M. Breivik, Comparing nonlinear adaptive motion controllers for marine surface vessels, *in Proceedings of the 10th IFAC Conference on Manoeuvring and Control of Marine Craft, Copenhagen, Denmark*, 2015. Referred to as Paper A.3
- M. E. N. Sørensen and M. Breivik, Comparing combinations of linear and nonlinear feedback terms for motion control of marine surface vessels, *in Proceedings of the 10th IFAC Conference on Control Applications in Marine Systems, Trondheim, Norway*, 2016. Referred to as Paper A.4
- M. E. N. Sørensen, E. S. Bjørne and M. Breivik, Performance comparison of backstepping-based adaptive controllers for marine surface vessels, *in Proceedings of the IEEE Multi-Conference on Systems and Control, Buenos Aires, Argentina*, 2016. Referred to as Paper A.5
- M. E. N. Sørensen, M. Breivik, and B.-O. H. Eriksen, A ship heading and speed control concept inherently satisfying actuator constraints, *in Proceedings of the 1st IEEE Conference on Control Technology and Applications, Hawai'i, USA*, 2017. Referred to as Paper A.6
- R. Skjetne, M. E. N. Sørensen, M. Breivik, S. A. T. Værnø, A. H. Brodtkorb, A. J. Sørensen, Ø. K. Kjerstad, V. Calabrò and B. O. Vinje, AMOS DP research cruise 2016: Academic full-scale testing of experimental dynamic positioning control algorithms onboard R/V Gunnerus, *in Proceedings of the 36th International Conference on Ocean, Offshore and Arctic Engineering, Trondheim, Norway*, 2017. Referred to as Paper A.7

- O. N. Lyngstadaas, T. E. Sæterdal, M. E. N. Sørensen and M. Breivik, Improvement of ship motion control using a magnitude-rate saturation model, *in Proceedings of the 2nd IEEE Conference on Control Technology and Applications, Copenhagen, Denmark*, 2018. Referred to as Paper A.8
- M. E. N. Sørensen, O. N. Lyngstadaas, B.-O. H. Eriksen and M. Breivik, A dynamic window-based controller for dynamic positioning satisfying actuator magnitude constraints, *in Proceedings of the 11th IFAC Conference on Control Applications in Marine Systems, Opatija, Croatia*, 2018. Referred to as Paper A.9

Publication not Included in the thesis

- M. E. N. Sørensen and M. Breivik, UAV fault-tolerant control by combined $\mathcal{L}_1$ adaptive backstepping and fault-dependent control allocation, *in Proceedings of the IEEE Multi-Conference on Systems and Control, Sydney, Australia*, 2015.

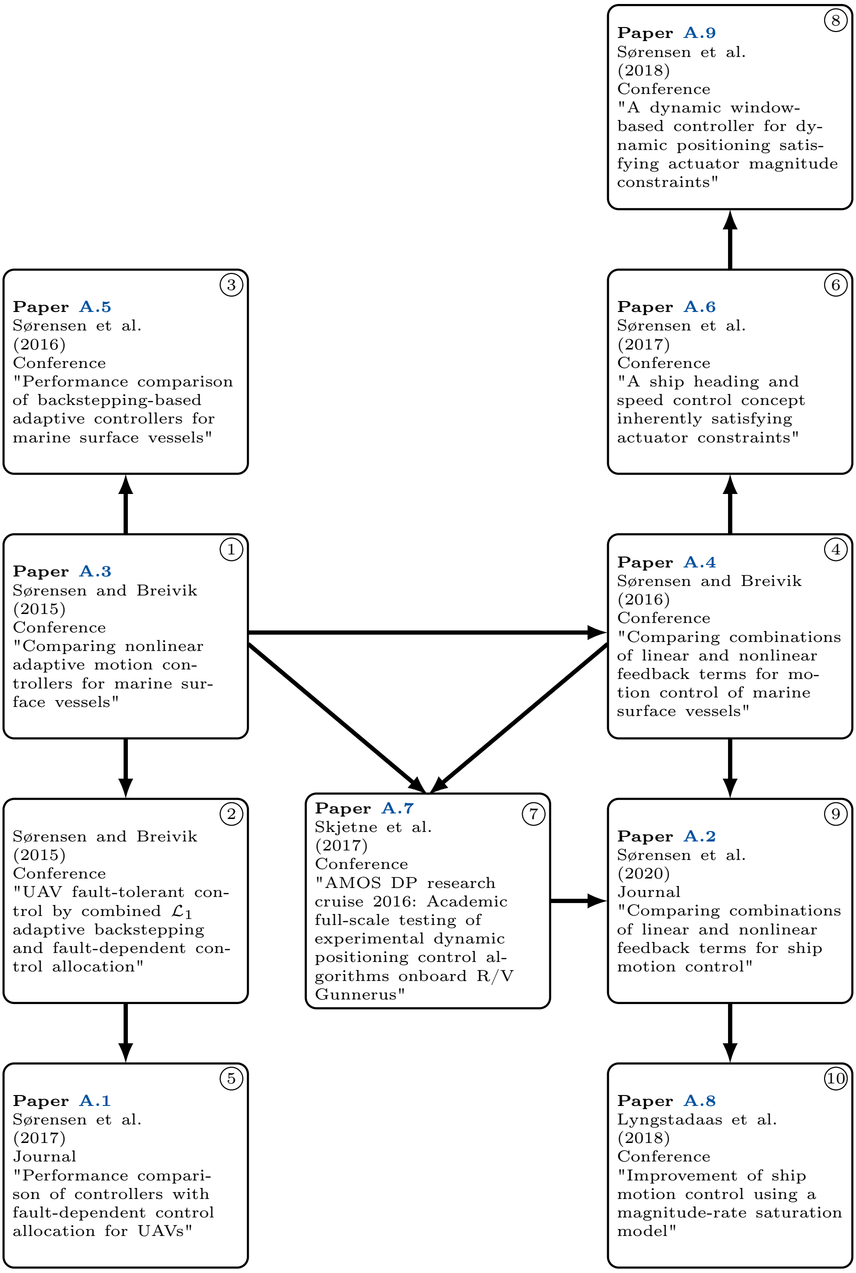

Figure 1.2: Causal relationships between the publications.

1.4 Thesis Outline

The structure of the thesis is as follows:

Chapter 2: Ship Modelling

This chapter starts out presenting a generic ship model with both kinematics and kinetics. In particular, the chapter presents modifications to two existing mathematical models of model-scale ships. This chapter is based on the work in:

- M. E. N. Sørensen, M. Breivik, and B.-O. H. Eriksen, A ship heading and speed control concept inherently satisfying actuator constraints, *in Proceedings of the 1st IEEE Conference on Control Technology and Applications, Hawai'i, USA*, 2017. Paper A.6.

- O. N. Lyngstadaas, T. E. Sæterdal, M. E. N. Sørensen and M. Breivik, Improvement of ship motion control using a magnitude-rate saturation model, *in Proceedings of the 2nd IEEE Conference on Control Technology and Applications, Copenhagen, Denmark*, 2018. Paper A.8.

- M. E. N. Sørensen, O. N. Lyngstadaas, B.-O. H. Eriksen and M. Breivik, A dynamic window-based controller for dynamic positioning satisfying actuator magnitude constraints, *in Proceedings of the 11th IFAC Conference on Control Applications in Marine Systems, Opatija, Croatia*, 2018. Paper A.9.

Chapter 3: Performance Metrics

Here the ideas behind performance metrics are described, in addition to illustrating which ones are normally used to evaluate the performance of a controller and how one can benefit by using the proposed performance metrics. Publications related to this chapter are:

- M. E. N. Sørensen, S. Hansen, M. Breivik and M. Blanke, Performance comparison of controllers with fault-dependent control allocation for UAVs, *Journal of Intelligent & Robotic Systems*, 87(1):187–207, 2017. Paper A.1.

- M. E. N. Sørensen and M. Breivik, Comparing nonlinear adaptive motion controllers for marine surface vessels, *in Proceedings of the 10th IFAC Conference on Manoeuvring and Control of Marine Craft, Copenhagen, Denmark*, 2015. Paper A.3.

- M. E. N. Sørensen, E. S. Bjørne and M. Breivik, Performance comparison of backstepping-based adaptive controllers for marine surface vessels, *in Proceedings of the IEEE Multi-Conference on Systems and Control, Buenos Aires, Argentina*, 2016. Paper A.5.

- O. N. Lyngstadaas, T. E. Sæterdal, M. E. N. Sørensen and M. Breivik, Improvement of ship motion control using a magnitude-rate saturation model, *in Proceedings of the 2nd IEEE Conference on Control Technology and Applications, Copenhagen, Denmark*, 2018. Paper A.8.

Chapter 4: Cascaded Nonlinear Feedback Control

In this chapter, the use of nonlinear feedback terms for control is investigated. Different combinations of linear and nonlinear feedback terms are analysed. The difference between the use of symmetric and asymmetric nonlinear feedback terms is also considered. The relevant publications are:

- M. E. N. Sørensen, M. Breivik, and R. Skjetne, Comparing combinations of linear and nonlinear feedback terms for ship motion control, *IEEE Access*, vol. 8, pp. 193813-193826, 2020. Paper A.2.
- M. E. N. Sørensen and M. Breivik, Comparing combinations of linear and nonlinear feedback terms for motion control of marine surface vessels, *in Proceedings of the 10th IFAC Conference on Control Applications in Marine Systems, Trondheim, Norway*, 2016. Paper A.4.

Chapter 5: Simplified Dynamic Window Algorithm

In this chapter, a simplification of a dynamic window algorithm [21] is used as a controller to handle the magnitude constraints of the actuators. Both high-speed and low-speed algorithms are presented, which are based on the following articles:

- M. E. N. Sørensen, M. Breivik, and B.-O. H. Eriksen, A ship heading and speed control concept inherently satisfying actuator constraints, *in Proceedings of the 1st IEEE Conference on Control Technology and Applications, Hawai'i, USA*, 2017. Paper A.6.
- M. E. N. Sørensen, O. N. Lyngstadaas, B.-O. H. Eriksen and M. Breivik, A dynamic window-based controller for dynamic positioning satisfying actuator magnitude constraints, *in Proceedings of the 11th IFAC Conference on Control Applications in Marine Systems, Opatija, Croatia*, 2018. Paper A.9.

Chapter 6: Adaptive Control

A survey of adaptive control concepts are presented in this chapter. The results are based on the following publications:

- M. E. N. Sørensen, S. Hansen, M. Breivik and M. Blanke, Performance comparison of controllers with fault-dependent control allocation for UAVs, *Journal of Intelligent & Robotic Systems*, 87(1):187–207, 2017. Paper A.1.
- M. E. N. Sørensen and M. Breivik, Comparing nonlinear adaptive motion controllers for marine surface vessels, *in Proceedings of the 10th IFAC Conference on Manoeuvring and Control of Marine Craft, Copenhagen, Denmark*, 2015. Paper A.3.
- M. E. N. Sørensen, E. S. Bjørne and M. Breivik, Performance comparison of backstepping-based adaptive controllers for marine surface vessels, *in Proceedings of the IEEE Multi-Conference on Systems and Control, Buenos Aires, Argentina*, 2016. Paper A.5.

Chapter 7: Experimental Work

This chapter presents and discusses the experimental work that has been conducted to verify and validate the performance of the controller. Both model-scale experiments in an ocean basin and full-scale experiments are considered. The chapter is based on the following articles:

- M. E. N. Sørensen, M. Breivik, and R. Skjetne, Comparing combinations of linear and nonlinear feedback terms for ship motion control, *IEEE Access*, vol. 8, pp. 193813-193826, 2020. Paper A.2.
- M. E. N. Sørensen and M. Breivik, Comparing combinations of linear and nonlinear feedback terms for motion control of marine surface vessels, *in Proceedings of the 10th IFAC Conference on Control Applications in Marine Systems, Trondheim, Norway*, 2016. Paper A.4.
- R. Skjetne, M. E. N. Sørensen, M. Breivik, S. A. T. Værnø, A. H. Brodtkorb, A. J. Sørensen, Ø. K. Kjerstad, V. Calabrò and B. O. Vinje, AMOS DP research cruise 2016: Academic full-scale testing of experimental dynamic positioning control algorithms onboard R/V Gunnerus, *in Proceedings of the 36th International Conference on Ocean, Offshore and Arctic Engineering,Trondheim, Norway*, 2017. Paper A.7.
- O. N. Lyngstadaas, T. E. Sæterdal, M. E. N. Sørensen and M. Breivik, Improvement of ship motion control using a magnitude-rate saturation model, *in Proceedings of the 2nd IEEE Conference on Control Technology and Applications, Copenhagen, Denmark*, 2018. Paper A.8.

Chapter 8: Concluding Remarks and Future Work

This chapter draws conclusions on the results of the thesis and presents suggestions for future work.

Appendix A: Original Publications

This appendix is composed of the full text of the nine published and submitted articles included in this thesis.

Chapter 2

Ship Modelling

2.1 Kinematics and Kinetics

The motion of a ship can be mathematically described by six degrees of freedom (6 DOF). In particular, the ship can be described by three linear velocities (u, v, w) and three angular velocities (p, q, r). All these motions are more commonly known as surge, sway, heave, roll, pitch, and yaw, respectively. Assuming that the ship is longitudinal and lateral metacentric stable for small amplitudes of $\phi \approx \theta \approx p \approx q \approx 0$, where ϕ and θ are the roll and pitch angle, respectively, the dynamics associated with the roll and pitch motion can be neglected. It is also reasonable to assume that the ship will have $w \approx z \approx 0$ on average, which means that the heave motion also can be disregarded. The resulting dynamics is a 3 DOF horizontal motion of a ship for the purpose of manoeuvring.

If we let an inertial frame be approximated by an earth-fixed reference frame and a body-fixed frame be attached to the ship, then the ship can be represented by the pose vector $\boldsymbol{\eta} = [x, y, \psi]^\top \in \mathbb{R}^2 \times \mathbb{S}$, where $\mathbb{S} = [-\pi, \pi)$ and the velocity vector $\boldsymbol{\nu} = [u, v, r]^\top \in \mathbb{R}^3$. Here, (x, y) represents the Cartesian position in the local reference frame, ψ is the yaw angle, (u, v) represents the body-fixed linear velocities and r is the yaw rate.

The 3 DOF dynamics of a ship can be expressed as [18]:

$$\dot{\boldsymbol{\eta}} = \boldsymbol{R}(\psi)\boldsymbol{\nu} \tag{2.1}$$

$$\boldsymbol{M}\dot{\boldsymbol{\nu}} + \boldsymbol{C}(\boldsymbol{\nu})\boldsymbol{\nu} + \boldsymbol{D}(\boldsymbol{\nu})\boldsymbol{\nu} = \boldsymbol{\tau}, \tag{2.2}$$

where $\boldsymbol{M} \in \mathbb{R}^{3\times3}$, $\boldsymbol{C}(\boldsymbol{\nu}) \in \mathbb{R}^{3\times3}$, $\boldsymbol{D}(\boldsymbol{\nu}) \in \mathbb{R}^{3\times3}$ and $\boldsymbol{\tau} = [\tau_1, \tau_2, \tau_3]^\top$ represent the inertia matrix, Coriolis and centripetal matrix, damping matrix and control input vector, respectively. The rotation matrix $\boldsymbol{R}(\psi) \in SO(3)$ is given by

$$\boldsymbol{R}(\psi) = \begin{bmatrix} \cos(\psi) & -\sin(\psi) & 0 \\ \sin(\psi) & \cos(\psi) & 0 \\ 0 & 0 & 1 \end{bmatrix}. \tag{2.3}$$

The system matrices are assumed to satisfy the properties $\boldsymbol{M} = \boldsymbol{M}^\top > 0$, $\boldsymbol{C}(\boldsymbol{\nu}) = -\boldsymbol{C}(\boldsymbol{\nu})^\top$ and $\boldsymbol{D}(\boldsymbol{\nu}) > 0$.

The inertia matrix is given as

$$\boldsymbol{M} \triangleq \boldsymbol{M}_{RB} + \boldsymbol{M}_A, \tag{2.4}$$

where

$$\boldsymbol{M}_{RB} = \begin{bmatrix} m & 0 & 0 \\ 0 & m & mx_g \\ 0 & mx_g & I_z \end{bmatrix} \tag{2.5}$$

$$\boldsymbol{M}_A = \begin{bmatrix} -X_{\dot{u}} & 0 & 0 \\ 0 & -Y_{\dot{v}} & -Y_{\dot{r}} \\ 0 & -N_{\dot{v}} & -N_{\dot{r}} \end{bmatrix}, \tag{2.6}$$

and m represents the mass of the ship, while x_g is the distance along the x-axis in the body from the centre of gravity and I_z is the moment of inertia about the z-axis in the body frame. The Coriolis and centripetal matrix is given as

$$\boldsymbol{C}(\boldsymbol{\nu}) \triangleq \mathbf{C}_{RB}(\boldsymbol{\nu}) + \mathbf{C}_A(\boldsymbol{\nu}), \tag{2.7}$$

with

$$\boldsymbol{C}_{RB}(\boldsymbol{\nu}) = \begin{bmatrix} 0 & 0 & -m(x_g r + v) \\ 0 & 0 & mu \\ m(x_g r + v) & -mu & 0 \end{bmatrix} \tag{2.8}$$

$$\boldsymbol{C}_A(\boldsymbol{\nu}) = \begin{bmatrix} 0 & 0 & c_{13}(\boldsymbol{\nu}) \\ 0 & 0 & c_{23}(\boldsymbol{\nu}) \\ -c_{13}(\boldsymbol{\nu}) & -c_{23}(\boldsymbol{\nu}) & 0 \end{bmatrix}, \tag{2.9}$$

where $c_{13}(\boldsymbol{\nu}) = Y_{\dot{v}} v + \frac{1}{2}(N_{\dot{v}} + Y_{\dot{r}})r$ and $c_{23}(\boldsymbol{\nu}) = -X_{\dot{u}} u$. Finally, the damping matrix $\boldsymbol{D}(\boldsymbol{\nu})$ is given as

$$\boldsymbol{D}(\boldsymbol{\nu}) \triangleq \boldsymbol{D}_L + \boldsymbol{D}_{NL}(\boldsymbol{\nu}), \tag{2.10}$$

where

$$\boldsymbol{D}_L = \begin{bmatrix} -X_u & 0 & 0 \\ 0 & -Y_v & -Y_r \\ 0 & -N_v & -N_r \end{bmatrix} \tag{2.11}$$

$$\boldsymbol{D}_{NL}(\boldsymbol{\nu}) = \begin{bmatrix} d_{11}(\boldsymbol{\nu}) & 0 & 0 \\ 0 & d_{22}(\boldsymbol{\nu}) & d_{23}(\boldsymbol{\nu}) \\ 0 & d_{32}(\boldsymbol{\nu}) & d_{33}(\boldsymbol{\nu}) \end{bmatrix}, \tag{2.12}$$

with

$$d_{11}(\boldsymbol{\nu}) = -X_{|u|u}|u| - X_{uuu}u^2 \tag{2.13}$$
$$d_{22}(\boldsymbol{\nu}) = -Y_{|v|v}|v| - Y_{|r|v}|r| \tag{2.14}$$
$$d_{23}(\boldsymbol{\nu}) = -Y_{|v|r}|v| - Y_{|r|r}|r| \tag{2.15}$$
$$d_{32}(\boldsymbol{\nu}) = -N_{|v|v}|v| - N_{|r|v}|r| \tag{2.16}$$
$$d_{33}(\boldsymbol{\nu}) = -N_{|v|r}|v| - N_{|r|r}|r|. \tag{2.17}$$

2.2 Modifications to CyberShip II

Most ships are fully actuated during low speed maneuvers. However, under high speed maneuvers the ship will become underactuated, since the sway-motion becomes diffucult to control while the ship is at higher speeds. We have therefore excluded the bow thrusters from the actuator model since they lose their effectiveness under these conditions. Inspired by [37], the modified ship actuator forces and moments can be modelled using two thrusters $\boldsymbol{n} = [n_1, n_2]^\top \in \mathbb{R}^2$ with revolutions per minute (RPM) and two rudder angles $\boldsymbol{\delta} = [\delta_1, \delta_2]^\top \in {\mathbb{S}^1}^2$. These are related to the input vector $\boldsymbol{\tau}$ through the actuator model

$$\boldsymbol{\tau}(\boldsymbol{\nu}, \boldsymbol{n}, \boldsymbol{\delta}) = \boldsymbol{B}\boldsymbol{\tau}_{act}(\boldsymbol{\nu}, \boldsymbol{n}, \boldsymbol{\delta}), \tag{2.18}$$

where $\boldsymbol{B} \in \mathbb{R}^{3\times 4}$ is an actuator configuration matrix. The function $\boldsymbol{\tau}_{act} : \mathbb{R}^3 \times \mathbb{R}^2 \times {\mathbb{S}^1}^2 \to \mathbb{R}^4$ relates the actuator variables $\boldsymbol{n}$ and $\boldsymbol{\delta}$ to the input vector $\boldsymbol{\tau}$ for a given velocity $\boldsymbol{\nu}$. Here, we assume that $n_1 = n_2$ and $\delta_1 = \delta_2$. We will only consider the control of the surge and yaw motion, since our model is underactuated.

Using this ship model, we map the steady-state solution of (2.2) associated with a given control input. In particular, the blue asterisks in Figure 2.1 represent the steady-state solutions for a set of uniformly distributed control inputs. Specifically, $\boldsymbol{n} \in [0, 2000]$ $[RPM]$ and is increased by 100 $[RPM]$ per increment, while $\boldsymbol{\delta} \in [-31.579, 31.579]$ $[deg]$ and is increased by 3.1579 $[deg]$ per increment. Analysing the model from [37], it is concluded that the modelled Munk moment, which is a destabilizing factor, gives rise to physically impossible motion. In this model, the equilibrium point at $r = 0$ is unstable, which is not consistent with the actual behavior of CyberShip II.

In [31], an analysis on how to accommodate for the Munk moment on an autonomous underwater vehicle (AUV) is made. It is suggested to add damping terms to the damping matrix that are linearly increasing with the forward speed. Based on the observation in [31], we change (2.15)-(2.17) to

$$d_{23}(\boldsymbol{\nu}) = -Y_{|v|r}|v| - Y_{|r|r}|r| - Y_{ur}u \tag{2.19}$$
$$d_{32}(\boldsymbol{\nu}) = -N_{|v|v}|v| - N_{|r|v}|r| - N_{uv}u \tag{2.20}$$
$$d_{33}(\boldsymbol{\nu}) = -N_{|v|r}|v| - N_{|r|r}|r| - N_{ur}u, \tag{2.21}$$

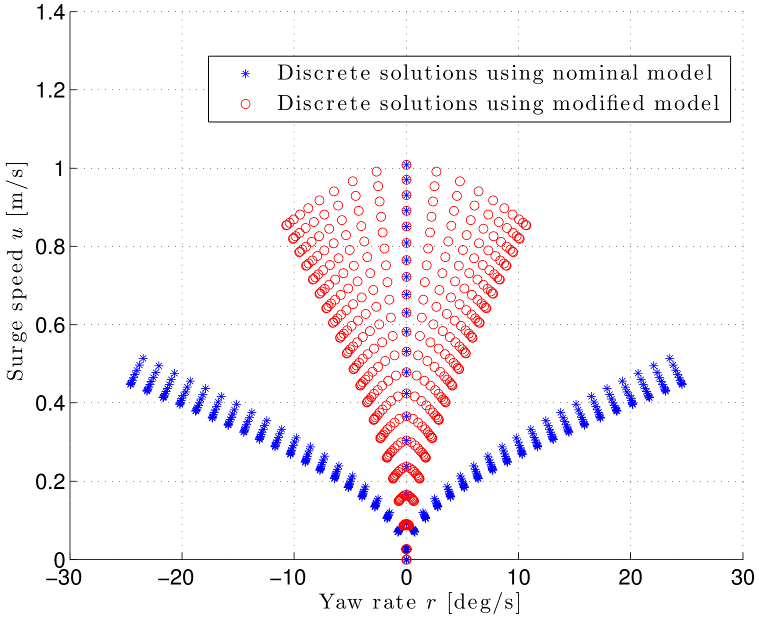

Figure 2.1: Possible combinations of surge speed and yaw rate using the same control inputs for the nominal model [37] (blue) and the modified model based on [31] (red).

where

$$Y_{ur} = X_{\dot{u}} \tag{2.22}$$
$$N_{uv} = -(Y_{\dot{v}} - X_{\dot{u}}) \tag{2.23}$$
$$N_{ur} = Y_{\dot{r}}, \tag{2.24}$$

to get a more physically realistic model behavior. The red circles in Figure 2.1 show the steady-state solutions for the combined [37] and [31] model using the same set of control inputs as previously. The steady-state response of this modified model qualitatively corresponds to the experimentally derived response of a high-speed vessel in [16].

2.3 Modifications to CyberShip Inocean Cat I Drillship

In [8], a ship model for CyberShip Inocean Cat I Drillship (CSAD), shown in Figure 2.2, is presented. However, analysing the steady-state point of the model, it is observed that there are some parameters which have the wrong sign or have a small influence on the model. These parameters are updated in Paper A.8 and A.9 to correspond better to the actual physical behavior of CSAD. In Table 2.1 the parameters of the ship from both [8] and Paper A.8 are presented. The parameters

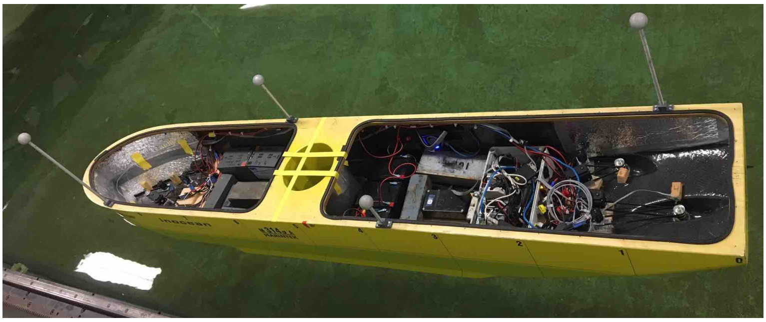

Figure 2.2: CyberShip Inocean Cat I Arctic Drillship in the Marine Cybernetics Laboratory at NTNU.

in Table 2.1 that are marked in bold are the ones that differ from the values presented in [8].

Further development of the model is done in [28], where the model in Paper A.8 is compared with experimental data and the model parameters are updated to match the behavior of the real ship. These updated parameters are also displayed in Table 2.1. In [28], step response tests for the surge, sway and yaw are conducted for the original model from Paper A.8 with experiment data. The results are shown in Figure 2.3. Additionally, the modified model from [28] is also plotted on this figure. The spikes in these figures are caused by a combination of a poorly calibrated laboratory camera positioning system and a velocity estimator which was not designed to handle the poor calibration.

Parameter	**Values from [8]**	**Values from Paper A.8**	**Values from [28]**
L	2.578	2.578	2.578
m	127.92	127.92	127.92
x_g	0	**0.0375**	**0.0375**
I_z	61.967	61.967	61.967
$X_{\dot{u}}$	-3.262	-3.262	**-10**
$Y_{\dot{v}}$	28.89	**-28.89**	**-105**
$Y_{\dot{r}}$	0.525	**-0.525**	**-0.525**
$N_{\dot{v}}$	0.157	**-0.157**	**-0.157**
$N_{\dot{r}}$	13.98	**-13.98**	**-13.98**
X_u	-2.332	-2.332	**-5.35**
$X_{\|u\|u}$	0	0	0
X_{uuu}	-8.557	-8.557	**-19.6312**
Y_v	-4.673	-4.673	**-10.16**
$Y_{\|v\|v}$	0.3967	**-0.3967**	**-0.8647**
Y_{vvv}	-313.3	-313.3	**-681.1745**
N_v	0	0	0
$N_{\|v\|v}$	-0.2088	-0.2088	-0.2088
Y_r	-7.25	-7.25	-7.25
$Y_{\|r\|r}$	-3.45	-3.45	-3.45
N_r	-0.0168	**-6.916**	**-14.55**
$N_{\|r\|r}$	-0.0115	**-4.734**	**-9.9597**
N_{rrr}	-0.000358	**-0.147**	**-0.3101**
$N_{\|v\|r}$	0.08	0.08	0.08
$N_{\|r\|v}$	0.08	0.08	0.08
$Y_{\|v\|r}$	-0.845	-0.845	-0.845
$Y_{\|r\|v}$	-0.805	-0.805	-0.805

Table 2.1: Numerical values for the ship model parameters for CSAD.

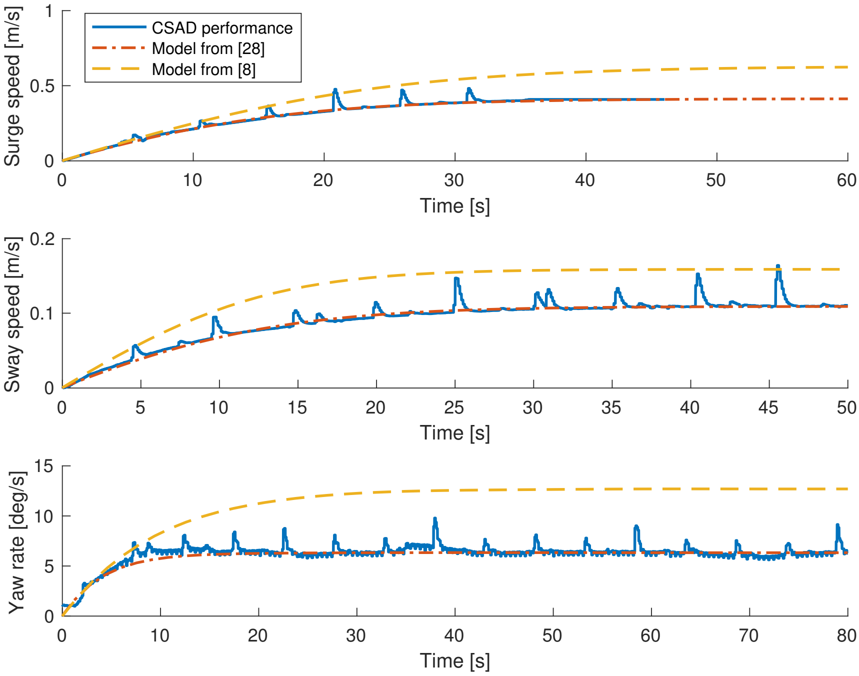

Figure 2.3: Surge speed, sway speed and yaw rate for the updated CSAD models with maximum force and moment as input. Courtesy of [28].

Chapter 3

Performance Metrics

3.1 Background

To evaluate and compare the performance of different control algorithms, evaluation criteria are introduced. It is often seen in the literature of marine control systems that the performance evaluation of the controller is done by plotting the control error and command control input. However, a large amount of information is lost when considering only these plots. Another criterion presented here to evaluate the performance is to determine whether a control system is stable or not and, if it is, what kind of stability it is.

The written history of performance measures dates back to 1942, which is the earliest date of any published material on the topic. This specific publication is [30], where the method of the derivative area to measure the control error is proposed for the first time, although not in an explicit mathematical form of a metric. Here, the derivative area is obtained by first writing the differential equation which describes the system as

$$a_0 \frac{d^n x}{dt^n} + a_1 \frac{d^{n-1} x}{dt^{n-1}} + ... + a_n x = 0. \tag{3.1}$$

Integration of (3.1) results in

$$0 = a_0 \left. \frac{d^{n-1} x}{dt^{n-1}} \right|_0^\infty + a_1 \left. \frac{d^{n-2} x}{dt^{n-2}} \right|_0^\infty + ... + a_{n-1} x \Big|_0^\infty + a_n F, \tag{3.2}$$

and, solving for F,

$$F = -\frac{1}{a_n} \left(a_0 \left. \frac{d^{n-1} x}{dt^{n-1}} \right|_0^\infty + a_1 \left. \frac{d^{n-2} x}{dt^{n-2}} \right|_0^\infty + ... + a_{n-1} x \Big|_0^\infty \right). \tag{3.3}$$

It concluded that a system has a good performance if the area F is small. Using F as a metric, we are able to get a number which represents a measure of the error of the system.

In [23] further development of a metric which can evaluate the performance is suggested. The proposed metric is defined as

$$ISE \triangleq \int_0^t e^2(\sigma) d\sigma, \tag{3.4}$$

where

$$e(t) = r(t) - c(t), \tag{3.5}$$

with $e(t)$ being the control error, $r(t)$ the reference and $c(t)$ the output of the system. In order to evaluate the performance when the control error is a vector, it is better to normalize, or scale and normalize, the control error. The metric is known as the integral of the square of the error (ISE), which can only be positive or zero. An additional property of this metric is that it penalizes large errors more than small errors. This will provide a clear indication on how good the particular control algorithm is at eliminating large errors.

In [17] the integral of the absolute value of the error (IAE) is proposed as a measure of the system error . The metric is defined as

$$IAE \triangleq \int_0^t |e(\sigma)| d\sigma. \tag{3.6}$$

A modification to the IAE metric is presented in [22]. Here, the integral of time multiplied by absolute value of the error (ITAE) is displayed. It is defined as

$$ITAE \triangleq \int_0^t \sigma |e(\sigma)| d\sigma. \tag{3.7}$$

In this metric the time weighting serves to reduce the contribution of the large initial error, as well as to make an emphasis on the error that may still be there at the end of the simulation or experiment.

In [35], multiple variations of these performance metrics and the advantages and disadvantages are discussed.

In recent years the performance metrics have been used as a tool to tune controllers, especially in process engineering. In [29], the optimal tuning for a PID controller is found by using the ITAE as a criterion, where the focus is to minimize the end value of the performance metric. In [6], the ISE is used as the objective function for tuning PID controllers for a multimachine power system.

Although the performance metrics are nowadays used as tools for tuning controllers, this thesis will use them as a way to evaluate and compare various control algorithms.

3.2 Performance Metrics

All the performance metrics previously presented evaluate only the output regulation or tracking error. However, it would be interesting to see what effect the control input has on these performance metrics, since two different systems could have similar IAE performance but different energy consumption. An example that uses both the state and control signal to evaluate the performance is a linear quadratic regulator. Here, the sum of the weighted square of the state and control input is integrated as a cost functional to find the optimal control values. We have, on the other hand, chosen performance metrics as products of subobjectives in order to avoid mixed units in a sum of physical quantities. In Paper A.3, a new evaluation criterion is proposed, which combines the IAE performance metric with the energy consumption. The integral of the absolute value of the error multiplied by the energy consumption (IAEW) is defined as

$$IAEW \triangleq \int_0^t |e(\sigma)| d\sigma \int_0^t P(\sigma) d\sigma, \tag{3.8}$$

where $P(t)$ is the power consumption of the system. Here, we have chosen

$$P(t) = |\boldsymbol{\nu}(t)^\top \boldsymbol{\tau}(t)|, \tag{3.9}$$

which represents the mechanical power. The IAEW indicates which controller has the best combined control accuracy and energy efficiency in one single metric.

In Paper A.5, a combination of IAEW and an evaluation of how smooth the controller is based on how fast the control input $\boldsymbol{\tau}$ changes, thus including $\dot{\boldsymbol{\tau}}$, is proposed. If the control input is smooth, it is more realistic that the “wear and tear” of the actuator is reduced. Multiplying all these effects together gives the metric integral of the absolute error with work, wear and tear (IAEW-WT), which is defined as

$$IAEW\text{-}WT \triangleq \int_0^t |e(\sigma)| d\sigma \int_0^t P(\sigma) d\sigma \int_0^t |\dot{\boldsymbol{\tau}}(\sigma)| d\sigma, \tag{3.10}$$

where the change of control input is typically computed as

$$\dot{\boldsymbol{\tau}}(t) = \frac{\boldsymbol{\tau}(t) - \boldsymbol{\tau}(t-h)}{h}, \tag{3.11}$$

with h being the sample time.

The integral of absolute differentiated control (IADC), which is also used as part of the IAEW-WT, is suggested in [16] as a separate metric. This performance metric is defined as

$$IADC \triangleq \int_0^t |\dot{\boldsymbol{\tau}}(\sigma)| d\sigma. \tag{3.12}$$

The IADC penalizes control input changes and serves as a measure of actuator wear and tear.

3.3 Results and Discussion

Comparing various controllers with each other can be difficult when using only the error and control signal plots, while the performance metrics can display some additional information which can be hard or almost impossible to see on such plots. Moreover, the proposed performance metrics are able to show properties such as how energy efficient the considered controller is. When comparing multiple controllers the IAEW is an invaluable tool to determine the best suitable controller for the specific scenario. As previously stated, the IAEW uses the mechanical power to determine the energy consumption. However, when using this performance metric in an experimental setting it would be ideal to have the actual energy consumption of the actuators, since when the velocity is zero the mechanical power is also zero, but the electrical power might not be zero. It is possible to evaluate how much wear and tear a specific controller does on the actuator by using the performance metric IADC. Additionally, in a simulated scenario the IADC can indicate whether the considered controller can be implemented in an experimental setup or not. The performance metrics ISE and ITAE are useful to see how good the considered controller is at suppressing large control error and at handling steady state errors, respectively.

The performance metrics have shown to be a useful tool to evaluate the performance of various controllers, as described in the publications in Appendix A. All these metrics are typically visualized in two main ways, depending on the purpose: sometimes it can be useful to see how they develop over time, and some other times perhaps only the final value is of interest. As an example, Table 3.1 and Figure 3.1 present a comparison between the performance metrics for a nonlinear pose and velocity feedback controller, denoted NP-NV, and for a nonlinear pose and velocity feedback controller combined with a magnitude-rate saturation model, denoted NP-NV-MRS. It can be seen that NP-NV has a marginally better IAE performance than the NP-NV-MRS. However, it can be concluded that the NP-NV has a higher energy consumption and that the controller has more aggressive changes in the control signal than the NP-NV-MRS.

	NP-NV	**NP-NV-MRS**
IAE	**89.49**	90.38
IAEW	460.08	**403.79**
IADC	118.26	**63.34**

Table 3.1: Final value of the performance metrics.

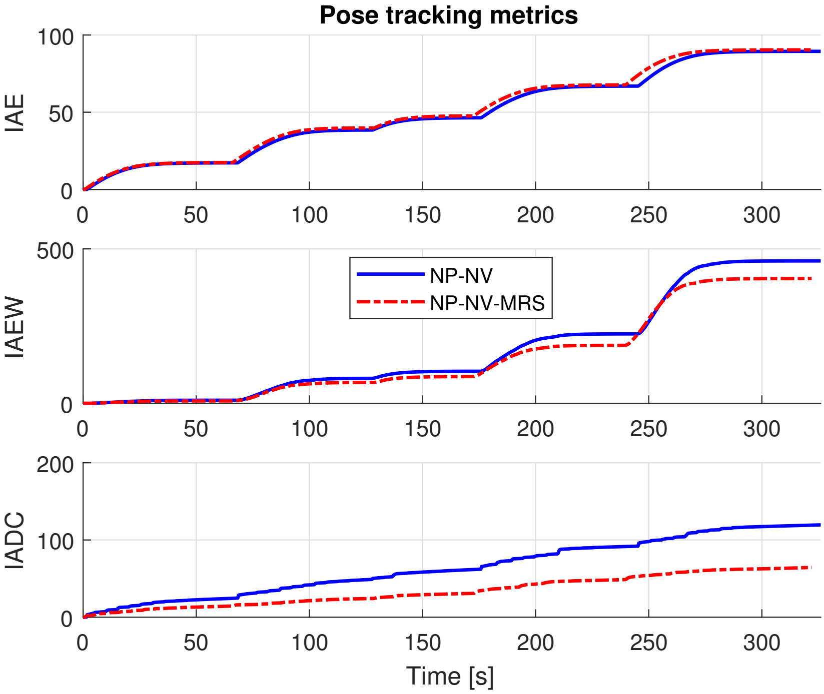

Figure 3.1: Graphical representation of the performance metrics. Originally shown in A.8.

Chapter 4

Linear and Nonlinear Feedback Control Concepts

4.1 Background

Nonlinear control algorithms that are found in the literature often have linear feedback terms, which result in nice globally exponential stability properties when assuming no actuator constraints. However, considering that all actuators have saturation constraints, such stability properties are not feasible in practice. Applying nonlinear feedback terms can be a step to handle such constraints. As a result, this chapter explores nonlinear feedback terms for both the kinematic and kinetic control loops. Stability properties and tuning rules for all the controllers are also provided. Interestingly, the use of nonlinear feedback terms gives the ability to constrain the feedback control inputs globally while simultaneously being able to change the convergence rates locally. The price to be paid is the introduction of additional tuning parameters.

The following control concepts will be explained using scalar examples.

4.2 Linear and Nonlinear Feedback Controllers

Here we investigate the use of nonlinear feedback terms and combine linear and nonlinear feedback terms for pose and velocity control of ships. In particular, the nonlinear feedback terms are developed based on constant bearing guidance principles, inspired by the guided dynamic positioning approach originally suggested in [11]. It should be noted that this section will consider scalar system to illustrate the development of the cascaded nonlinear feedback controllers.

A nonlinear pose feedback inspired by the constant bearing guidance concept is discussed in [9]. In [10] it is shown that the constant bearing guidance can also be implemented through the direct velocity assignment

$$v_d = v_t - \kappa(\bar{p})\frac{\bar{p}}{|\bar{p}|}, \tag{4.1}$$

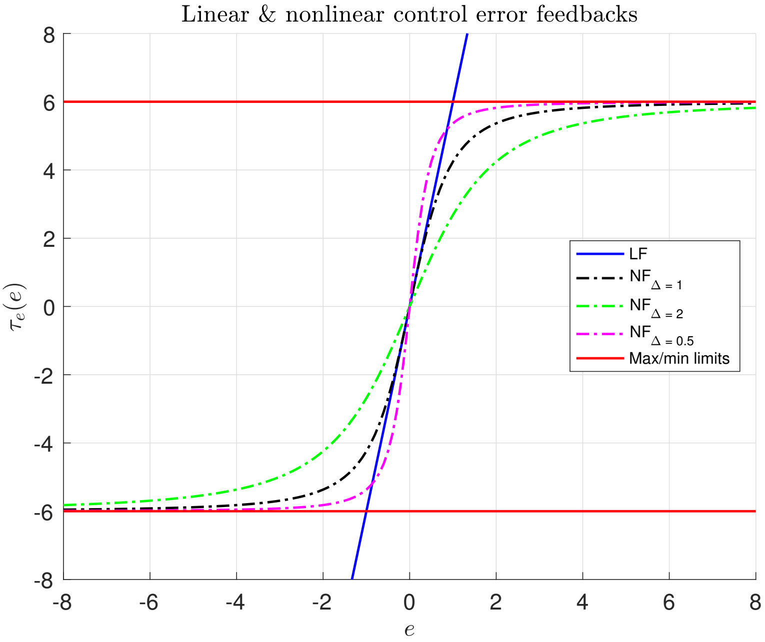

Figure 4.1: The abbreviation LF represents a linear feedback term as a function of the control error e, while NF represents a nonlinear feedback term based on a sigmoid function of e using a tuning parameter Δ, such as in (4.3) and (4.7).

where $v_t \in \mathbb{R}$ is the target velocity, and

$$\bar{p} \overset{\triangle}{=} p - p_t \tag{4.2}$$

is the line-of-sight between the interceptor position $p \in \mathbb{R}$ and the target position $p_t \in \mathbb{R}$. Additionally, $\kappa \geq 0$ can be chosen as

$$\kappa(\bar{p}) = v_{a,max} \frac{|\bar{p}|}{\sqrt{\bar{p}^2 + \Delta^2}}, \tag{4.3}$$

where $v_{a,max} > 0$ represents the maximum approach speed toward the target and $\Delta > 0$ is a tuning parameter that affects the transient convergence behavior between the interceptor and the target.

The result of using such nonlinear feedback is shown for a scalar error $e \in \mathbb{R}$ in Figure 4.1, where the effects of varying Δ gains are shown. The linear and nonlinear functions displayed in Figure 4.1 are respectively given as $\tau(e) = \kappa e$ (LF) and $\tau(e) = \kappa \frac{e}{\sqrt{e^2+\Delta}}$ (NF), where $\kappa = 6$.

A comparison of three cascaded controllers is made. The specific controllers employ linear feedback on both pose and velocity control error (LP-LV), nonlinear

	LP-LV	**NP-LV**	**NP-NV**
Pose error $\bar{p}$:	$p - p_t$	$p - p_t$	$p - p_t$
Velocity error $\bar{v}$:	$v - v_d$	$v - v_d$	$v - v_d$
Desired velocity v_d:	$v_t - v_{a,max}\bar{p}$	$v_t - v_{a,max}\frac{\bar{p}}{\sqrt{\bar{p}^2+\Delta_p^2}}$	$v_t - v_{a,max}\frac{\bar{p}}{\sqrt{\bar{p}^2+\Delta_p^2}}$
Desired acceleration a_d:	$a_t - v_{a,max}\bar{v}$	$a_t - v_{a,max}\Delta_p^2\frac{\bar{v}}{(\bar{p}^2+\Delta_p^2)^{3/2}}$	$a_t - v_{a,max}\Delta_p^2\frac{\bar{v}}{(\bar{p}^2+\Delta_p^2)^{3/2}}$
Control law τ:	$Ma_d + Dv_d - \Gamma_v\bar{v}$	$Ma_d + Dv_d - \Gamma_v\bar{v}$	$Ma_d + Dv_d - \Gamma_v\frac{\bar{v}}{\sqrt{\bar{v}^2+\Delta_v^2}}$
Stability properties:	UGES	UGAS and UES	UGAS and UES

Table 4.1: Cascaded control laws.

feedback on the pose control error and linear feedback control error (NP-LV) and nonlinear feedback for both the pose and velocity control errors (NP-NV), respectively. Here, $\Gamma_v > 0$ is the control gain for the velocity control error and a_t is the target acceleration. In Table 4.1 the control laws of the three controllers are listed, in order to show their differences.

The origin $(\bar{p}, \bar{v}) = (0, 0)$ of the LP-LV controller is proven to be uniformly globally exponentially stable (UGES), since both subsystems can be proven to be UGES and the controller satisfies the conditions for UGES of the cascaded system. See Paper A.2 for more details. In this paper, it is also shown that the origin $(\bar{p}, \bar{v}) = (0, 0)$ for the NP-LV and NP-NV controller is uniformly globally asymptotically stable (UGAS), and on each compact set $B \subset \mathbb{R}^2$ containing the origin, it is uniformly exponentially stable (UES). It should be noted that the stability for the NP-LV and NP-NV controller is elsewhere referred to as UGAS + uniformly semiglobally exponentially stable (USGES); see e.g. [19]. USGES implies that for each given compact set $B \subset \mathbb{R}^2$ the region of exponential convergence can be made to include B, typically by design of control parameters. In our case above, for each given $\Delta > 0$, exponential convergence is guaranteed on any compact set $B \subset \mathbb{R}^2$ (that is, B does not depend on Δ), but not for $B = \mathbb{R}^2$. Hence, we have called this UGAS + UES on any compact set B.

4.2.1 Suggested Tuning Rules

Based on knowledge gained from various simulation and experimental work, a set of suggested tuning rules has been developed in order to tune the suggested cascaded controller first presented in Paper A.2. Said rules are based on the time constants of the pose and velocity subsystems, which in turn are determined based on the control gain of the feedback terms in the linear regions. In the following, we define $\Gamma_p = v_{a,max}$. It is shown that the time constants are inversely proportional to the control gains, which means that the time constant for the pose dynamics can be defined as

$$\Gamma_p \triangleq T_p^{-1}, \tag{4.4}$$

where $T_p > 0$ is the time constant for the pose controller and $\Gamma_p > 0$ is the control gain. A similar observation can be made for the time constant of the velocity subsystem, which is then defined as

$$\Gamma_v \triangleq T_v^{-1}, \tag{4.5}$$

with $T_v > 0$. It is suggested to tune the two subsystems so that the velocity subsystem is faster than the pose subsystem. Hence, the velocity dynamics must have the smallest time constants of the two subsystems, that is

$$T_v < T_p. \tag{4.6}$$

This means that the velocity control gain must be larger than the pose gain in order to satisfy the inequality in (4.6). The Δ-values in the nonlinear feedback terms must also be chosen. Here the Δ-values scale the linear feedback gains, and therefore also the time constants of the linear region. Δ-values equal to 1 will result in the same responses as for the linear controllers in the linear region. If $\Delta > 1$ they will give a slower response in this region. If $\Delta < 1$ they will give a faster response. Hence, the Δ-values for the NP and NV feedback terms must be chosen such that the condition in (4.6) is not broken in the linear region. The linear region of the time constants for the NP and NV feedback terms will be $(\Gamma_p/\Delta_p)^{-1}$ and $(\Gamma_v/\Delta_v)^{-1}$.

4.3 Velocity-based Cascaded Control

It has been previously shown that a linear position feedback gives rise to a physically unrealistic behaviour. Motivated by the challenge of limiting the control signal, this section will propose a modification to the control design of the cascaded nonlinear feedback controller, shown in papers A.2 and A.4. Here, an asymmetric velocity assignment controller is suggested in order to handle a problem which may occur for the symmetric velocity assignment controller when doing target tracking. We will consider a scalar system to show the development of the modification to the control design of the cascaded nonlinear feedback controller.

4.3.1 Symmetric Cascaded Control

In Paper A.2 the nonlinear function in (4.3), inspired by the constant bearing guidance law in [12], is used as the feedback term in a cascaded motion control setup. This function is compared with its linear counterpart. Here, $\bar{p} = p_t - p$ is the position error, $v_{a,max} > 0$ represents the saturation term of (4.3), and $\Delta > 0$ is a constant control gain used to define the linear region of (4.3). $\bar{p}$ have been inverted compared to (4.2) to lessen the mathematical complexity of the following. The result of using such nonlinear feedback is shown in Figure 4.1, where the effects of various Δ gains are shown. However, other sigmoid-like functions such as

$$\kappa(\bar{p}) = v_{a,max} \tanh\left(\frac{\bar{p}}{\Delta}\right), \tag{4.7}$$

can be used to achieve a similar behavior. Using one of these nonlinear functions in a control law, the desired velocity can be assigned as

$$v_d = v_t + v_{a,max} \tanh\left(\frac{\bar{p}}{\Delta}\right), \tag{4.8}$$

where v_t is the velocity of the target. In addition, to be able to use (4.7) to control the system the corresponding acceleration must also be calculated. The desired acceleration can be expressed as

$$\begin{aligned} a_d &= \dot{v}_d && (4.9) \\ &= a_t + a_a(\bar{p}, \bar{v}) && (4.10) \end{aligned}$$

where

$$a_a(\bar{p}, \bar{v}) = v_{max} \left(1 - \tanh\left(\frac{\bar{p}}{\Delta}\right)^2\right) \frac{\bar{v}}{\Delta}. \tag{4.11}$$

Using the CLF for $\bar{v}$, which is defined as

$$V_2 = \frac{1}{2} M \bar{v}^2, \tag{4.12}$$

the control input can now be chosen as

$$\tau = M a_d + D v_d, \tag{4.13}$$

which makes the origin of the $\bar{v}$-dynamics UGAS. However, this is possible only if the given assumption of no internal uncertainties and no environmental disturbances are fulfilled. The control law in (4.13) then calculates the exact forces required to move the system according to the given velocity and acceleration assignment. The term Dv_d represents the steady-state term required to move at the desired velocity v_d, while Ma_d represents the transient term required to move towards the desired velocity v_d without overshoot or time delay. In a real world scenario (4.13) has to be modified to

$$\tau = M a_d + D v_d + \Gamma_2 \bar{v}, \tag{4.14}$$

since there will be uncertainties in the system.

4.3.2 Asymmetric Cascaded Control

In order to constrain the system, it is important that $v_{a,max}$ is chosen such that

$$v_{min} \leq v_d(v_t, \bar{p}) \leq v_{max} \tag{4.15}$$

is satisfied at all times, with v_{min} and v_{max} assumed to be constant. However, it is not trivial to choose $v_{a,max}$ because of the symmetric nature of the assignment (4.3) and (4.7). In particular, defining

$$\begin{aligned} v_{range} &\triangleq v_{max} - v_{min}, && (4.16) \\ v_{middle} &\triangleq (v_{max} - v_{min})/2 && (4.17) \\ v_{below}(v_t) &\triangleq v_{max} - v_t && (4.18) \\ v_{above}(v_t) &\triangleq v_t - v_{min}, && (4.19) \end{aligned}$$

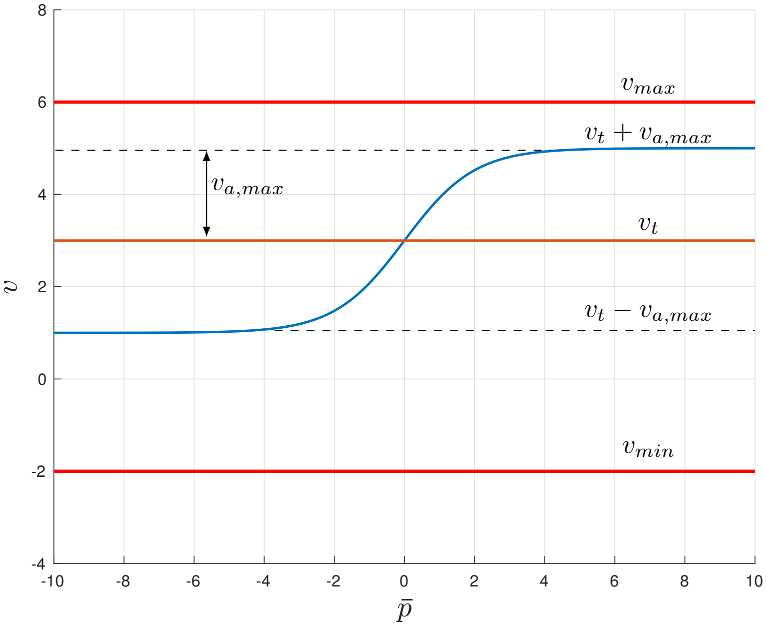

Figure 4.2: The velocity assignment (4.3) gives a nonlinear, symmetric velocity profile which has a predictable and smooth relative approach toward the target point.

we require that $v_{a,max}$ is a function of the target velocity such that

$$v_{a,max}(v_t) \leq \begin{cases} v_{below}(v_t) & \text{if } v_t > v_{middle} \\ v_{range}/2 & \text{if } v_t = v_{middle} \\ v_{above}(v_t) & \text{if } v_t < v_{middle} \end{cases} \tag{4.20}$$

in order to satisfy (4.15), see also Figure 4.2. It should be noted that it is assumed that $v_t \in (v_{min}, v_{max})$. Otherwise, it will generally not be possible to track the target.

In order to take advantage of the entire velocity range, an asymmetric velocity assignment relative to the target velocity is required. In particular, the following desired velocity is proposed

$$v_d(v_{range}, \bar{p}_m) = v_{min} + \frac{v_{range}}{2}\left(1 + \tanh\left(\frac{\bar{p}_m(\bar{p}, v_t)}{\Delta}\right)\right), \tag{4.21}$$

where v_{range} as defined in (4.16) represents the full velocity range available to the system, $\Delta > 0$ is a constant tuning gain, and

$$\bar{p}_m(\bar{p}, v_t) = \bar{p} + \bar{p}_o(v_t) \tag{4.22}$$

is a modified position error which can shift the velocity profile along the horizontal $\bar{p}$-axis so that it intersects the vertical v-axis in v_t to satisfy the basic criterion

$$v_d(v_t, \bar{p} = 0) = v_t, \tag{4.23}$$

by using the offset

$$\bar{p}_o(v_t) = \Delta \text{atanh}\left(\frac{2v_{above}(v_t)}{v_{range}} - 1\right) \tag{4.24}$$

see also Figure 4.3.

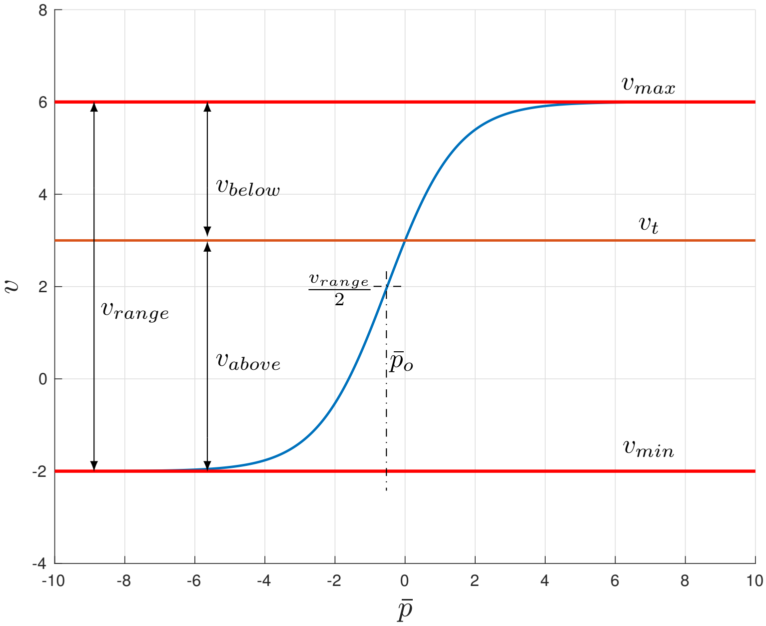

Figure 4.3: The velocity assignment (4.21) which is asymmetric about the target velocity and which takes advantage of the entire velocity range.

Notice that the only tuning variable in this velocity assignment is Δ, which decides how steep the assignment should be as a function of the position error $\bar{p}$. The remaining constants of this assignment are automatically decided by v_{min}, v_{max} and v_t. Taking the time derivative of (4.21) the desired acceleration becomes

$$a_d(v_{range}, \bar{p}_m, \bar{v}_m) = \frac{v_{range}}{2}\left(1 - \tanh\left(\frac{\bar{p}_m(\bar{p}, v_t)}{\Delta}\right)^2\right)\frac{\bar{v}_m(\bar{v}, a_t)}{\Delta} \tag{4.25}$$

where

$$\bar{v}_m(\bar{v}, a_t) = \bar{v} + \bar{v}_o(a_t) \tag{4.26}$$

with

$$\bar{v}_o(a_t) = \frac{\Delta}{2} \frac{a_t}{v_{above}(1 - v_{above}/v_{range})}. \tag{4.27}$$

The control input chosen for the asymmetric cascaded controller is the same one previously introduced for the symmetric controller, that is (4.13).

4.3.3 3 DOF Extensions of the Velocity-based Cascaded Controllers

These two control laws are now extended to control the 3 DOFs surge, sway and yaw. We start by defining the error variables $\boldsymbol{z}_1$ and $\boldsymbol{z}_2$ as

$$\boldsymbol{z}_1 \triangleq \boldsymbol{R}^\top(\boldsymbol{\eta}_t - \boldsymbol{\eta}) \tag{4.28}$$

$$\boldsymbol{z}_2 \triangleq \boldsymbol{\alpha} - \boldsymbol{\nu}. \tag{4.29}$$

Here, $\boldsymbol{\eta}_t$ is the pose associated with a target point, the rotation matrix $\boldsymbol{R}$ is defined in (2.3) and $\boldsymbol{\alpha}$ is a vector of stabilising functions, which can be interpreted as a desired velocity. By taking the time derivative of (4.28) we get

$$\dot{\boldsymbol{z}}_1 = \boldsymbol{S}^\top \boldsymbol{z}_1 - \boldsymbol{\nu} + \boldsymbol{R}^\top \dot{\boldsymbol{\eta}}_t, \tag{4.30}$$

where

$$\boldsymbol{S} = \begin{bmatrix} 0 & -r & 0 \\ r & 0 & 0 \\ 0 & 0 & 0 \end{bmatrix}. \tag{4.31}$$

The desired velocity in (4.8) is used as the base to expand the symmetric cascaded control concept to a 3 DOF system by choosing the vector of stabilising functions as

$$\boldsymbol{\alpha} = \boldsymbol{v}_{a,max} \tanh\left(\boldsymbol{\Delta}^{-1}\boldsymbol{z}_1\right) + \boldsymbol{R}^\top \dot{\boldsymbol{\eta}}_t, \tag{4.32}$$

where $\boldsymbol{v}_{a,max} > 0$ and $\boldsymbol{\Delta} > 0$. The time derivative of (4.32) becomes

$$\dot{\boldsymbol{\alpha}} = \dot{\boldsymbol{\alpha}}_1 + \boldsymbol{R}^\top \ddot{\boldsymbol{\eta}}_t + \boldsymbol{S}^\top \boldsymbol{R}^\top \dot{\boldsymbol{\eta}}_t, \tag{4.33}$$

where

$$\dot{\boldsymbol{\alpha}}_1 = \begin{bmatrix} v_{a,max,1} \left(1 - \tanh\left(\frac{z_{1,1}}{\Delta_1}\right)^2\right) \frac{\dot{z}_{1,1}}{\Delta_1} \\ v_{a,max,2} \left(1 - \tanh\left(\frac{z_{1,2}}{\Delta_2}\right)^2\right) \frac{\dot{z}_{1,2}}{\Delta_2} \\ v_{a,max,3} \left(1 - \tanh\left(\frac{z_{1,3}}{\Delta_3}\right)^2\right) \frac{\dot{z}_{1,3}}{\Delta_3} \end{bmatrix}, \tag{4.34}$$

Using the CLF

$$V_2 = \frac{1}{2}\boldsymbol{z}_2^\top \boldsymbol{M} \boldsymbol{z}_2, \tag{4.35}$$

the control input can now be chosen as

$$\boldsymbol{\tau} = \boldsymbol{M}\dot{\boldsymbol{\alpha}} + \boldsymbol{D}\boldsymbol{\alpha}. \tag{4.36}$$

It should be noted that it is assumed that the system is perfectly known, such that the control laws in (4.36) do not need an additional feedback term.

Introducing the asymmetric cascaded control concept to the pose control part, the vector of stabilising functions can be chosen as

$$\boldsymbol{\alpha} = \begin{bmatrix} V_{min,1} + v_{range,1}\tanh\left(\frac{z_{m,1}}{\Delta_1}\right) \\ V_{min,2} + v_{range,2}\tanh\left(\frac{z_{m,2}}{\Delta_2}\right) \\ V_{min,3} + v_{range,3}\tanh\left(\frac{z_{m,3}}{\Delta_3}\right) \end{bmatrix}, \tag{4.37}$$

where

$$\boldsymbol{z}_m = \begin{bmatrix} z_{1,1} + \Delta_1\tanh^{-1}\left(\frac{2v_{above,1}}{v_{range,1}} - 1\right) \\ z_{1,2} + \Delta_2\tanh^{-1}\left(\frac{2v_{above,2}}{v_{range,2}} - 1\right) \\ z_{1,3} + \Delta_3\tanh^{-1}\left(\frac{2v_{above,3}}{v_{range,3}} - 1\right) \end{bmatrix}. \tag{4.38}$$

Taking the time derivative of (4.37) we get

$$\dot{\boldsymbol{\alpha}} = \begin{bmatrix} \frac{v_{above,1}}{2}\left(1 - \tanh\left(\frac{z_{m,1}}{\Delta_1}\right)^2\right)\frac{\dot{z}_{m,1}}{\Delta_1} \\ \frac{v_{above,2}}{2}\left(1 - \tanh\left(\frac{z_{m,2}}{\Delta_2}\right)^2\right)\frac{\dot{z}_{m,2}}{\Delta_2} \\ \frac{v_{above,3}}{2}\left(1 - \tanh\left(\frac{z_{m,3}}{\Delta_3}\right)^2\right)\frac{\dot{z}_{m,3}}{\Delta_3}, \end{bmatrix} \tag{4.39}$$

where

$$\dot{\boldsymbol{z}}_m = \begin{bmatrix} \dot{z}_{1,1} + \frac{\Delta_1}{2}\frac{a_{t,1}}{v_{above,1}\left(1-\frac{v_{above,1}}{v_{range,1}}\right)} \\ \dot{z}_{1,2} + \frac{\Delta_2}{2}\frac{a_{t,2}}{v_{above,2}\left(1-\frac{v_{above,2}}{v_{range,2}}\right)} \\ \dot{z}_{1,3} + \frac{\Delta_3}{2}\frac{a_{t,3}}{v_{above,3}\left(1-\frac{v_{above,3}}{v_{range,3}}\right)} \end{bmatrix}, \tag{4.40}$$

and

$$\boldsymbol{a}_t = \boldsymbol{R}^\top\ddot{\boldsymbol{\eta}}_t + \boldsymbol{S}^\top\boldsymbol{R}^\top\dot{\boldsymbol{\eta}}_t. \tag{4.41}$$

The control law is chosen as in (4.36).

4.4 Results and Discussion

In papers A.2 and A.4, an investigation is presented on what influence nonlinear feedback terms have on the performance compared to linear feedback terms. This is done both through simulations and small scale experiments. It is shown that introducing a nonlinear feedback term to the pose controller has a larger impact on the performance than introducing a nonlinear feedback term to the velocity controller. The control system with a nonlinear feedback pose controller and a linear feedback velocity controller has shown to be the best of the considered combinations, since it has the best energy efficiency as shown by the IAEW metric, and it is close to the best tracking performance as shown by the IAE metric.

In addition to the results shown in papers A.2 and A.4, a comparison between using a symmetric or asymmetric cascaded controller is done through simulation. The specific task of the ship is to track a straight-line motion where the target is given a piecewise constant velocity that starts at $v_t(t) = v_{max}/4$ and after 100 seconds it increases to $v_t(t) = 3v_{max}/4$. Both the ship and the target start at rest. The target motion is given as

$$x_t(t) = v_t t \cos(\phi_t) \tag{4.42}$$

$$y_t(t) = v_t t \sin(\phi_t) \tag{4.43}$$

$$\dot{x}_t(t) = v_t \cos(\phi_t) \tag{4.44}$$

$$\dot{y}_t(t) = v_t \sin(\phi_t), \tag{4.45}$$

where ϕ_t is the target angle, in this case a constant angle.

Figure 4.4 displays the pose errors, where the dashed blue line represents the symmetric cascaded controller and the dash-dotted black line represents the asymmetric cascaded controller. It can been seen that both controllers have similar convergence rates when the target has a velocity of $v_t(t) = V_{max}/4$. However, the symmetric cascaded controller converges faster to the target motion than the asymmetric cascaded controller after the velocity of the target is increased to $v_t(t) = 3V_{max}/4$. The reason why the symmetric cascaded controller converges faster is shown in Figure 4.5 and 4.6.

The command control inputs for the two controllers are shown in Figure 4.5. Two interesting results can be shown. First, the asymmetric cascaded controller has a higher force and moment output in the beginning of the simulation. Second, the symmetric cascaded controller has higher force output on τ_1 after the velocity is increased to $v_t(t) = 3V_{max}/4$ than the asymmetric cascaded controller. However, the symmetric cascaded controller is exceeding the magnitude constraints, which is indicated by the red line on Figure 4.5. This shows that the tuning for the symmetric cascaded controller is unsuitable for the entire control objective and the performance shown in Figure 4.4 is not physically possible.

In Figure 4.6 the velocities of the ship and the desired velocities of the two controllers are shown. The desired velocity of the asymmetric cascaded controller is equal to V_{max} whenever there is a velocity change in the target motion. The problem with the symmetric cascaded controller exceeding the saturation constraints is due to the desired velocity assignment.

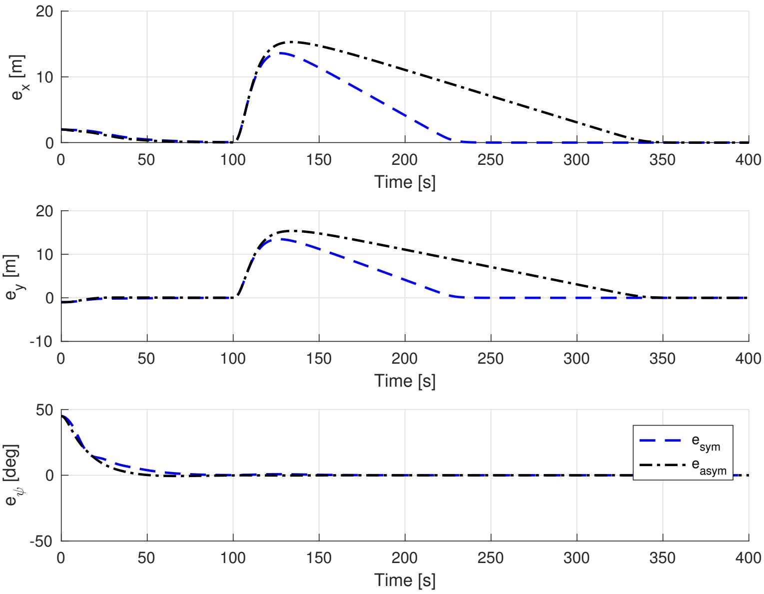

Figure 4.4: Error plot of the two controllers in the straight-line motion. Before $t = 100$s the target velocity is $v_t(t) = V_{max}/4$, then at $t = 100$s it is increased to $v_t(t) = 3V_{max}/4$.

The simulation scenario has shown the major disadvantage of using symmetric cascaded controller. Additionally, it has been shown that the asymmetric cascaded controller is a better choice than the symmetric counterpart since it is able to make the control signal stay within the saturation constraints as shown on Figure 4.5.

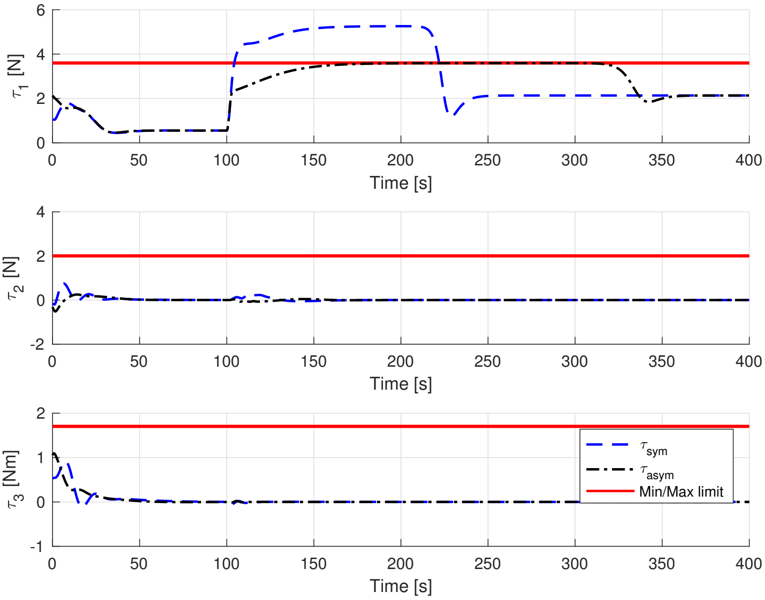

Figure 4.5: The commanded control inputs. Before $t = 100$s the target velocity is $v_t(t) = V_{max}/4$, then at $t = 100$s it is increased to $v_t(t) = 3V_{max}/4$.

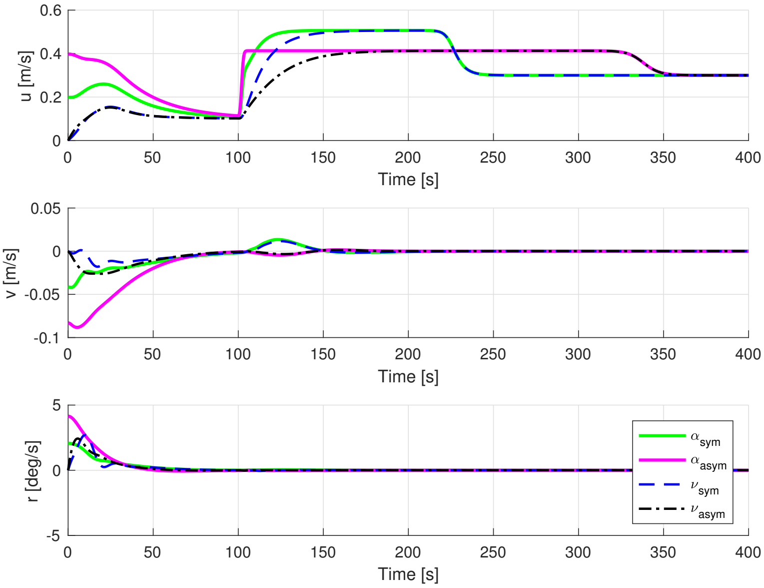

Figure 4.6: Plot of the both the desired and actual velocity for the two controllers in the straight-line motion. Before $t = 100$s the target velocity is $v_t(t) = V_{max}/4$, then at $t = 100$s it is increased to $v_t(t) = 3V_{max}/4$.

Chapter 5

Simplified Dynamic Window Algorithm

5.1 Background

When a ship sails the sea, its autopilot system usually leads the ship along the desired path. Numerous motion controllers and autopilots have been proposed over the years. However, many control algorithms found in the literature do not consider saturation constraints for the actuators. Not considering actuator constraints may lead to unsatisfying performance or stability issues.

Optimal control algorithms are probably the best algorithms when it comes to handling magnitude and rate constraints on the control input. One specific method of high interest is model predictive control (MPC). The MPC algorithm can directly handle constraints, including constraints on the control inputs, system outputs and internal states [36]. In [14], MPC is applied to spacecraft rendezvous and proximity maneuvering problems in the orbital plane. Here, it is demonstrated that various constraints arising in these maneuvers can be effectively handled with the MPC approach.

One of the lesser known, but still interesting optimal control algorithms, is the dynamic window algorithm [21]. The algorithm suggested in [21] is used as a method to perform collision avoidance and deal with constraints imposed by limited velocities and accelerations for mobile robots. The dynamic window algorithm first generates a set of possible trajectories. Based on these trajectories, a search space of possible velocities can be approximated. Acceleration constraints are considered by limiting the search space to reachable velocities within the next time interval. To reduce the search space even further, all velocities that corresponds to a collision are removed and leaving all the dynamically feasible velocities. This makes the vehicle able to stop safely before it reaches the closest obstacle on the corresponding trajectory. The dynamic window algorithm is modified for AUVs in [15] and shows promising results for handling magnitude and rate constraints for the actuators.

5.2 2 DOF High-speed Dynamic Window-based Control

Based on the ship model and its actuator magnitude constraints, a set of possible velocities can be found. This set contains all velocities the ship can achieve, with respect to the actuator magnitude constraints. The possible velocities can be found by computing the steady-state solutions of the kinetics for all possible control inputs. The steady-state solutions for a uniformly distributed set of the control inputs are shown in Figure 5.1.

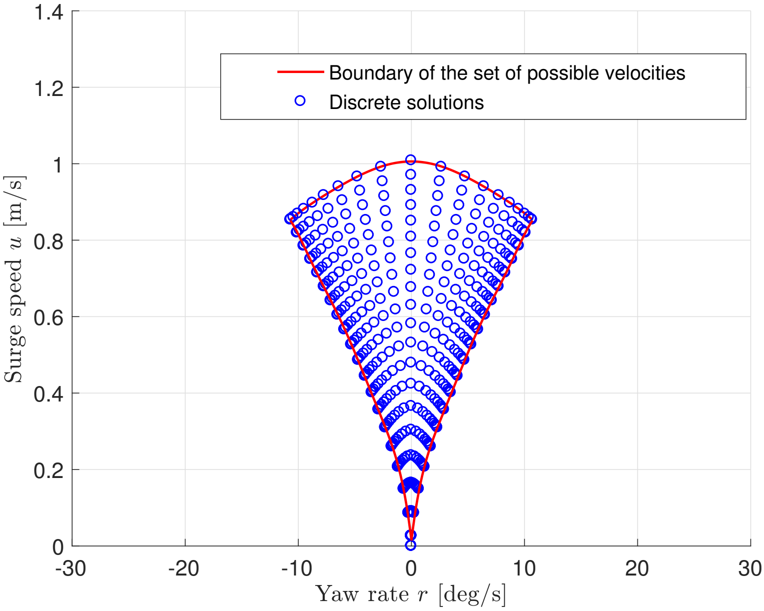

Figure 5.1: Possible combinations of surge speed and yaw rate, with respect to actuator magnitude constraints for CyberShip II, see Paper A.6. The approximated boundary of the set of possible velocities is shown as the red line.

By designing an approximation of the boundaries, the set of possible velocities can be defined by a function $g(u, r)$ that returns a value greater than or equal to zero for valid solutions of the search space, and negative otherwise. Given m approximated boundaries, defined by the functions $h_a(u, r) = 0$, $a \in \{1, 2, ..., m\}$ where $\nabla h_a(u, r)$ is required to be pointing inwards to the valid solutions, the approximated function is found as:

$$g(u, r) = \min(h_1(u, r), h_2(u, r), ..., h_m(u, r)). \tag{5.1}$$

Figure 5.2 shows a plot of the function $g(u, r)$.

Next, the space of reachable points within a time step T needs to be defined.

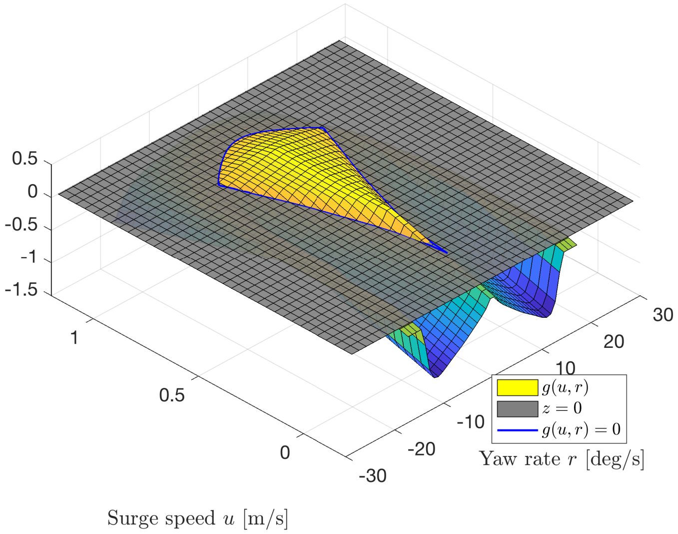

Figure 5.2: Function to find possible velocities.

This is done by finding acceleration limits, and based on these, the set of reachable velocities can be computed. The possible ship accelerations can be found by evaluating the kinetics for the current velocity and boundaries of the control input vector. Using T as the time allowed for acceleration during the next time step, the dynamic velocity window around the current velocity is then defined using the acceleration limits. By taking the union of the set of possible velocities and dynamic velocity window, the set of dynamically feasible velocities is defined. Next, the optimal velocity pair is found by using an objective function, which uses the target velocity as an input in order to minimise the scaled 1-norm of the entire set of dynamically feasible velocities. Figure 5.3 illustrates the set of possible velocities, dynamic velocity window, set of dynamically feasible velocities and the optimal velocity pair given a current ship velocity pair.

We now combine the traditional control design with the simplified dynamic window algorithm in order to develop a dynamic window-based controller (DWC). After the optimal velocity pair is found, the vector of stabilising functions can be given by combining the optimal velocity pair and a dynamic feedback controller, where the dynamics of the uncontrolled sway mode enters the yaw control law [20]. The vector of stabilising functions and its derivative are used in the kinetic control law.

5.3 3 DOF Low-speed Dynamic Window-based Control

As for the 2 DOF DWC approach, which is presented in details in Paper A.6, a set of possible velocities are found based on the ship model and its actuator

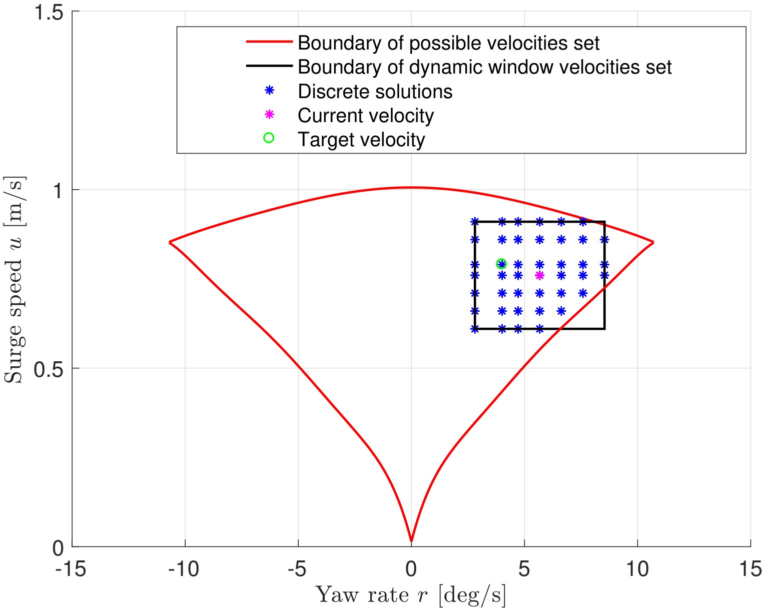

Figure 5.3: The set of dynamically feasible velocities, surrounded by the boundaries of the dynamic velocity window and set of possible velocities.

magnitude constraints. This part of the work is made in collaboration with Ole Nikolai Lyngstadaas [28]. The considered ship has to move at low speed in order to be fully actuated for dynamic positioning (DP) operations. Assuming low-speed maneuvers, the kinetic model in (2.2) can be simplified to

$$\boldsymbol{M}\dot{\boldsymbol{\nu}} + \boldsymbol{D}_L\boldsymbol{\nu} = \boldsymbol{\tau}, \tag{5.2}$$

since in low-speed maneuvers the linear damping will dominate over both the nonlinear damping and the Coriolis and centripetal forces [18]. The steady-state kinetics then become

$$\boldsymbol{D}_L\boldsymbol{\nu} = \boldsymbol{\tau}. \tag{5.3}$$

Solving (5.3) for a uniformly distributed set of control inputs will yield the steady-state velocities needed to find a set of possible velocities. The steady-state solutions of (5.3) for a uniformly distributed set of control inputs, are shown in Figure 5.4.

The set of possible velocities is defined as

$$V_p = \{(u, v, r) \in \mathbb{R} \times \mathbb{R} \times \mathbb{R} \mid g(u, v, r) \geq 0\}, \tag{5.4}$$

where $g(u, v, r)$ is 3 DOF extension of (5.1) and is a positive semidefinite function for feasible velocities with respect to the actuator constraints. This means that a 3D function needs to be found to describe the structure shown in Figure 5.5.

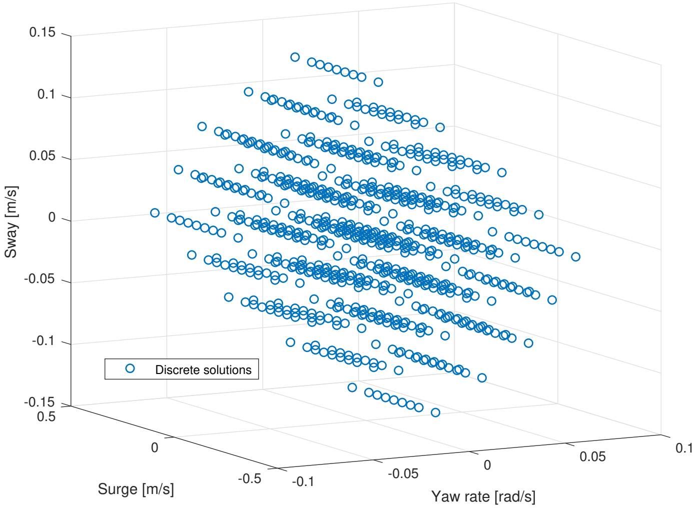

Figure 5.4: Steady-state solutions of low-speed maneuvering model for a uniformly distributed set of control inputs.

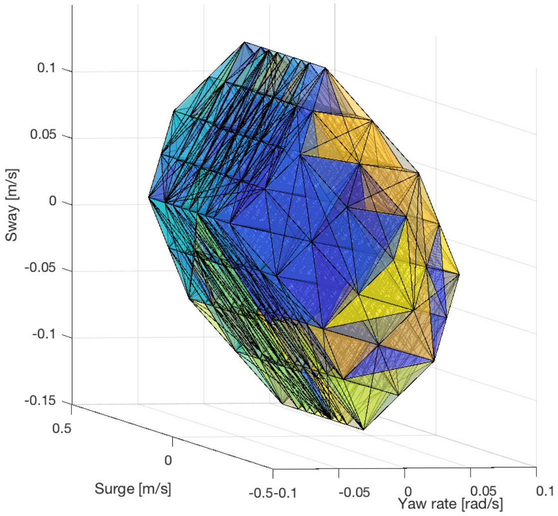

Figure 5.5: Showing the boundary of the steady-state solutions of low-speed maneuvering model for a uniformly distributed set of control inputs.

An approximation of the 3 DOF set is created by projecting the set into three 2 DOF sets to simplify the calculations, since we need to approximate boundary lines instead of surfaces. We justify this approximation by noting that each of the steady-state solution boundary faces are almost parallel with one axis, see Figure 5.6. Following this, faces that are parallel with one axis can be parameterized by the remaining two variables. Notice, however, that we lose information where all three variables are correlated, and can therefore not model faces which are not parallel with one of the axes.

The result of the approximation is the following three sets of possible velocities:

$$\begin{aligned} V_{p,(u,r)} &= \{(u,r) \in \mathbb{R} \times \mathbb{R} \mid g_{(u,r)}(u,r) \geq 0\} && (5.5)\\ V_{p,(v,r)} &= \{(v,r) \in \mathbb{R} \times \mathbb{R} \mid g_{(v,r)}(v,r) \geq 0\} && (5.6)\\ V_{p,(u,v)} &= \{(u,v) \in \mathbb{R} \times \mathbb{R} \mid g_{(u,v)}(u,v) \geq 0\}, && (5.7) \end{aligned}$$

where $g_{(u,r)}(u,r)$, $g_{(v,r)}(v,r)$ and $g_{(u,v)}(u,v)$ are positive semidefinite for velocities inside the corresponding boundaries. Given m, n and k approximated boundaries, defined by the functions $h_{a,(u,r)}(u,r) = h_{b,(v,r)}(v,r) = h_{c,(u,v)}(u,v) = 0$, $a \in \{1,2,...,m\}$, $b \in \{1,2,...,n\}$ and $c \in \{1,2,...,k\}$, the approximated functions are given as:

$$\begin{aligned} g_{(u,r)}(u,r) &= \min(h_{1,(u,r)}(u,r), h_{2,(u,r)}(u,r), ..., h_{m,(u,r)}(u,r)) && (5.8)\\ g_{(v,r)}(v,r) &= \min(h_{1,(v,r)}(v,r), h_{2,(v,r)}(v,r), ..., h_{n,(v,r)}(v,r)) && (5.9)\\ g_{(u,v)}(u,v) &= \min(h_{1,(u,v)}(u,v), h_{2,(u,v)}(u,v), ..., h_{k,(u,v)}(u,v)). && (5.10) \end{aligned}$$

Here, the functions $h_{a,(u,r)}(u,r) = h_{b,(v,r)}(v,r) = h_{c,(u,v)}(u,v) = 0$ are defined by using regression on the boundary of the sets $V_{p_{(u,r)}}$, $V_{p_{(v,r)}}$ and $V_{p_{(u,v)}}$, where $\nabla h_{a,(u,r)}(u,r)$, $\nabla h_{b,(v,r)}(v,r)$ and $\nabla h_{c,(u,v)}(u,v)$ are required to be pointing inwards to the valid solutions.

The design process is subsequently similar to the 2 DOF dynamic window-based controller described in Paper A.6, since for the three 2 DOF cases, this algorithm is modified to fit 2 DOF and run once for each velocity pair scenario; surge speed and yaw rate, sway speed and yaw rate, and surge and sway speed. However, this will result in three components of dynamically feasible velocities:

$$\boldsymbol{\nu}_{f,(u,r)} = \begin{bmatrix} u_{f,(u,r)} \\ r_{f,(u,r)} \end{bmatrix} \qquad \boldsymbol{\nu}_{f,(v,r)} = \begin{bmatrix} v_{f,(v,r)} \\ r_{f,(v,r)} \end{bmatrix} \qquad \boldsymbol{\nu}_{f,(u,v)} \begin{bmatrix} u_{f,(u,v)} \\ v_{f,(u,v)} \end{bmatrix}, \tag{5.11}$$

which are to be combined into one vector of dynamically feasible velocities for the full 3 DOF case. First each vector is extended into three dimensions where the velocity that is not represented in the velocity pair is 0 which gives

$$\boldsymbol{\nu}_{f3,(u,r)} = \begin{bmatrix} u_{f,(u,r)} \\ 0 \\ r_{f,(u,r)} \end{bmatrix} \qquad \boldsymbol{\nu}_{f3,(v,r)} = \begin{bmatrix} 0 \\ v_{f,(v,r)} \\ r_{f,(v,r)} \end{bmatrix} \qquad \boldsymbol{\nu}_{f3,(u,v)} \begin{bmatrix} u_{f,(u,v)} \\ v_{f,(u,v)} \\ 0 \end{bmatrix}. \tag{5.12}$$

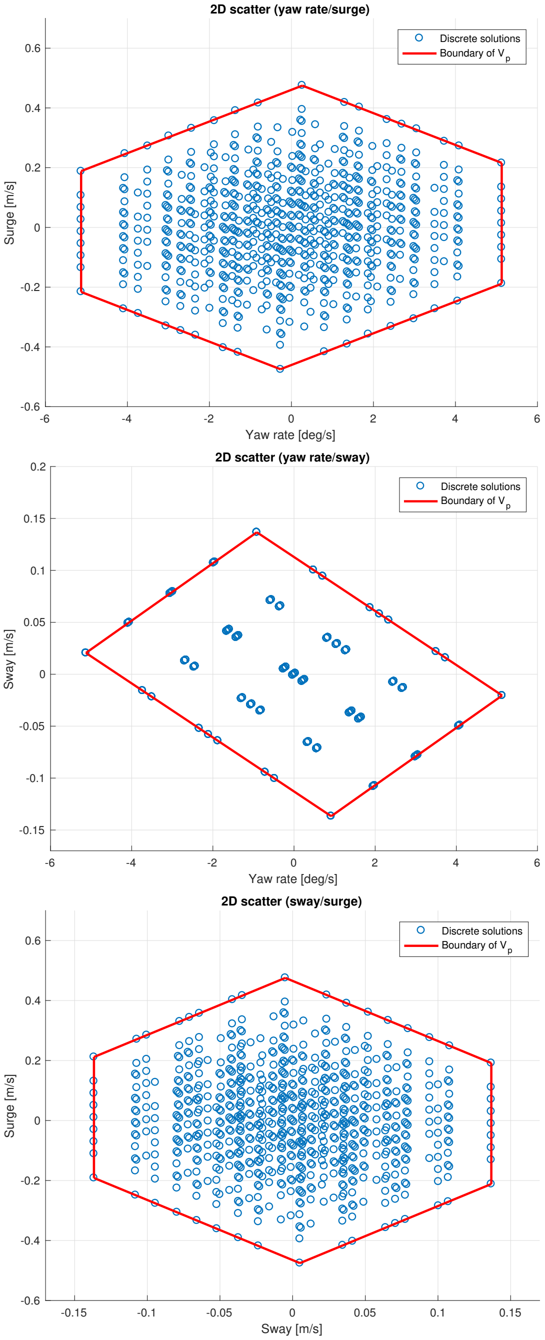

Figure 5.6: Possible combinations of surge speed, sway speed and yaw rate, with respect to the actuator magnitude saturation limits.

The full 3 DOF case then becomes

$$\boldsymbol{\nu}_f = \frac{\boldsymbol{\nu}_{f_3,(u,r)} + \boldsymbol{\nu}_{f_3,(v,r)} + \boldsymbol{\nu}_{f_3,(u,v)}}{2}, \tag{5.13}$$

where the surge speed, sway speed and yaw rate are represented elementwise twice in total of the three components of dynamically feasible velocities and are therefore divided by 2.

A cascaded control design is then combined with the simplified dynamic window algorithm for the 3 DOF case, since the algorithm needs a desired velocity as an input to generate the optimal dynamically feasible velocity. Additionally, the output velocity of the algorithm needs to be transformed into a force and moment input for the actuators. The combination of a cascaded control design and the simplified dynamic window algorithm for the 3 DOF case will be referred to as the 3 DOF DWC. The control law chosen in Paper A.9 is the cascaded nonlinear feedback controller, which is discussed in details in Paper A.2. However, the control law does not have a feedback term in the velocity controller since the dynamic window-based controller makes the feasible velocity track the desired velocity based on a objective function.

5.4 Results and Discussion

5.4.1 Simulation Results

The 2 DOF dynamic window-based controller is used as a heading and speed controller in Paper A.6. This controller is applied on a simulation model of CyberShip II where the actuator constraints are included. Here, the 2 DOF DWC is compared to a benchmark controller. The results show that both control laws manage to converge to the target heading, but the 2 DOF DWC has a slightly faster convergence. The 2 DOF DWC holds the control inputs at the maximum magnitude constraints of the actuators for a longer time than the benchmark controller. This is because 2 DOF DWC tracks the optimal velocity pair which is on the boundaries for the window unless the target velocity pair is inside the velocity window, while the control inputs from benchmark controller have a more conservative behavior. Using two performance metrics, it is shown that the 2 DOF DWC have a better performance with respect to control accuracy and energy efficiency. Additionally, it is shown that 2 DOF DWC is able to inherently handle actuator magnitude constraints.

The 3 DOF dynamic window-based controller is tested in a numerical simulation and in experimental setting where the ship should move in a four corner pattern. The specific pattern is inspired by the test from Paper A.7. The ship is first initialized in dynamic positioning to point straight North at heading 0 (deg). Then the following setpoint changes are commanded:

1. Position change 2 (m) straight North: Tests a pure surge movement ahead.
2. Position change 2 (m) straight East: Tests a pure sway movement in starboard direction.

3. Heading change 45 (*deg*) clockwise: Tests a pure yaw motion while keeping position steady.
4. Position change 2 (*m*) straight South: Tests a combined surge-sway movement while keeping heading steady.
5. Position change 2 (*m*) straight West and heading change 45 (*deg*) counter-clockwise: Tests combined surge-sway-yaw movement.

The 4-corner test is illustrated in Figure 5.7.

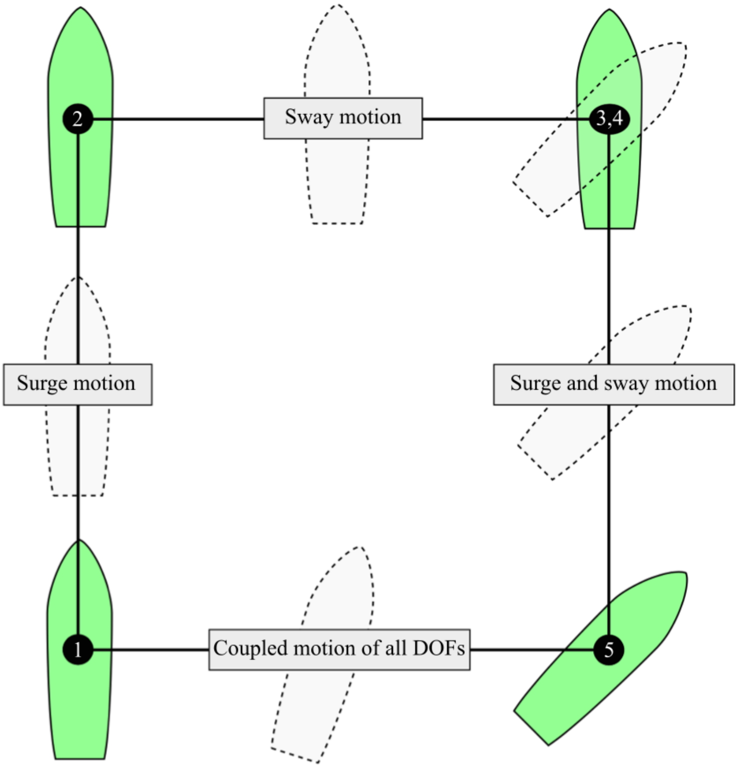

Figure 5.7: The 4-corner dynamic positioning test. Modified from Paper A.7.

The system is implemented such that the target will automatically change setpoint when the ship is within 0.003 (*m*) from the target in both x and y direction and 0.2 (*deg*) from the target heading. When the 4-corner test is completed, the ship will have returned to its initial position and heading, ready for a new test at the same pose and along the same track.

As with the 2 DOF simulations, the performance is computed against a benchmark controller in Paper A.9. The results show that 3 DOF DWC still outperform the benchmark controller. However, it is less obvious than for the 2 DOF case, since the pose plots are almost identical. Using the two performance metrics, it is shown that the 3 DOF DWC has a slightly faster transient response since it converges faster to a stationary value than the benchmark controller. The IAEW shows that the 3 DOF DWC has a slightly better overall performance than the benchmark controller when taking both control accuracy and energy use into account. However, it is also shown that the 3 DOF DWC has a higher energy consumption than the benchmark controller when doing the 4-corner scenario.

5.4.2 Experimental Results

Experimental test of the 3 DOF DWC was done the 16th of May 2018 at the Marine Cybernetics laboratory using CSAD. In Figure 5.8, the outline of the ship pose is plotted to show the pose motion pattern of the 3 DOF DWC. Here, it can be seen that the ship follows the surge motion fairly good. During the sway motion a problem starts to show, since the ship starts to oscillate around the target path. However, for the last two sides of the 4-corner test the 3 DOF DWC is not able to follow the target path.

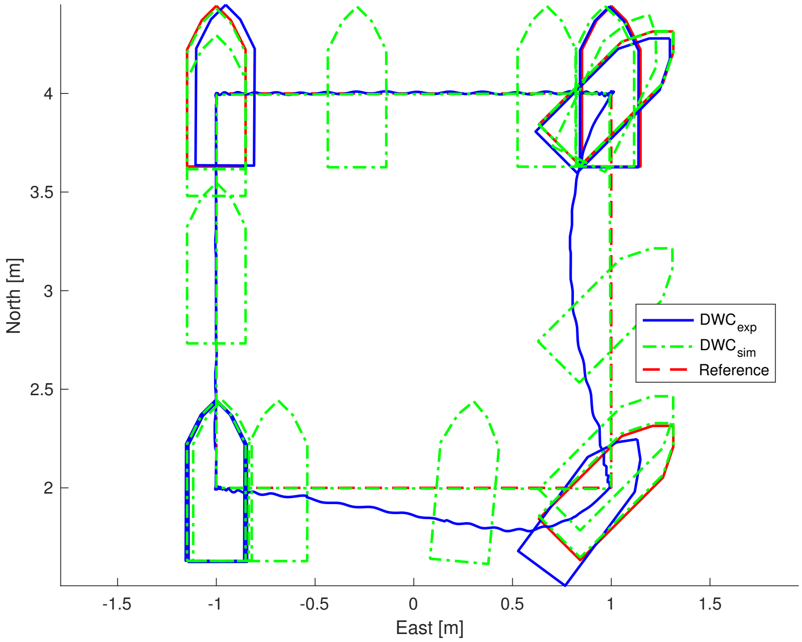

Figure 5.8: The 4-corner path plot of both the experiment and numerical simulation with the dynamic window-based controller. Courtesy of [28].

Figure 5.9 shows the commanded control inputs for the 3 DOF DWC. The control input has a large amount of oscillations, which causes the actuator to wear itself down. In [28], it was investigated what causes these oscillations which was not present in the simulations. Here, it was investigated what effect adding 50% model uncertainties to the inertia matrix, Coriolis and centripetal matrix and damping matrix had on the simulation results. Additionally, it was investigated what effect adding a time delay of 0.2 seconds to the commanded actuator input had. Based on this investigation, it was concluded that model uncertainties result in the offset to the path while a time delay was the main reason for the oscillations in the control input from the experiments.

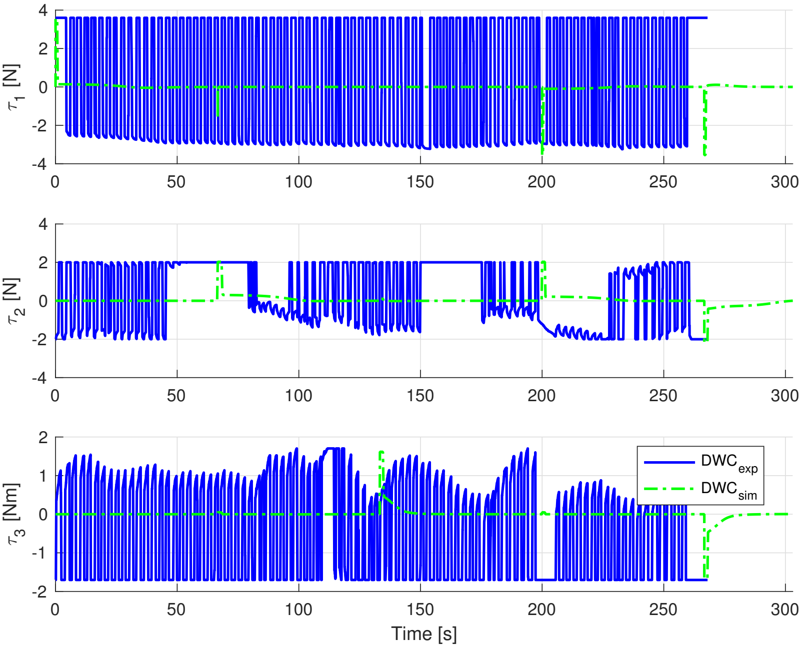

Figure 5.9: Commanded actuator inputs of both the experiment and numerical simulation the dynamic window-based controller. Courtesy of [28].

5.4.3 Discussion

The dynamic window-based controller for 2 DOF and 3 DOF cases have shown to have both advantages and disadvantages. Through the simulation results in papers A.6 and A.9 it has been shown that the dynamic window-based controller is able to handle actuator magnitude constraints. The simulation results show that the dynamic window-based controller has the potential to have the best performance of the considered controllers. However, the experimental results have shown that the biggest disadvantage of dynamic window-based controller is that the controller are prone to instabilities due to the presence of disturbances and time delays. In [28], a plausible reason to why the controller is sensitive to time delays is discussed. Here, it is believed that the reason is that when a time delay which is larger than one sample is present, the controller will overshoot the desired velocity, practically making the window slide past the desired velocity. At the next time step, the desired velocity will then be outside the window again, making the command control input at maximum thrust in the opposite direction, effectively making the control signal oscillate while trying to track the desired velocity.

Chapter 6

Adaptive Control

6.1 Background

Before describing specific adaptive control algorithms, it is first necessary to get an understanding of what an adaptive control method is. This description is based on [5] and [25].

The word "to adapt" means to change the behaviour so that it can handle new conditions [25]. Using this definition, an adaptive control method is a way to modify the behaviour of the input response so that the dynamics of a plant is changed and disturbances are counteracted. A normal feedback law attempts reduce the effect of the disturbances and the uncertainties in the plant but it is not guaranteed that the normal feedback law will succeed.

Over the years, many have tried to define adaptive control formally. However, a meaningful definition on how to distinguish adaptive control from other control algorithms is still missing [25]. There is a common understanding in the field of control theory that constant gain feedback control is not classified as adaptive control. An adaptive control method can be thought of as a system with two loops: a) one loop for the normal feedback with the control and the plant and b) another loop for the parameter adjustments, where the disturbances and uncertainties of the plant are estimated. A schematic illustrating the general idea of an adaptive control algorithm is displayed in Figure 6.1, where r, u, $\hat{\theta}$ and y represent the reference signal, control signal, estimated unknown parameters and output signal, respectively.

Note that there exists other methods that are able to handle uncertainties in a system. The most known methods are robust control and gain scheduling. Compared to adaptive control, robust feedback has a constant feedback gain. This gain is designed so that it can cope with parameter changes which are within certain bounds. Gain scheduling is a method that has a closer resemblance to adaptive control than robust control has, since gain scheduling changes the control parameters. However, gain scheduling does this by precomputing a lookup table of control

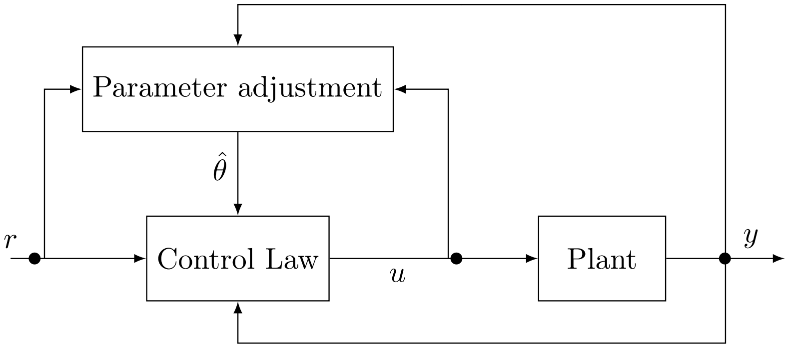

Figure 6.1: A general schematic of an adaptive control algorithm.

gains offline with the operation point as the input. The main drawback with this is that the gain scheduling may not cope with unpredicted changes in the plant.

In adaptive control, two different approaches exist for estimating the unknown system parameters online. The first approach is referred to as indirect adaptive control, which estimates the unknown system parameters online and then these parameters are used to calculate the controller parameters. The objective of the indirect technique is to design a controller for each time t, so that it satisfies the performance requirements for the plant model with the estimated uncertainties. This may be different than the real uncertainties. The problems in indirect adaptive control are to choose the class of control laws and the class of parameter estimators as well as the algebraic function, which transforms the estimated uncertainties to the controller gains so that the control laws meets the performance requirements for the plant [25].

The second approach is referred to as direct adaptive control, where the system is parametrised in terms of the unknown control parameters. These parameters are then estimated directly without intermediate calculation of the system uncertainties such that they can meet the performance requirements. The control parameter estimators give an estimate of these parameters by processing the plant input u and output y. The fundamental problems of direct adaptive control are to choose the class of control laws and the class of parameter estimators such that the controller meets the performance requirements for the plant. In addition, the properties of the plant are crucial for obtaining the parametrised plant, which restricts the direct adaptive control algorithm to a certain class of plant models. Examples of these classes are given in [25].

It is worth mentioning that achieving a control objective of an adaptive control algorithm does not necessarily mean that the algorithm estimates the uncertainties correctly. The adaptive control algorithm creates a control signal to track the reference and counteract the perturbation from the uncertainties by estimating the parameters. However, these parameters may not be equal to the real parameters. This means that a condition must be introduced to system identification if it is desired to both track a reference and estimate the parameters correctly. This condition is in general referred to as persistent excitation, which is one method to characterise plant inputs. This condition is a sufficient condition for ensuring that the estimation errors of the parameters converge to zero exponentially fast. The signal vector $\mathbf{u}$ gives persistent excitation in $\mathbb{R}^n$ with a level of excitation $\alpha_0 > 0$, if there exist constants α_1, $T_0 > 0$ and $\mathbf{u} : \mathbb{R}^+ \to \mathbb{R}^n$ is a piecewise continuous signal vector, such that

$$\alpha_1 I \geq \frac{1}{T_0} \int_t^{t+T_0} \mathbf{u}(\tau)\mathbf{u}(\tau)^\top d\tau \geq \alpha_0 I \quad \forall t \geq 0, \tag{6.1}$$

is satisfied [25].

6.2 History, Challenges and Open Problems

The objective to invent, design and build systems capable of controlling uncertainties in plants or adapting to unexpected changes in the environment has a long and rich history. In the 1950s and 1960s the major advances of control theory encouraged the researchers to think about more sophisticated forms of feedback systems. One idea, which emerged in this period and has firmly remained a popular research topic, is adaptive control. Even though the field of adaptive control is quite old, it has experienced an increased interest and research effort during the latest decades. This has lead to some new and promising control techniques such as the adaptive backstepping and $\mathcal{L}_1$ adaptive control. One of the reasons for this rapid growth of adaptive control is its ability to control plants with unknown parameters.

The adaptive control of aircraft has been studied vastly, and several papers and textbooks have been published in the area since the 1950s; see e.g. [5] and [25]. In the 1980s, a new adaptive technique is introduced, which is called robust adaptive control. An adaptive controller can be defined as robust if it guarantees signal boundedness in the presence of uncertainties and bounded disturbances. Even though the field of adaptive control is quite old, new methods are still found and developed. One of the first and still widely used adaptive control methods are model reference adaptive control (MRAC). An overview of the development of MRAC for aerospace applications is given in [27].

Many different adaptive control algorithms have been developed since the 1950s. The current state-of-the-art adaptive control algorithms include

- adaptive backstepping [26],
- MRAC methods [27],
- the novel command governor-based adaptive control technique [40] and
- the $\mathcal{L}_1$ adaptive control algorithm [24].

Over the last 70 years, fundamental challenges which have been discussed, including time scales, bursting and inaccurate system modelling. The problems and how to handle them are summarised in [3] and [4]. In the 1950s, a method for designing adaptive controllers called the MIT rule is developed. However, this method did not work every time. After analysing what could be the cause of this, researchers concluded that it is due to the underlying problem of time scales in the adaptive control. The term time scale describes how fast the dynamics of the system are. There may exist different time scales in an adaptive control system. The most important time scales are the adaptation time scale and the system time scale. The problem of instability in the MIT rule method occurs often when the adaptation time scale is coinciding with the time scale of the plant dynamics. Both [3] and [4] suggest a separation of time scales of the adaptation mechanism and the unadapted plant is employed to get a safer adaptive control design, but without elaborating on how this can be done. In addition, it is more easy to analyse the stability properties when the time scales are separated.

Another issue with adaptive control is the problem of bursting, which arose in the 1970s. There are reports of adaptive systems that have worked well over an extended period, which suddenly started to have oscillations which shortly after died away again. The cause was that the system was in steady state and the adaptive control law started to adapt to the measurement noise. This would make the system start oscillating and the control law would force the system back to steady state. The oscillation phenomena is called bursting. The general idea to avoid this is to switch off the adaptation mechanism under steady state operation. However, it is hard to find a good solution in order to detect when the system leaves the steady state condition without the possibility of introducing the bursting problem again.

The last problem is unmodelled dynamics, which could lead to instability. An example of this is a system with a time delay which is neglected from the design of the adaptive algorithm. This makes the algorithm more likely to fail since it is missing some dynamics. The conclusion of this is that a model may be suitable for some controllers but it is not guaranteed that the model is suitable for all controllers.

The following problems still remain open, which are inspired by [39]. Some of the open problems are: Reference model design, parameter tuning guidelines, gain and phase margins for adaptive systems and adaptive structural mode suppression. The design of an adaptive controller using a reference model is a challenging problem for some systems such as aircraft. The reason is that the desired command tracking of a manoeuvre for the reference model without a disturbance, such as wind, is not the same as the reference model for disturbance rejection [39].

Parameter tuning guidelines is challenging since there does not exist any guidelines on how to tune the adaptation rate gain Γ. The problem is that by choosing a gain too low, the system will adapt too slowly, while for a gain too large, high frequency oscillation will occur. To deal with the high frequency oscillation, a low-pass filter is added in the adaptive control law developed by [24].

The last open problem addressed is gain and phase margins for adaptive systems. It has been verified from simulations that systems with high adaptation rates are not robust against time delays in the feedback.

The main points of the open problems in adaptive control are listed below:

- Implementing a separation of time scales on a real system.
- Bursting, a phenomenon where the adaptive control law starts to adapt on the measurement noise.
- Changing model structure makes it a challenging problem for designing a reference model.
- General guidelines on how to tune the adaptation rates do not exist.

6.3 Adaptive Control Concepts

In Chapter 4 and 5 it has been discussed how to handle magnitude constraints. However, the proposed algorithms are only applicable if the internal uncertainties and the external disturbances are small or non-existing. Different adaptive concepts have therefore been applied to the ship model to investigate which adaptive concept has the best performance.

6.3.1 $\mathcal{L}_1$ Adaptive Control

In Paper A.3, adaptive backstepping control algorithm from [26] is compared with the newer $\mathcal{L}_1$ adaptive control algorithm. When introducing uncertainties and disturbances into the system, the backstepping control law is changed to only include an estimate of the uncertainties and the disturbance instead of the actual parameters. In order to update the estimate of uncertainties and disturbances, the update laws are found using a control Lyapunov functions (CLF), and the assumption that the uncertainties and the disturbance are constant or slowly varying relative to the ship dynamics.

A main difference between the $\mathcal{L}_1$ adaptive controller and many of the other state-of-the-art adaptive controllers is that $\mathcal{L}_1$ adaptive control has a state predictor which estimates the uncertainties and disturbance. A block diagram that depicts the general idea behind the $\mathcal{L}_1$ adaptive controller is shown in Figure 6.2.

The state predictor is designed by first defining the prediction errors. Here, these error are defined as

$$\tilde{\boldsymbol{\eta}} \triangleq \hat{\boldsymbol{\eta}} - \boldsymbol{\eta} \tag{6.2}$$

$$\tilde{\boldsymbol{\nu}} \triangleq \hat{\boldsymbol{\nu}} - \boldsymbol{\nu}, \tag{6.3}$$

where $\hat{\boldsymbol{\eta}}$, $\hat{\boldsymbol{\nu}}$, $\boldsymbol{\eta}$ and $\boldsymbol{\nu}$ represent the estimated pose, estimated velocity, real pose and real velocity, respectively. The ideal prediction error dynamics are chosen to

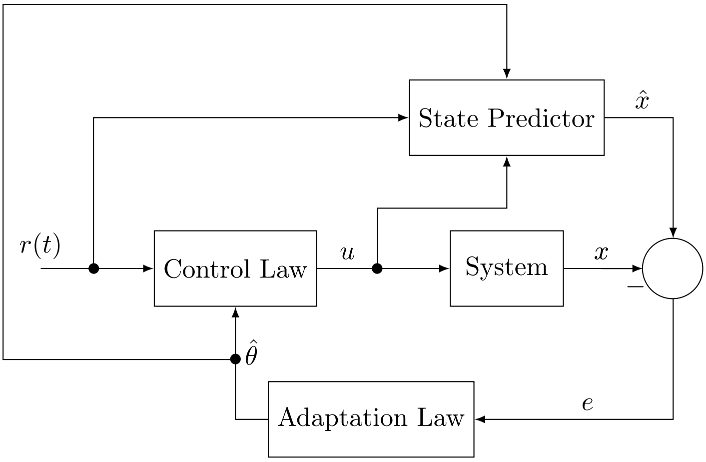

Figure 6.2: Block diagram of the $\mathcal{L}_1$ adaptive control.

be

$$\dot{\tilde{\boldsymbol{\eta}}}_{ideal} = -\boldsymbol{L}_1\tilde{\boldsymbol{\eta}} \tag{6.4}$$

$$\dot{\tilde{\boldsymbol{\nu}}}_{ideal} = -\boldsymbol{L}_2\tilde{\boldsymbol{\nu}}, \tag{6.5}$$

where $\boldsymbol{L}_1 > 0$ and $\boldsymbol{L}_2 > 0$, such that their origins are exponentially stable. The convergence rate is decided through the positive definite gain matrices. The state predictor then becomes a combination of the ship dynamic and the prediction error. Using a positive definite CLF and assuming the uncertainties and the disturbance are constant or slowly varying relative to the ship dynamics, the update laws can be derived.

6.3.2 Concurrent Learning

In collaboration with Elias Bjørne [7], an extension to adaptive backstepping is proposed in Paper A.5. This extension is the adaptive concept concurrent learning which is based on the intuition that if the recorded data is sufficiently rich, i.e., there is a linear independence in the data, concurrent learning adaptation can be used to estimate true values without the need for persistency of excitation in the instantaneous data. However, Condition 1 from [13] needs to be fulfilled, which states:

Condition 1: The recorded data has as many linearly independent elements as the dimension of the regressor matrix $\boldsymbol{\Omega}(\boldsymbol{x}(t)) \in \mathbb{R}^{l\times m}$. That is if

$$\mathbf{Z} = [\boldsymbol{\Omega}(\boldsymbol{x}(t_1))^\top, \boldsymbol{\Omega}(\boldsymbol{x}(t_2))^\top, ..., \boldsymbol{\Omega}(\boldsymbol{x}(t_p))^\top], \tag{6.6}$$

then $rank(\mathbf{Z}) = m$. If condition 1 is satisfied for the regressor matrix $\boldsymbol{\phi}$, the following term is added to update law

$$\sum_{j=1}^{p} \boldsymbol{\Phi}_j^\top \boldsymbol{\epsilon}_j, \tag{6.7}$$

where $j \in \{1, 2, ...p\}$ denotes the index of a recorded data point $\boldsymbol{x}_j = [\boldsymbol{\eta}_j^\top, \boldsymbol{\nu}_j^\top]^\top$ and $\boldsymbol{\Phi}_j$ is the regressor matrix evaluated at point $\boldsymbol{x}_j$, while $\boldsymbol{\epsilon}$ is an approximation error defined as

$$\boldsymbol{\epsilon} \overset{\triangle}{=} \boldsymbol{y} - \hat{\boldsymbol{y}}, \tag{6.8}$$

where $\boldsymbol{y}$ are measured uncertainties which are found solving the ship dynamics for the uncertainties and $\hat{\boldsymbol{y}}$ are the estimated uncertainties. In order to find the measured uncertainties it is assumed that the acceleration can be measured. A modification in the update law is to have adaptation dynamics in a cascade with the controller instead of using the concurrent learning as a composite adaptation law. This can be done by changing the entire update law to

$$\dot{\hat{\boldsymbol{\varphi}}} = \boldsymbol{\Gamma}_\varphi \left(\boldsymbol{\Phi}^\top \boldsymbol{\epsilon} + \sum_{j=1}^{p} \boldsymbol{\Phi}_j^\top \boldsymbol{\epsilon}_j \right), \tag{6.9}$$

so that it only uses the approximation error to calculate the estimate of the model uncertainties.

6.4 Results and Discussion

6.4.1 $\mathcal{L}_1$ Adaptive Control

In Paper A.3, a comparative analysis of the methods is made in order to find out which controller has the best performance. The simulation results show that all the considered controllers have good tracking performance and ability to compensate for internal and external uncertainties. However, utilising the benefit which $\mathcal{L}_1$ adaptive control gives, we are able to choose higher adaptation rates without encountering the problem of high-frequency oscillations in the control signal and therefore get a better tracking performance than for adaptive backstepping. It is also shown that the $\mathcal{L}_1$ adaptive backstepping controller has a better energy efficiency.

In collaboration with Tore Sæterdal [33], the $\mathcal{L}_1$ adaptive control algorithm is combined with the cascaded nonlinear feedback controller for Section 4.2. The control and update law become

$$\boldsymbol{\tau} = \boldsymbol{M}\dot{\boldsymbol{\alpha}} + (\boldsymbol{C} + \boldsymbol{D})\boldsymbol{\alpha} - \boldsymbol{K}_2(\boldsymbol{z}_2)\boldsymbol{z}_2 - \hat{\boldsymbol{\omega}} \tag{6.10}$$

$$\dot{\hat{\boldsymbol{\omega}}} = -\boldsymbol{\Gamma}_\omega \tilde{\boldsymbol{\nu}}, \tag{6.11}$$

where $\boldsymbol{\Gamma}_\omega > 0$ is the adaptation gain. It should be noted that all the internal uncertainties and external disturbances have been parametrised into one variable vector

$\boldsymbol{\omega}$. Using this parameterization of only estimating one variable vector the adaptation get a similar task to the integral action of the PID controller, since it tries to counteract all the uncertainties and disturbances as one uncertainty. However, this can only be achieved when all the uncertainties and disturbances are constant or slowly varying relative to the ship dynamics. Additional advantages of using this parameterization are that one does not need the error dynamics to be persistently excited in order to estimate the sum of all the uncertainties in the system and the phenomena of bursting can be avoided. For details about how the state predictor is designed, see Paper A.1, A.3 and [33]. It should be noted that this controller is unconstrained which means that the lowpass filter that normally has been added to the $\mathcal{L}_1$ adaptive control algorithm to remove high-frequency oscillations in the control signal is neglected here. This controller is tested in an experimental setting using the 4-corner test presented in Section 5.4. The $\mathcal{L}_1$ adaptive control algorithm is combined with the cascaded nonlinear feedback controller and is compared to the cascaded nonlinear feedback controller.

Experiments ware conducted in the Marine Cybernetics laboratory the 16th of May 2018 where the $\mathcal{L}_1$ adaptive control algorithm is combined with the cascaded nonlinear feedback controller, labelled as $\mathcal{L}_1$-NP-NV, was tested against a cascaded nonlinear feedback controller a benchmark controller, labelled as NP-NV. The control gains for the controller are given in Table 6.1.

	NP-NV	**$\mathcal{L}_1$-NP-NV**
$\boldsymbol{\Gamma}_1$	diag([0.08, 0.08, 0.0698])	-||-
$\boldsymbol{\Gamma}_2$	diag([0.08, 0.08, 0.0698])	-||-
$\Delta_{\tilde{p}}$	0.5	-||-
$\Delta_{\tilde{\psi}}$	0.5	-||-
$\Delta_{\tilde{v}}$	0.7	-||-
$\Delta_{\tilde{r}}$	1	-||-
$\boldsymbol{L}_1$	-	$\boldsymbol{I}(2\pi)^2$
$\boldsymbol{L}_2$	-	$\boldsymbol{I}(14.4\pi)$
$\boldsymbol{\Gamma}_\omega$	-	$(20\pi)^2/4$

Table 6.1: Control parameters.

In Figure 6.3, the outline of the ship pose is plotted to show the pose motion pattern. Here the dash-dotted blue outline represents NP-NV, the dashed red outline represents unconstrained $\mathcal{L}_1$-NP-NV, while the black outline represent the 4-corner box.

Figure 6.4 shows the commanded control signals for the two controllers. Note that the amount of time each of the controllers use to complete the 4-corner test is different, since the adaptation makes the convergence rate faster due to the added force term in the control (6.10). Figure 6.4 also shows that there is some high-frequency oscillations in the control signal which probably could have been removed using the lowpass filter, but it comes with a cost in time spent to complete the 4-corner

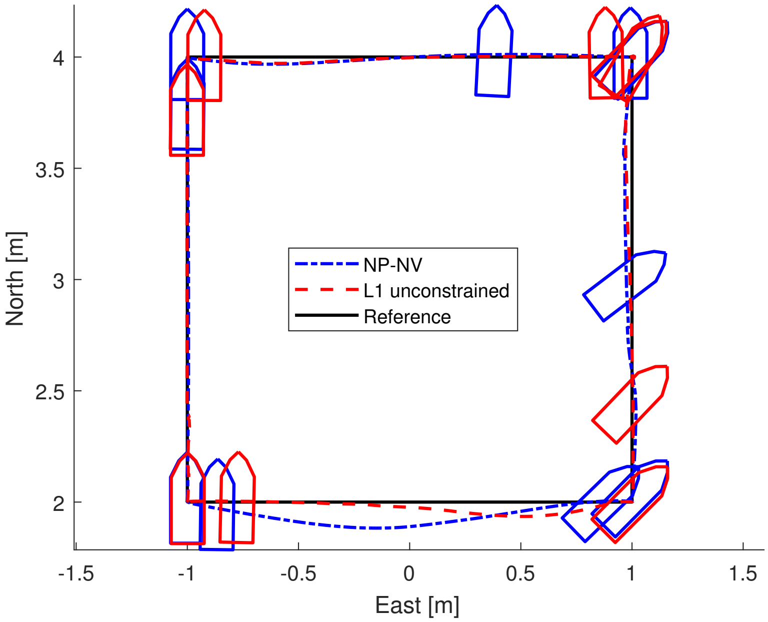

Figure 6.3: The 4-corner experiment: Using NP-NV and unconstrained $\mathcal{L}_1$-NP-NV. Courtesy of [33].

test.

In Figure 6.5, the performance metrics IAE, IAEW and IADC of the two controllers are shown. The IAE shows that the unconstrained $\mathcal{L}_1$-NP-NV has the best performance with respect to tracking of the two controllers. However, when including the energy use into the performance metric, the result changes so that the NP-NV has the best performance. The IADC has shown that the NP-NV has the best performance with respect to wear and tear. This is due to the high-frequency oscillations which occur on the control inputs for the unconstrained $\mathcal{L}_1$-NP-NV. The use of a lowpass filter would minimise the high-frequency oscillations. However it would probably also make the $\mathcal{L}_1$-NP-NV have poorer tracking performance. It therefore comes down to which metric is the most important when one needs to evaluate the overall performance.

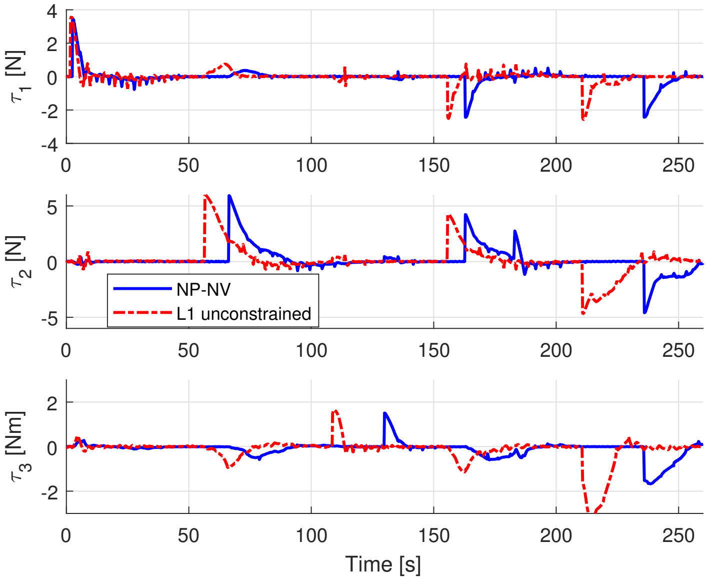

Figure 6.4: The 4-corner experiment: The commanded control inputs. Courtesy of [33].

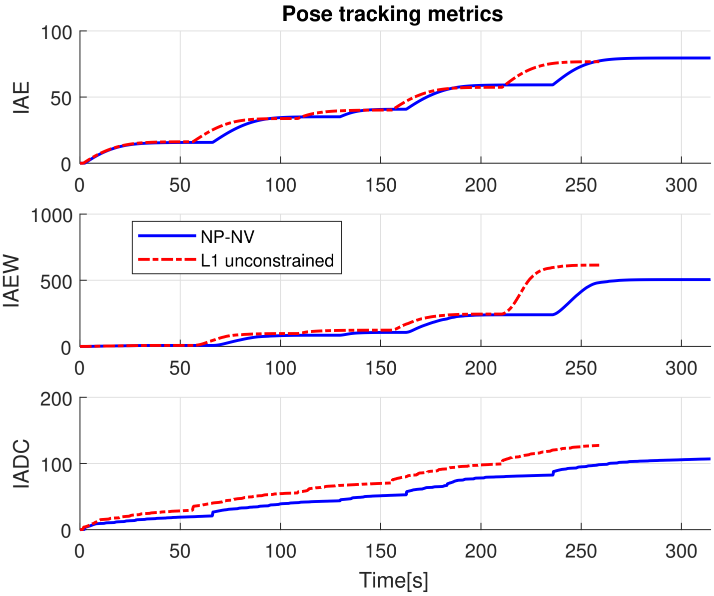

Figure 6.5: The 4-corner experiment: IAE, IAEW and IADC performance metrics. Courtesy of [33].

6.4.2 Concurrent Learning

In Paper A.5, the adaptive backstepping controller is used as a benchmark controller to evaluate the control performance of two different combinations of the concurrent learning concept with the traditional backstepping controller: A concurrent learning backstepping controller with a composite adaptation law and a concurrent learning backstepping controller with a cascaded adaptation law. The evaluation is done with numerical simulations where the control objective is to track a target along an elliptic path and the ship model parameters are uncertain. The simulations show that the concurrent learning backstepping controller with cascaded adaptation has the best control performance and is better at handling uncertainties than the other two controllers. The IAE shows that concurrent learning backstepping controller with cascaded adaptation has the fastest transient response since it quickly establishes the smallest IAE value. In addition, the IAEW-WT shows that concurrent learning backstepping controller with cascaded adaptation has a significantly smaller value for the combined control accuracy, energy use and actuator wear and tear. Some of the key results of this paper is shown in Figure 6.6 and 6.7. In these figures AB refers to the adaptive backstepping controller, CL-CO refers to the concurrent learning backstepping controller with the composite adaptation law, while CL-CA refers to the concurrent learning backstepping controller with the cascaded adaptation law.

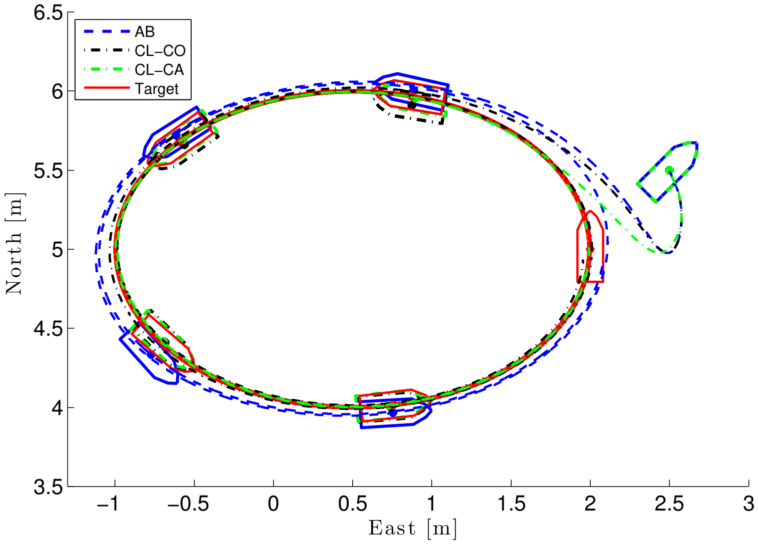

Figure 6.6: The ship tracking the target which is moving along an elliptic path. Originally shown in A.5.

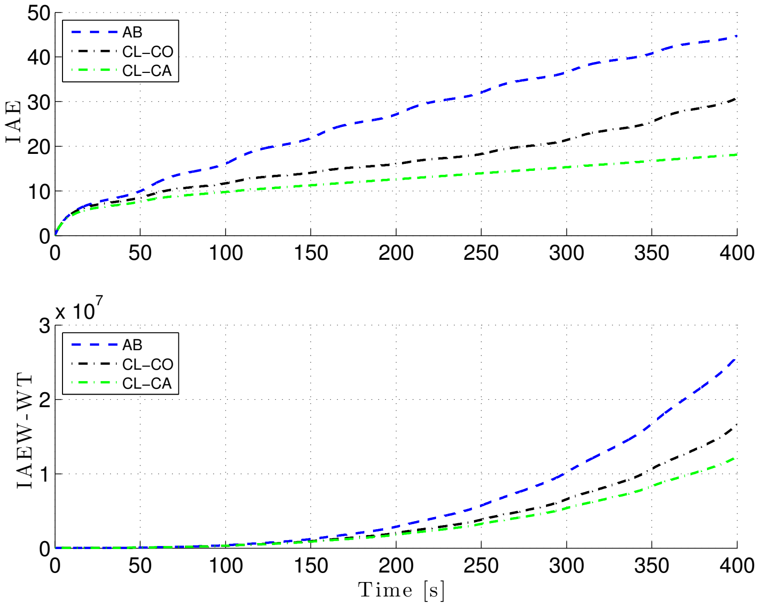

Figure 6.7: The IAE and IAEW-WT performance metrics. Originally shown in A.5.

Chapter 7

Experimental Work

This chapter will discuss the experimental work, which is presented in the papers from Appendix A. The experiments were conducted as model-scale experiments in the Marine Cybernetics Laboratory and as full-scale experiments using the research vessel R/V Gunnerus. A description of these testbeds are also included in this chapter.

7.1 Model-scale Experiments in the Marine Cybernetics Laboratory

The Marine Cybernetics laboratory (MC-lab) is a small ocean basin laboratory at the department of marine technology at NTNU. The facility is especially suited for tests of motion control system for model-scale ships, due to its relatively small size and advanced instrumental package. However, it is also suitable for more specialized hydrodynamic tests, since the MC-lab is equipped with an advanced towing carriage, which has capability for precise movement of models up to 6 DOF for both ships and submersibles. The basin displayed in Figure 7.1 measures [40x6.45x1.5] meter in length, width and depth, respectively.

Figure 7.1: MC-Lab basin and control room.

7.1.1 Laboratory Hardware

The MC-lab is equipped with a Qualisys track manager (QTM) system for motion capture, which is used for position and attitude measurements for an onboard control system of the model-scale ships. The inputs to the Qualisys system come from three Oqus high-speed infrared (IR) cameras, which track the IR reflector orbs fitted on the model-scale ship in the basin. The QTM system is installed on a dedicated workstation, using P2P communication with the Oqus cameras. Experiments can be fully supervised from a control room equipped with a dedicated computer for the QTM system and a TV connected to two high-resolution video cameras. The internal communications in the MC-lab is done over IP on a dedicated WLAN network, allowing wireless control of the model-scale ships as well as transfer of recorded data from the onboard computer. The model-scale ship is equipped with a National Instrument CompactRIO (cRIO) embedded computer system for control computation.

7.1.2 Laboratory Software

To communicate with the model-scale ship, the dedicated laptops are fitted with a substantial software suite, which includes a LabVIEW full development system, MATLAB with Simulink package, as well as the National Instruments Veristand complete software package. The full list of dependency software is listed in the MC-lab Handbook [1]. As stated earlier, the QTM system only supplies the control system with position and attitude measurements. However, most of the test algorithms also require velocity and rate measurements to be functional. Using the position and attitude measurements and a derivative filter, an estimate of the pose and body-fixed velocities can be found. A block diagram of the control system is shown in Figure 7.2.

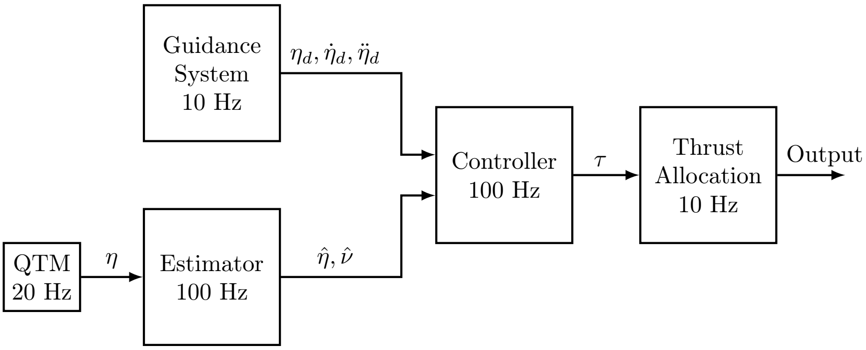

Figure 7.2: MC-lab block diagram.

Here, it can be seen that the different parts of the control system run at different frequencies. The main system runs at 100 Hz, which includes the controller and the estimator, while the QTM transmits updated position measurements to the control system at 20 Hz. The guidance system and the thrust allocation update the reference target and the commanded actuator inputs, respectively, at a frequency of 10 Hz. This is the main setup for the experiments, and will be used throughout the experiments unless anything else is stated.

It was discovered during the experiments in the MC-lab that the pose and velocity estimator was not designed to handle a poorly calibrated camera system. This resulted in spikes on the estimated velocity signal, which affected the performance of the tested controller. The poor calibration resulted in occasionally frozen position measurement that lead the control system to believe that the ship was stationary. When the signal freeze was over, the measured position would be updated, effectively giving a huge rise in the estimated velocity for this time step, which affected the overall performance. A redesign of the pose and velocity estimator, that can handle all mentioned issues, is made. The issue with the signal spikes is handled by limiting the allowed accelerations in the estimator. These limits are based on the highest achievable accelerations of the ship. In the case that the camera system could not detect the ship a dead reckoning algorithm updates the pose of the ship with the assumption that the ship moves with a constant velocity. Further details about the modification to the pose and velocity estimator can found in [28] and [33].

7.1.3 Results

In Paper A.4, a comparison between a LP-LV controller and NP-NV is experimentally tested. Here, the two controllers have been implemented and experimentally tested for the model-scale ship Cybership Enterprise I [34] in the MC-lab at NTNU, for a scenario concerning point stabilisation toward a stationary target. The result of the experiment shows that the NP-NV gives a smooth and energy-efficient motion toward the target, while the LP-LV moves almost sideways in the beginning, only changing heading toward the end. The results in Paper A.4 also show that the ship is not able to track the stationary target completely but it has a steady-state error. This is due to a poorly designed control allocation, which means that the actual output from the actuators is zero even though the controllers command a non-zero output. Some of the key results from Paper A.4 are shown in figures 7.3 and 7.4

The Paper A.2 extends on the results shown in Paper A.4, since on the AMOS DP Research Cruise 2016 discussed in A.7 new turning rules for the cascaded feedback controllers were found. In addition, a more comprehensive DP test scenario is used in Paper A.2 compared to the one in Paper A.4. In Paper A.2, three cascaded controller combinations of linear and nonlinear terms are tested using the 4-corner test. The three controllers, LP-LV, NP-LV and NP-NV, have been implemented and experimentally tested on the model-scale ship CSAD in the MC-lab. Here, the results show consistency between the simulation and the experiments with respect to the amount of time the different controllers need to complete the test and introducing a nonlinear feedback term to the pose controller seems to be advantageous. The price to be paid is the introduction of more tuning parameters. These Δ-values

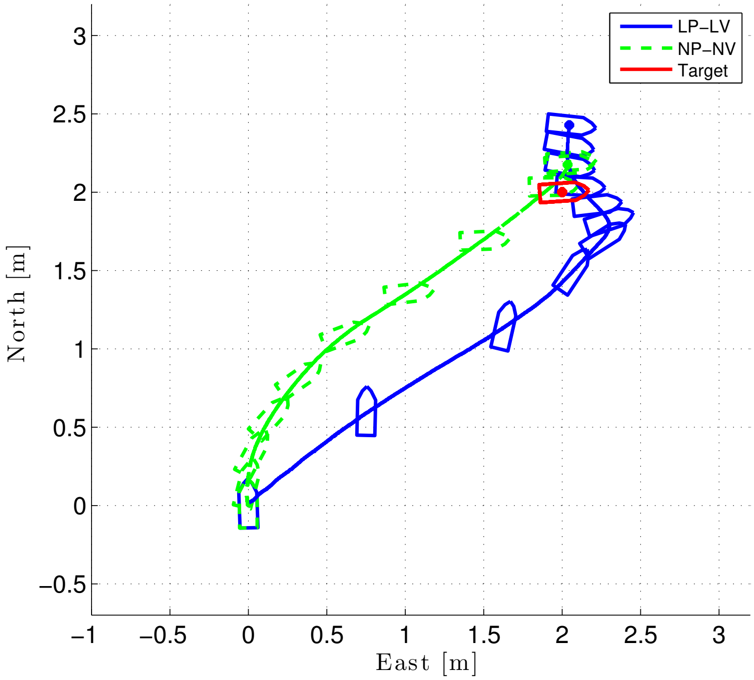

Figure 7.3: Experimental results of point stabilisation using LP-LV and NP-NV controllers. Originally shown in A.4.

must also be chosen carefully. If they are chosen too small, the control signal can get a discontinuous behavior and make the control signal exceed the saturation constraints in the linear region.

In Paper A.8, the NP-NV controller is combined with a magnitude-rate saturation (MRS) model and compared against the NP-NV controller using the 4-corner test. The considered MRS model has been introduced to decrease the wear and tear of the actuator but also to see if it could increase the performance for the controller. Both of the controllers are implemented on the CSAD. Here, it can be seen that MRS does not degrade the overall tracking performance. However, the NP-NV controller combined with the MRS model has a better energy efficiency and reduces the wear and tear on the actuator. In addition, MRS model has the potential to improve overall energy efficiency and pose tracking abilities, as can be seen from the performance metrics and trajectory plots, and can thus have positive effects on ship performance in setpoint navigation.

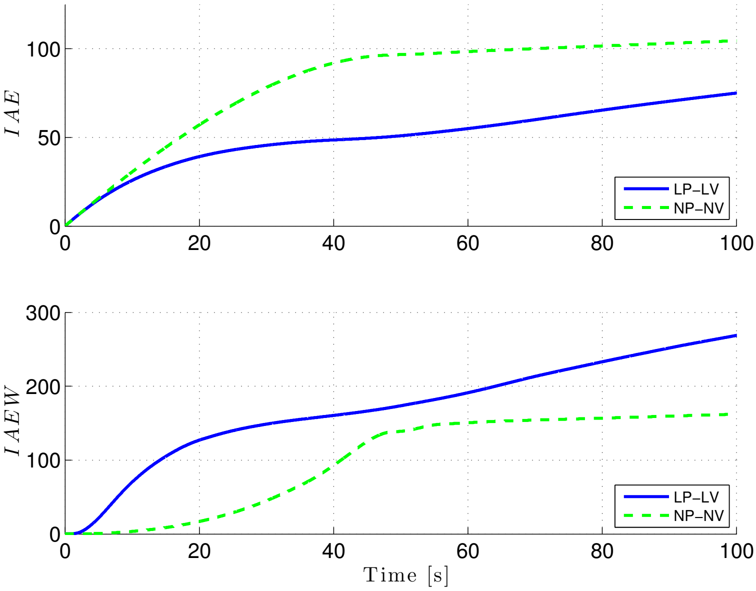

Figure 7.4: IAE and IAEW performance metrics of point stabilisation using LP-LV and NP-NV controllers. Originally shown in A.4.

7.2 Full-scale Experiments with R/V Gunnerus

7.2.1 Vessel

The research vessel R/V Gunnerus, shown in Figure 7.5, was launched to sea in 2006. The ship is owned and operated by NTNU. The ship has operated as an experimental platform within marine biology, marine archeology, oceanography, subsea geology, fisheries, and marine technology, since it was launched. Gunnerus is a diesel-electric ship of 31.25m length overall and powered by two 500kW gensets. When the ship was launched, it was equipped with two main propellers, shaftlines, rudders, and steering gear for conventional propulsion and steering, in addition to a tunnel thruster from Brunvoll. However, in spring 2015 it was retrofitted, since Gunnerus is a platform for testing innovative marine technology. Here, the conventional propulsion and steering were replaced by two new main azimuth permanent magnet rim drive thrusters in a prototype development project by Rolls-Royce [32]. The new thruster system makes the vessel highly maneuverable and capable of DP in a wide range of sea-states. Then later the same year, Kongsberg Maritime donated a new DP control system to Gunnerus, where the older Kongsberg SDP-11 system was replaced by a new K-Pos DP-11 system [2]. This makes use of the thrusters and ensures that the vessel can keep its position with high accuracy.

Figure 7.5: The NTNU-owned R/V Gunnerus that was used in the DP trials. Photo: Fredrik Skoglund.

7.2.2 DP Control System

As stated earlier the onboard DP control system is a K-Pos DP-11, which satisfies IMO DP Class 1 [38]. However, during the research campaign in Paper A.7, the DP computer software (and necessary hardware) was replaced by the next generation DP software development by Kongsberg Maritime. In this upgrade Kongsberg Maritime provided an API, or test module, where one has access to all relevant DP library and header files. In this way, it is possible to develop and implement experimental DP algorithms into the full-scale DP system without accessing Kongsberg source code. Since the architecture of the next generation DP system is modular, with a well-defined interface between the modules, this is now feasible and makes such testing possible. A topology drawing is shown in Figure 7.6 to illustrate the setup.

The figure shows that the NTNU test module is a new layer within the core DP software, where this module gets access to sensor signals from the signal processing modules, guidance signals (reference filter, the “carrot”, etc.), and estimated states from the KM Kalman filter. Then the module can command force/moment control actions using the KM built-in thrust allocation module that computes individual thruster setpoints. During these experiments the vessel is equipped with four Kongsberg Seatex MRU 5+ motion sensors. These are interfaced to the DP control system so that acceleration measurements can be used. In addition, an external computer with a customized Software-In-the-Loop (SIL) simulator of Gunnerus and the DP control software, so that testing and tuning of control parameters can be done on this simulator, while other experiments are conducted on the real DP system. This proves instrumental for efficient debugging and preparations before the actual experiment.

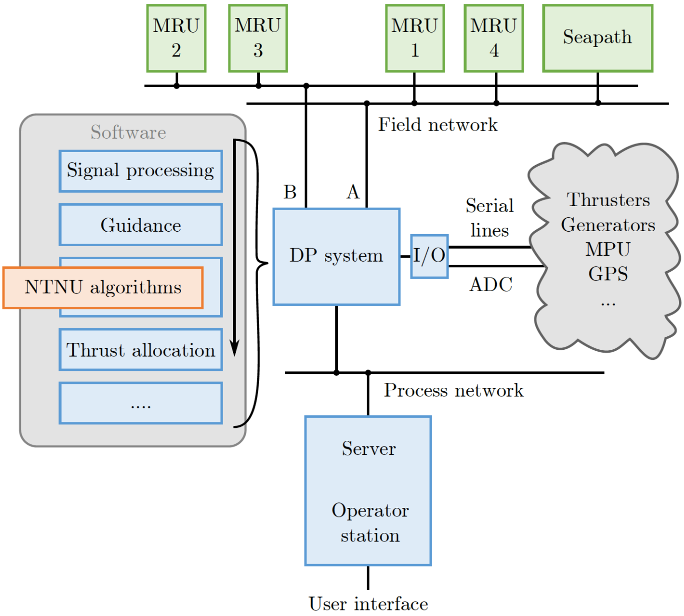

Figure 7.6: Topology drawing of the DP test interface that made it possible to test academic algorithms on the full-scale DP control system. Source: A.7.

7.2.3 Results

Only the results regarding nonlinear adaptive DP control laws in Paper A.7 are included in this thesis. Here, three adaptive DP control laws are proposed for full-scale experiments. The adaptive DP control laws are based on work in Paper A.3 and A.4. The 4-corner test is used as the desired trajectory for the vessel to track. This test was made in calm sea with insignificant current and wind. The results have shown that the adaptive controllers have a similar behavior in terms of tracking the target trajectory. Additionally, the results have shown that the considered algorithms have an issue of tracking during the combined backwards surge and sway motion. Of the three considered controllers the cascaded feedback controller with nonlinear feedback combined with a adaptation law has shown to have the overall best performance of the test. This is due to that it has best tracking performance of the heading and it does not diverge too much away from the setpoint when the vessel is doing a pure yaw motion. Experimental data from the 16th of November 2016 is shown in figures 7.7 and 7.8. Here, a 3 DOF NP-NV controller has been implemented. It is shown that the controllers do somewhat a good job of tracking the target.

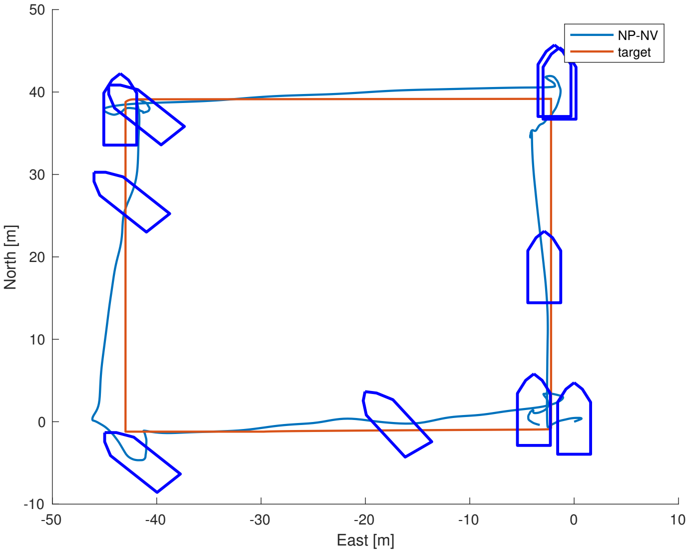

Figure 7.7: The ship tracking the target moving in the modified 4-corner test. The ship shown is a 1:4 scaled version.

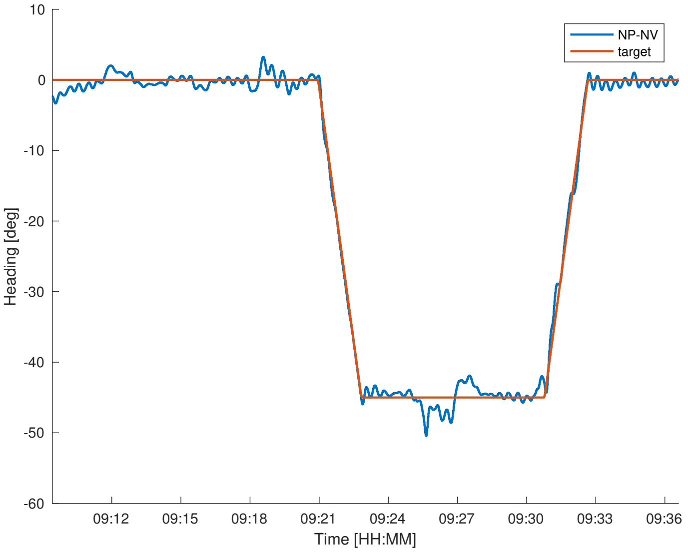

Figure 7.8: The ship tracking the heading of the 4-corner test.

Chapter 8

Concluding Remarks and Future Work

8.1 Conclusions

The work carried out in this thesis has presented new theoretical results and experimental verification in the topic of nonlinear and model-based control of ships. The control algorithms developed in this thesis are model-based, which enables the opportunity for formal stability analysis. Subjects such as investigation and modifications of the mathematical model, performance evaluation and specific control algorithms were discussed.

In Chapter 2, a generic model of a ship was presented, followed by an investigation of two specific ship models presented in previous literature. During the investigation of the steady-state solution of the kinetic model presented in [37], it was discovered that the modelled Munk moment, which is a destabilizing factor, gave rise to physically impossible motion. By modifying the damping matrix, so that the Munk moment would be cancelled out, it was shown that physically realistic model behavior could be achived. From the analyses of the steady-state point of the model from [8], it was shown that some parameters had the wrong sign or had a small influence on the model. These parameters are updated in papers A.8 and A.9 to correspond better with the actual physical behavior of CSAD. Further development of the model is done in [28], which is based on experimental data. The main results of [28] was also shown in this thesis.

To evaluate and compare the performance of different control algorithms, evaluation criteria were introduced. These evaluation criteria are defined as the performance metrics. Chapter 3 discussed the use of performance metrics as a way to evaluate the performance of various controller algorithms against each other. Nowadays, these performance metrics, which originally were suggested as a performance measures back in the early 1940s, are used as a tool to tune controllers. In addition to the performance metrics found in the literature study, new performance metrics were proposed, which consider both control accuracy and energy efficiency, and serve as a measure of actuator wear and tear, respectively.

Chapter 4, 5 and 6 present three different building blocks of a control system. In Chapter 4, an investigation of the use of nonlinear feedback terms was done. Hereafter, the use of linear and nonlinear feedback terms for pose and velocity control of ships, was composed. In addition to the controller discussed in papers A.2 and A.4, an asymmetric cascaded control algorithm was proposed. The results from papers A.2 and A.4 have shown that the nonlinear feedback controllers outperformed their linear counterpart in all scenarios, concerning both the handling of actuator saturation limits and the combined performance of control accuracy and energy use. The result of comparing a symmetric or asymmetric cascaded controller through simulation showed that the symmetric cascaded controller can exceed the saturation constraints due to the desired velocity assignment while asymmetric cascaded controller will hold the commanded control input just below the saturation constraints.

Chapter 5 proposed the use of a simplified dynamic window algorithm as a way to ensure that the actuator constraints of a ship is satisfied. The dynamic window algorithm was originally designed as a method to perform collision avoidance. The dynamic window algorithm was simplified by removing the collision avoidance part of the algorithm. This algorithm has been used as a dynamic window-based controller to guarantee that that ship velocities remain within a feasible set. In A.6, a DWC is evaluated against a heading and speed controller, which is used as a benchmark controller. Both methods were compared through numerical simulations. Two performance metrics were used to compare the behaviour of the controllers. The simulation results showed good tracking performance of the considered controllers, and that the dynamic window-based controller was able to inherently handle actuator magnitude constraints. As a way to ensure that the actuator magnitude constraints of a fully actuated ship are satisfied, an extension of a simplified dynamic window algorithm from 2 DOF to 3 DOF is proposed in A.9. The simulation results show that the proposed 3 DOF DWC controller has good tracking performance and is able to handle actuator magnitude constraints. Chapter 5 also showed experimental testing of the 3 DOF DWC controller. Here, it was shown that the control input has a large amount of oscillations and it was discovered that system uncertainties and time delays are the main reason causing the oscillations in the control input.

In Chapter 6, different adaptive concepts were applied to the vessel model to investigate which of these has the best performance. Here, two state-of-the-art adaptive controllers were compared against each other through numerical simulations. It was shown that the $\mathcal{L}_1$ adaptive backstepping controller has a better tracking performance and a better energy efficiency than for adaptive backstepping. An extension to the adaptive backstepping was designed and compared against adaptive backstepping. Simulations are conducted with a nonlinear 3 DOF model of a ship, showing the considered controllers have a good tracking performance and the ability to adapt for model uncertainties. It was also shown that the concurrent learning backstepping controller has a better performance than the adaptive backstepping.

Additionally, Chapter 6 has shown experimental results of the $\mathcal{L}_1$ adaptive cascaded nonlinear feedback controller, which were done in collaboration with Tore Sæterdal [33]. The experimental results showed that $\mathcal{L}_1$ adaptive cascaded nonlinear feedback controller has a better performance in terms of energy consumption, improving reference tracking and wear and tear than its baseline counterpart.

Finally, Chapter 7 has explained the experimental setup for both small-scale experiment at the marine cybernetics laboratory and full-scale experiment onboard the research vessel Gunnerus. The experimental results of publications shown in Appendix A, have been summaries in Chapter 7. The experimental results have validated the numerical simulation results of the various suggested control algorithms. As a concluding remark, this thesis has shown various building blocks to improve the performance for pose and velocity controller, with respect to magnitude constrains and handling uncertainties and disturbances. It should also be noted that these build blocks do not give one perfect controller. However, this is a steppingstone towards a complete solution.

8.2 Suggestions for Future Work

Finalising a PhD is a balance between new ideas and limited time. Many of the suggest algorithms have mainly been tested in simulations or in a controlled environment. The results of this thesis could be further elaborated considering the following suggestions for future work.

- The concurrent learning adaptation algorithm should be improved so that it does not require acceleration measurements.
- The effect of time-varying Δ_i-parameters for the cascaded nonlinear feedback controller should be investigated and compared against a controller with static Δ_i-parameters.
- The dynamic window-based controller needs to be modified so that it can handle model uncertainties, unknown disturbances and time delays. This is both valid for the 2 DOF and 3 DOF case. Furthermore, it is also relevant to consider actuator rate constraints in addition to magnitude constraints.
- Extend the 3 DOF DWC to include the full nonlinear ship model to achieve an overall better control performance, and possibly compute the set through analytical methods to obtain a more precise 3 DOF set of possible velocities.
- Make a thorough stability analysis of the DWC to obtain a better understanding about under which conditions the control algorithm is stable.
- The MRS model should be optimised to further improve performance. This includes, further tuning of the gain matrix $\boldsymbol{K}$ and the desired magnitude and rate saturation effects to obtain optimal ship control for the wanted ship operational environment.
- The proposed controllers should be implemented and tested in full-scale experiments.

References

[1] *Marine Cybernetics Laboratory Handbook.* Marine Technology, Norwegian University of Science and Technology, Trondheim, Norway, 2017.

[2] Adresseavisen. Gunnerus utstyrt til å ligge helt i ro. April, 2015, Accessed: 2018-07-20.

[3] B. D. O. Anderson. Failures of adaptive control theory and their resolution. *Communications in Information and Systems*, 05(1):1–20, 2005.

[4] B. D. O. Anderson and A. Dehghani. Challenges of adaptive control-past, present and future. *Annual Reviews in Control*, 32(2):123–135, 2008.

[5] K. Åström and B. Wittenmark. *Adaptive Control: Second Edition.* Dover Publications, 2013. ISBN 9780486319148.

[6] P. Bera, D. Das, and T. Basu. Tuning of excitation and tcsc-based stabilizers for multimachine power system. *International Journal of Engineering, Transactions B: Applications*, 23(1):37 – 52, 2010.

[7] E. S. Bjørne. *Nonlinear Adaptive Motion Control and Model-Error Analysis for Ships.* MSc thesis, Department of Engineering Cybernetics, Norwegian University of Science and Technology, Trondheim, Norway, 2016.

[8] J. Bjørnø, H.-M. Heyn, R. Skjetne, A. R. Dahl, and P. Frederich. Modeling, parameter identification and thruster-assisted position mooring of C/S Inocean CAT I Drillship. *in Proceedings of the 36th International Conference on Ocean, Offshore and Arctic Engineering, Trondheim, Norway*, 2017.

[9] M. Breivik and T. I. Fossen. Applying missile guidance concepts to motion control of marine craft. *in Proceedings of the 7th IFAC Conference on Control Applications in Marine Systems, Bol, Croatia*, 2007.

[10] M. Breivik and T. I. Fossen. *Guidance laws for autonomous underwater vehicles.* in A. V. Inzartsev, *Underwater Vehicles*, IN-TECH Education and Publishing, 51-76, 2009.

[11] M. Breivik, J. P. Strand, and T. I. Fossen. Guided dynamic positioning for fully actuated marine surface vessels. *in Proceedings of the 7th IFAC Conference on Manoeuvring and Control of Marine Craft, Lisbon, Portugal*, 2006.

[12] M. Breivik, V. E. Hovstein, and T. I. Fossen. Straight-line target trackingfor unmanned surface vehicles. *Modeling, Identification and Control*, 29(4): 131—149, 2008.

[13] G. Chowdhary and E. Johnson. Concurrent learning for convergence in adaptive control without persistency of excitation. *in Proceedings of the 49th IEEE Conference on Decision and Control. Atlanta, USA*, 2010.

[14] S. Di Cairano, H. Park, and I. Kolmanovsky. Model predictive control approach for guidance of spacecraft rendezvous and proximity maneuvering. *International Journal of Robust and Nonlinear Control*, 22(12):1398–1427, 2008.

[15] B.-O. H. Eriksen, M. Breivik, K. Y. Pettersen, and M. S. Wiig. A modified dynamic window algorithm for horizontal collision avoidance for AUVs. *in Proceedings of the IEEE Multi-Conference on Systems and Control, Buenos Aires, Argentina*, 2016.

[16] B.-O. H. Eriksen and M. Breivik. *Modeling, Identification and Control of High-Speed ASVs: Theory and Experiments*, pages 407–431. Sensing and Control for Autonomous Vehicles: Applications to Land, Water and Air Vehicles, Springer International Publishing, 2017.

[17] F. C. Fickeisen and T. M. Stout. Analogue methods for optimum servomechanism design. *Transactions of the American Institute of Electrical Engineers*, 71(5):244 – 250, 1952.

[18] T. I. Fossen. *Handbook of Marine Craft Hydrodynamics and Motion Control.* Wiley, 2011. ISBN 9781119998686.

[19] T. I. Fossen and K. Y. Pettersen. On uniform semiglobal exponential stability (USGES) of proportional line-of-sight guidance laws. *Automatica*, 50(11): 2912–2917, 2014.

[20] T. I. Fossen, M. Breivik, and R. Skjetne. Line-of-sight path following of underactuated marine craft. *in Proceedings of the 6th IFAC Conference on Manoeuvring and Control of Marine Craft, Girona, Spain*, 2003.

[21] D. Fox, W. Burgard, and S. Thrun. The dynamic window approach to collision avoidance. *IEEE Robotics & Automation Magazine*, 4(1):23–33, 1997.

[22] D. Graham and R. C. Lathrop. The synthesis of "optimum" transient response: Criteria and standard forms. *Transactions of the American Institute of Electrical Engineers*, 72(5):273 – 288, 1953.

[23] A. C. Hall. *The Analysis and Synthesis of Linear Servomechanisms.* PhD thesis, Department of Electrical Engineering, Massachusetts Institute of Technology, Cambridge, USA, 1943.

[24] N. Hovakimyan and C. Cao. *$\mathcal{L}1$ adaptive control theory : Guaranteed robustness with fast adaptation.* SIAM, 2010. ISBN 9780898717044.

[25] P. A. Ioannou and J. Sun. *Robust Adaptive Control.* Dover Publications, 1996. ISBN 9780846498171.

[26] M. Krstic, I. Kanellakopoulos, and P. V. Kokotovic. *Nonlinear and adaptive control design.* Wiley, 1995. ISBN 9780471127321.

[27] E. Lavretsky and K. A. Wise. *Robust and adaptive control : with aerospace applications.* Springer, 2013. ISBN 9781447143956.

[28] O. N. Lyngstadaas. *Ship Motion Control Concepts Considering Actuator Constraints.* MSc thesis, Department of Engineering Cybernetics, Norwegian University of Science and Technology, Trondheim, Norway, 2018.

[29] D. Maiti, A. Acharya, M. Chakraborty, A. Konar, and R. Janarthanan. Tuning pid and pi$^{\lambda}$d$^{\delta}$controllers using the integral time absolute error criterion. *in Proceedings of the 4th International Conference on Information and Automation for Sustainability, Colombo, Sri Lanka*, 2008.

[30] I. Obradovic. Die abweichungsfläche bei schnellregelvorgängen beitrag zur theorie der schnellregelung. *Archiv für Elektrotechnik*, 36(6):382–390, 1942.

[31] J. E. Refsnes. *Nonlinear Model-Based Control of Slender Body AUVs.* PhD thesis, Department of Marine Technology, Norwegian University of Science and Technology, Trondheim, Norway, 2008.

[32] Rolls-Royce. New: Azimuthing permanent magnet thruster. *Tech. rep. Rolls-Royce, Aug. 19.*, 2016.

[33] T. E. Sæterdal. *Nonlinear Adaptive Motion Controllers for Ships: Model-Scale Experiments in an Ocean Basin.* MSc thesis, Department of Engineering Cybernetics, Norwegian University of Science and Technology, Trondheim, Norway, 2018.

[34] F. Sandved. *Remote Control and Automatic Path-following for C/S Enterprise I and ROV Neptunus.* MSc thesis. Department of Marine Technology, Norwegian University of Science and Technology, Trondheim, Norway, 2015.

[35] W. C. Schultz and V. C. Rideout. Control system performance measures: Past, present, and future. *IRE Transactions on Automatic Control*, AC-6(1): 22 – 35, 1961.

[36] M. M. Seron, J. A. D. Dona, and G. C. Goodwin. Global analytical model predictive control with input constraints. *in Proceedings of the 39th IEEE Conference on Decision and Control, Colombo, Sydney, Australia*, 2000.

[37] R. Skjetne. *The Maneuvering Problem.* PhD thesis, Department of Engineering Cybernetics, Norwegian University of Science and Technology, Trondheim, Norway, 2005.

[38] International Maritime Organization. Guidelines for vessels with dynamic positioning systems. *Standard MSC/Circular.645, IMO, London, England, June 6. Ref. T4/3.03.*

[39] K. Wise, E. Lavretsky, and N. Hovakimyan. Adaptive control of flight: Theory, applications, and open problems. *in Proceedings of the American Control Conference, Minneapolis, USA*, 2006.

[40] T. Yucelen and E. Johnson. Command governor-based adaptive control. *in Proceedings of AIAA Guidance, Navigation, and Control Conference, Minneapolis, USA*, 2012.

Appendix A

Publications

A.1 Performance Comparison of Controllers with Fault-dependent Control Allocation for UAVs

M. E. N. Sørensen, S. Hansen, M. Breivik and M. Blanke, Performance comparison of controllers with fault-dependent control allocation for UAVs, *Journal of Intelligent & Robotic Systems*, 87(1):187–207, 2017.

Journal of Intelligent and Robotic Systems manuscript No.
(will be inserted by the editor)

Performance Comparison of Controllers with Fault-Dependent Control Allocation for UAVs

Mikkel Eske Nørgaard Sørensen[1] · **Søren Hansen**[2] · **Morten Breivik**[1] · **Mogens Blanke**[1,2]

Received: date / Accepted: date

Abstract This paper combines fault-dependent control allocation with three different control schemes to obtain fault tolerance in the longitudinal control of unmanned aerial vehicles. The paper shows that fault-dependent control allocation is able to accommodate actuator faults that would otherwise be critical and it makes a performance assessment for the different control algorithms: an $\mathcal{L}_1$ adaptive backstepping controller; a robust sliding mode controller; and a standard PID controller. The actuator faults considered are the partial to total loss of the elevator, which is a critical component for the safe operation of unmanned aerial vehicles. During nominal operation, only the main actuator, namely the elevator, is active for pitch control. In the event of a partial or total loss of the elevator, fault-dependent control allocation is used to redistribute control to available healthy actuators. Using simulations of a Cessna 182 aircraft model, controller performance and robustness are evaluated by metrics that assess control accuracy and energy use. System uncertainties are investigated over an envelope of pertinent variation, showing that sliding mode and $\mathcal{L}_1$ adaptive backstepping provide robustness, where PID control falls short. Additionally, a key finding is that the fault-dependent control allocation is instrumental when handling actuator faults.

Keywords Nonlinear longitudinal motion control · Fault-tolerant UAV control · $\mathcal{L}_1$ adaptive backstepping control · Sliding mode control · Fault-dependent control allocation · Performance metrics

Acknowledgements This work was supported by the Research Council of Norway through the Centres of Excellence funding scheme, the AMOS project, grant number 223254.

1 Introduction

Critical safety issues must be considered when dealing with aircraft such as unmanned aerial vehicles (UAVs). In order to minimize risk of failure, comprehensive checks are performed, and meticulous maintenance is done regularly. Failures nevertheless occur, and actuator and control surfaces have particularly high criticality. Actuator redundancy can deal with some of the safety issues for UAVs, and fault-tolerant control (FTC) strategies can be employed to utilise such redundancy in the actuators.

Several different control methods have been applied to improve aircraft reliability. An overview of the recent development of FTC methods for aerial vehicles are given in [1], [2], [3] and [4]. Specific fault diagnosis approaches are treated in [5], [6], [7] and [8] related to control surfaces, and in [9] to the airspeed sensor system. Two control techniques, sliding mode control (SMC) [10], [11] and $\mathcal{L}_1$ adaptive control [12], are claimed to offer robust properties against matched uncertainties. The performance of SMC for attitude control of a fixed-wing UAV is investigated in [13] where SMC is able to

---

[1] Centre for Autonomous Marine Operations and Systems,
Department of Engineering Cybernetics,
Norwegian University of Science and Technology,
NO-7491 Trondheim, Norway
E-mail: mikkel.sorensen@itk.ntnu.no, morten.breivik@ieee.org

[2] Automation and Control Group,
Department of Electrical Engineering,
Technical University of Denmark, Elektrovej B. 326,
DK-2800 Kgs. Lyngby, Denmark.
E-mail: sh@elektro.dtu.dk, mb@elektro.dtu.dk

handle partial loss of a control surface. To make the system fault tolerant against the total loss of a control surface, a sliding mode observer is introduced in [14], making it possible to estimate a specific actuator fault. The authors of [15] use SMC on a linear aircraft model for FTC without the use of fault detection and isolation (FDI), which is referred to as passive FTC. The same authors implement SMC using control allocation in [16] and apply this method on the SIMONA research simulator in [17], showing that the controller is redistributed to the functioning actuator when a fault happens on the elevator. The $\mathcal{L}_1$ adaptive control technique is shown in [18] to be robust against faulty actuators, while the $\mathcal{L}_1$ adaptive backstepping control (L1-AB) technique is used in [19] as the pitch autopilot for an agile missile.

Control allocation (CA) is based on separating the control law from the signal distribution task, which gives CA the possibility to be combined with many different control laws. This is done in [20] by designing a controller to provide a "virtual control" which is mapped to the actual control signals sent to the actuators. The CA approach can manage the redundancy of an over-actuated system [21]. The combination of L1-AB and CA is explored in [22] to control an F16 in a fault-free case. In [23], a fault-dependent control allocation scheme was developed and combined with L1-AB. In [1], SMC and CA is combined to analyse the performance for FTC applications. A further improvement is proposed in [24] using an integral sliding mode (ISM), which combines a controller that handles uncertainties of a system with the sliding mode control. If the system is subjected to external bounded disturbances, the ISM will compensate using sliding mode control while the original controller handles the unperturbed system [25]. In [26], an FTC structure which handles control surface failure is introduced by a combined use of generalized dynamic inversion control and ISM control. An over-actuated aircraft can easily maintain the required forces and moments even though a fault has occurred by applying the CA approaches suggested in [1] and [25]. However, many small aircraft and UAVs are not over-actuated and hence using the CA from [1] is not possible.

This paper is based on the work in [23]. Here, we suggest a new control allocation approach to handle the non-over-actuated control surface configuration usually found on smaller aircraft. Balancing the obtainable forces and moments, the CA is shown to help achieve a necessary flight envelope in case of faults, and simultaneously being able to preserve stabilisability. The fault-hiding property of the CA is then utilised by stabilising control to obtain a total fault-tolerant control system. The achievable performance is compared for three controller designs: A conventional PID, a robust controller in the form of sliding mode and an adaptive controller in the form of $\mathcal{L}_1$ adaptive backstepping. The PID is employed being a widely used baseline design in industry. The performance of the control concepts are explored through numerical simulations with a model of a Cessna 182 [27], which has been chosen because a high-fidelity aircraft model is available and that the aircraft, like most UAVs, have non-redundant actuation: an elevator to control pitch; a rudder for control of yaw; a pair of ailerons to control roll; a throttle to control forward thrust. Like most aircraft, the control surfaces available have limited redundancy. It is shown that the fault-dependent control allocation makes it possible for all the considered controllers to achieve excellent tracking performance even though a fault is occurring, and that the controllers have the ability to compensate for internal uncertainties. Additionally, it is shown that an adaptive controller in the form of $\mathcal{L}_1$ adaptive backstepping and a robust controller in the form of sliding mode perform better than the PID controller.

The structure of the paper is as follows: A mathematical model, assumptions and fault modelling are presented in Section 2; Section 3 deals with control allocation; Section 4 presents the controllers developed for the fixed-wing UAV; Section 5 includes definition of metrics, simulation results and performance evaluation obtained from the combination of the control laws and the control allocation; while Section 6 concludes the paper.

2 Aircraft Dynamics

Longitudinal aircraft motion is considered, where the state vector $\mathbf{x}_{lon} \triangleq [\theta, Q, \alpha, V_t]^\top$ is defined, with the components pitch angle θ [rad], pitch rate Q [rad/s], angle of attack α [rad] and true airspeed V_t [m/s] , see Fig. 1. The dynamics of the longitudinal aircraft model can be stated as [28]:

$$\dot{\theta} = Q \tag{1}$$

$$\begin{aligned} I_y\dot{Q} =& \bar{m}(Q, \alpha, \dot{\alpha}, V_t, \delta_e) \\ =& \bar{q}\bar{S}\bar{c}\Big(c_{m0} + c^*_{m\alpha}\alpha + c_{m\delta e}\delta_e \\ &+ \frac{\bar{c}}{2V_t}\left(c^*_{m\dot{\alpha}}\dot{\alpha} + c^*_{mQ}Q\right)\Big) \end{aligned} \tag{2}$$

$$mV_t\dot{\alpha} = mg\cos(\theta - \alpha) - T\sin(\alpha) - L + mV_tQ \tag{3}$$

$$m\dot{V}_t = T\cos(\alpha) - D - mg\sin(\theta - \alpha), \tag{4}$$

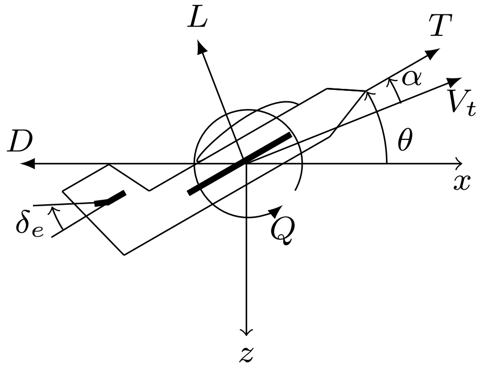

Fig. 1: Schematic of the longitudinal motion of an aircraft

where $m > 0$ [kg] is the mass of the aircraft, $g = 9.81$ [m/s^2] the gravity constant, I_y the y-moment of inertia, $\bar{q} = \frac{1}{2}\rho V_t^2$ the dynamic pressure, $\bar{S}$ wing area, $\bar{c}$ the mean aerodynamic chord of the wing, ρ air density, δ_e deflection angle of the elevator and T engine thrust, which is modelled as

$$T = \frac{\eta\delta_t}{V_t}, \tag{5}$$

where η is the propeller efficiency [%] and δ_t is input power [W]. Furthermore, the relations between the drag D, lift L, side force Y, roll moment $\bar{l}$, pitch moment $\bar{m}$, yaw moment $\bar{n}$ and the deflection of the control surfaces are [28]:

$$D = \bar{q}\bar{S}[c_D(\mathbf{x}_{lon}, \delta_e) + \Delta_D(\mathbf{x}_{lon}, \delta_e)] \tag{6}$$
$$L = \bar{q}\bar{S}[c_L(\mathbf{x}_{lon}, \delta_e) + \Delta_L(\mathbf{x}_{lon}, \delta_e)] \tag{7}$$
$$Y = \bar{q}\bar{S}[c_Y(\mathbf{x}_{lat}, \delta_a, \delta_r) + \Delta_Y(\mathbf{x}_{lat}, \delta_a, \delta_r)] \tag{8}$$
$$\bar{l} = \bar{q}\bar{S}b[c_l(\mathbf{x}_{lat}, \delta_a, \delta_r) + \Delta_l(\mathbf{x}_{lat}, \delta_a, \delta_r)] \tag{9}$$
$$\bar{m} = \bar{q}\bar{S}\bar{c}[c_m(\mathbf{x}_{lon}, \delta_e) + \Delta_m(\mathbf{x}_{lon}, \delta_e)] \tag{10}$$
$$\bar{n} = \bar{q}\bar{S}b[c_n(\mathbf{x}_{lat}, \delta_a, \delta_r) + \Delta_n(\mathbf{x}_{lat}, \delta_a, \delta_r)], \tag{11}$$

where $\mathbf{x}_{lat} \triangleq [\phi, \psi, P, R, \beta]^\top$ represents the lateral aircraft states, b the wing span, δ_a the deflection angle of the ailerons and δ_r the deflection angle of the rudder. The $\Delta_i(\mathbf{x}, \boldsymbol{\delta})$ terms, where the index i refers to forces and moments of (6)-(11), are unmodelled dynamics caused by uncertainty of the aerodynamic coefficients. It is assumed that $\Delta_i(\mathbf{x}, \boldsymbol{\delta})$ are unknown but bounded, as

$$||\Delta_i(\mathbf{x}, \boldsymbol{\delta})|| \leq \upsilon_i(\mathbf{x}, \boldsymbol{\delta}), \tag{12}$$

where $\upsilon_i(\mathbf{x}, \boldsymbol{\delta}) > 0$ is a known function.

2.1 Assumptions

The control objective is to track a reference signal of the pitch angle θ_d, see Section 4. In order to design a controller which fulfils this control objective, it is assumed that the true airspeed can be controlled separately and therefore can be neglected from the pitch controller design.

The angle of attack and true airspeed need to meet the conditions:

$$|\alpha| \leq \alpha_{max} \tag{13}$$
$$|\dot{\alpha}| \leq \dot{\alpha}_{max} \tag{14}$$
$$V_{t,min} \leq V_t \leq V_{t,max}. \tag{15}$$

The stall condition and the fear of structural damage to the wings are the reasons for these assumptions. It is assumed that uncertainties only exist in the coefficients of the pitch moment $\bar{m}$ and that the aerodynamic coefficients c_{m0} and $c_{m\delta e}$ are known. In [29] and [30], it is shown through system identification that these coefficients are almost perfectly identified, which gives the justification for this assumption about these coefficients.

For the rest of the aerodynamic coefficients, the relationship between the real and assumed coefficients is parametrised as

$$c^*_{m\alpha} = \sigma_\alpha c_{m\alpha} \tag{16}$$
$$c^*_{m\dot{\alpha}} = \sigma_{\dot{\alpha}} c_{m\dot{\alpha}} \tag{17}$$
$$c^*_{mQ} = \sigma_Q c_{mQ}, \tag{18}$$

where c^*_{mi} represents the true coefficients, $\sigma_\alpha \in \mathbb{R}^+$ is the uncertainty associated with the coefficient of pitch moment with respect to the angle of attack, $\sigma_{\dot{\alpha}} \in \mathbb{R}^+$ is the uncertainty associated with the coefficient of pitch moment with respect to the derivative of the angle of attack, and $\sigma_Q \in \mathbb{R}^+$ is the uncertainty associated with the coefficient of pitch moment with respect to the pitch rate. Additionally, it is assumed that $\dot{\sigma}_\alpha = \dot{\sigma}_{\dot{\alpha}} = \dot{\sigma}_Q = 0$, i.e. the uncertainties are constant or slowly varying relative to the aircraft dynamics.

Using these assumptions, the longitudinal motion in (1)-(4) becomes

$$\dot{\theta} = Q \tag{19}$$
$$I_y\dot{Q} = \bar{q}\bar{S}\bar{c}\Bigg(c_{m0} + \sigma_\alpha c_{m\alpha}\alpha + c_{m\delta e}\delta_e + \frac{\bar{c}}{2V_t}\left(\sigma_{\dot{\alpha}} c_{m\dot{\alpha}}\dot{\alpha} + \sigma_Q c_{mQ} Q\right)\Bigg). \tag{20}$$

2.2 Possible Faults

The following fault models are based on [1] and [15]. In this paper, it is assumed that only the elevator can be faulty. Elevator faults can be categorised as:

(a) Partial faults, which are commonly occurring in small aircraft, are
  - Partial loss of effectiveness, which is defined as an actuator that have a limited area of operation
  - Partial loss of control surface.

  A partial actuator fault can be modelled as

$$\boldsymbol{\delta}^e(t) = \mathbf{W}(t)\boldsymbol{\delta}(t), \tag{21}$$

  where $\boldsymbol{\delta}^e \in \mathbb{R}^3$ is the effective control vector, $\boldsymbol{\delta} \in \mathbb{R}^3$ is the control vector and $\mathbf{W}(t)$ represents the effectiveness of the actuators. The matrix $\mathbf{W}(t) \in \mathbb{R}^{3\times3}$ is defined as

$$\mathbf{W}(t) \overset{\triangle}{=} \mathrm{diag}(w_1(t), w_2(t), w_3(t)) = \mathbf{I} - \mathbf{K}(t), \tag{22}$$

  where $\mathbf{I} \in \mathbb{R}^{3\times3}$ is the identity matrix and $\mathbf{K}(t) \in \mathbb{R}^{3\times3}$ is the multiplicative fault matrix, which is defined for the aircraft as

$$\mathbf{K}(t) \overset{\triangle}{=} diag(k_1(t), k_2(t), k_3(t)) \tag{23}$$

  with $k_i(t) \in [0, 1)$, which is associated with the elevator, ailerons and rudder control surfaces. Here, $k_i = 0$ means that the ith control surface is in a fault-free condition, while $k_i = 1$ indicates that a total loss of effectiveness on the ith control surface has occurred.

(b) Total faults, which include
  - Stuck-in-place, which is defined as an actuator stuck at a fixed position being immovable
  - Hard-over, which is a special case of a stuck-in-place fault, where an actuator is stuck at an extreme position being immovable
  - Physically loss of control surface
  - Floating control surface.

  A total fault is modelled as

$$\delta_i^e(t) = k_i\delta_{i,f}, \tag{24}$$

  where $\delta_{i,f}$ is the control input which the ith control surface receives if it has a total fault. If the fault that has occurred is a stuck-in-place actuator fault then $\delta_{i,f} = c$ with $c \in [\delta_{i,min}, \delta_{i,max}]$ and $\dot{c} = 0$. A hard-over fault is a special case of a stuck-in-place fault where $\delta_{i,f} = \delta_{i,min}$ or $\delta_{i,f} = \delta_{i,max}$. A total loss of effectiveness on the ith control surface could also occur if the control surface is detached from the plane, i.e. $\delta_{i,f} = 0$. A floating control surface could occur of the actuator stop working and the control surface moves according to the wind, i.e. $\delta_{i,f} = \mathcal{N}(\mu, \sigma^2)$, where μ is the mean of deflection and σ is the stand deviation of deflection.

It is assumed in this paper that we have a fault detection and isolation scheme which is able to estimate the faults. For a real-world scenario, $\mathbf{W}(t)$ in (22) can be obtained by a separate fault identification scheme, see e.g. [1], [4], [9] and [31].

3 Fault-dependent Control Allocation

The role of the Control allocation (CA) is the following: Given commanded forces and moments from the controllers, calculate deflection of the control surfaces such that the commands are fulfilled. "A control allocation algorithm's primary objective is to compute a control input that ensures that the virtual control command is produced jointly by the effectors at all time" [20]. A general schematic of the proposed fault-dependent control allocation scheme is displayed in Fig. 2.

Three quantities are particularly important to derive the deflection angles on control surfaces: lift force, roll moment and yaw moment. The lift force ensures the aircraft remains airborne, while the roll and yaw moment are needed to stabilize the aircraft. We note that the control allocation does not take into account that some uncertainty exist in the pitch moment. For notational simplicity, time t is omitted in the following. Omitting the uncertainties $\Delta_i(\mathbf{x}, \boldsymbol{\delta})$, the lift force, roll moment and yaw moment in (7), (9) and (11) are

$$L = \bar{q}\bar{S}\left(c_L(\mathbf{x}_{lon}) + \frac{\partial c_L}{\partial \delta_e}\delta_e\right) \tag{25}$$

$$\bar{l} = \bar{q}\bar{S}b\left(c_l(\mathbf{x}_{lat}) + \frac{\partial c_l}{\partial \delta_a}\delta_a + \frac{\partial c_l}{\partial \delta_r}\delta_r\right) \tag{26}$$

$$\bar{n} = \bar{q}\bar{S}b\left(c_n(\mathbf{x}_{lat}) + \frac{\partial c_n}{\partial \delta_a}\delta_a + \frac{\partial c_n}{\partial \delta_r}\delta_r\right). \tag{27}$$

In the fault-free case, the deflection angles on the control surfaces are

$$\delta_{e,nom} = \frac{1}{\bar{q}\bar{S}\frac{\partial c_L}{\partial \delta_e}}\left(L - \bar{q}\bar{S}c_L(\mathbf{x}_{lon})\right), \tag{28}$$

$$\delta_{a,nom} = \frac{1}{\bar{q}\bar{S}b\frac{\partial c_l}{\partial \delta_a}}\left(\bar{l} - \bar{q}\bar{S}b\left(c_l(\mathbf{x}_{lat}) + \frac{\partial c_l}{\partial \delta_r}\delta_r\right)\right), \tag{29}$$

$$\begin{aligned}\delta_{r,nom} =& \frac{1}{\bar{q}\bar{S}b\left(\frac{\partial c_l}{\partial \delta_a}\frac{\partial c_n}{\partial \delta_r} - \frac{\partial c_l}{\partial \delta_r}\frac{\partial c_n}{\partial \delta_a}\right)}\left(\frac{\partial c_n}{\partial \delta_a}\left(\bar{q}\bar{S}bc_l(\mathbf{x}_{lat})\right.\right.\\ &\left.\left. -\bar{l}\right) + \frac{\partial c_l}{\partial \delta_a}\left(\bar{n} - \bar{q}\bar{S}bc_n(\mathbf{x}_{lat})\right)\right),\end{aligned} \tag{30}$$

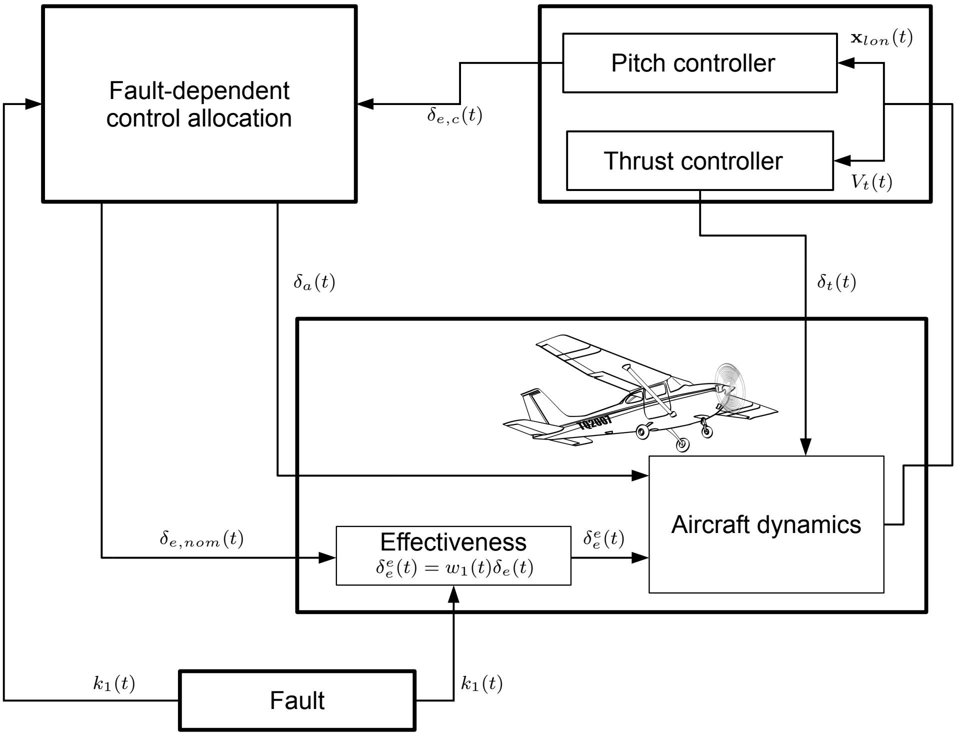

Fig. 2: Schematic of the fault-dependent control allocation implementation

where it is assumed that the aerodynamic coefficients $\frac{\partial c_L}{\partial \delta_e}$, $\frac{\partial c_l}{\partial \delta_a}$, $\frac{\partial c_l}{\partial \delta_r}$, $\frac{\partial c_n}{\partial \delta_a}$ and $\frac{\partial c_n}{\partial \delta_r}$ are constant and nonzero around a stationary condition. This assumption is based on results from wind tunnel tests [32].

Saturation of deflection angle is

$$\delta_{i,min} \leq \delta_i \leq \delta_{i,max}, \tag{31}$$

where the index i refers to elevator, ailerons or rudder.

3.1 Handling of Faults

In the following example, we consider a scenario where the elevator is faulty. However, this procedure can be incorporated into a general case. To overcome a partial or total elevator fault, the ailerons are subsequently reconfigured such that they work as a second set of elevators. The deflection angle for the ailerons δ_a is then recalculated for the drag force, lift force and pitch moment. It was concluded in [30] that the pitch moment is most difficult to maintain in the longitudinal system and the goal is therefore to maintain pitch moment. It is there desired to control the pitch moment, which also affects the other inputs in the longitudinal system, in this paper. The deflection angle for the ailerons δ_a is a function of effectiveness on the elevator, where the goal is to maintain the pitch moment $\bar{m}$

$$\delta_a = \frac{1}{\bar{q}\bar{S}\bar{c}\frac{\partial c_m}{\partial \delta_a}} \left(\bar{m} - \bar{q}\bar{S}\bar{c} \left(c_m(\mathbf{x}_{lon}) + \frac{\partial c_m}{\partial \delta_e} w_1 \delta_e \right) \right). \tag{32}$$

The CA approach for the elevator is evaluated in Fig. 3 over the range $[\delta_{e,min}, \delta_{e,max}]$ for the fault-free case and with a partial loss on the elevator. The input for the evaluation is the demanded deflection on the elevator $\delta_{e,nom}$, which has a limitation of [-22:18] degrees, and the output is the pitch moment which the fault-dependent control allocation using the aileron redistribution manages to obtain. Fig. 3 also shows the difference between the fault-free and the faulty cases and from which set point it is possible to maintain the same pitch moment by compensating the loss of the elevator with the ailerons. The span where the error is zero will decrease with the loss of effectiveness of the elevator.

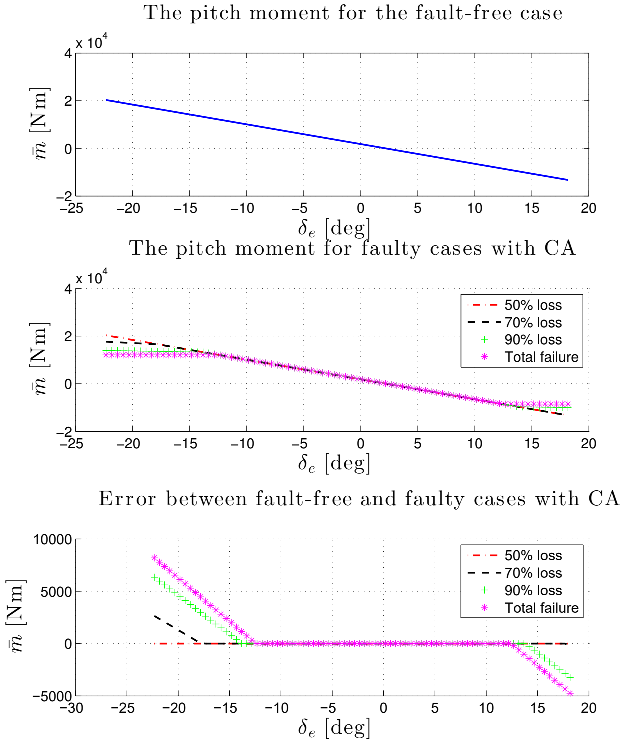

Fig. 3: Plots of the fault-free, faulty and difference between the fault-free and faulty cases with fault-dependent control allocation for the pitch moment

A method to improve the allocation span is

$$\delta_e = \frac{\delta_{e,nom}}{w_1 + \varrho} \tag{33}$$

$$\delta_a = \frac{1}{\bar{q}\bar{S}\bar{c}\frac{\partial c_m}{\partial \delta_a}}\left(\bar{m} - \bar{q}\bar{S}\bar{c}\left(c_m(\mathbf{x}_{lon}) + \frac{\partial c_m}{\partial \delta_e}\delta_e w_1\right)\right), \tag{34}$$

where $\varrho > 0$ is a small positive constant. However, this is only possible if the elevator is not saturated and only if it is a partial fault. The result of the approach in (33)-(34) gives a small improvement in the span where the pitch moment of the fault-free and faulty cases are the same.

In order to compensate for model uncertainties, a robust controller in the form of sliding mode and an adaptive controller in the form of $\mathcal{L}_1$ adaptive backstepping, which are known to handle unknown system parameters, are implemented. Additionally, a PID controller is implemented as a baseline.

4 Controller Design

This section presents procedures for a conventional PID controller, a robust controller in the form of sliding mode and an adaptive controller in the form of $\mathcal{L}_1$ adaptive backstepping for the longitudinal dynamics. The controller receives the pitch angle θ and pitch rate Q and gives a commanded control input as the deflection angle on the elevator $\delta_{e,c}$, which is converted into demanded force and moment in the control allocation block. The control objective is to make $|\theta(t) - \theta_d(t)| \to 0$, where the desired pitch angle $\theta_d(t)$ is $\mathcal{C}^2$ and bounded. This reference signal is typically defined by a human or generated by a guidance system. For notational simplicity, time t is omitted in the following. Note that in these derivation of control laws is the fault model not included since the purpose of the controllers are to operate in fault-free conditions and not handle the faults by themselves.

4.1 PID Control

The control law for a PID controller can be chosen as

$$\delta_{e,c} = K_{p,\theta}\frac{\tau_i s+1}{\tau_i s}\frac{\tau_d s+1}{a\tau_d s+1}e_p, \tag{35}$$

where

$$e_p \overset{\triangle}{=} \theta_d - \theta. \tag{36}$$

By making an input-output linearisation of (19)-(20) and since it is known from [32] that $c_m(\cdot) < 0$, the transfer function has a negative numerator, which changes the control law to

$$\delta_{e,c} = -K_{p,\theta}\frac{\tau_i s+1}{\tau_i s}\frac{\tau_d s+1}{a\tau_d s+1}e_p, \tag{37}$$

We have additionally introduced an anti-windup method to the PID controller since the elevator can saturate.

4.2 Sliding Mode Control (SMC)

The SMC design is divided into two stages: The first concerns the design of the sliding surface, while the second stage is designing the control law where the sliding mode is obtained. For the design of the control law, the assumed model parameters in Section 2.1 are used.

4.2.1 Sliding Surface Design

First, a sliding surface is defined by $\mathcal{S} \overset{\triangle}{=} \{\mathbf{e} : s = 0\}$, where $\mathbf{e}$ is vector of tracking errors and s is the switching function. The design of this sliding surface is formulated in [10] and [33], while this paper will use an approach inspired by [33].

The error signals are

$$e_1 \overset{\triangle}{=} \theta - \theta_d \tag{38}$$

$$e_2 \overset{\triangle}{=} \dot{e_1} = \dot{\theta} - \dot{\theta}_d = Q - Q_d, \tag{39}$$

and their derivatives are

$$\dot{e}_1 = e_2 \tag{40}$$

$$\dot{e}_2 = \dot{Q} - \dot{Q}_d. \tag{41}$$

Let the sliding surface be

$$s = e_2 + A_1 e_1 = 0, \quad A_1 > 0. \tag{42}$$

On this surface, the motion is governed by

$$\dot{e}_1 = -A_1 e_1. \tag{43}$$

4.2.2 Control Law Design

The derivative of the switching function s can be expressed as

$$\begin{aligned}\dot{s} &= \dot{e_2} + A_1\dot{e_1} \\ &= \frac{\bar{q}\bar{S}\bar{c}}{I_y}\Bigg(c_{m0} + c_{m\alpha}\alpha + c_{m\delta e}\delta_e \\ &\quad + \frac{\bar{c}}{2V_t}\left(c_{m\dot{\alpha}}\dot{\alpha} + c_{mQ}\left(s + Q_d - A_1 e_1\right)\right)\Bigg) \\ &\quad - \dot{Q}_d + A_1 e_2.\end{aligned} \tag{44}$$

For SMC, a sign function is ideally used to force $s \to 0$ in finite time. However, instead of the sign function, a saturation function has been chosen to minimise chattering. To ensure stability, the use of feedback control needs to turn (44) into a negative definite function, which is shown by (54). The input δ_e is chosen to be

$$\delta_{e,c} = \frac{-1}{c_{m\delta e}}\left(c_{m0} + \frac{I_y}{\bar{q}\bar{S}\bar{c}}\left(A_1 e_2 - \dot{Q}_d\right) - v\right), \tag{45}$$

where v is an additional control signal. Inserting δ_e from (45) into (44), the switching function is rewritten as

$$\dot{s} = \frac{\bar{q}\bar{S}\bar{c}}{I_y}\left(v + \zeta\right), \tag{46}$$

where

$$\zeta = c_{m\alpha}\alpha + \frac{\bar{c}}{2V_t}\left(c_{m\dot{\alpha}}\dot{\alpha} + c_{mQ}\left(s + Q_d - A_1 e_1\right)\right) \tag{47}$$

$$\tag{48}$$

such that

$$\begin{aligned}|\zeta| \le\ & |c_{m\alpha}|\alpha_{max} + \frac{\bar{c}}{2V_{t,min}}\left(|c_{m\dot{\alpha}}|\dot{\alpha}_{max}\right. \\ & \left. + |c_{mQ}||s + Q_d - A_1 e_1|\right).\end{aligned} \tag{49}$$

Then taking

$$v = -\beta \mathrm{sat}\left(\frac{s}{\varepsilon}\right), \ \varepsilon > 0, \tag{50}$$

and

$$\begin{aligned}\beta \ge\ & |c_{m\alpha}|\alpha_{max} + \frac{\bar{c}}{2V_{t_{min}}}\left(|c_{m\dot{\alpha}}|\dot{\alpha}_{max}\right. \\ & \left. + |c_{mQ}||s + Q_d - A_1 e_1|\right) + \beta_0,\end{aligned} \tag{51}$$

where $\beta_0 > 0$.

The derived control law is assessed by using a positive definite control Lyapunov function (CLF)

$$V_{SMC,1} = \frac{1}{2}s^2. \tag{52}$$

Taking the derivative yields

$$\dot{V}_{SMC,1} = s\dot{s} = s\frac{\bar{q}\bar{S}\bar{c}}{I_y}\left(c_{m\alpha}\alpha + \frac{\bar{c}}{2V_t}\left(c_{m\dot{\alpha}}\dot{\alpha} + c_{mQ}\left(s + Q_d - A_1e_1\right)\right) - \beta\right). \quad (53)$$

By inserting β, it can be said that for $|s| \geq \varepsilon$,

$$s\dot{s} \leq -\beta_0|s|\frac{\bar{q}\bar{S}\bar{c}}{I_y}, \quad (54)$$

which implies that the trajectories reach the boundary layer $\{|s| \leq \varepsilon\}$ in finite time. Inside the boundary layer

$$\dot{e}_1 = -A_1e_1 + s, \quad (55)$$

and choosing the CLF $V_{SMC,2} = \frac{1}{2}e_1^2$ and where $|s| \leq \varepsilon$, the derivative is

$$\dot{V}_{SMC,2} = e_1\dot{e_1} = -A_1e_1^2 + e_1s \leq -A_1e_1^2 + |e_1|\varepsilon. \quad (56)$$

By taking $A_1 = 2$

$$e_1\dot{e_1} \leq -2e_1^2 + |e_1|\varepsilon \leq -e_1^2 \text{ , } \forall \ |e_1| \geq \varepsilon. \quad (57)$$

By choosing this method it is not possible to stabilise the origin but it achieves ultimate boundedness with an ultimate bound which can be reduced by decreasing ε. From this knowledge, one should be aware of a small stationary control error. Finally, the commanded control signal becomes

$$\delta_{e,c} = \frac{-1}{c_{m\delta e}}\left(c_{m0} + \frac{I_y}{\bar{q}\bar{S}\bar{c}}\left(2e_2 - \dot{Q}_d\right) + \beta \text{ sat}\left(\frac{s}{\varepsilon}\right)\right). \quad (58)$$

4.3 $\mathcal{L}_1$ Adaptive Backstepping Control (L1-AB)

The design of the $\mathcal{L}_1$ adaptive backstepping controller can also be performed in two steps: The first stage concerns the design of the adaptation laws, while the second stage focus on the control law. The design is inspired by the approach in [19].

4.3.1 State Predictor

The prediction errors $\tilde{\theta}$ and $\tilde{Q}$ are defined as

$$\tilde{\theta} \overset{\triangle}{=} \hat{\theta} - \theta \quad (59)$$

$$\tilde{Q} \overset{\triangle}{=} \hat{Q} - Q, \quad (60)$$

where $\hat{\theta}$, $\hat{Q}$, θ and Q represent the estimated pitch angle, estimated pitch rate, real pitch angle and real pitch rate, respectively. The desired prediction error dynamics are chosen to be

$$\dot{\tilde{\theta}}_{ideal} = -L_1\tilde{\theta} \quad (61)$$

$$\dot{\tilde{Q}}_{ideal} = -L_2\tilde{Q}, \quad (62)$$

where the convergence rate is defined through the positive gains $L_1 > 0$ and $L_2 > 0$, to ensure that their origins are exponentially stable. From the latter, the state prediction dynamics are given as

$$\dot{\hat{\theta}} = -L_1\tilde{\theta} + Q \quad (63)$$

$$\dot{\hat{Q}} = -L_2\tilde{Q} + \frac{\bar{q}\bar{S}\bar{c}}{I_y}\left(c_{m0} + \hat{\sigma}_\alpha c_{m\alpha}\alpha + c_{m\delta e}\delta_e + \frac{\bar{c}}{2V_t}\left(\hat{\sigma}_{\dot{\alpha}}c_{m\dot{\alpha}}\dot{\alpha} + \hat{\sigma}_Q c_{mQ}Q\right)\right), \quad (64)$$

where $\hat{\sigma}_\alpha$, $\hat{\sigma}_{\dot{\alpha}}$ and $\hat{\sigma}_Q$ are the estimates of the aerodynamic parameter uncertainties. The design of adaptation laws for the uncertainties is based on Lyapunov stability analysis. Substituting (19), (20), (63) and (64) into (59) and (60), the prediction error dynamics become

$$\dot{\tilde{\theta}} = -L_1\tilde{\theta} \quad (65)$$

$$\dot{\tilde{Q}} = -L_2\tilde{Q} + \frac{\bar{q}\bar{S}\bar{c}}{I_y}\left(\tilde{\sigma}_\alpha c_{m\alpha}\alpha + \frac{\bar{c}}{2V_t}\left(\tilde{\sigma}_{\dot{\alpha}}c_{m\dot{\alpha}}\dot{\alpha} + \tilde{\sigma}_Q c_{mQ}Q\right)\right). \quad (66)$$

Let's consider the positive definite CLF

$$V_{pred} = \frac{1}{2}\left(\frac{1}{\gamma_\alpha}\tilde{\sigma}_\alpha^2 + \frac{1}{\gamma_{\dot{\alpha}}}\tilde{\sigma}_{\dot{\alpha}}^2 + \frac{1}{\gamma_Q}\tilde{\sigma}_Q^2\right) + \frac{1}{2}\tilde{\theta}^2 + \frac{1}{2}\tilde{Q}^2. \quad (67)$$

Taking the time derivative of (67) yields

$$\dot{V}_{pred} = \frac{1}{\gamma_\alpha}\tilde{\sigma}_\alpha\dot{\tilde{\sigma}}_\alpha + \frac{1}{\gamma_{\dot{\alpha}}}\tilde{\sigma}_{\dot{\alpha}}\dot{\tilde{\sigma}}_{\dot{\alpha}} + \frac{1}{\gamma_Q}\tilde{\sigma}_Q\dot{\tilde{\sigma}}_Q - L_1\tilde{\theta}^2 - L_2\tilde{Q}^2 + \tilde{Q}\left(\frac{\bar{q}\bar{S}\bar{c}}{I_y}\left(\tilde{\sigma}_\alpha c_{m\alpha}\alpha + \frac{\bar{c}}{2V_t}\left(\tilde{\sigma}_{\dot{\alpha}}c_{m\dot{\alpha}}\dot{\alpha} + \tilde{\sigma}_Q c_{mQ}Q\right)\right)\right). \quad (68)$$

Since it is assumed that $\dot{\sigma}_\alpha = \dot{\sigma}_{\dot{\alpha}} = \dot{\sigma}_Q = 0$, (68) can be rewritten as

$$\dot{V}_{pred} = -L_1\tilde{\theta}^2 - L_2\tilde{Q}^2 + \tilde{\sigma}_\alpha\left(\frac{1}{\gamma_\alpha}\dot{\hat{\sigma}}_\alpha + \tilde{Q}\frac{\bar{q}\bar{S}\bar{c}}{I_y}c_{m\alpha}\alpha\right) + \tilde{\sigma}_{\dot{\alpha}}\left(\frac{1}{\gamma_{\dot{\alpha}}}\dot{\hat{\sigma}}_{\dot{\alpha}} + \tilde{Q}\frac{\bar{q}\bar{S}\bar{c}}{I_y}\frac{\bar{c}}{2V_t}c_{m\dot{\alpha}}\dot{\alpha}\right) + \tilde{\sigma}_Q\left(\frac{1}{\gamma_Q}\dot{\hat{\sigma}}_Q + \tilde{Q}\frac{\bar{q}\bar{S}\bar{c}}{I_y}\frac{\bar{c}}{2V_t}c_{mQ}Q\right). \quad (69)$$

To eliminate the uncertainty terms $\hat{\sigma}_\alpha$, $\hat{\sigma}_{\dot{\alpha}}$ and $\hat{\sigma}_Q$, the adaptive update laws are chosen as

$$\dot{\hat{\sigma}}_\alpha = \gamma_\alpha \text{Proj}\left(\hat{\sigma}_\alpha, -\tilde{Q}\frac{\bar{q}\bar{S}\bar{c}}{I_y}c_{m\alpha}\alpha\right) \tag{70}$$

$$\dot{\hat{\sigma}}_{\dot{\alpha}} = \gamma_{\dot{\alpha}} \text{Proj}\left(\hat{\sigma}_{\dot{\alpha}}, -\tilde{Q}\frac{\bar{q}\bar{S}\bar{c}}{I_y}\frac{\bar{c}}{2V_t}c_{m\dot{\alpha}}\dot{\alpha}\right) \tag{71}$$

$$\dot{\hat{\sigma}}_Q = \gamma_Q \text{Proj}\left(\hat{\sigma}_Q, -\tilde{Q}\frac{\bar{q}\bar{S}\bar{c}}{I_y}\frac{\bar{c}}{2V_t}c_{mQ}Q\right), \tag{72}$$

where Proj$(\cdot)$ denotes the projection operator [12]. Then (69) becomes

$$\dot{V}_{pred} = -L_1\tilde{\theta}^2 - L_2\tilde{Q}^2 \leq 0 \quad \forall\tilde{\theta}, \tilde{Q} \neq 0. \tag{73}$$

4.3.2 Control Law

We start by defining the error variables z_1 and z_2 as

$$z_1 \overset{\triangle}{=} \theta - \theta_d \tag{74}$$

$$z_2 \overset{\triangle}{=} Q - \alpha_1, \tag{75}$$

where α_1 is a stabilising function to be designed. Consider the positive definite CLF

$$V_{ctrl,1} = \frac{1}{2}z_1^2, \tag{76}$$

whose derivative with respect to time along the z_1 dynamics becomes

$$\begin{aligned}\dot{V}_{ctrl,1} &= z_1\dot{z}_1 \\ &= z_1(\dot{\theta} - \dot{\theta}_d) \\ &= z_1(Q - Q_d) \\ &= z_1(z_2 + \alpha_1 - Q_d).\end{aligned} \tag{77}$$

By substituting (75) into (77), the CLF becomes

$$\dot{V}_{ctrl,1} = z_1z_2 + z_1(\alpha_1 - Q_d).$$

The stabilising function can be chosen as

$$\alpha_1 = -K_1z_1 + Q_d, \tag{78}$$

where $K_1 > 0$, which gives

$$\dot{V}_{ctrl,1} = -K_1z_1^2 + z_1z_2. \tag{79}$$

The CLF is then extended to

$$V_{ctrl,2} = \frac{1}{2}z_2^2 + V_{ctrl,1}, \tag{80}$$

such that it includes both z_1 and z_2. The derivative of the new CLF is

$$\begin{aligned}\dot{V}_{ctrl,2} =& z_2\dot{z}_2 + \dot{V}_{ctrl,1} \\ =& z_2\left(\frac{\bar{q}\bar{S}\bar{c}}{I_y}\left(c_{m0} + \sigma_\alpha c_{m\alpha}\alpha + c_{m\delta e}\delta_e\right.\right. \\ &\left.\left. + \frac{\bar{c}}{2V_t}\left(\sigma_{\dot{\alpha}}c_{m\dot{\alpha}}\dot{\alpha} + \sigma_Q c_{mQ}Q\right)\right) - \dot{\alpha}_1\right) \\ &- K_1z_1^2 + z_1z_2 \\ =& - K_1z_1^2 + z_2\left(\frac{\bar{q}\bar{S}\bar{c}}{I_y}\left(c_{m0} + \sigma_\alpha c_{m\alpha}\alpha + c_{m\delta e}\delta_e\right.\right. \\ &\left.\left. + \frac{\bar{c}}{2V_t}\left(\sigma_{\dot{\alpha}}c_{m\dot{\alpha}}\dot{\alpha} + \sigma_Q c_{mQ}Q\right)\right) - \dot{\alpha}_1 + z_1\right).\end{aligned}$$

The control law is chosen as

$$\begin{aligned}\delta_{e,com} =& \frac{-1}{c_{m\delta e}}\left(c_{m0} + \hat{\sigma}_\alpha c_{m\alpha}\alpha + \frac{\bar{c}}{2V_t}\left(\hat{\sigma}_{\dot{\alpha}}c_{m\dot{\alpha}}\dot{\alpha}\right.\right. \\ &\left.\left. + \hat{\sigma}_Q c_{mQ}Q\right) + \frac{I_y}{\bar{q}\bar{S}\bar{c}}\left(z_1 - \dot{\alpha}_1 + K_2z_2\right)\right),\end{aligned} \tag{81}$$

where $K_2 > 0$. It is assumed that uncertainties can be estimated perfectly through $\hat{\sigma}_\alpha$, $\hat{\sigma}_{\dot{\alpha}}$ and $\hat{\sigma}_Q$ using the state predictor as a cascade system. This leads to

$$\dot{V}_{ctrl,2} = -K_1z_1^2 - K_2z_2^2 < 0 \quad \forall z_1, z_2 \neq 0. \tag{82}$$

The adaptation of the uncertainties may contain high-frequency signals. To avoid introducing such frequencies into the control input, a lowpass filter is introduced to the control signals such that

$$\delta_{e,c} = C(s)\delta_{e,com},$$

where

$$C(s) = \frac{k}{s+k},$$

is applied to the control signal and the gain $k > 0$ is a design parameter.

5 Simulation Results and Performance Evaluation

This section first states the parameters of the aircraft model, followed by the initial states and control parameters used in the simulations. Subsequently, the metrics used to evaluate performance are defined. Finally, results associated with the different controllers are shown and discussed.

5.1 Simulation Setup

For simulation purposes, the controllers are implemented in Matlab. A Cessna 182 from [32] will be used to demonstrate the performance of the proposed methods. The parameter values for the aircraft are listed in Table 1.

Table 1: Parameters for a Cessna 182 [32]

m	1202.02 [kg]	c_{m0}	0.04
g	9.81 [m/s^2]	$c^*_{m\alpha}$	-0.613
I_y	56.72 [kg m^2]	$c_{m\delta e}$	-1.122
$\bar{S}$	16.17 [m^2]	$c^*_{m\dot{\alpha}}$	-7.27
$\bar{c}$	0.46 [m]	c^*_{mQ}	-12.4
$\bar{q}$	2 375.31 [N/m^2]		

The elevator δ_e and ailerons δ_a have a limitation of [-22:18] and [-24:24] degrees in deflection angle, respectively. Here, the effectiveness matrix $\mathbf{W}(t)$ from (22) is assumed to be known. The aerodynamic constants for the reconfigured ailerons are chosen to be $c_{L\delta a} = 2c_{L\delta e}$ and $c_{m\delta a} = \frac{1}{2}c_{m\delta e}$.

5.1.1 Initial States, Reference Signal, and Control Parameters

The initial conditions of the aircraft are that it is flying straight and level, which means $\dot{Q} = \dot{\theta} = \dot{\alpha} = \dot{V}_t = 0$ and $\theta = \alpha \approx 0$. The simulation starts at an altitude of 1524 [m] and a true airspeed of 67 [m/s].

The uncertainties for the system are chosen as $\sigma_\alpha = 4$, $\sigma_{\dot{\alpha}} = 5$ and $\sigma_Q = 7$. The initial values for the estimated uncertainties are $\hat{\sigma}_\alpha(0) = \hat{\sigma}_{\dot{\alpha}}(0) = \hat{\sigma}_Q(0) = 1$. The elevator actuator fault is set to occur at 30 [s].

It is desired for the aircraft to track first a constant pitch angle $\theta_{ref} = 10$ [deg] from $t = 0$ and then a constant pitch angle $\theta_{ref} = 5$ [deg] from $t = 50$. To obtain a reference signal of θ_d that is in $\mathcal{C}^2$ and bounded, the constant pitch angle is put through a third-order lowpass filter with the structure

$$\dot{\boldsymbol{\theta}}_d(t) = \mathbf{A}\boldsymbol{\theta}_d(t) + \mathbf{B}\theta_{ref}, \tag{83}$$

where $\boldsymbol{\theta}_d(t) = [\theta_d, Q_d, \dot{Q}_d]^\top$ and

$$\mathbf{A} = \begin{bmatrix} 0 & 1 & 0 \\ 0 & 0 & 1 \\ -\omega_0^3 & -(2\zeta+1)\omega_0^2 & -(2\zeta+1)\omega_0 \end{bmatrix} \quad \mathbf{B} = \begin{bmatrix} 0 \\ 0 \\ \omega_0^3 \end{bmatrix}. \tag{84}$$

The initial condition of the reference signal is chosen to be $\boldsymbol{\theta}_d(0) = [0 \text{ [deg]}, 0 \text{ [deg/s]}, 0 \text{ [deg/s}^2\text{]}]^\top$. Additionally, it is desirable to lower the true airspeed to the optimal climb speed of 50 [m/s], which is passed through a similar third-order lowpass filter to obtain a time-varying reference signal for the true airspeed.

The gain for designing the control law for the SMC is chosen to be $\varepsilon = 0.005$ and $\beta_0 = 0.5$.

The L1-AB controller has a lowpass filter integrated in the control law to reject high frequency oscillations in the estimation of the uncertainties. Utilising this benefit, the control law for the L1-AB is designed with $K_1 = 21$ and $K_2 = 130$. The gains for the state predictor are chosen to be $L_1 = L_2 = 300$. The adaptation gains for the estimation of the uncertainties are chosen to be $\gamma_{\sigma,\alpha} = \gamma_{\sigma,\dot{\alpha}} = \gamma_{\sigma,Q} = 4000$. The gain for the lowpass filter is chosen to be $k = 300$.

The baseline PID controller for the pitch motion has been implemented with the gains $K_{p,\theta} = 1.5$, $\tau_i = 1.5$, $\tau_d = 0.15$ and $a = 0.1$ obtained through tuning by assuming that the parameters $c_{m\alpha}$, $c_{m\dot{\alpha}}$ and c_{mQ} are the true values. These control gains are chosen conservatively in order to cope with uncertainties in the aircraft model.

To control the airspeed during the simulation, a PI-controller has been implemented in a speed control loop. The gains $K_{P,Vt} = 20$ and $K_{I,Vt} = 0.5$ have been chosen for the proportional and integral gains, respectively.

5.1.2 Performance Metrics

To evaluate and compare the performance of the different control algorithms, it is advantageous to use performance metrics. These include the integral of the absolute error (IAE), integral of the square of the error (ISE) and integral of the absolute error multiplied by time (ITAE). Here, the error e is defined as the pitch angle error

$$e \overset{\triangle}{=} \theta - \theta_d. \tag{85}$$

The formula for the IAE is given as

$$IAE = \int_0^t |e| d\tau, \tag{86}$$

which simply describes the temporal evolution of the absolute value of the error without adding any weight to the error. The ISE is defined as

$$ISE = \int_0^t e^2 d\tau \tag{87}$$

and penalises large errors more than smaller ones, indicating how good the particular algorithm is at eliminating large errors. The computation of ITAE is given as

$$ITAE = \int_0^t \tau |e| d\tau, \tag{88}$$

which penalises errors which have been present for a long time more heavily than those at the beginning. ITAE will show if there is a steady error present in the system.

A final performance metric is also proposed, namely the integral of the absolute error multiplied by the energy consumption (IAEW), which can be computed by

$$IAEW = \int_0^t |e| d\tau \int_0^t P d\tau, \tag{89}$$

where

$$P = |Q\delta_{e,c}|, \tag{90}$$

which represents the mechanical power and not the actual power consumption. It is noted that it is the control command $\delta_{e,c}$, the input to the control allocation block, which is used for calculation of P, since it is desired to evaluate the performance of the controllers. The reason for considering IAEW is to get an indication of which control algorithm has the best combination of tracking performance and energy consumption.

5.2 Results

In the following sections, the simulation results of the different controllers are illustrated for both a fault-free and a faulty case. The performance metrics defined previously are used to evaluate the performance of the controllers.

5.2.1 Fault-Free Case

Fig. 4 displays the desired and actual trajectories of the state of the aircraft in the fault-free case, which shows that the methods are able to track the pitch angle and pitch rate. The PID controller is slower than the others, which is a trade-off by tuning it conservatively such that it can handle uncertainties. Additionally, it takes some time to achieve the desired true airspeed, which depends on how well the airspeed PI-controller has been tuned. Be advised that the length of the time axis is different in figures 4, 5 and 6, in order for the reader to easily see the properties of controllers.

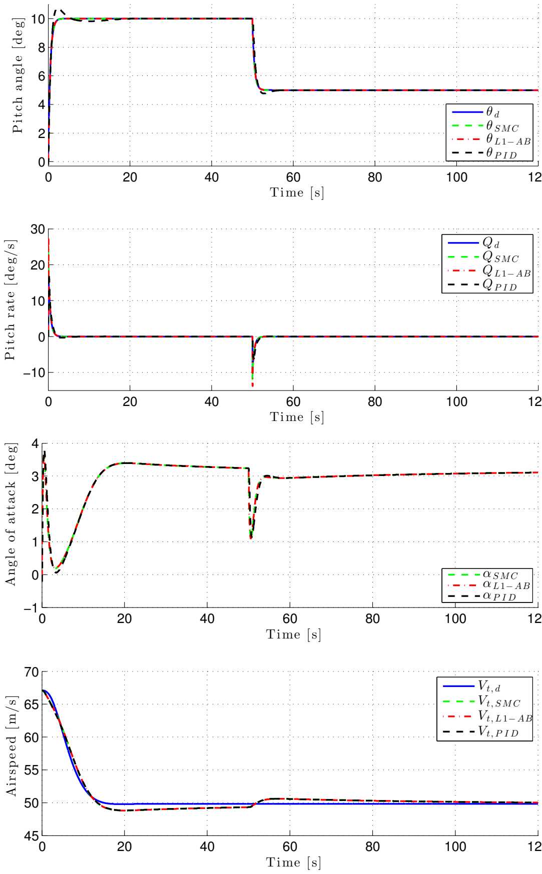

Fig. 4: States in the fault-free case

The control signals are shown in Fig. 5, where the three controllers have the same control signal after 0.3 seconds. Both the L1-AB and SMC have some high-frequency oscillations on the elevator in the start of the simulation. Since there is no fault present in the system there is no control signal distribution to the ailerons. In the simulations, the motor power shows a drop around 10 seconds after the simulation has started. This is a caused by the control system as a reaction to stabilize the angle of attack α.

The tracking errors of the pitch angle and rate are dis-

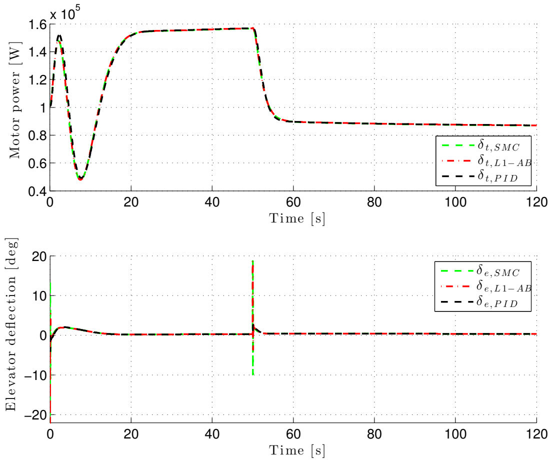

Fig. 5: Inputs in the fault-free case

played in Fig. 6, showing that the two nonlinear controllers track the pitch angle and rate fast, while the PID controller requires almost 20 seconds for the pitch angle error to go to zero. Additionally, the L1-AB has a small overshoot and the PID is oscillating on the pitch angle, which makes them use more time to track the reference signal compared to the SMC. However, the L1-AB and PID controllers have the advantage that they do not result in a stationary tracking error. The SMC is a robust controller without integral action, which is why it has a stationary tracking error.

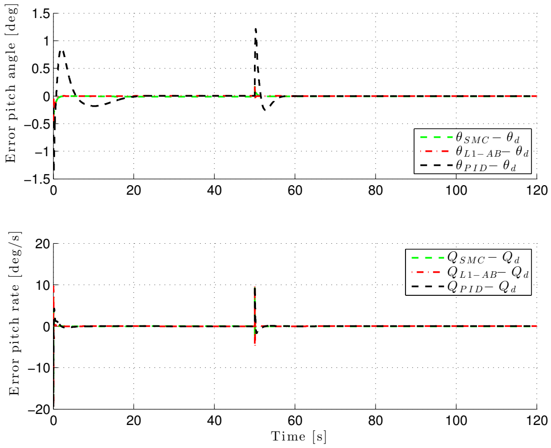

Fig. 6: Errors in the fault-free case

5.2.2 Faulty Case: Total Elevator Loss without Fault-dependent Control Allocation

In the faulty case, the elevator goes to zero at 30 sec. The states in Fig. 7 show that the aircraft is no longer able to track the desired pitch angle and true airspeed after the fault has occurred.

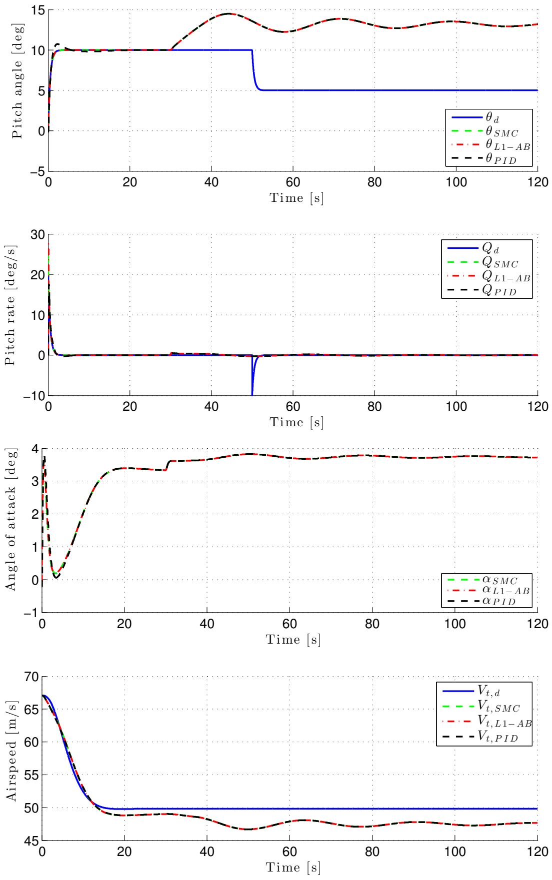

Fig. 7: States in the faulty case without fault-dependent control allocation

From Fig. 8 it can be concluded that this scenario has a high risk of going into an irreversible stall or spin. Since the elevator is stuck, there is no redundancy and the engine is already producing the maximum amount of power.

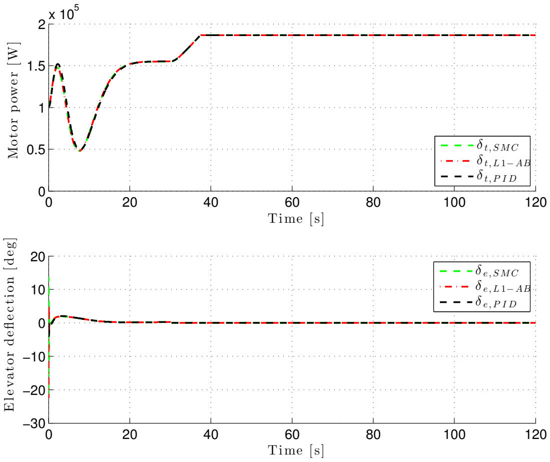

Fig. 8: Inputs in the faulty case without fault-dependent control allocation

5.2.3 Faulty Case: Total Elevator Loss with Fault-dependent Control Allocation

As in Section 5.2.2, the elevator goes to zero and holds this position from 30 seconds. The results of loosing the elevator completely is displayed in Fig. 9-11. The only noticeable difference in the states compared to the fault-free case is the angle of attack, which has a smaller stationary value.

By inspecting the inputs in Fig. 10, the change in the angle of attack α is caused by the amount of engine power. Additionally, Fig. 10 shows that when the effect of the elevator is lost, the ailerons become active since the control signal is reallocated to the ailerons.

Comparing the results with the fault-free case concerning the pitch angle and pitch rate tracking errors in figures 6 and 11 shows no degradation in the performance even when the elevator is faulty.

5.2.4 Performance Evaluation

Figures 12 and 13 display the curves of IAE, ISE, ITAE and IAEW for the pitch angle tracking error. Fig. 12 clearly indicates that the L1-AB has the best performance both in terms of tracking and handling quickly-varying signals. It is easier to see to from Fig. 12 that SMC has a stationary error since the IAE is constantly growing.

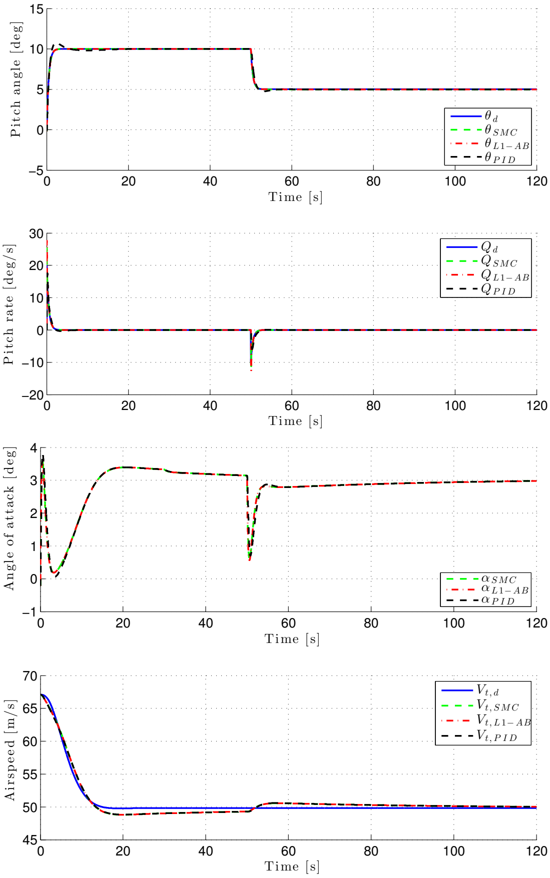

Fig. 9: States in the faulty case with fault-dependent control allocation

The ITAE shown in Fig. 13 clearly indicates that L1-AB yields convergence of the pitch angle tracking error to zero. The plots of the ITAE illustrate that the SMC has a better performance than the PID. In the evaluation between tracking performance versus energy consumption when uncertainties are affecting the system, the L1-AB controller performs best, while the SMC performs better than the PID controller. The SMC has an increasing IAEW because it has a stationary error which is multiplied with a constant high energy use.

The simulations also show that the nonlinear control algorithms perform better than the PID controller. However, utilising the benefit which $\mathcal{L}_1$ adaptive backstepping control gives, we are able to choose higher adaptation rates and minimising the effects of high-frequency oscillations in the control signal and therefore get a better tracking performance than for SMC.

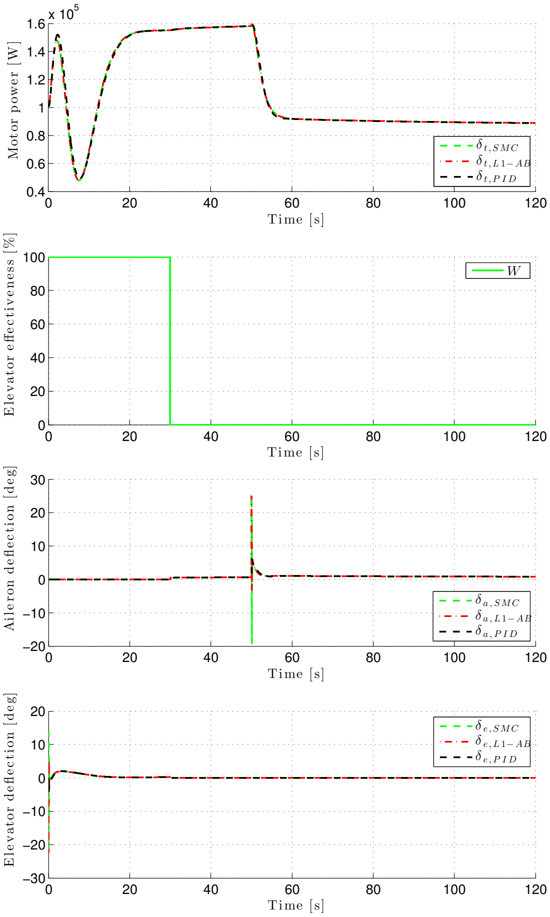

Fig. 10: Inputs in the faulty case with fault-dependent control allocation

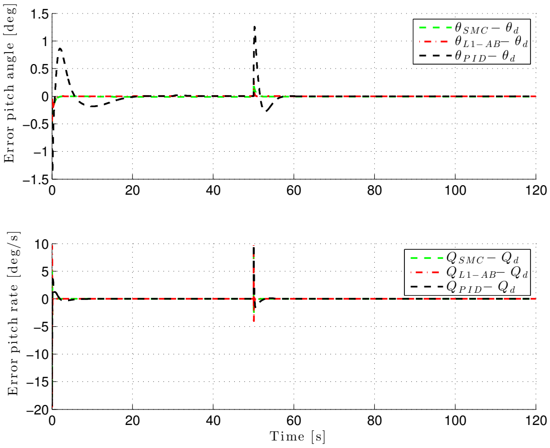

Fig. 11: Errors in the faulty case with fault-dependent control allocation

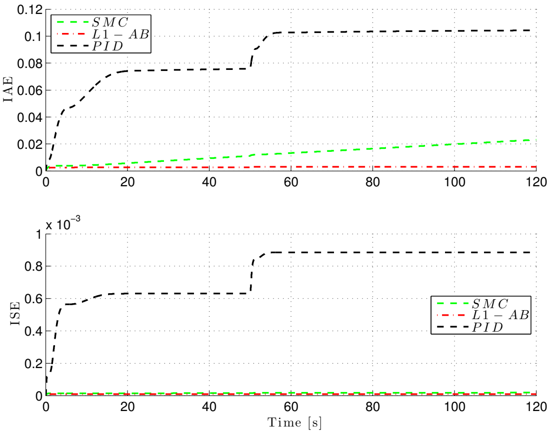

Fig. 12: The IAE and ISE of the pitch angle error in the fault-free scenario

The considered controllers have both advantages and disadvantages:

- The PID has a simple design, which makes it require less computational power than the nonlinear controllers. However, the PID is conservatively tuned since the aircraft model include uncertainties, which results in a slower tracking performance.
- The sliding mode controller is able overcome the model uncertainties, but it does not have integral action, which leads to a stationary tracking error.
- The $\mathcal{L}_1$ adaptive backstepping controller is able to overcome the model uncertainties and track the reference signal. However, in order to do so it requires a large amount of power for a small period of time and it has some high-frequency oscillations in the control signal.

In Table 2, the results of the following properties are listed on a scale of 1-5:

- Energy: The amount of energy the controller requires to perform the task.
- Convergence speed: How fast the controller converges to a set point.
- Robustness: How good the controller is in accommodating for uncertainties in the system.
- Control accuracy: How the controller's ability is to converge to and stay on target.

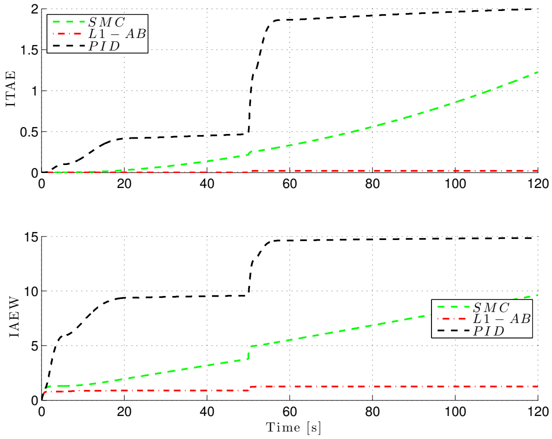

Fig. 13: The ITAE and IAEW of the pitch angle error in the fault-free scenario

- Actuator stress: How much stress the controller puts on the actuator in order to perform the given task.

Table 2: Strengths and weaknesses of the particular control algorithms in this evaluation. On a scale 1 (worst) to 5 (best)

	PID	**SMC**	**L1-AB**
Energy	3	2	2
Convergence speed	3	4	5
Robustness	3	5	5
Control accuracy	3	2	4
Actuator stress	3	3	2
Total	15	16	18

To validate that the advanced controllers are able to run in real time, the controllers were implemented as discrete-time algorithms running a sampling rate of 200 Hz. Using Matlab/Simulink we are able to measure the execution time of the three controllers. The results are presented in Table 3, which shows that all the controllers easily run in real time and the advanced controllers have an execution-time penalty that is below a factor of 2 compared with the PID. Hence, the $\mathcal{L}_1$ adaptive backstepping controller gives a better tracking performance in exchange for a slightly increased execution time.

Table 3: Execution time for the three controllers in a discrete simulation for modeling real-time performance

Controller	**Execution Time**
PID	90 μs
SMC	137 μs
L1-AB	160 μs

6 Conclusion

This paper combined fault-dependent control allocation with three different control schemes to obtain fault tolerance in the longitudinal control of unmanned aerial vehicles. The paper has shown that fault-dependent control allocation is able to accommodate actuator faults that would otherwise be critical, and made a performance assessment for the different control algorithms: an $\mathcal{L}_1$ adaptive backstepping controller; a robust sliding mode controller; and a standard PID controller. This approach allowed the controllers to operate in nominal fault-free conditions using only the main actuator, which is the elevator. By adding fault-dependent control allocation which redistributes the control signal to redundant actuators, the system was shown to be fault tolerant against the total effective loss of the main actuator. A comparative analysis of the controllers was made in order to find out which had the best performance. Simulations were conducted on a high-fidelity model of a Cessna 182, showing that the considered controllers all have good tracking performance and the ability to compensate for model uncertainties. The results indicate that the fault-dependent control allocation scheme ensures excellent performance for both the nominal and faulty cases since the system is uniformly able to track a reference signal. The simulations also show that the nonlinear control algorithms perform better than the PID controller. From the performance metrics, it can be concluded that the $\mathcal{L}_1$ adaptive backstepping controller has the best overall performance. The advantages and disadvantages of the different controllers have been discussed. Also, by combining a controller with fault-dependent control allocation, it was shown that fault tolerance for the nonlinear longitudinal motion of an aircraft could be achieved.

Future work includes comparing the adaptive controller with an integral sliding mode controller, and proving stability and robustness of the closed-loop systems. A performance evaluation of the control algorithms covering the range of all possible faults could be a subject to cover as a supplemental investigation. Additionally, it is desirable to experimentally verify the results by implementing the methods on a UAV in a controlled environment.

References

1. C. Edwards, T. Lombaerts, and H. Smaili, *Fault tolerant flight control: A benchmark challenge*. Springer, 2010.
2. A. Zolghadri, "Advanced model-based FDIR techniques for aerospace systems: Today challenges and opportunities," *Progress in Aerospace Sciences*, vol. 53, pp. 18–29, 2012.
3. X. Qi, J. Qi, D. Theilliol, Y. Zhang, J. Han, D. Song, and C. Hua, "A review on fault diagnosis and fault tolerant control methods for single-rotor aerial vehicles," *Journal of Intelligent and Robotic Systems*, vol. 73, no. 1, pp. 535–555, 2014.
4. P. Goupil, "Oscillatory failure case detection in the A380 electrical flight control system by analytical redundancy," *Control Engineering Practice*, vol. 18, no. 9, pp. 1110–1119, 2012.
5. E. Alcorta-Garcia, A. Zolghadri, and P. Goupil, "A nonlinear observer-based strategy for aircraft oscillatory failure detection: A380 case study," *IEEE Transactions on Aerospace and Electronic Systems*, vol. 47, no. 4, pp. 2792–2806, 2011.
6. S. Hansen and M. Blanke, "Control surface fault diagnosis with specified detection probability - Real event experiences," in *Proceedings of the 2013 International Conference on Unmanned Aircraft System (ICUAS), Atlanta, USA*, 2013.
7. D. Efimov, J. Cieslak, A. Zolghadri, and D. Henry, "Actuator fault detection in aircraft systems: Oscillatory failure case study," *Annual Reviews in Control*, vol. 37, pp. 180–190, 2013.
8. M. Blanke and S. Hansen, "Towards self-tuning residual generators for UAVcontrol surface fault diagnosis," in *Proceedings of the 2nd International Conference on Control and Fault-Tolerant Systems, Nice, France*, 2013.
9. S. Hansen and M. Blanke, "Diagnosis of airspeed measurement faults for unmanned aerial vehicle," *IEEE Transactions on Aerospace and Electronic Systems*, vol. 50, no. 1, pp. 224–239, 2014.
10. Y. Shtessel, *Sliding mode control and observation*. Birkhauser, 2013.
11. C. Edwards and S. K. Spurgeon, *Sliding mode control: Theory and applications*. Taylor and Francis Ltd, 1998.
12. N. Hovakimyan and C. Cao, *$\mathcal{L}_1$ adaptive control theory: Guaranteed robustness with fast adaptation*. SIAM, 2010.
13. T. Espinoza, A. Dzul, R. Lozano, and P. Parada, "Backstepping - sliding mode controllers applied to a fixed-wing UAV," *Journal of Intelligent and Robotic Systems*, vol. 73, no. 1, pp. 67–79, 2014.
14. C. Edwards and C. P. Tan, "Fault tolerant control using sliding mode observers," *in Proceedings of the IEEE Conference on Decision and Control, Nassau, Bahamas*, 2004.
15. H. Alwi and C. Edwards, "Fault tolerant control of a civil aircraft using a sliding mode based scheme," *in Proceedings of the IEEE Conference on Decision and Control and European Control Conference, Seville, Spain*, 2005.
16. H. Alwi and C. Edwards, "Fault tolerant control using sliding modes with on-line control allocation," *Automatica*, vol. 44, no. 7, pp. 1859 – 1866, 2008.
17. H. Alwi, C. Edwards, O. Stroosma, and J. A. Mulder, "Simona flight simulator implementation of a fault tolerant sliding mode scheme with on-line control allocation," *in Proceedings of the American Control Conference, Seattle, USA*, 2008.
18. V. V. Patel, K. A. Wise, N. Hovakimyan, C. Cao, and E. Lavretsky, "$\mathcal{L}_1$ adaptive controller for tailless unstable aircraft in the presence of unknown actuator failures," *in Proceedings of the AIAA Guidance, Navigation, and Control Conference, Hilton Head, South Carolina, USA*, 2007.
19. C.-H. Lee, M.-J. Tahk, and B.-E. Jun, "Autopilot design for an agile missile using $\mathcal{L}_1$ adaptive backstepping control," *in Proceedings of the 28th Congress of the International Council of the Aeronautical Sciences, Brisbane, Australia*, 2012.
20. T. A. Johansen and T. I. Fossen, "Control allocation - A survey," *Automatica*, vol. 49, no. 5, pp. 1087–1103, 2013.
21. J. D. Boskovic and R. K. Mehra, "Control allocation in overactuated aircraft under position and rate limiting," in *Proceedings of the American Control Conference, Anchorage, USA*, 2002.
22. K. Liu, J. Zhu, and B. Yu, "Longitudinal controller design for a fighter aircraft using $\mathcal{L}_1$ adaptive backstepping," *in Proceedings of the World Congress on Intelligent Control and Automation, Taipei, Taiwan*, 2011.
23. M. E. N. Sørensen and M. Breivik, "UAV fault-tolerant control by combined $\mathcal{L}_1$ adaptive backstepping and fault-dependent control allocation," *in Proceedings of the IEEE Multi-Conference on Systems and Control, Sydney, Australia*, 2015.
24. C. Edwards, H. Alwi, and M. T. Hamayun, "Integral sliding mode fault tolerant control incorporating on-line control allocation," *in Proceedings of the 11th International Workshop on Variable Structure Systems, Mexico City, Mexico*, 2010.
25. M. T. Hamayun, H. Alwi, and C. Edwards, "An output integral sliding mode FTC scheme using control allocation," in *Proceedings of the 50th IEEE Conference on Decision, Orlando, USA*, 2011.
26. A. Bajodah, H. Tariq, K. Pakki, B. Chandra, R. Ahmed, and D.-W. Gu, "Fault tolerant control of aircraft actuating surfaces using generalized DI and integral SM control," *Journal of Intelligent and Robotic Systems*, vol. 69, no. 1, pp. 181–188, 2013.
27. G. J. J. Ducard, *Fault-tolerant flight control and guidance systems: Practical methods for small unmanned aerial vehicles*. Springer-Verlag, 2009.
28. B. L. Stevens and F. L. Lewis, *Aircraft control and simulation*. John Wiley and Sons, 2003.
29. D. Sanseverinati, *Identification and Fault Diagnosis for Autonomous Aircraft*. MSc thesis. Dept. of Electrical Eng., Technical University of Denmark, 2010.
30. M. E. N. Sørensen, *Fault-Tolerant Control for Unmanned Aerial Vehicle*. MSc thesis. Dept. of Electrical Eng., Technical University of Denmark, 2014.
31. M. Blanke, M. Kinnaert, J. Lunze, and M. Staroswiecki, *Diagnosis and fault-tolerant control*. Springer, 2006.
32. J. Roskam, *Airplane flight dynamics and automatic flight controls*. DARcorporation, 2003.
33. H. K. Khalil, *Nonlinear systems*. Prentice Hall, 2002.

A.2 Comparing Combinations of Linear and Nonlinear Feedback Terms for Ship Motion Control

M. E. N. Sørensen, M. Breivik, and R. Skjetne, Comparing combinations of linear and nonlinear feedback terms for ship motion control, *IEEE Access*, vol. 8, pp. 193813-193826, 2020.

IEEE Access
Multidisciplinary ⋮ Rapid Review ⋮ Open Access Journal

Received September 27, 2020, accepted October 14, 2020, date of publication October 27, 2020, date of current version November 4, 2020.

Digital Object Identifier 10.1109/ACCESS.2020.3033409

Comparing Combinations of Linear and Nonlinear Feedback Terms for Ship Motion Control

MIKKEL ESKE NØRGAARD SØRENSEN[1,2], MORTEN BREIVIK[1,2], (Member, IEEE), AND ROGER SKJETNE[1,3], (Member, IEEE)
[1]Centre for Autonomous Marine Operations and Systems, Norwegian University of Science and Technology (NTNU), 7491 Trondheim, Norway
[2]Department of Engineering Cybernetics, Norwegian University of Science and Technology (NTNU), 7491 Trondheim, Norway
[3]Department of Marine Technology, Norwegian University of Science and Technology (NTNU), 7491 Trondheim, Norway

Corresponding author: Mikkel Eske Nørgaard Sørensen (mikkel.e.n.sorensen@ieee.org)

This work was supported by the Research Council of Norway through the Centres of Excellence Funding Scheme under Project 223254.

ABSTRACT In this article, combinations of linear and nonlinear feedback terms are investigated for 3 degrees-of-freedom pose and velocity control of ships. Nonlinear control algorithms that are found in the literature often have linear feedback terms, which result in nice globally exponential stability properties when assuming no actuator constraints. However, considering that all actuators have saturation constraints, such stability properties are not feasible in practice. Applying nonlinear feedback terms can be a step to handle such constraints. As a result, this article explores nonlinear feedback terms for both the kinematic and kinetic control loops. Specifically, three controllers based on a cascaded backstepping control design are implemented and compared through simulations and model-scale experiments in an ocean basin. Stability properties and tuning rules for all the controllers are also provided. Interestingly, the use of nonlinear feedback terms gives the ability to constrain the feedback control inputs globally while simultaneously being able to change the convergence rates locally. The price to be paid is the introduction of additional tuning parameters. The three controller types are compared using performance metrics which consider both control accuracy and energy use.

INDEX TERMS Ship motion control, dynamic positioning, cascaded backstepping control design, nonlinear feedback terms, tuning rules, performance metrics, experimental results.

I. INTRODUCTION

Automatic motion control of ships has been an active research topic since the early 20th century [1]. In recent years, the research has expanded from control of manned ships to also include unmanned ships. In this regard, many ship motion control algorithms found in the literature do not take into account saturation constraints for the actuators. For example, the nonlinear control algorithms in [2]–[5] and [6] are all designed with linear feedback terms.

This article therefore investigates the use of nonlinear feedback terms, and in particular the use of combinations of linear and nonlinear feedback terms for 3 degrees-of-freedom (DOFs) pose and velocity control of ships. These feedback terms are developed based on constant bearing (CB) guidance principles, inspired by the guided dynamic positioning approach originally suggested in [7], and further developments on the concept of guided motion control as explored in [8] and [9].

Specifically, this article is a further development of the work in [10], concerning the development of three 3-DOFs motion controllers based on a cascaded backstepping control design, where the feedback connection between pose and velocity, traditionally found in backstepping designs as in [2] and [5], has been removed. The considered controllers respectively employ linear feedback for both the pose and velocity control errors (LP-LV), nonlinear feedback for the pose control error and linear feedback for the velocity control error (NP-LV), as well as nonlinear feedback for both the pose and velocity control errors (NP-NV). Compared to [10], this article presents stability properties associated with all the controllers, suggests suitable tuning rules, and evaluates the controller performance through new simulations and model-scale experiments using a so-called 4-corner test. For this, the LP-LV controller is used as a baseline controller. Specifically, the controllers are compared using performance

The associate editor coordinating the review of this manuscript and approving it for publication was Chao-Yang Chen.

metrics which consider both control accuracy and energy use. Additional work considering the nonlinear feedback controllers from [10] is presented in [11], where a magnitude-rate saturation (MRS) model is added to the system and the effects are explored through model-scale experiments. Other recent work which consider the use of nonlinear feedback terms include [12] and [11], where sine and arctan functions, respectively, are employed for the purpose of 1-DOF ship heading control. In [14], an adaptive fuzzy tracking algorithm was proposed for vessel motion control to handle external disturbances. However, such adaptive mechanisms make it difficult to trace the resulting vessel performance back to the detailed behavior of the feedbacks and is therefore not directly comparable to the studied feedbacks of this article.

The structure of the rest of the paper is as follows: A mathematical ship model and relevant assumptions are presented in Section II; Section III presents the design of three cascaded control laws based on backstepping and CB guidance; Section IV proposes a set of tuning rules; Section V includes simulation results, experimental results and a performance comparison; while Section VI concludes the paper.

II. SHIP MODEL

The horizontal motion of a ship can be represented by the pose vector $\boldsymbol{\eta} = [x, y, \psi]^\top \in \mathbb{R}^2 \times \mathbb{S}$ and the velocity vector $\boldsymbol{\nu} = [u, v, r]^\top \in \mathbb{R}^3$, where $\mathbb{S} = [-\pi, \pi)$. Here, (x, y) represents the Cartesian position in the local earth-fixed reference frame, ψ is the yaw angle, (u, v) represents the body-fixed linear velocities, and r is the yaw rate. The 3 degrees-of-freedom (DOFs) dynamics of a ship is then stated as [5]:

$$\dot{\boldsymbol{\eta}} = \mathbf{R}(\psi)\boldsymbol{\nu} \tag{1}$$

$$\mathbf{M}\dot{\boldsymbol{\nu}} + \mathbf{C}(\boldsymbol{\nu})\boldsymbol{\nu} + \mathbf{D}(\boldsymbol{\nu})\boldsymbol{\nu} = \boldsymbol{\tau}, \tag{2}$$

where

$$\mathbf{R}(\psi) = \begin{bmatrix} \cos(\psi) & -\sin(\psi) & 0 \\ \sin(\psi) & \cos(\psi) & 0 \\ 0 & 0 & 1 \end{bmatrix} \tag{3}$$

is a rotation matrix $\mathbf{R} \in SO(3)$, while $\mathbf{M}$, $\mathbf{C}(\boldsymbol{\nu})$, $\mathbf{D}(\boldsymbol{\nu})$, and $\boldsymbol{\tau}$ represent the inertia matrix, Coriolis and centripetal matrix, damping matrix, and control input vector, respectively. The system matrices are assumed to satisfy the properties $\mathbf{M} = \mathbf{M}^\top > 0$, $\mathbf{C}(\boldsymbol{\nu}) = -\mathbf{C}(\boldsymbol{\nu})^\top$, and $\mathbf{D}(\boldsymbol{\nu}) > 0$.

III. CONTROL DESIGN

The control objective is to make $\tilde{\boldsymbol{\eta}}(t) \triangleq \boldsymbol{\eta}(t) - \boldsymbol{\eta}_t(t) \rightarrow \mathbf{0}$ as $t \rightarrow \infty$, where $\boldsymbol{\eta}_t(t) = [x_t(t), y_t(t), \psi_t(t)]^\top \in \mathbb{R}^2 \times \mathbb{S}$ is $\mathcal{C}^2$ and bounded, representing the pose associated with a target point that is to be reached. The motion of the target is typically defined by a human or generated by a guidance system.

The control design is divided into two stages, including definition of new state variables and deriving the control laws through control Lyapunov functions (CLFs). The design is similar to the backstepping method, which has been applied in e.g. [2], [6] and [15], but omits the coupling between the pose and velocity control loops, which results in a cascaded system. Hence, we call this approach for cascaded backstepping control design. Such a decoupling is similar to what is achieved by using an LgV backstepping design [16]. The resulting cascaded system corresponds to a classical inner-outer loop guidance and control structure, where the outer loop handles the kinematics and the inner loop handles the kinetics. The total system is then analysed by cascade theory [17]. In particular, it is of interest to investigate the effect of using nonlinear feedback terms in the control loops. Consequently, we investigate three combinations of linear and nonlinear feedback terms. Fig. 1 shows a block diagram of these combinations.

For notational simplicity, the time t is omitted in the rest of this section.

A. LINEAR POSE AND VELOCITY FEEDBACKS (LP-LV)

We start by defining the error variables $\mathbf{z}_1$ and $\mathbf{z}_2$:

$$\mathbf{z}_1 \triangleq \mathbf{R}^\top(\psi)(\boldsymbol{\eta} - \boldsymbol{\eta}_t) \tag{4}$$

$$\mathbf{z}_2 \triangleq \boldsymbol{\nu} - \boldsymbol{\alpha}, \tag{5}$$

where $\boldsymbol{\alpha} \in \mathbb{R}^3$ is a vector of stabilising functions, which can be interpreted as a desired velocity to be designed.

1) KINEMATIC CONTROL

Choosing the positive definite CLF

$$V_1 \triangleq \frac{1}{2}\mathbf{z}_1^\top \mathbf{z}_1, \tag{6}$$

the derivative of V_1 with respect to time along the $\mathbf{z}_1$-dynamics gives

$$\begin{aligned} \dot{V}_1 &= \mathbf{z}_1^\top \dot{\mathbf{z}}_1 \\ &= \mathbf{z}_1^\top (\mathbf{S}(r)^\top \mathbf{R}^\top(\psi)(\boldsymbol{\eta} - \boldsymbol{\eta}_t) + \mathbf{R}^\top(\psi)(\dot{\boldsymbol{\eta}} - \dot{\boldsymbol{\eta}}_t)) \\ &= \mathbf{z}_1^\top (\mathbf{S}(r)^\top \mathbf{z}_1 + \mathbf{R}^\top(\psi)(\dot{\boldsymbol{\eta}} - \dot{\boldsymbol{\eta}}_t)), \end{aligned} \tag{7}$$

where

$$\mathbf{S}(r) = \begin{bmatrix} 0 & -r & 0 \\ r & 0 & 0 \\ 0 & 0 & 0 \end{bmatrix} = -\mathbf{S}(r)^\top \tag{8}$$

is a skew-symmetric matrix satisfying $\mathbf{z}_1^\top \mathbf{S}(r)^\top \mathbf{z}_1 = 0$, $\forall \mathbf{z}_1$. This gives

$$\dot{V}_1 = \mathbf{z}_1^\top (\boldsymbol{\nu} - \mathbf{R}^\top(\psi)\dot{\boldsymbol{\eta}}_t). \tag{9}$$

Using (5), the CLF becomes

$$\begin{aligned} \dot{V}_1 &= \mathbf{z}_1^\top (\mathbf{z}_2 + \boldsymbol{\alpha} - \mathbf{R}^\top(\psi)\dot{\boldsymbol{\eta}}_t) \\ &= \mathbf{z}_1^\top \mathbf{z}_2 + \mathbf{z}_1^\top (\boldsymbol{\alpha} - \mathbf{R}^\top(\psi)\dot{\boldsymbol{\eta}}_t), \end{aligned} \tag{10}$$

where the stabilising function can be chosen as

$$\boldsymbol{\alpha} = \mathbf{R}^\top(\psi)\dot{\boldsymbol{\eta}}_t - \boldsymbol{\Gamma}_1 \mathbf{z}_1 \tag{11}$$

with $\boldsymbol{\Gamma}_1 = \boldsymbol{\Gamma}_1^\top > 0$, resulting in

$$\dot{V}_1 = -\mathbf{z}_1^\top \boldsymbol{\Gamma}_1 \mathbf{z}_1 + \mathbf{z}_1^\top \mathbf{z}_2. \tag{12}$$

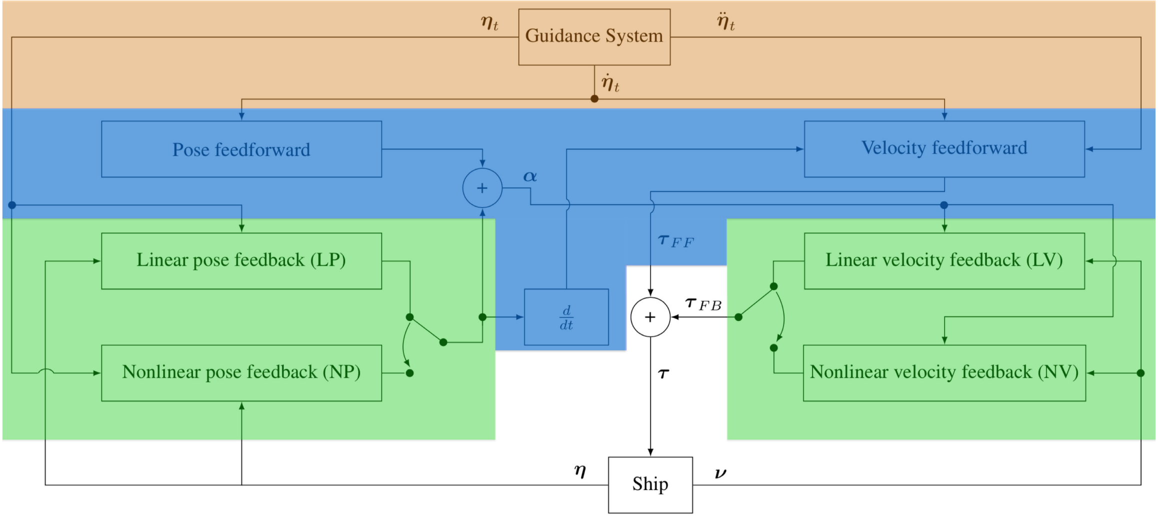

FIGURE 1. The possible combinations of the feedforward and feedback control loops considered in this article.

It can be concluded that the origin of $\mathbf{z}_1$ is uniformly globally exponentially stable (UGES) for $\mathbf{z}_2 = \mathbf{0}$. Consequently, it can be concluded by Lemma 4.6 in [18] that the subsystem

$$\dot{\mathbf{z}}_1 = \mathbf{S}(r)^\top \mathbf{z}_1 - \boldsymbol{\Gamma}_1 \mathbf{z}_1 + \mathbf{z}_2 \tag{13}$$

is input-to-state stable (ISS). Note that (12) shows that $\mathbf{S}(r)$ in (13) does not affect the ISS property.

2) KINETIC CONTROL

The $\mathbf{z}_2$-dynamics can be written as

$$\begin{aligned} \mathbf{M}\dot{\mathbf{z}}_2 &= \mathbf{M}(\dot{\boldsymbol{\nu}} - \dot{\boldsymbol{\alpha}}) \\ &= \boldsymbol{\tau} - \mathbf{C}(\boldsymbol{\nu})\boldsymbol{\nu} - \mathbf{D}(\boldsymbol{\nu})\boldsymbol{\nu} - \mathbf{M}\dot{\boldsymbol{\alpha}}, \end{aligned} \tag{14}$$

where the time derivative of (11) becomes

$$\dot{\boldsymbol{\alpha}} = \mathbf{R}^\top(\psi)\ddot{\boldsymbol{\eta}}_t + \mathbf{S}(r)^\top \mathbf{R}^\top(\psi)\dot{\boldsymbol{\eta}}_t - \boldsymbol{\Gamma}_1 \dot{\mathbf{z}}_1 \tag{15}$$

where $\boldsymbol{\eta}_t$ is the pose of the target point and $\dot{\mathbf{z}}_1$ is given by (13). The CLF for $\mathbf{z}_2$ is defined as

$$V_2 \overset{\triangle}{=} \frac{1}{2}\mathbf{z}_2^\top \mathbf{M}\mathbf{z}_2. \tag{16}$$

Simplifying $\mathbf{C}(\boldsymbol{\nu}) = \mathbf{C}$, $\mathbf{D}(\boldsymbol{\nu}) = \mathbf{D}$, $\mathbf{R}(\psi) = \mathbf{R}$ and $\mathbf{S}(r) = \mathbf{S}$ for notational brevity, the derivative of (16) becomes

$$\begin{aligned} \dot{V}_2 &= \mathbf{z}_2^\top \mathbf{M}\dot{\mathbf{z}}_2 \\ &= \mathbf{z}_2^\top(\boldsymbol{\tau} - \mathbf{C}\boldsymbol{\nu} - \mathbf{D}\boldsymbol{\nu} - \mathbf{M}\dot{\boldsymbol{\alpha}}). \end{aligned} \tag{17}$$

The control input can now be chosen as

$$\begin{aligned} \boldsymbol{\tau} &= \boldsymbol{\tau}_{FF} + \boldsymbol{\tau}_{FB} && (18) \\ &= \mathbf{M}\dot{\boldsymbol{\alpha}} + \mathbf{C}\boldsymbol{\nu} + \mathbf{D}\boldsymbol{\nu} - \boldsymbol{\Gamma}_2\mathbf{z}_2, && (19) \end{aligned}$$

where $\boldsymbol{\tau}_{FF}$ represents the feedforward terms and $\boldsymbol{\tau}_{FB}$ represents the feedback terms

$$\boldsymbol{\tau}_{FF} = \mathbf{M}\dot{\boldsymbol{\alpha}} + \mathbf{C}\boldsymbol{\nu} + \mathbf{D}\boldsymbol{\nu} \tag{20}$$

$$\boldsymbol{\tau}_{FB} = -\boldsymbol{\Gamma}_2\mathbf{z}_2 \tag{21}$$

with $\boldsymbol{\Gamma}_2 > 0$, which results in

$$\dot{V}_2 = -\mathbf{z}_2^\top \boldsymbol{\Gamma}_2 \mathbf{z}_2 < 0, \tag{22}$$

which makes the origin of the $\mathbf{z}_2$-dynamics

$$\dot{\mathbf{z}}_2 = -\mathbf{M}^{-1}\boldsymbol{\Gamma}_2\mathbf{z}_2 \tag{23}$$

UGES.

Remark 1: It is also possible to choose $\boldsymbol{\tau}$ in (19) as

$$\boldsymbol{\tau} = \mathbf{M}\dot{\boldsymbol{\alpha}} + \mathbf{C}\boldsymbol{\alpha} + \mathbf{D}\boldsymbol{\alpha} - \boldsymbol{\Gamma}_2\mathbf{z}_2, \tag{24}$$

which changes (23) to

$$\dot{\mathbf{z}}_2 = -\mathbf{M}^{-1}(\mathbf{C} + \mathbf{D} + \boldsymbol{\Gamma}_2)\mathbf{z}_2, \tag{25}$$

where the convergence rate of the $\mathbf{z}_2$-dynamics now becomes influenced by the ship's $\mathbf{C}$ and $\mathbf{D}$ matrices. However, since $\dot{V}_2 = -\mathbf{z}_2{}^\top(\boldsymbol{\Gamma}_2 + \mathbf{D})\,\mathbf{z}_2 \leq -\mathbf{z}_2{}^\top \boldsymbol{\Gamma}_2\mathbf{z}_2$, the convergence rate is no worse than what is achieved by (19).
The total closed-loop dynamics based on (19) become

$$\begin{aligned} \dot{\mathbf{z}}_1 &= \mathbf{S}^\top \mathbf{z}_1 - \boldsymbol{\Gamma}_1\mathbf{z}_1 + \mathbf{z}_2 && (26) \\ \dot{\mathbf{z}}_2 &= -\mathbf{M}^{-1}\boldsymbol{\Gamma}_2\mathbf{z}_2. && (27) \end{aligned}$$

Theorem 1: The origin $(\mathbf{z}_1, \mathbf{z}_2) = (\mathbf{0}, \mathbf{0})$ of the overall system (26)-(27) is UGES.

Proof: As shown earlier, the two subsystems (26) and (27) are separately UGES. Additionally, since the interconnection term $\mathbf{z}_2$ enters linearly in (26), all the necessary conditions for UGES of the cascaded system are met according to Proposition 2.3 in [17]. ■

Note that the above UGES result is based on the assumption that unbounded control input is available, due to the choice of (11) and (21). However, this is not physically possible to achieve since the saturation constraints of the actuators limit the achievable control input. In the following sections, we introduce nonlinear feedback terms which are bounded.

B. NONLINEAR POSE FEEDBACK AND LINEAR VELOCITY FEEDBACK (NP-LV)

We now introduce nonlinear pose feedback, inspired by the constant bearing (CB) guidance concept, which was originally used for ship control in [7]. CB guidance is a so-called two-point guidance scheme developed for interceptor missiles, where the interceptor is supposed to align the relative interceptor-target velocity along the line-of-sight (LOS) vector between the interceptor and the target. The most common method of implementing CB guidance is to make the rotation rate of the interceptor velocity directly proportional to the rotation rate of the interceptor-target LOS, which is widely known as proportional navigation. However, CB guidance can also be implemented through the direct velocity assignment

$$\mathbf{v}_d = \mathbf{v}_t - U_{a,max}\frac{\tilde{\mathbf{p}}}{\sqrt{\tilde{\mathbf{p}}^\top\tilde{\mathbf{p}} + \Delta_p^2}}, \tag{28}$$

where $\mathbf{v}_t \in \mathbb{R}^2$ is a target velocity, and

$$\tilde{\mathbf{p}} \triangleq \mathbf{p} - \mathbf{p}_t \tag{29}$$

is the LOS vector from the target position $\mathbf{p}_t = [x_t, y_t]^\top \in \mathbb{R}^2$ to the interceptor position $\mathbf{p} = [x, y]^\top \in \mathbb{R}^2$. Additionally, $U_{a,max} > 0$ represents the maximum approach speed toward the target, and $\Delta_{\tilde{p}} > 0$ is a tuning parameter that affects the transient convergence behavior between the interceptor and the target. The direct velocity assignment (28) can be seen as a CB guidance approach since in addition to assigning the target speed, a relative approach velocity is assigned along the interceptor-target LOS vector $\tilde{\mathbf{p}}$ to ensure a smooth rendezvous. This relative approach velocity is bounded by $U_{a,max}$ for large $\tilde{\mathbf{p}}$ relative to Δ_p. The result of using such nonlinear feedback is shown for a scalar error $e \in \mathbb{R}$ in Fig. 2, where the effect of varying Δ gains are shown. The linear and nonlinear functions displayed in Fig. 2 are respectively given as $\sigma(e) = \kappa e$ (LF) and $\sigma(e) = \kappa\frac{e}{\sqrt{e^2+\Delta^2}}$ (NF), where $\kappa = 6$.

By introducing nonlinear feedback to the pose control part, the stabilising function is now chosen as

$$\boldsymbol{\alpha} = \mathbf{R}^\top\dot{\boldsymbol{\eta}}_t - \mathbf{K}_1(\mathbf{z}_1)\mathbf{z}_1, \tag{30}$$

where

$$\mathbf{K}_1(\mathbf{z}_1) \triangleq \boldsymbol{\Gamma}_1\boldsymbol{\Omega}(\mathbf{z}_1), \tag{31}$$

and

$$\boldsymbol{\Omega}(\mathbf{z}_1) \triangleq \begin{bmatrix} \frac{1}{\sqrt{\mathbf{z}_{1,\tilde{p}}^\top\mathbf{z}_{1,\tilde{p}} + \Delta_p^2}}\mathbf{I}_{2\times2} & \mathbf{0}_{2\times1} \\ \mathbf{0}_{1\times2} & \frac{1}{\sqrt{z_{1,\tilde{\psi}}^2 + \Delta_\psi^2}} \end{bmatrix} \tag{32}$$

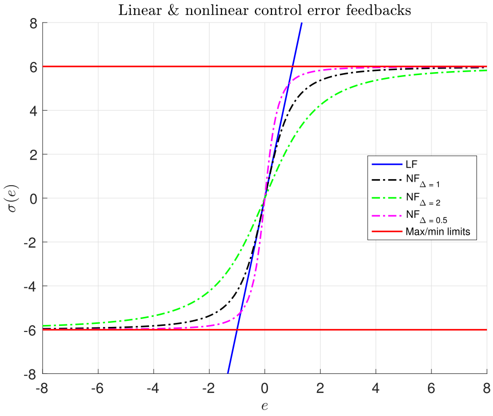

FIGURE 2. The abbreviation LF represents a linear feedback term as a function of the control error *e*, while NF represents a nonlinear feedback term based on a sigmoid function of *e* with a tuning parameter Δ, such as in (28).

with $\boldsymbol{\Gamma}_1 > 0$ as before, $\mathbf{z}_{1,\tilde{p}} \triangleq [z_{1,1}, z_{1,2}]^\top$, $z_{1,\tilde{\psi}} \triangleq z_{1,3}$, $\Delta_p > 0$ and $\Delta_\psi > 0$. It is also possible to choose

$$\boldsymbol{\Omega}(\mathbf{z}_1) = \frac{1}{\sqrt{\mathbf{z}_1^\top\mathbf{z}_1 + \Delta^2}}\mathbf{I}_{3\times3}, \tag{33}$$

if $\Delta_p = \Delta_\psi = \Delta > 0$, but then it is not possible to define a different transient behavior for the position and heading.

Choosing (32) leads to

$$\dot{V}_1 = -\mathbf{z}_1^\top\mathbf{K}_1(\mathbf{z}_1)\mathbf{z}_1 + \mathbf{z}_1^\top\mathbf{z}_2, \tag{34}$$

and

$$\dot{\boldsymbol{\alpha}} = \mathbf{R}^\top\ddot{\boldsymbol{\eta}}_t + \mathbf{S}^\top\mathbf{R}^\top\dot{\boldsymbol{\eta}}_t - \dot{\mathbf{K}}_1(\mathbf{z}_1)\mathbf{z}_1 - \mathbf{K}_1(\mathbf{z}_1)\dot{\mathbf{z}}_1, \tag{35}$$

where

$$\dot{\mathbf{K}}_1(\mathbf{z}_1) = -\boldsymbol{\Gamma}_1\begin{bmatrix} \frac{\mathbf{z}_{1,\tilde{p}}^\top\dot{\mathbf{z}}_{1,\tilde{p}}\mathbf{I}_{2\times2}}{(\mathbf{z}_{1,\tilde{p}}^\top\mathbf{z}_{1,\tilde{p}} + \Delta_p^2)^{\frac{3}{2}}} & \mathbf{0}_{2\times1} \\ \mathbf{0}_{1\times2} & \frac{z_{1,\tilde{\psi}}\dot{z}_{1,\tilde{\psi}}}{(z_{1,\tilde{\psi}}^2 + \Delta_\psi^2)^{\frac{3}{2}}} \end{bmatrix}. \tag{36}$$

The total closed-loop dynamics now changes from (26)-(27) to

$$\dot{\mathbf{z}}_1 = \mathbf{S}^\top\mathbf{z}_1 - \mathbf{K}_1(\mathbf{z}_1)\mathbf{z}_1 + \mathbf{z}_2 \tag{37}$$

$$\dot{\mathbf{z}}_2 = -\mathbf{M}^{-1}\boldsymbol{\Gamma}_2\mathbf{z}_2. \tag{38}$$

Here, we notice that when the control error is large, i.e., when

$$|\mathbf{z}_1| \gg 1 \Rightarrow \dot{\mathbf{z}}_1 \approx \mathbf{S}^\top\mathbf{z}_1 - \boldsymbol{\Gamma}_1\boldsymbol{\rho}(\mathbf{z}_1) + \mathbf{z}_2, \tag{39}$$

where $\boldsymbol{\rho}(\mathbf{z}_1) = \mathrm{col}(\mathbf{z}_{1,\tilde{p}}/|\mathbf{z}_{1,\tilde{p}}|, \mathbf{z}_{1,\tilde{\psi}}/|\mathbf{z}_{1,\tilde{\psi}}|)$ is a vectorial sign-like function that saturates the error $\mathbf{z}_1$. Additionally, when the control error is small, i.e., when

$$|\mathbf{z}_1| \approx 0 \Rightarrow \dot{\mathbf{z}}_1 = \mathbf{S}^\top\mathbf{z}_1 - \boldsymbol{\Gamma}_1\begin{bmatrix} \frac{1}{\Delta_p}\mathbf{I}_{2\times2} & \mathbf{0}_{2\times1} \\ \mathbf{0}_{1\times2} & \frac{1}{\Delta_\psi} \end{bmatrix}\mathbf{z}_1 + \mathbf{z}_2, \tag{40}$$

where the linear dynamics is recovered, scaled by Δ_p and Δ_ψ, around the origin. It should be noted that $\boldsymbol{\rho}(\mathbf{z}_1)$ only saturates the $\mathbf{z}_1$ error dynamics and does not have a direct relationship with the actuator saturation level.

Theorem 2: The origin $(\mathbf{z}_1, \mathbf{z}_2) = (\mathbf{0}, \mathbf{0})$ is uniformly globally asymptotically stable (UGAS), and on each compact set $B \subset \mathbb{R}^6$ containing the origin, it is uniformly exponentially stable (UES).

Proof: We have that the $\mathbf{z}_2$-dynamics is UGES, the unperturbed $\mathbf{z}_1$-dynamics is UGAS, since (6) is $\mathcal{C}^1$ and positive definite, $\dot{V}_1$ is negative definite $\forall \mathbf{z}_1 \neq \mathbf{0}$ and (6) is radially unbounded $\forall \mathbf{z}_1 \neq \mathbf{0}$.

Next, it can be shown that the $\mathbf{z}_1$-subsystem is growth restricted by satisfying Assumption 7 in [17], where $\alpha_4(s) = s$, $\alpha_5(s) = 1$, $\alpha_1(s) = \frac{1}{2}s^2$ and $\alpha_6(s) = \sqrt{2s}$. Additionally, Assumption 8 in [17] is satisfied by having $\lambda = 2$, $V = \frac{1}{2}\mathbf{z}_1^\top \mathbf{z}_1$ and $W_1(\mathbf{z}_1) = \mathbf{z}_1^\top \mathbf{K}_1(\mathbf{z}_1)\mathbf{z}_1$. With these conditions satisfied, Theorem 2.3 in [17] states that the origin $(\mathbf{z}_1, \mathbf{z}_2) = (\mathbf{0}, \mathbf{0})$ is UGAS.

For $|\mathbf{z}(t_0)| \in B$ and the definition of UGAS, there exists $L > 0$ so that $|\mathbf{z}(t)| \leq L$, $\forall t \geq t_0 \geq 0$. This also means that $\left|\mathbf{z}_{1,\tilde{p}}\right| \leq L$ and $\left|\mathbf{z}_{1,\tilde{\psi}}\right| \leq L$, which further implies $\exists \gamma > 0$ such that $\boldsymbol{\Gamma}_1 \boldsymbol{\Omega}(\mathbf{z}_1) + \boldsymbol{\Omega}(\mathbf{z}_1)\boldsymbol{\Gamma}_1 > \gamma \mathbf{I}$. Using the quadratic Lyapunov function

$$V(\mathbf{z}_1, \mathbf{z}_2) = \mathbf{z}_1^\top \mathbf{z}_1 + \frac{1}{2} b_2 \mathbf{z}_2^\top \mathbf{M} \mathbf{z}_2, \tag{41}$$

where $b_2 > 0$, we get

$$\begin{aligned}
\dot{V} &= 2\mathbf{z}_1^\top \left[-\mathbf{S}\mathbf{z}_1 - \boldsymbol{\Gamma}_1 \boldsymbol{\Omega}(\mathbf{z}_1)\mathbf{z}_1 + \mathbf{z}_2\right] \\
&\quad + b_2 \mathbf{z}_2^\top \mathbf{M}\left[-\mathbf{M}^{-1}\boldsymbol{\Gamma}_2 \mathbf{z}_2\right] && (42)\\
&= -\mathbf{z}_1^\top \left[\boldsymbol{\Gamma}_1 \boldsymbol{\Omega}(\mathbf{z}_1) + \boldsymbol{\Omega}(\mathbf{z}_1)\boldsymbol{\Gamma}_1\right]\mathbf{z}_1 + 2\mathbf{z}_1^\top \mathbf{z}_2 \\
&\quad - b_2 \mathbf{z}_2^\top \boldsymbol{\Gamma}_2 \mathbf{z}_2 && (43)\\
&\leq -\gamma |\mathbf{z}_1|^2 + 2|\mathbf{z}_1||\mathbf{z}_2| - b_2 \lambda_{\min}(\boldsymbol{\Gamma}_2)|\mathbf{z}_2|^2 && (44)\\
&= -\frac{\gamma}{2}|\mathbf{z}_1|^2 - \frac{\gamma}{2}|\mathbf{z}_1|^2 + \kappa|\mathbf{z}_1|^2 + \frac{1}{\kappa}|\mathbf{z}_2|^2 \\
&\quad - b_2 \lambda_{\min}(\boldsymbol{\Gamma}_2)|\mathbf{z}_2|^2 && (45)\\
&= -\frac{\gamma}{2}|\mathbf{z}_1|^2 - \left(b_2 \lambda_{\min}(\boldsymbol{\Gamma}_2) - \frac{2}{\gamma}\right)|\mathbf{z}_2|^2, && (46)
\end{aligned}$$

where we used Young's inequality $xy \leq \kappa x^2 + \frac{1}{4\kappa}y^2$, $\kappa = \frac{\gamma}{2} > 0$. Choosing for instance

$$b_2 = \frac{1}{\lambda_{\min}(\boldsymbol{\Gamma}_2)}\left(\frac{\gamma}{2} + \frac{2}{\gamma}\right), \tag{47}$$

gives

$$\dot{V} \leq -\frac{\gamma}{2}|\mathbf{z}|^2, \tag{48}$$

which proves UES on the compact set B. ■

Remark 2: UGAS shows that stability of this system is global. The second part of the theorem shows that for any practical set B of initial conditions, the convergence is in fact exponential.

C. NONLINEAR POSE AND VELOCITY FEEDBACKS (NP-NV)

We now also introduce nonlinear velocity feedback, which changes the control law (19) to

$$\boldsymbol{\tau} = \mathbf{M}\dot{\boldsymbol{\alpha}} + \mathbf{C}\boldsymbol{\nu} + \mathbf{D}\boldsymbol{\nu} - \mathbf{K}_2(\mathbf{z}_2)\mathbf{z}_2, \tag{49}$$

where

$$\mathbf{K}_2(\mathbf{z}_2) = \boldsymbol{\Gamma}_2 \begin{bmatrix} \dfrac{1}{\sqrt{\mathbf{z}_{2,\tilde{v}}^\top \mathbf{z}_{2,\tilde{v}} + \Delta_v^2}}\mathbf{I}_{2\times 2} & \mathbf{0}_{2\times 1} \\ \mathbf{0}_{1\times 2} & \frac{1}{\sqrt{z_{2,\tilde{r}}^2 + \Delta_r^2}} \end{bmatrix} \tag{50}$$

with $\boldsymbol{\Gamma}_2 > 0$ as before, $\mathbf{z}_{2,\tilde{v}} \triangleq [z_{2,1}, z_{2,2}]^\top$, $z_{2,\tilde{r}} \triangleq z_{2,3}$, $\Delta_v > 0$ and $\Delta_r > 0$. In this case, the derivative of V_2 becomes

$$\dot{V}_2 = -\mathbf{z}_2^\top \mathbf{K}_2(\mathbf{z}_2)\mathbf{z}_2, \tag{51}$$

and the total closed-loop dynamics become

$$\begin{aligned}
\dot{\mathbf{z}}_1 &= \mathbf{S}^\top \mathbf{z}_1 - \mathbf{K}_1(\mathbf{z}_1)\mathbf{z}_1 + \mathbf{z}_2 && (52)\\
\dot{\mathbf{z}}_2 &= -\mathbf{M}^{-1}\mathbf{K}_2(\mathbf{z}_2)\mathbf{z}_2. && (53)
\end{aligned}$$

Theorem 3: The origin $(\mathbf{z}_1, \mathbf{z}_2) = (\mathbf{0}, \mathbf{0})$ is UGAS, and on each compact set $B \subset \mathbb{R}^6$ containing the origin, it is UES.

Proof: The $\mathbf{z}_2$-dynamics can be proven to be UGAS using Theorem 4.9 in [18], since (16) is $\mathcal{C}^1$ and positive definite, $\dot{V}_2$ is negative definite $\forall \mathbf{z}_2 \neq \mathbf{0}$ and (16) is radially unbounded $\forall \mathbf{z}_2 \neq \mathbf{0}$. A similar conclusion can be made for the unperturbed $\mathbf{z}_1$-dynamics, as shown in Theorem 3.

Next, it can be shown that the $\mathbf{z}_1$-subsystem is growth restricted by satisfying Assumption 7 in [17], where $\alpha_4(s) = s$, $\alpha_5(s) = 1$, $\alpha_1(s) = \frac{1}{2}s^2$ and $\alpha_6(s) = \sqrt{2s}$. Additionally, Assumption 8 in [17], is satisfied by having $\lambda = 2$, $V = \frac{1}{2}\mathbf{z}_1^\top \mathbf{z}_1$ and $W_1(\mathbf{z}_1) = \mathbf{z}_1^\top \mathbf{K}_1(\mathbf{z}_1)\mathbf{z}_1$. With these conditions satisfied, Theorem 2.3 in [17] states that the origin $(\mathbf{z}_1, \mathbf{z}_2) = (\mathbf{0}, \mathbf{0})$ is UGAS.

For $|\mathbf{z}(t_0)| \in B$ and the definition of UGAS, there exists $L > 0$ so that $|\mathbf{z}(t)| \leq L$, $\forall t \geq t_0 \geq 0$. This also means that $\left|\mathbf{z}_{1,p}\right| \leq L$, $\left|\mathbf{z}_{1,\psi}\right| \leq L$, $\left|\mathbf{z}_{2,v}\right| \leq L$ and $\left|\mathbf{z}_{2,r}\right| \leq L$, which further implies $\exists \gamma_i > 0$ such that $\boldsymbol{\Gamma}_i \boldsymbol{\Omega}(\mathbf{z}_i) + \boldsymbol{\Omega}(\mathbf{z}_i)\boldsymbol{\Gamma}_i > \gamma_i \mathbf{I}$, $i = 1, 2$. Using the quadratic Lyapunov function

$$V(\mathbf{z}_1, \mathbf{z}_2) = \mathbf{z}_1^\top \mathbf{z}_1 + b_2 \mathbf{z}_2^\top \mathbf{M} \mathbf{z}_2 \tag{54}$$

where $b_2 > 0$, we get

$$\begin{aligned}
\dot{V} &= 2\mathbf{z}_1^\top \left[-\mathbf{S}\mathbf{z}_1 - \boldsymbol{\Gamma}_1 \boldsymbol{\Omega}(\mathbf{z}_1)\mathbf{z}_1 + \mathbf{z}_2\right] \\
&\quad + 2b_2 \mathbf{z}_2^\top \mathbf{M}\left[-\mathbf{M}^{-1}\boldsymbol{\Gamma}_2 \boldsymbol{\Omega}(\mathbf{z}_2)\mathbf{z}_2\right] && (55)\\
&= -\mathbf{z}_1^\top \left[\boldsymbol{\Gamma}_1 \boldsymbol{\Omega}(\mathbf{z}_1) + \boldsymbol{\Omega}(\mathbf{z}_1)\boldsymbol{\Gamma}_1\right]\mathbf{z}_1 + 2\mathbf{z}_1^\top \mathbf{z}_2 \\
&\quad - b_2 \mathbf{z}_2^\top \left[\boldsymbol{\Gamma}_2 \boldsymbol{\Omega}(\mathbf{z}_2) + \boldsymbol{\Omega}(\mathbf{z}_2)\boldsymbol{\Gamma}_2\right]\mathbf{z}_2 && (56)\\
&\leq -\gamma_1 |\mathbf{z}_1|^2 + 2|\mathbf{z}_1||\mathbf{z}_2| - b_2 \gamma_2 |\mathbf{z}_2|^2 && (57)\\
&= -\frac{\gamma_1}{2}|\mathbf{z}_1|^2 - \frac{\gamma_1}{2}|\mathbf{z}_1|^2 + \kappa|\mathbf{z}_1|^2 + \frac{1}{\kappa}|\mathbf{z}_2|^2 \\
&\quad - b_2 \gamma_2 |\mathbf{z}_2|^2 && (58)\\
&= -\frac{\gamma_1}{2}|\mathbf{z}_1|^2 - \left(b_2 \gamma_2 - \frac{2}{\gamma_1}\right)|\mathbf{z}_2|^2, && (59)
\end{aligned}$$

where we used Young's inequality. Choosing for instance

$$b_2 = \frac{1}{\gamma_2}\left(\frac{\gamma_1}{2} + \frac{2}{\gamma_1}\right) \tag{60}$$

gives

$$\dot{V} \leq -\frac{\gamma_1}{2}\left|\mathbf{z}\right|^2, \tag{61}$$

which proves UES on the compact set B. ■

IV. SUGGESTED TUNING RULES

Considering the $\mathbf{z}_1$-dynamics in (26), (37), and (52), it can be seen that the choice of the $\mathbf{\Gamma}_1$ gain matrix determines the time constants of the $\mathbf{z}_1$-dynamics with linear feedback only. Hence, a time-constant matrix for the kinematic subsystem can be used to define the linear gain matrix as

$$\mathbf{\Gamma}_1 \triangleq \mathbf{T}_1^{-1} \tag{62}$$

where

$$\mathbf{T}_1 = \begin{bmatrix} T_p & 0 & 0 \\ 0 & T_p & 0 \\ 0 & 0 & T_\psi \end{bmatrix}, \tag{63}$$

with $T_p > 0$ and $T_\psi > 0$ being the time constants for position control and heading control, respectively.

A similar observation can be made for the $\mathbf{z}_2$-dynamics in (27), (38), and (53), where the choice of the $\mathbf{\Gamma}_2$ gain matrix determines the time constants of the $\mathbf{z}_2$-dynamics with linear feedback only. Similarly, we can define the choice of linear gain matrix for the kinetic subsystem based on a time-constant matrix as

$$\mathbf{\Gamma}_2 \triangleq \mathbf{M}\mathbf{T}_2^{-1}, \tag{64}$$

where

$$\mathbf{T}_2 = \begin{bmatrix} T_v & 0 & 0 \\ 0 & T_v & 0 \\ 0 & 0 & T_r \end{bmatrix},$$

with $T_v > 0$ and $T_r > 0$ are the time constants for linear velocity control and yaw rate control, respectively.

It is favorable for the kinetic subsystem to have faster dynamics than the kinematic subsystem. Hence, the kinetic dynamics must have smaller time constants, that is

$$T_v < T_p \tag{65}$$

$$T_r < T_\psi. \tag{66}$$

Also, Δ_p, Δ_ψ, Δ_v and Δ_r must be chosen. The control parameter Δ is usually known as the lookahead distance in line of sight guidance [9]. In [19], it is shown that a small Δ-value corresponds to fast convergence to the path, but with a large overshoot, while a large Δ-value reduces overshoot and results in smooth but slow convergence. Here, the Δ-values scale the linear feedback gains and therefore the time constants of the linear region around the origin. If the Δ-values are equal to 1, they will result in the same response as the linear controllers in the linear region. But if they are larger than 1, they will give a slower response in this region. If they are chosen to be smaller than 1, they will give a faster response. Hence, the Δ-values for the NP and NV feedback terms must be chosen such that the conditions in (65)-(66) are still satisfied in the linear region, where the time constants will be related to $\mathbf{\Gamma}_1(1,1)/\Delta_p$, $\mathbf{\Gamma}_1(3,3)/\Delta_\psi$, $\mathbf{\Gamma}_2(1,1)/\Delta_v$, and $\mathbf{\Gamma}_2(3,3)/\Delta_r$.

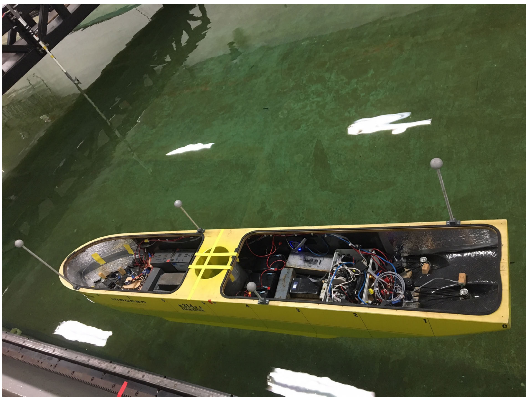
FIGURE 3. C/S inocean cat I arctic drillship in the marine cybernetics laboratory at NTNU.

V. SIMULATION AND EXPERIMENTAL RESULTS

A. SHIP MODEL

The model-scale cybership *C/S Inocean Cat I Arctic Drillship* (CSAD), with parameters from [20], is used to test the performance of the proposed motion controllers through both simulations and experiments. CSAD is a 1:90 scale replica of the full-scale Equinor Cat I Drillship, with a length of $L = 2.578$ (m), shown in Fig 3. The ship is fully actuated with six azimuth thrusters.

B. PERFORMANCE METRICS

To evaluate and compare the performance of the different controllers, some suitable performance metrics must be used. We define

$$e(t) \triangleq \sqrt{\tilde{\boldsymbol{\eta}}(t)^\top \tilde{\boldsymbol{\eta}}(t)}, \tag{67}$$

as the error input to be used in the performance metrics, with $\tilde{\boldsymbol{\eta}} = [\tilde{x}, \tilde{y}, \tilde{\psi}]^\top \triangleq \boldsymbol{\eta} - \boldsymbol{\eta}_t$. Here, since the position and yaw angle have different units, we define the normalized signals $\tilde{x}$, $\tilde{y}$, and $\tilde{\psi}$ in the intervals $[-0.5, 0.5]$ in the expected operational space of the ship [21]. To obtain this normalization, the position errors are divided by 4 (m) and the yaw error is divided by $\frac{\pi}{2}$ (rad), since the position errors will be in the intervals $[-2, 2]$ (m) and the yaw error will be in the interval $[-\frac{\pi}{4}, \frac{\pi}{4}]$ (rad). In addition, these signals represent the instantaneous control errors, while we would like to consider the accumulated errors over time. Hence, we use the performance metric IAE (integral of the absolute error)

$$IAE(t) \triangleq \int_0^t |e(\tau)| d\tau, \tag{68}$$

which integrates the temporal evolution of the absolute value of the error without adding any weight to the error. We will also use the so-called IAEW metric, which scales the IAE metric by the energy consumption, and which was proposed in [15]. Specifically, the IAEW can be computed as

$$IAEW(t) \triangleq \int_0^t |e(\tau)| d\tau \int_0^t P(\tau) d\tau, \tag{69}$$

where

$$P(t) = |\boldsymbol{\nu}(t)^\top \boldsymbol{\tau}(t)| \tag{70}$$

represents the mechanical power of the ship. IAEW thus indicates which controller has the best combined control accuracy and energy use in one single metric. Normally, the sum of the weighted square of the state and control input is integrated as a cost function to find optimal control values. We have, on the other hand, chosen performance metrics as multiplication of sub-objectives in order to avoid mixed units in a sum of physical quantities.

C. TEST SETUP AND CONTROLLER TUNING

Since this article concerns the comparison of combinations of feedback terms, we have chosen to use a so-called 4-corner test to be able to effectively demonstrate the closed-loop control performance differences. This test is illustrated in Fig. 4, and has e.g. been used in [22] and [11] to evaluate the performance of dynamic positioning control algorithms. Since the test consists of a set of setpoint-change maneuvers, both moving forwards and backwards, the feedforward terms associated with the $\mathbf{C}(\boldsymbol{\nu})$ and $\mathbf{D}(\boldsymbol{\nu})$ matrices are removed from the control laws. This removal also serves to better illustrate the main differences between the considered feedback control combinations.

In particular, the 4-corner test is performed as follows: The ship is first initialized to point straight North, at heading 0 (*deg*). Then the following setpoint changes are executed:

1) Position change 2 (*m*) straight North: Tests a pure surge movement ahead.
2) Position change 2 (*m*) straight East: Tests a pure sway movement in the starboard direction.
3) Heading change 45 (*deg*) clockwise: Tests a pure yaw motion while keeping position steady.
4) Position change 2 (*m*) straight South: Tests a combined surge-sway movement while keeping the heading steady.
5) Position change 2 (*m*) straight West and heading change 45 (*deg*) counterclockwise: Tests a combined surge-sway-yaw movement.

Through these setpoint changes, this test simplifies the control problem down to three 1-DOF motions in surge, sway, and yaw, respectively. The final two setpoint changes represent 2-DOFs and 3-DOFs coupled motions. The system is implemented such that the target will automatically change setpoint when the ship is within 0.003 (*m*) from the target in both x and y direction and 0.2 (*deg*) from the target heading. When the 4-corner test is completed, the ship will have returned to its initial position and heading, ready for a new test run from the same pose and along the same track.

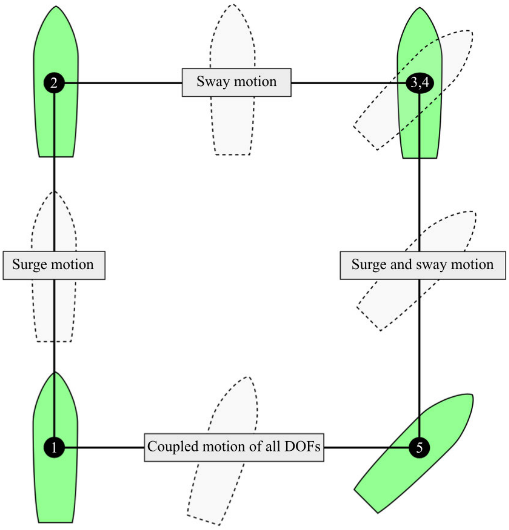

FIGURE 4. **The 4-corner test. Modified from [22].**

Hence, the control laws used in the test are simplified to their feedback essence as follows.

LP-LV:

$$\boldsymbol{\alpha} = -\boldsymbol{\Gamma}_1 \mathbf{z}_1 \tag{71a}$$
$$\dot{\boldsymbol{\alpha}} = -\boldsymbol{\Gamma}_1 \dot{\mathbf{z}}_1 \tag{71b}$$
$$\boldsymbol{\tau} = \mathbf{M}\dot{\boldsymbol{\alpha}} - \boldsymbol{\Gamma}_2 \mathbf{z}_2, \tag{71c}$$

The control gains have been chosen such that the LP-LV control input stays within the magnitude saturations of the actuators. This has lead us to the gains $\boldsymbol{\Gamma}_1 = diag([0.08, 0.08, 0.0698])$ and $\boldsymbol{\Gamma}_2 = diag([0.2, 0.2, 0.1745])\mathbf{M}$. Using (62) and (64), we get the following corresponding time-constant matrices:

$$\mathbf{T}_1 = \begin{bmatrix} T_p & 0 & 0 \\ 0 & T_p & 0 \\ 0 & 0 & T_\psi \end{bmatrix} = \boldsymbol{\Gamma}_1^{-1} = \begin{bmatrix} 12.5 & 0 & 0 \\ 0 & 12.5 & 0 \\ 0 & 0 & 14.32 \end{bmatrix} \tag{72}$$

and

$$\mathbf{T}_2 = \begin{bmatrix} T_v & 0 & 0 \\ 0 & T_v & 0 \\ 0 & 0 & T_r \end{bmatrix} = \mathbf{M}^{-1}\boldsymbol{\Gamma}_2^{-1}$$

$$= \begin{bmatrix} 5 & 0 & 0 \\ 0 & 5 & 0 \\ 0 & 0 & 5.73 \end{bmatrix}. \tag{73}$$

The corresponding LP-LV time constants for the kinematic and kinetic controllers are thus $T_p = 12.5 > T_v = 5$ and $T_\psi = 14.32 > T_r = 5.73$, which satisfy the tuning rules.

NP-LV:

$$\begin{aligned} \boldsymbol{\alpha} &= -\mathbf{K}_1(\mathbf{z}_1)\mathbf{z}_1 & (74a) \\ \dot{\boldsymbol{\alpha}} &= -\dot{\mathbf{K}}_1(\mathbf{z}_1)\mathbf{z}_1 - \mathbf{K}_1(\mathbf{z}_1)\dot{\mathbf{z}}_1 & (74b) \\ \boldsymbol{\tau} &= \mathbf{M}\dot{\boldsymbol{\alpha}} - \boldsymbol{\Gamma}_2\mathbf{z}_2, & (74c) \end{aligned}$$

Here, we reuse the gains found for the LP-LV controller in order to be able to clearly see the effects of introducing the delta-parameters on the performance. Also, Δ_p and Δ_ψ are chosen so that the time constants associated with the kinematic control loop do not become smaller than that of the kinetic control loop. We have therefore chosen $\Delta_p = 0.5$ and $\Delta_\psi = 0.5$. This gives us the following corresponding time-constant matrices:

$$\mathbf{T}_1 = \begin{bmatrix} T_p & 0 & 0 \\ 0 & T_p & 0 \\ 0 & 0 & T_\psi \end{bmatrix} = \left(\boldsymbol{\Gamma}_1 \begin{bmatrix} \frac{1}{\Delta_p} & 0 & 0 \\ 0 & \frac{1}{\Delta_p} & 0 \\ 0 & 0 & \frac{1}{\Delta_\psi} \end{bmatrix} \right)^{-1}$$
$$= \begin{bmatrix} 12.5 * 0.5 & 0 & 0 \\ 0 & 12.5 * 0.5 & 0 \\ 0 & 0 & 14.32 * 0.5 \end{bmatrix}$$
$$= \begin{bmatrix} 6.25 & 0 & 0 \\ 0 & 6.25 & 0 \\ 0 & 0 & 7.16 \end{bmatrix} \tag{75}$$

and

$$\mathbf{T}_2 = \begin{bmatrix} 5 & 0 & 0 \\ 0 & 5 & 0 \\ 0 & 0 & 5.73 \end{bmatrix}. \tag{76}$$

With the chosen Δ-values, the time constants in the linear region associated with the NP-LV controller are $T_p = 6.25 > T_v = 5$ and $T_\psi = 7.16 > T_r = 5.73$

NP-NV:

$$\begin{aligned} \boldsymbol{\alpha} &= -\mathbf{K}_1(\mathbf{z}_1)\mathbf{z}_1 & (77a) \\ \dot{\boldsymbol{\alpha}} &= -\dot{\mathbf{K}}_1(\mathbf{z}_1)\mathbf{z}_1 - \mathbf{K}_1(\mathbf{z}_1)\dot{\mathbf{z}}_1 & (77b) \\ \boldsymbol{\tau} &= \mathbf{M}\dot{\boldsymbol{\alpha}} - \mathbf{K}_2(\mathbf{z}_2)\mathbf{z}_2. & (77c) \end{aligned}$$

TABLE 1. Control gains for the 4-corner test.

	LP-LV	NP-LV	NP-NV
$\boldsymbol{\Gamma}_1$	$diag([0.08, 0.08, 0.0698])$	$-\|\|-$	$-\|\|-$
$\boldsymbol{\Gamma}_2$	$diag([0.2, 0.2, 0.1745])\mathbf{M}$	$-\|\|-$	$-\|\|-$
$\Delta_{\tilde{p},\tilde{\psi}}$	-	$[0.5\,,0.5]$	$-\|\|-$
$\Delta_{\tilde{v},\tilde{r}}$	-	-	$[0.7\,,1]$

Similar to the NP-LV controller, we reuse the gains for the LP-LV controller, and the Δ-values Δ_p, Δ_ψ, Δ_v and Δ_r for the NP-NV controller are chosen such that the time constants associated with the kinematic control loop do not become smaller than that of the kinetic control loop. We have therefore chosen $\Delta_p = 0.5$, $\Delta_\psi = 0.5$, $\Delta_v = 0.7$ and $\Delta_r = 1$. This gives us the following corresponding time-constant matrices:

$$\mathbf{T}_1 = \begin{bmatrix} T_p & 0 & 0 \\ 0 & T_p & 0 \\ 0 & 0 & T_\psi \end{bmatrix}$$
$$= \begin{bmatrix} 12.5 * 0.5 & 0 & 0 \\ 0 & 12.5 * 0.5 & 0 \\ 0 & 0 & 14.32 * 0.5 \end{bmatrix}$$
$$= \begin{bmatrix} 6.25 & 0 & 0 \\ 0 & 6.25 & 0 \\ 0 & 0 & 7.16 \end{bmatrix} \tag{78}$$

and

$$\mathbf{T}_2 = \begin{bmatrix} T_v & 0 & 0 \\ 0 & T_v & 0 \\ 0 & 0 & T_r \end{bmatrix} = \begin{bmatrix} 5 * 0.7 & 0 & 0 \\ 0 & 5 * 0.7 & 0 \\ 0 & 0 & 5.73 * 1 \end{bmatrix}$$
$$= \begin{bmatrix} 3.5 & 0 & 0 \\ 0 & 3.5 & 0 \\ 0 & 0 & 5.73 \end{bmatrix}. \tag{79}$$

With the chosen Δ-values, the time constants in the linear region associated with the NP-NV controller are $T_p = 6.25 > T_v = 3.5$ and $T_\psi = 7.16 > T_r = 5.73$. Finally, the chosen control gains are summarised in Table 1.

D. SIMULATION RESULTS

Since this article focuses on fundamental motion control aspects, it is assumed for simulation purposes that no disturbances and uncertainties are affecting the system. Such disturbances and uncertainties need to be handled with other additional algorithms tailored for the purpose. Also, it is assumed that both the pose vector $\boldsymbol{\eta}$ and velocity vector $\boldsymbol{\nu}$ can be measured.

In Fig. 5-7, the outline of the ship pose is plotted to show the pose motion patterns. Here, the blue outline represents the LP-LV-controlled ship, the dash-dotted black outline represents the NP-LV-controlled ship, the dashed green outline represents the NP-NV-controlled ship, while the red outline represents the 4-corner test box outline. Notice that the vessel has a larger position error when moving from point 5 to point 1, which is natural given that this is the most challenging maneuver to perform, with coupled motion change in all 3-DOFs.

Fig. 8 shows the commanded control inputs for the three controllers. Note that the amount of time each of the controllers use to complete the 4-corner test is different, since the nonlinear feedback controllers modify the convergence

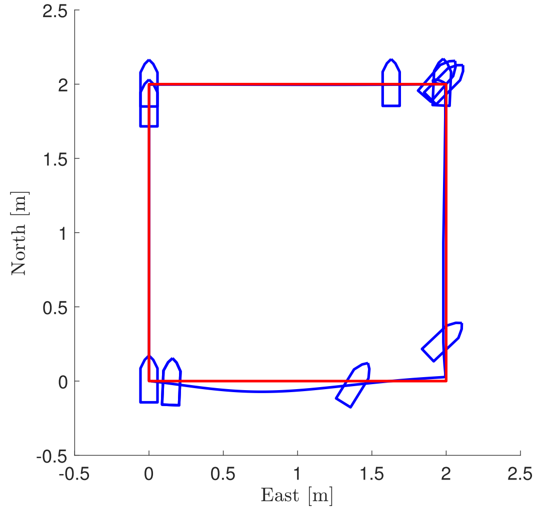

FIGURE 5. **The 4-corner simulation: Using LP-LV feedback terms.**

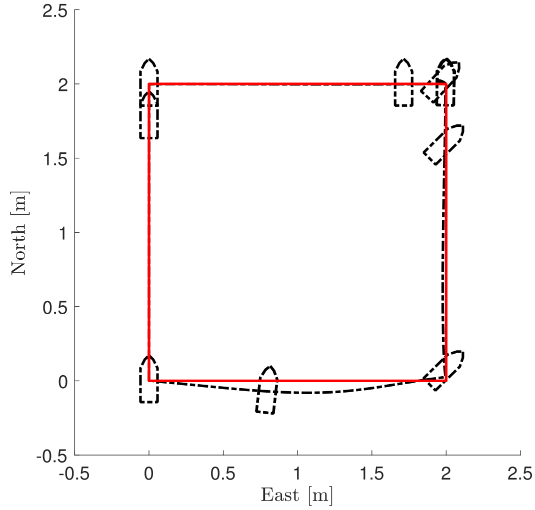

FIGURE 6. **The 4-corner simulation: Using NP-LV feedback terms.**

rate to be faster than the linear feedback controller in the linear regions. Two main results can be seen from Fig. 8. First, the NP-LV controller is the fastest of the three controllers to complete the 4-corner test, followed by the NP-NV and lastly the LP-LV controller. Second, the magnitude of τ_1 and τ_2 are lowest for the NP-LV controller, closely followed by the NP-NV controller. However, τ_3 has the same magnitude for all the considered controllers. Based on this, it can be concluded that the nonlinear position feedback terms of (32) limit the control signal while the nonlinear heading feedback term of (32) does not.

Fig. 9 illustrates how the contribution of the kinematic feedback terms in $\boldsymbol{\alpha}$ are dependent on the error $\mathbf{z}_1$ for the three

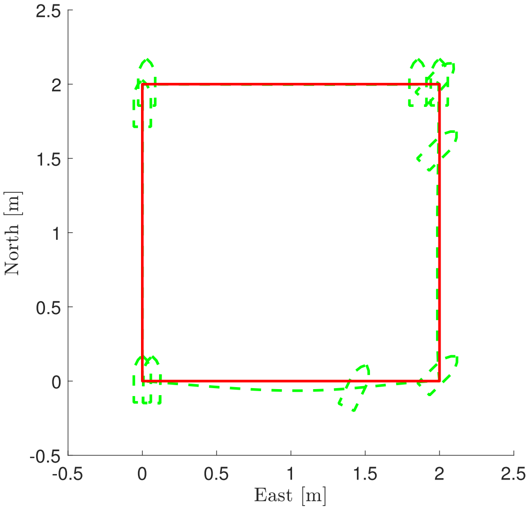

FIGURE 7. **The 4-corner simulation: Using NP-NV feedback terms.**

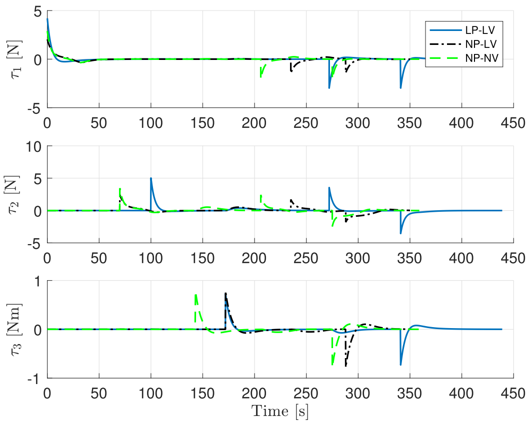

FIGURE 8. **The 4-corner simulation: The commanded control inputs.**

controllers. In [23], it is shown that the maximum velocities of CSAD are 0.4142 [m/s], 0.109 [m/s] and 6.327 [deg/s] in surge, sway and yaw, respectively. These velocity boundaries are illustrated in Fig. 9, for the plots where the feedback terms get close to or exceed these boundaries. Keep in mind that the velocity terms α_1, α_2, and α_3 are components of the so-called stabilizing function $\boldsymbol{\alpha} = [\alpha_1, \alpha_2, \alpha_2]^\top$. Specifically, it can be seen that α_1 and α_2 are limited for the controllers with a nonlinear feedback term, while the one which has a linear feedback term evolves linearly without any bounds. It is also noticed that there are two different curves for both the NP-LP and NP-NV controllers, which is due to the construction of the denominator in (32) for the position feedback terms. Since the denominator of these feedback terms is both dependent on the error in $z_{1,1}$ and $z_{1,2}$, it is natural that the curves are lower for the setpoint changes associated with 4) and 5) than 1) and 2) from Fig. 4. It should also be noted that

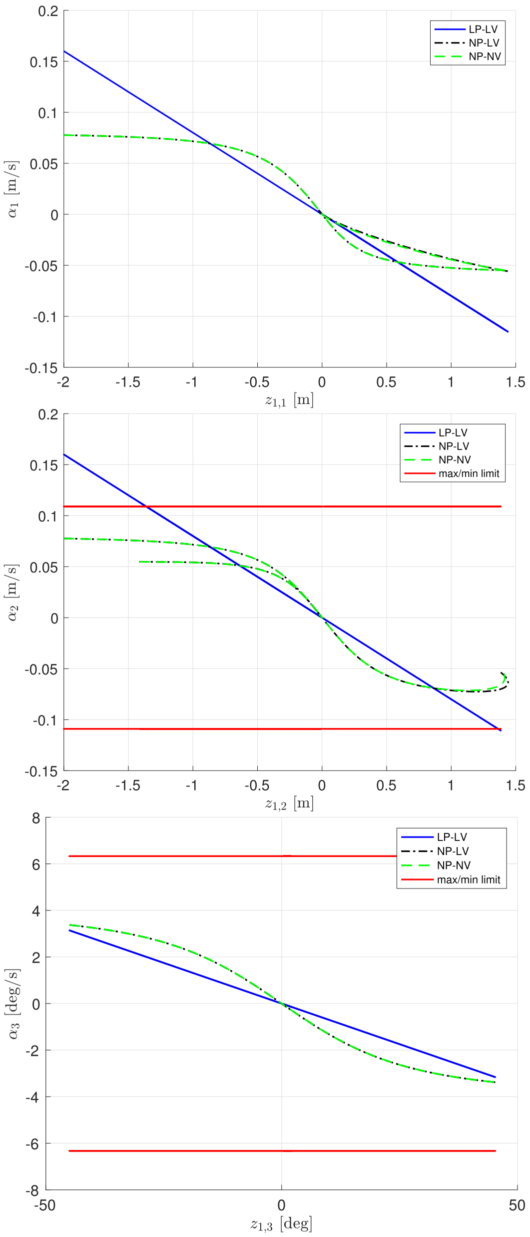

FIGURE 9. The 4-corner simulation: The pose feedback terms as functions of the pose errors.

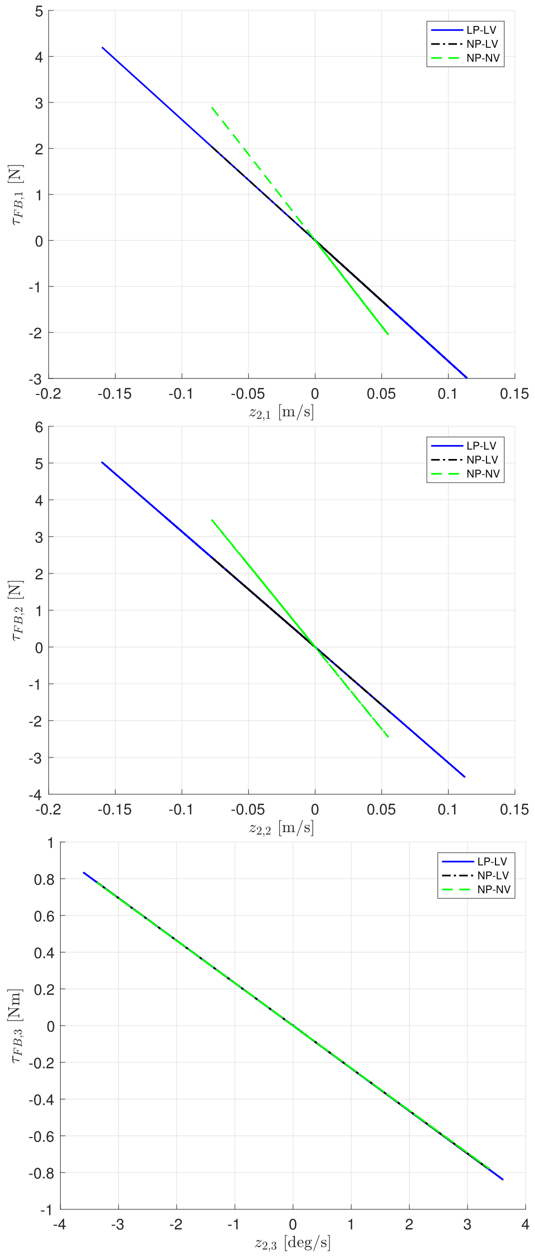

FIGURE 10. The 4-corner simulation: The velocity feedback terms as functions of the velocity errors.

the LP-LV controller's α_2 goes outside the achievable range of the CSAD, while the two nonlinear controllers do not.

Similar to Fig. 9, Fig. 10 shows the feedback contribution for the kinetic part of the three considered controllers. Here, it can been seen that the NP-NV controller has a steeper curve than the two other controllers, which means that it is a bit more aggressive. The plots in figures 9 and 10 correlate with the behavior of the control signals in Fig. 8.

Fig. 11 shows the time evolution of the performance metrics IAE and IAEW of the three controllers. In particular, the IAE plot shows that the LP-LV controller has the poorest performance of three controllers with respect to control accuracy, while the NP-NV controller has the best performance. However, by including the energy use into the performance metric as in IAEW, this result changes such that the NP-LV

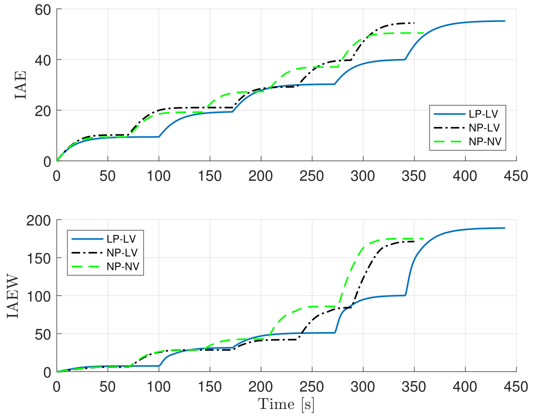

FIGURE 11. The 4-corner simulation: IAE and IAEW performance metrics.

TABLE 2. Final values of the performance metrics for the simulations.

	LP-LV	NP-LV	NP-NV
IAE	55.21	54.35	**50.48**
IAEW	189	**171**	175

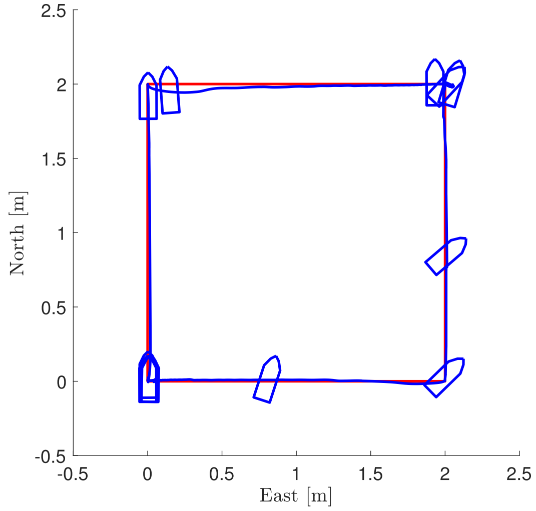

FIGURE 12. The 4-corner experiment: Using LP-LV feedback terms.

controller has the best performance, while the LP-LV controller has the poorest performance. Table 2 shows the final values of the performance metrics for the simulations.

E. EXPERIMENTAL RESULTS

The three controllers have been implemented and experimentally tested on the model-scale ship CSAD [20] in the Marine Cybernetics Laboratory (MC-Lab) at NTNU, for the same 4-corner scenario as in the simulations, see Fig 4. The MC-Lab is equipped with a Qualisys motion capture system in order to measure the pose $\boldsymbol{\eta}$ of the ship. An estimator of the velocity $\boldsymbol{\nu}$ has also been implemented. The control parameters are the same as for the simulations, see Table 1. The controllers are simple to implement and none of them have any significant computational complexity.

Figs. 12-14 show the ship pose and box outlines for the 4-corner test for the LP-LV, NP-LV and NP-NV controllers, respectively. Considering the commanded control inputs of the three controllers, which is shown in Fig. 15, the intensity of the peak values of the control signal is similar to the ones from the simulation shown in Fig. 8. Here, we also see that the three controllers finish the 4-corner test at different times, which is similar to the simulations.

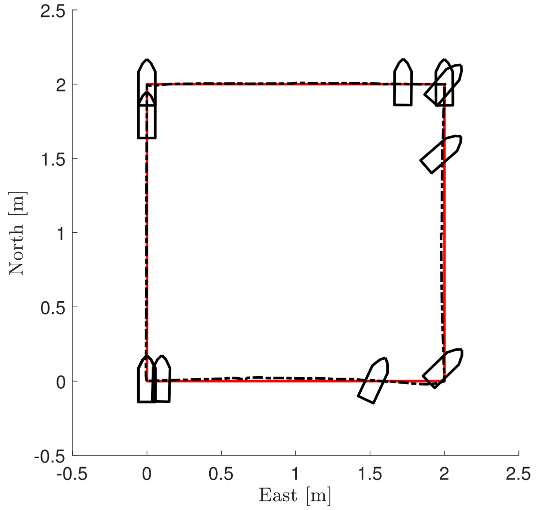

FIGURE 13. The 4-corner experiment: Using NP-LV feedback terms.

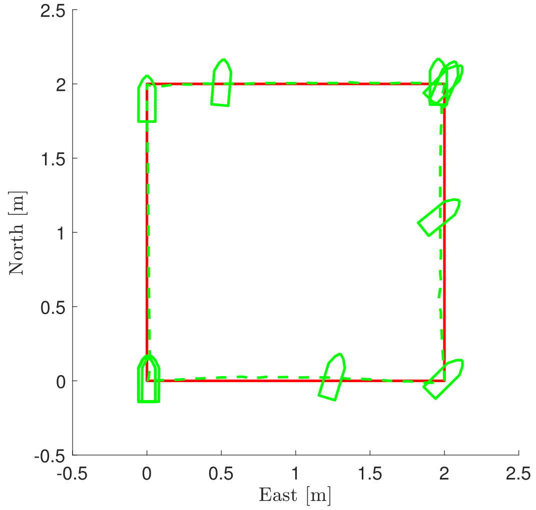

FIGURE 14. The 4-corner experiment: Using NP-NV feedback terms.

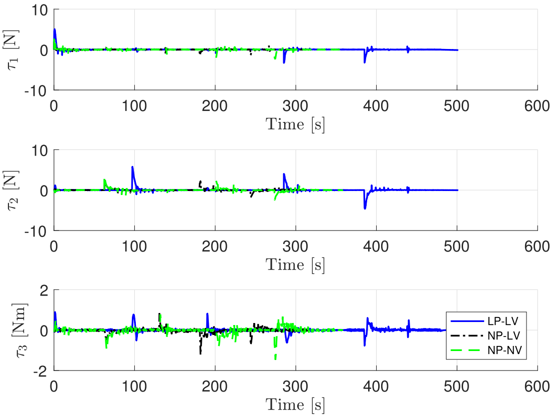

FIGURE 15. **The 4-corner experiment: The commanded control inputs.**

TABLE 3. **Final values of the performance metrics for the experiments.**

	LP-LV	**NP-LV**	**NP-NV**
IAE	49.92	45.04	**44.92**
IAEW	147.6	**76.14**	102.8

Comparing Fig. 16 with Fig. 9 and Fig. 17 with Fig. 10, similar observations can be made for the experiments as for the simulations.

Fig. 18 shows the performance metrics IAE and IAEW for the three controllers, which also shows a similar result as in the simulations. Table 3 shows the final values of the performance metrics for the experiments.

F. DISCUSSION

This article has shown some additional findings compared to the original findings in [10], using the suggested tuning rules and a different test scenario.

Comparing the results between the simulated and experimental 4-corner tests, similar performance is obtained with respect to the amount of time that the different controllers need to complete the test. Additionally, the NP-NV controller gives the best IAE performance for the considered controllers for both the simulated and experimental tests, while the NP-LV controller consistently uses the least amount of energy among the considered controllers.

Based on the simulation and experimental results, the NP-LV controller comes out on top since it uses the shortest amount of time to complete the 4-corner test. In addition, it has the best energy efficiency as shown by the IAEW metric, and it has a similar tracking performance as the NP-NV controller as shown by the IAE metric. In contrast, the purely linear feedback controller LP-LV uses significantly more time to complete the test, with higher IAE and IAEW as a consequence. Thus, the combined ability to constrain the feedback control input globally while changing the convergence rate locally, for the nonlinear feedback controllers, seems to be advantageous. The price to be paid is the introduction of more tuning parameters, represented by the Δ-parameters, which must be chosen carefully. If they are chosen too small, the control signal will get a discontinuous behavior and can make the control signal exceed the saturation constraints in the linear region.

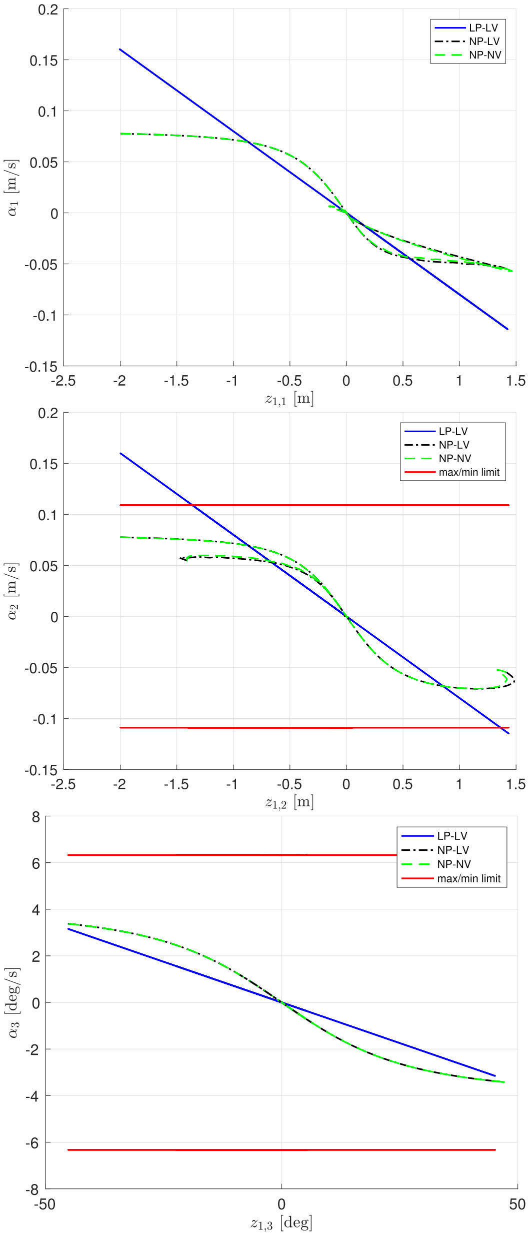

FIGURE 16. **The 4-corner experiment: The pose feedback terms as functions of the pose errors.**

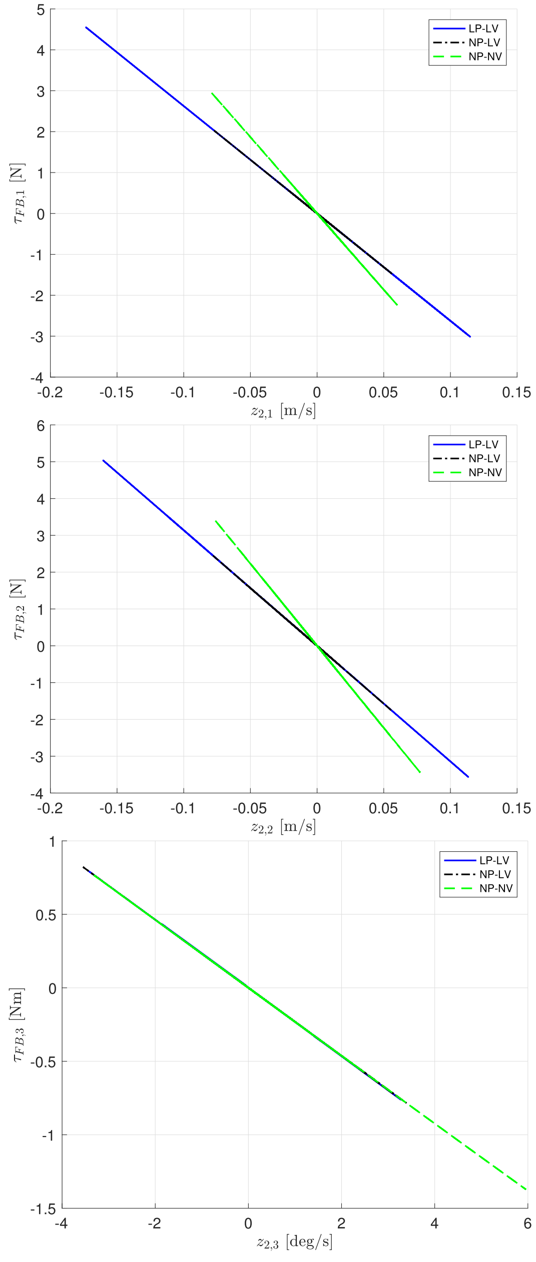

FIGURE 17. **The 4-corner experiment: The velocity feedback terms as functions of the velocity errors.**

The nonlinear feedback control concept suggested in this article is an initial step toward handling actuator saturation constraints, as well as resulting in improved transient behavior. Also, the cascaded control approach makes it possible to combine the controller with explicit constraint-handling algorithms such as e.g. the dynamic window algorithm [24], as preliminary suggested by the results in [25].

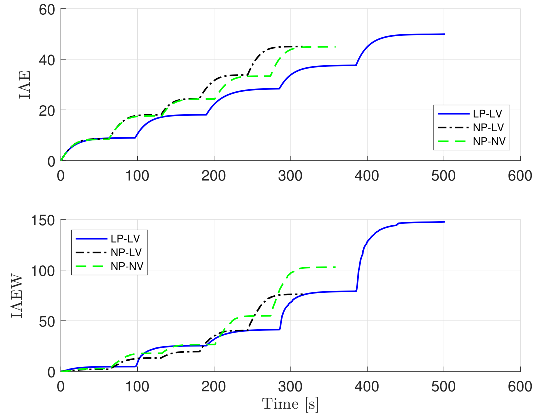

FIGURE 18. **The 4-corner experiment: IAE and IAEW performance metrics.**

VI. CONCLUSION

This article has further investigated combinations of linear and nonlinear feedback terms for pose and velocity control of ships. Through numerical simulations and model-scale experiments in a ocean basin, three cascaded controllers are compared using performance metrics that consider both control accuracy and energy use. The performance metrics show that the nonlinear feedback controllers outperform the linear baseline controller for the considered step-change maneuvers of the 4-corner test. The combined ability to constrain the feedback control inputs globally and to change the convergence rates locally, for the nonlinear feedback controllers, seems to be advantageous. The price to be paid is the introduction of additional tuning parameters, namely the Δ-parameters. The paper also suggests appropriate tuning rules for the considered controllers. Moreover, stability proofs for the considered closed-loop control systems are provided. Future work includes introducing model uncertainties and unknown disturbances to the ship system. In addition to the mitigation of magnitude saturation constraints considered in this article, it is also relevant to consider how actuator rate saturation constrains can be handled.

ACKNOWLEDGMENT

The authors gratefully acknowledge Senior Engineer Torgeir Wahl and Ph.D. candidate Andreas R. Dahl at NTNU's Department of Marine Technology for valuable support during the experiments.

REFERENCES

[1] N. Minorsky, "Directional stability of automatically steered bodies," *J. Amer. Soc. Nav. Eng.*, vol. 34, no. 2, pp. 280–309, Mar. 2009.

[2] T. I. Fossen and J. P. Strand, "Tutorial on nonlinear backstepping: Applications to ship control," *Model., Identificat. Control, Norwegian Res. Bull.*, vol. 20, no. 2, pp. 83–135, 1999.

[3] T. I. Fossen, "Nonlinear passive control and observer design for ships," *Model., Identificat. Control, Norwegian Res. Bull.*, vol. 21, no. 3, pp. 129–184, 2000.

[4] J. E. Refsnes, A. J. Sorensen, and K. Y. Pettersen, "Model-based output feedback control of slender-body underactuated AUVs: Theory and experiments," *IEEE Trans. Control Syst. Technol.*, vol. 16, no. 5, pp. 930–946, Sep. 2008.

[5] T. I. Fossen, *Handbook of Marine Craft Hydrodynamics and Motion Control*. Hoboken, NJ, USA: Wiley, 2011.

[6] T. I. Fossen, M. Breivik, and R. Skjetne, "Line-of-sight path following of underactuated marine craft," in *Proc. 6th IFAC Conf. Manoeuvring Control Mar. Craft*, Girona, Spain, 2003.

[7] M. Breivik, J. P. Strand, and T. I. Fossen, "Guided dynamic positioning for fully actuated marine surface vessels," in *Proc. 7th IFAC Conf. Manoeuvring Control*, Lisbon, Portugal, 2006, pp. 1–6.

[8] M. Breivik and T. I. Fossen, "Applying missile guidance concepts to motion control of marine craft," in *Proc. 7th IFAC Conf. Control Appl. Marine Syst.*, Bol, Croatia, 2007.

[9] M. Breivik and T. I. Fossen, "Guidance laws for autonomous underwater vehicles," in *Underwater Vehicles*, A. V. Inzartsev, Ed. In-Tech Education and Publishing, 2009, pp. 51–76.

[10] M. E. N. Sørensen and M. Breivik, "Comparing combinations of linear and nonlinear feedback terms for motion control of marine surface vessels," in *Proc. 10th IFAC Conf. Control Appl. Mar. Syst.*, Trondheim, Norway, 2016, pp. 1–8.

[11] O. N. Lyngstadaas, T. E. Saeterdal, M. E. N. Sorensen, and M. Breivik, "Improvement of ship motion control using a magnitude-rate saturation model," in *Proc. IEEE Conf. Control Technol. Appl. (CCTA)*, Copenhagen, Denmark, Aug. 2018, pp. 75–81.

[12] X.-K. Zhang and G.-Q. Zhang, "Design of ship course-keeping autopilot using a sine function-based nonlinear feedback technique," *J. Navigat.*, vol. 69, no. 2, pp. 246–256, Mar. 2016.

[13] Q. Zhang and X. Zhang, "Nonlinear improved concise backstepping control of course keeping for ships," *IEEE Access*, vol. 7, pp. 19258–19265, 2019.

[14] Y. Deng, X. Zhang, N. Im, G. Zhang, and Q. Zhang, "Adaptive fuzzy tracking control for underactuated surface vessels with unmodeled dynamics and input saturation," *ISA Trans.*, vol. 103, pp. 52–62, Aug. 2020.

[15] M. E. N. Sørensen and M. Breivik, "Comparing nonlinear adaptive motion controllers for marine surface vessels," in *Proc. 10th IFAC Conf. Manoeuvring Control Mar. Craft*, Copenhagen, Denmark, 2015.

[16] M. Arcak, M. Seron, J. Braslavsky, and P. Kokotovic, "Robustification of backstepping against input unmodeled dynamics," *IEEE Trans. Autom. Control*, vol. 45, no. 7, pp. 1358–1363, Jul. 2000.

[17] F. Lamnabhi-Lagarrigue, E. Panteley, E. Lefeber, and A. Loría, *Advanced Topics in Control Systems Theory: Lecture Notes from FAP 2004*. Springer, 2005.

[18] H. K. Khalil, *Nonlinear Systems*. Upper Saddle River, NJ, USA: Prentice-Hall, 2002.

[19] A. Pavlov, H. Nordahl, and M. Breivik, "MPC-based optimal path following for underactuated vessels," in *Proc. 8th IFAC Conf. Manoeuvring Control Mar. Craft*, Guarujá, Brazil, 2009.

[20] J. Bjørnø, H.-M. Heyn, R. Skjetne, A. R. Dahl, and P. Frederich, "Modeling, parameter identification and thruster-assisted position mooring of C/S Inocean CAT I Drillship," in *Proc. 36th Int. Conf. Ocean, Offshore Arctic Eng.*, Trondheim, Norway, Jun. 2017, pp. 1–10.

[21] B.-O. H. Eriksen and M. Breivik, "Modeling, identification and control of high-speed ASVs: Theory and experiments," in *Sensing and Control for Autonomous Vehicles: Applications to Land, Water and Air Vehicles*. Springer, 2017, pp. 407–431.

[22] R. Skjetne, M. E. N. Sørensen, M. Breivik, S. A. T. Værnø, A. H. Brodtkorb, A. J. Sørensen, O. K. Kjerstad, V. Calabrò, and B. O. Vinje, "AMOS DP research cruise 2016: Academic full-scale testing of experimental dynamic positioning control algorithms onboard R/V Gunnerus," in *Proc. 36th Int. Conf. Ocean, Offshore Arctic Eng.*, vol. 1. Trondheim, Norway: Offshore Technology, 2017, pp. 1–10.

[23] O. N. Lyngstadaas, "Ship motion control concepts considering actuator constraints," MSc thesis, Dept. Eng. Cybern., Norwegian Univ. Sci. Technol., Trondheim, Norway, 2018.

[24] D. Fox, W. Burgard, and S. Thrun, "The dynamic window approach to collision avoidance," *IEEE Robot. Autom. Mag.*, vol. 4, no. 1, pp. 23–33, Mar. 1997.

[25] M. E. N. Sorensen, M. Breivik, and B.-O.-H. Eriksen, "A ship heading and speed control concept inherently satisfying actuator constraints," in *Proc. IEEE Conf. Control Technol. Appl. (CCTA)*, Mauna Lani, HI, USA, Aug. 2017, pp. 323–330.

MIKKEL ESKE NØRGAARD SØRENSEN received the M.Sc. degree in electrical engineering from the Technical University of Denmark (DTU), Lyngby, Denmark, in 2014. He is currently pursuing the Ph.D. degree in engineering cybernetics with the Norwegian University of Science and Technology (NTNU), Trondheim, Norway. He is also working at MAN Energy Solutions. His research interest includes nonlinear and adaptive motion control of unmanned vehicles.

MORTEN BREIVIK (Member, IEEE) received the M.Sc. and Ph.D. degrees in engineering cybernetics from NTNU, in 2003 and 2010, respectively. He is currently the Head of the NTNU's Department of Engineering Cybernetics and an Associate Researcher with the Centre for Autonomous Marine Operations and Systems (NTNU AMOS). He has previously worked as an Assistant Professor and a Researcher at NTNU, a Scientific Advisor at Maritime Robotics, and a Principal Engineer and the Department Manager of Applied Cybernetics at Kongsberg Maritime. His research interest includes nonlinear and adaptive motion control of unmanned vehicles in general and autonomous ships in particular. He is also a member of the Norwegian Board of Technology.

ROGER SKJETNE (Member, IEEE) received the M.Sc. degree from the University of California at Santa Barbara (UCSB), in 2000, and the Ph.D. degree in control engineering from the Norwegian University of Science and Technology (NTNU), in 2005. He holds the Exxon Mobil Prize for his Ph.D. thesis at NTNU. Prior to his studies, he worked as a Certified Electrician at Aker Elektro AS, worked on numerous oil installations for the North Sea, and from 2004 to 2009, he was employed at Marine Cybernetics AS, working on hardware-in-the-loop simulation for verification of marine control systems. Since August 2009, he has been holding the Kongsberg Maritime Chair of Professor in Marine Control Engineering at the Department of Marine Technology, NTNU. From 2017 to 2018, he was a Visiting Research Scholar with the Center for Control, Dynamical Systems and Computation, UCSB. His research interests include dynamic positioning of marine vessels, Arctic stationkeeping and ice management systems, control of shipboard hybrid electric power systems, nonlinear motion control of marine vehicles, and autonomous ships and marine robots.

A.3 Comparing Nonlinear Adaptive Motion Controllers for Marine Surface Vessels

M. E. N. Sørensen and M. Breivik, Comparing nonlinear adaptive motion controllers for marine surface vessels, *in Proceedings of the 10th IFAC Conference on Manoeuvring and Control of Marine Craft, Copenhagen, Denmark*, 2015.

Comparing Nonlinear Adaptive Motion Controllers for Marine Surface Vessels

Mikkel Eske Nørgaard Sørensen Morten Breivik

*Centre for Autonomous Marine Operations and Systems,
Department of Engineering Cybernetics, Norwegian University of
Science and Technology, NO-7491 Trondheim, Norway
E-mail: mikkel.sorensen@itk.ntnu.no, morten.breivik@ieee.org*

Abstract: This paper deals with the design and evaluation of four controllers based on backstepping and different adaptive control schemes, which are applied to the motion control of a nonlinear 3 degrees-of-freedom model of a marine surface vessel. The goal is to make a comparative analysis of the controllers in order to find out which one has the best performance. The considered controllers are: Adaptive backstepping, adaptive backstepping with command governor, $\mathcal{L}_1$ adaptive backstepping and $\mathcal{L}_1$ adaptive backstepping with command governor. Numerical simulations are performed for target tracking along both straight-line and circular paths, with uncertain model parameters and an unknown disturbance. Motion control performance is evaluated by performance metrics such as IAE, ISE, ITAE and a novel metric named IAEW which combines control accuracy and energy use in one single metric.

Keywords: Marine surface vessel, Nonlinear motion control, Adaptive backstepping, $\mathcal{L}_1$ adaptive backstepping, Command governor, Performance metrics

1. INTRODUCTION

Automated motion control of marine surface vessels has been a research topic since the early 20th century. In recent years, the research has expanded from control of manned vessels to also include unmanned vessels. When dealing with surface vessels in general, uncertain nonlinear hydrodynamics and external disturbances must be considered. To minimise uncertainties, experiments can be conducted to find the hydrodynamical coefficients. Changes in coefficients nevertheless occur. Also, external disturbances are difficult or impossible to measure. Adaptive control methods can be employed to deal with such uncertainties such that the vessel can still achieve its control objectives.

Even though the field of adaptive control dates back to the early 1950s, it has experienced an increased amount of interest and research effort during the last decade. This effort has lead to some new and promising control techniques such as $\mathcal{L}_1$ adaptive control (Hovakimyan and Cao, 2010) and the novel command governor architecture for adaptive stabilization and command following (Yucelen and Johnson, 2012a).

The $\mathcal{L}_1$ adaptive control method has been used in many fields, especially within aerial applications (Patel et al., 2007), where parameters can change very rapidly. However, it has still not been widely used for motion control of marine vessels. Examples include (Breu and Fossen, 2011), where $\mathcal{L}_1$ adaptive control was applied to deal with the parametric resonance problem for ships. In (Svendsen et al., 2012), an adaptive robust control system was developed to govern the steering of a high-speed unmanned watercraft maintaining uniform performance across the operational envelope. Based on these results, the authors in (Theisen et al., 2013) developed an $\mathcal{L}_1$ adaptive hovering control of an unmanned watercraft in a station-keeping mode. In addition, (Ren et al., 2014) used $\mathcal{L}_1$ adaptive control to improve the steering of a surface vessel along a predefined path.

In (Yucelen and Johnson, 2012a), a linear command governor was combined with the model reference adaptive control method to improve transient performance. In (Yucelen and Johnson, 2012b), a lowpass filter was applied to achieve a more robust adaptive control solution. Also, constrained adaptive control was combined with the command governor in (Schatz et al., 2013).

This paper will compare and evaluate the performance of the adaptive backstepping control method (Krstic et al., 1995) and the $\mathcal{L}_1$ adaptive backstepping control method applied to nonlinear motion control of marine surface vessels. In addition, it will be investigated if it is possible to improve the performance of these control methods by combining them with a modified command governor architecture.

The structure of this paper is as follows: A mathematical model and assumptions are presented in Section 2; Section 3 presents the design of the adaptive control laws applied to the vessel model; Section 4 includes simulation results and performance evaluation; while Section 5 concludes the paper.

2. SURFACE VESSEL MODEL

The motion of a surface vessel can be represented by the pose vector $\boldsymbol{\eta} = [x, y, \psi]^\top \in \mathbb{R}^2 \times \mathbb{S}$ and the velocity vector $\boldsymbol{\nu} = [u, v, r]^\top \in \mathbb{R}^3$, where $\mathbb{S} \in [-\pi, \pi]$. Here, (x, y)

represents the Cartesian position in the local reference frame, ψ is the yaw angle, (u, v) represents the body-fixed linear velocities and r is the yaw rate.

The 3 DOF dynamics of a surface vessel can be stated as (Fossen, 2011):

$$\dot{\boldsymbol{\eta}} = \mathbf{R}(\psi)\boldsymbol{\nu} \tag{1}$$

$$\boldsymbol{M}^*\dot{\boldsymbol{\nu}} + \boldsymbol{C}^*(\boldsymbol{\nu})\boldsymbol{\nu} + \boldsymbol{D}^*(\boldsymbol{\nu})\boldsymbol{\nu} = \boldsymbol{\tau}^* + \mathbf{R}^\top(\psi)\boldsymbol{w}^*, \tag{2}$$

where

$$\mathbf{R}(\psi) = \begin{bmatrix} \cos(\psi) & -\sin(\psi) & 0 \\ \sin(\psi) & \cos(\psi) & 0 \\ 0 & 0 & 1 \end{bmatrix} \tag{3}$$

is a rotation matrix $\mathbf{R} \in SO(3)$, and where $\mathbf{M}^*$, $\boldsymbol{C}^*(\boldsymbol{\nu})$, $\boldsymbol{D}^*(\boldsymbol{\nu})$, $\boldsymbol{\tau}^*$ and $\boldsymbol{w}^*$ represent the real inertia matrix, Coriolis and centripetal matrix, damping matrix, control input vector and disturbance vector, respectively. Here, the system matrices are assumed to satisfy the properties $\mathbf{M}^* = \mathbf{M}^{*\top} > 0$, $\mathbf{C}^*(\boldsymbol{\nu}) = -\mathbf{C}^*(\boldsymbol{\nu})^\top$ and $\mathbf{D}^*(\boldsymbol{\nu}) > 0$.

However, there are uncertainties associated with the real matrices and vectors. Therefore, we assume that the relationship between the real and considered system matrices is parametrised as

$$\mathbf{M}^* = \delta\mathbf{M}, \tag{4}$$

$$\boldsymbol{C}^*(\boldsymbol{\nu}) = \delta\boldsymbol{C}(\boldsymbol{\nu}), \tag{5}$$

$$\boldsymbol{D}^*(\boldsymbol{\nu}) = \sigma\boldsymbol{D}(\boldsymbol{\nu}), \tag{6}$$

$$\boldsymbol{\tau}^* = \rho\boldsymbol{\tau}, \tag{7}$$

where $\delta \in \mathbb{R}^+$ is the uncertainty associated with the inertia matrix, $\sigma \in \mathbb{R}^+$ is the uncertainty associated with the damping matrix and $\rho \in \mathbb{R}^+$ is the uncertainty associated with the control input vector. Additionally, it is assumed that $\dot{\delta} = 0$, $\dot{\sigma} = 0$, $\dot{\rho} = 0$ and $\dot{\boldsymbol{w}}^* = \mathbf{0}$, i.e., that the uncertainties and disturbance are constant or slowly varying relative to the vessel dynamics.

Applying (4)-(7) into (2), the vessel model can also be stated as

$$\dot{\boldsymbol{\eta}} = \mathbf{R}(\psi)\boldsymbol{\nu} \tag{8}$$

$$\delta[\mathbf{M}\dot{\boldsymbol{\nu}} + \mathbf{C}(\boldsymbol{\nu})\boldsymbol{\nu}] + \sigma\mathbf{D}(\boldsymbol{\nu})\boldsymbol{\nu} = \rho\boldsymbol{\tau} + \mathbf{R}^\top(\psi)\boldsymbol{w}^*. \tag{9}$$

3. NONLINEAR ADAPTIVE MOTION CONTROLLERS

In this section, a step-by-step design procedure for the different nonlinear adaptive motion controllers will be presented. It is assumed that both the pose vector $\boldsymbol{\eta}$ and velocity vector $\boldsymbol{\nu}$ can be measured. In addition, it is assumed that there are no magnitude or rate saturations for the control input $\boldsymbol{\tau}^*$.

The control objective is to make $|\boldsymbol{\eta}(t) - \boldsymbol{\eta}_d(t)| \to 0$, where $\boldsymbol{\eta}_d(t)$ is $\mathcal{C}^2$ and bounded. This reference signal is typically defined by a human or generated by a guidance system.

3.1 Adaptive Backstepping

The design approach of an adaptive backstepping controller is divided into several stages, including the definition of new state variables, finding the control law through control Lyapunov functions (CLF) and designing the adaptation laws. For notational simplicity, the time t is omitted. The design procedure of this approach is inspired by (Krstic et al., 1995), (Fossen and Strand, 1999) and (Fossen, 2011).

Start by defining the error variables $\mathbf{z}_1$ and $\mathbf{z}_2$:

$$\mathbf{z}_1 \triangleq \mathbf{R}^\top(\psi)(\boldsymbol{\eta} - \boldsymbol{\eta}_d) \tag{10}$$

$$\mathbf{z}_2 \triangleq \boldsymbol{\nu} - \boldsymbol{\alpha}, \tag{11}$$

where $\boldsymbol{\alpha} \in \mathbb{R}^3$ is a vector of stabilising functions to be designed.

Step 1:
Choosing a positive definite (CLF)

$$V_1 = \frac{1}{2}\mathbf{z}_1^\top\mathbf{z}_1, \tag{12}$$

the derivative of V_1 with respect to (w.r.t) time along the $\mathbf{z}_1$-dynamics gives

$$\begin{aligned} \dot{V}_1 &= \mathbf{z}_1^\top\dot{\mathbf{z}}_1 \\ &= \mathbf{z}_1^\top(\mathbf{S}(r)^\top\mathbf{R}^\top(\psi)(\boldsymbol{\eta} - \boldsymbol{\eta}_d) + \mathbf{R}^\top(\psi)(\dot{\boldsymbol{\eta}} - \dot{\boldsymbol{\eta}}_d)) \\ &= \mathbf{z}_1^\top(\mathbf{S}(r)^\top\mathbf{z}_1 + \mathbf{R}^\top(\psi)(\dot{\boldsymbol{\eta}} - \dot{\boldsymbol{\eta}}_d)), \end{aligned}$$

where

$$\mathbf{S}(r) = \begin{bmatrix} 0 & -r & 0 \\ r & 0 & 0 \\ 0 & 0 & 0 \end{bmatrix},$$

and by applying the skew-symmetric property $\mathbf{z}_1^\top\mathbf{S}(r)^\top\mathbf{z}_1 = 0$, gives

$$\dot{V}_1 = \mathbf{z}_1^\top(\boldsymbol{\nu} - \mathbf{R}^\top(\psi)\dot{\boldsymbol{\eta}}_d).$$

Using (11), the CLF becomes

$$\begin{aligned} \dot{V}_1 &= \mathbf{z}_1^\top(\mathbf{z}_2 + \boldsymbol{\alpha} - \mathbf{R}^\top(\psi)\dot{\boldsymbol{\eta}}_d) \\ &= \mathbf{z}_1^\top\mathbf{z}_2 + \mathbf{z}_1^\top(\boldsymbol{\alpha} - \mathbf{R}^\top(\psi)\dot{\boldsymbol{\eta}}_d). \end{aligned}$$

The stabilising function can now be chosen as

$$\boldsymbol{\alpha} = \mathbf{R}^\top(\psi)\dot{\boldsymbol{\eta}}_d - \mathbf{K}_1\mathbf{z}_1, \tag{13}$$

where $\mathbf{K}_1 > 0$, which results in

$$\dot{V}_1 = -\mathbf{z}_1^\top\mathbf{K}_1\mathbf{z}_1 + \mathbf{z}_2^\top\mathbf{z}_1,$$

which concludes Step 1.

Step 2:
By defining

$$\delta_\rho \triangleq \frac{\delta}{\rho}, \quad \sigma_\rho \triangleq \frac{\sigma}{\rho}, \quad \boldsymbol{w}_\rho^* = \frac{1}{\rho}\boldsymbol{w}^*, \tag{14}$$

the $\mathbf{z}_2$ dynamics can be written as

$$\begin{aligned} \delta_\rho\mathbf{M}\dot{\mathbf{z}}_2 =& \delta_\rho\mathbf{M}(\dot{\boldsymbol{\nu}} - \dot{\boldsymbol{\alpha}}) \\ =& \boldsymbol{\tau} + \mathbf{R}^\top(\psi)\boldsymbol{w}_\rho^* - \delta_\rho\mathbf{C}(\boldsymbol{\nu})\boldsymbol{\nu} - \sigma_\rho\mathbf{D}(\boldsymbol{\nu})\boldsymbol{\nu} - \delta_\rho\mathbf{M}\dot{\boldsymbol{\alpha}}, \end{aligned}$$

where

$$\dot{\boldsymbol{\alpha}} = \mathbf{R}^\top(\psi)\ddot{\boldsymbol{\eta}}_d + \mathbf{S}(r)^\top\mathbf{R}^\top(\psi)\dot{\boldsymbol{\eta}}_d - \mathbf{K}_1\dot{\mathbf{z}}_1.$$

By including both $\mathbf{z}_1$ and $\mathbf{z}_2$, the CLF is modified to

$$V_2 = \frac{1}{2}\mathbf{z}_2^\top\delta_\rho\mathbf{M}\mathbf{z}_2 + V_1. \tag{15}$$

Rewriting $\mathbf{C}(\boldsymbol{\nu}) = \mathbf{C}$, $\mathbf{D}(\boldsymbol{\nu}) = \mathbf{D}$ and $\mathbf{R}(\psi) = \mathbf{R}$ for notational brevity, the derivative of this CLF is

$$\begin{aligned} \dot{V}_2 =& \mathbf{z}_2^\top\delta_\rho\mathbf{M}\dot{\mathbf{z}}_2 + \dot{V}_1, \\ =& \mathbf{z}_2^\top[\boldsymbol{\tau} + \mathbf{R}^\top\boldsymbol{w}_\rho^* - \delta_\rho\mathbf{C}\boldsymbol{\nu} - \sigma_\rho\mathbf{D}\boldsymbol{\nu} - \delta_\rho\mathbf{M}\dot{\boldsymbol{\alpha}}] \\ & - \mathbf{z}_1^\top\mathbf{K}_1\mathbf{z}_1 + \mathbf{z}_2^\top\mathbf{z}_1. \end{aligned}$$

Utilising the fact that $\boldsymbol{\nu} = \mathbf{z}_2 + \boldsymbol{\alpha}$, we obtain

$$\begin{aligned} \dot{V}_2 =& \mathbf{z}_2^\top[\mathbf{z}_1 + \boldsymbol{\tau} + \mathbf{R}^\top\boldsymbol{w}_\rho^* - \delta_\rho\mathbf{C}\boldsymbol{\alpha} - \sigma_\rho\mathbf{D}\boldsymbol{\alpha} - \delta_\rho\mathbf{M}\dot{\boldsymbol{\alpha}}] \\ & - \mathbf{z}_1^\top\mathbf{K}_1\mathbf{z}_1 - \mathbf{z}_2^\top\delta_\rho\mathbf{C}\mathbf{z}_2 - \mathbf{z}_2^\top\sigma_\rho\mathbf{D}\mathbf{z}_2. \end{aligned}$$

Applying the skew-symmetric property $\mathbf{z}_2^\top \delta_\rho \mathbf{C}\mathbf{z}_2 = 0$, yields

$$\begin{aligned}\dot V_2 =& \mathbf{z}_2^\top[\mathbf{z}_1 + \boldsymbol{\tau} + \mathbf{R}^\top \boldsymbol{w}_\rho^* - \delta_\rho \mathbf{C}\boldsymbol{\alpha} - \sigma_\rho \mathbf{D}\boldsymbol{\alpha} - \delta_\rho \mathbf{M}\dot{\boldsymbol{\alpha}}]\\ &- \mathbf{z}_1^\top \mathbf{K}_1 \mathbf{z}_1 - \mathbf{z}_2^\top \sigma_\rho \mathbf{D}\mathbf{z}_2.\end{aligned}$$

The control law can be chosen as

$$\begin{aligned}\boldsymbol{\tau} =& -\mathbf{R}^\top \boldsymbol{w}_\rho^* + \delta_\rho[\mathbf{M}\dot{\boldsymbol{\alpha}} + \mathbf{C}\boldsymbol{\alpha}] + \sigma_\rho \mathbf{D}\boldsymbol{\alpha}\\ &- \mathbf{z}_1 - \mathbf{K}_2\mathbf{z}_2,\end{aligned} \tag{16}$$

where $\mathbf{K}_2 > 0$. This results in

$$\dot V_2 = -\mathbf{z}_1^\top \mathbf{K}_1 \mathbf{z}_1 - \mathbf{z}_2^\top(\mathbf{K}_2 + \sigma_\rho \mathbf{D})\mathbf{z}_2 \leq 0.$$

Step 3:
The parameters δ_ρ, σ_ρ and $\boldsymbol{w}_\rho^*$ are not known in the control laws in (16), and the CLF is expanded to

$$V_3 = \frac{1}{2}\left[\frac{1}{\gamma_{\delta_\rho}}\tilde\delta_\rho^2 + \frac{1}{\gamma_{\sigma_\rho}}\tilde\sigma_\rho^2 + \frac{1}{\gamma_{w_\rho}}\tilde{\boldsymbol{w}}_\rho{}^\top\tilde{\boldsymbol{w}}_\rho\right] + V_2, \tag{17}$$

where γ_{δ_ρ}, γ_{σ_ρ} and γ_{w_ρ} are the adaptation gains. Also, $\tilde\delta_\rho \triangleq \hat\delta_\rho - \delta_\rho$, $\tilde\sigma_\rho \triangleq \hat\sigma_\rho - \sigma_\rho$, $\tilde{\boldsymbol{w}}_\rho \triangleq \hat{\boldsymbol{w}}_\rho - \boldsymbol{w}_\rho^*$. The derivative of V_3 then becomes

$$\begin{aligned}\dot V_3 =& \frac{1}{\gamma_{\delta_\rho}}\tilde\delta_\rho\dot{\hat\delta}_\rho + \frac{1}{\gamma_{\sigma_\rho}}\tilde\sigma_\rho\dot{\hat\sigma}_\rho + \frac{1}{\gamma_{w_\rho}}\tilde{\boldsymbol{w}}_\rho{}^\top\dot{\hat{\boldsymbol{w}}}_\rho + \mathbf{z}_2^\top[\tilde\delta_\rho(\mathbf{M}\dot{\boldsymbol{\alpha}} + \mathbf{C}\boldsymbol{\alpha})\\ &+ \tilde\sigma_\rho(\mathbf{D}\boldsymbol{\alpha}) - (\mathbf{K}_2 + \sigma_\rho\mathbf{D})\mathbf{z}_2 - \mathbf{R}^\top\tilde{\boldsymbol{w}}_\rho] - \mathbf{z}_1^\top\mathbf{K}_1\mathbf{z}_1.\end{aligned}$$

To eliminate the uncertainty terms $\tilde\delta_\rho$ and $\tilde\sigma_\rho$, the update laws are chosen as

$$\dot{\hat\delta}_\rho = -\gamma_{\delta_\rho}\mathbf{z}_2^\top[\mathbf{M}\dot{\boldsymbol{\alpha}} + \mathbf{C}\boldsymbol{\alpha}], \tag{18}$$

$$\dot{\hat\sigma}_\rho = -\gamma_{\sigma_\rho}\mathbf{z}_2^\top\mathbf{D}\boldsymbol{\alpha}, \tag{19}$$

$$\dot{\hat{\boldsymbol{w}}}_\rho = \gamma_{w_\rho}\mathbf{R}\mathbf{z}_2, \tag{20}$$

which results in

$$\dot V_3 = -\mathbf{z}_1^\top\mathbf{K}_1\mathbf{z}_1 - \mathbf{z}_2^\top\mathbf{K}_2\mathbf{z}_2 \leq 0, \quad \forall \mathbf{z}_1, \mathbf{z}_2 \neq 0.$$

It can be concluded that the origin of the error system $(\mathbf{z}_1, \mathbf{z}_2, \tilde\delta_\rho, \tilde\sigma_\rho, \tilde{\boldsymbol{w}}_\rho)$ is uniformly globally asymptotically stable (UGAS) by utilising Theorem A.6 from (Fossen, 2011).

3.2 $\mathcal{L}_1$ Adaptive Backstepping

The design of the $\mathcal{L}_1$ adaptive backstepping controller is divided into two stages. The first stage concerns design of the adaptation laws and the second stage of the control law, inspired by the approach in (Lee et al., 2012).

State Predictor and Adaptation Laws
First, a state predictor is designed, where the prediction errors are defined as

$$\tilde{\boldsymbol{\eta}} \triangleq \hat{\boldsymbol{\eta}} - \boldsymbol{\eta}, \quad \tilde{\boldsymbol{\nu}} \triangleq \hat{\boldsymbol{\nu}} - \boldsymbol{\nu}, \tag{21}$$

where $\hat{\boldsymbol{\eta}}$, $\hat{\boldsymbol{\nu}}$, $\boldsymbol{\eta}$ and $\boldsymbol{\nu}$ represent the estimated pose, estimated velocity, real pose and real velocity, respectively. The ideal prediction error dynamics are chosen to be

$$\dot{\tilde{\boldsymbol{\eta}}}_{ideal} = -\mathbf{L}_1\tilde{\boldsymbol{\eta}}, \quad \dot{\tilde{\boldsymbol{\nu}}}_{ideal} = -\mathbf{L}_2\tilde{\boldsymbol{\nu}},$$

where $\mathbf{L}_1 > 0$ and $\mathbf{L}_2 > 0$, such that their origins are exponentially stable. The convergence rate is decided through the positive definite gain matrices. The state predictor dynamics becomes

$$\dot{\hat{\boldsymbol{\eta}}} = -\mathbf{L}_1\tilde{\boldsymbol{\eta}} + \mathbf{R}\boldsymbol{\nu}, \tag{22}$$

$$\dot{\hat{\boldsymbol{\nu}}} = -\mathbf{L}_2\tilde{\boldsymbol{\nu}} + \mathbf{M}^{-1}(\hat\rho_\delta\boldsymbol{\tau} + \mathbf{R}^\top\hat{\boldsymbol{w}}_\delta - \mathbf{C}\boldsymbol{\nu} - \hat\sigma_\delta\mathbf{D}\boldsymbol{\nu}), \tag{23}$$

where $\hat\sigma_\delta \triangleq \frac{\hat\sigma}{\hat\delta}$, $\hat\rho_\delta \triangleq \frac{\hat\rho}{\hat\delta}$, $\hat{\boldsymbol{w}}_\delta \triangleq \frac{1}{\hat\delta}\hat{\boldsymbol{w}}$, and $\hat\sigma$, $\hat\rho$ and $\hat\delta$ are estimates of the damping, control input and inertia uncertainties. Here, it is assumed that $\hat\delta \in \mathbb{R}^+$. The dynamics of $\hat\sigma_\delta$, $\hat\rho_\delta$ and $\hat{\boldsymbol{w}}_\delta$ must subsequently be designed.

It is desired to design adaptation laws for the uncertainties. The derivation of these laws are based on Lyapunov functions. However, the prediction error dynamics are first defined as

$$\dot{\tilde{\boldsymbol{\eta}}} = -\mathbf{L}_1\tilde{\boldsymbol{\eta}}, \tag{24}$$

$$\dot{\tilde{\boldsymbol{\nu}}} = -\mathbf{L}_2\tilde{\boldsymbol{\nu}} + \mathbf{M}^{-1}(\tilde\rho_\delta\boldsymbol{\tau} + \mathbf{R}^\top\tilde{\boldsymbol{w}}_\delta - \tilde\sigma_\delta\mathbf{D}\boldsymbol{\nu}). \tag{25}$$

Then consider the positive definite CLF

$$\begin{aligned}V_{pred} =& \frac{1}{2}\left(\frac{1}{\gamma_{\rho_\delta}}\tilde\rho_\delta^2 + \frac{1}{\gamma_{\sigma_\delta}}\tilde\sigma_\delta^2 + \frac{1}{\gamma_{w_\delta}}\tilde{\boldsymbol{w}}_\delta{}^\top\tilde{\boldsymbol{w}}_\delta\right)\\ &+ \frac{1}{2}\tilde{\boldsymbol{\nu}}^\top\mathbf{M}\tilde{\boldsymbol{\nu}} + \frac{1}{2}\tilde{\boldsymbol{\eta}}^\top\tilde{\boldsymbol{\eta}}.\end{aligned} \tag{26}$$

Taking the derivative of (26) yields

$$\begin{aligned}\dot V_{pred} =& \frac{1}{\gamma_{\rho_\delta}}\tilde\rho_\delta\dot{\hat\rho}_\delta + \frac{1}{\gamma_{\sigma_\delta}}\tilde\sigma_\delta\dot{\hat\sigma}_\delta + \frac{1}{\gamma_{w_\delta}}\tilde{\boldsymbol{w}}_\delta{}^\top\dot{\hat{\boldsymbol{w}}}_\delta - \tilde{\boldsymbol{\eta}}^\top\mathbf{L}_1\tilde{\boldsymbol{\eta}}\\ &+ \tilde{\boldsymbol{\nu}}^\top(-\mathbf{M}\mathbf{L}_2\tilde{\boldsymbol{\nu}} + \tilde\rho_\delta\boldsymbol{\tau} + \mathbf{R}^\top\tilde{\boldsymbol{w}}_\delta - \tilde\sigma_\delta\mathbf{D}\boldsymbol{\nu})\\ =& \tilde\rho_\delta\left(\frac{1}{\gamma_{\rho_\delta}}\dot{\hat\rho}_\delta + \tilde{\boldsymbol{\nu}}^\top\boldsymbol{\tau}\right) + \tilde\sigma_\delta\left(\frac{1}{\gamma_{\sigma_\delta}}\dot{\hat\sigma}_\delta - \tilde{\boldsymbol{\nu}}^\top\mathbf{D}\boldsymbol{\nu}\right)\\ &+ \tilde{\boldsymbol{w}}_\delta{}^\top\left(\frac{1}{\gamma_{w_\delta}}\dot{\hat{\boldsymbol{w}}}_\delta + \mathbf{R}\tilde{\boldsymbol{\nu}}\right) + \tilde{\boldsymbol{\nu}}^\top(-\mathbf{M}\mathbf{L}_2\tilde{\boldsymbol{\nu}})\\ &- \tilde{\boldsymbol{\eta}}^\top\mathbf{L}_1\tilde{\boldsymbol{\eta}}.\end{aligned} \tag{27}$$

By introducing the following adaptation laws

$$\dot{\hat\rho}_\delta = -\gamma_{\rho_\delta}\tilde{\boldsymbol{\nu}}^\top\boldsymbol{\tau}, \tag{28}$$

$$\dot{\hat\sigma}_\delta = \gamma_{\sigma_\delta}\tilde{\boldsymbol{\nu}}^\top\mathbf{D}\boldsymbol{\nu}, \tag{29}$$

$$\dot{\hat{\boldsymbol{w}}}_\delta = -\gamma_{w_\delta}\mathbf{R}\tilde{\boldsymbol{\nu}}, \tag{30}$$

then (27) becomes

$$\dot V_{pred} = -\tilde{\boldsymbol{\eta}}^\top\mathbf{L}_1\tilde{\boldsymbol{\eta}} - \tilde{\boldsymbol{\nu}}^\top\mathbf{M}\mathbf{L}_2\tilde{\boldsymbol{\nu}} \leq 0, \quad \forall \boldsymbol{\eta}, \boldsymbol{\nu} \neq 0.$$

Control Law
By following Step 1 and 2 in the design procedure of adaptive backstepping, the control law is derived through the following CLF

$$V_{ctrl} = \frac{1}{2}\mathbf{z}_2^\top\mathbf{M}\mathbf{z}_2 + \frac{1}{2}\mathbf{z}_1^\top\mathbf{z}_1, \tag{31}$$

where the derivative is

$$\begin{aligned}\dot V_{ctrl} =& \mathbf{z}_2^\top[\mathbf{z}_1 + \hat\rho_\delta\boldsymbol{\tau} + \mathbf{R}^\top\hat{\boldsymbol{w}}_\delta - \mathbf{C}\boldsymbol{\alpha} - \hat\sigma_\delta\mathbf{D}\boldsymbol{\alpha} - \mathbf{M}\dot{\boldsymbol{\alpha}}]\\ &- \mathbf{z}_1^\top\mathbf{K}_1\mathbf{z}_1 - \mathbf{z}_2^\top\hat\sigma_\delta\mathbf{D}\mathbf{z}_2\end{aligned} \tag{32}$$

and chosen to be

$$\begin{aligned}\hat\rho_\delta\boldsymbol{\tau} =& -\mathbf{R}^\top\hat{\boldsymbol{w}}_\delta + \mathbf{M}\dot{\boldsymbol{\alpha}} + \mathbf{C}\boldsymbol{\alpha} + \hat\sigma_\delta\mathbf{D}\boldsymbol{\alpha}\\ &- \mathbf{z}_1 - \mathbf{K}_2\mathbf{z}_2,\end{aligned} \tag{33}$$

which leads to

$$\dot V_{ctrl} = -\mathbf{z}_1^\top\mathbf{K}_1\mathbf{z}_1 - \mathbf{z}_2^\top\mathbf{K}_2\mathbf{z}_2 \leq 0, \quad \forall \mathbf{z}_1, \mathbf{z}_2 \neq 0. \tag{34}$$

The adaptation of the uncertainties may contain high-frequency signals. To avoid introducing such frequencies into the control input, a lowpass filter is applied to the control signals such that

$$\boldsymbol{\tau}_c = C(s)\boldsymbol{\tau},$$

where

$$C(s) = \frac{\hat\rho_0 k}{s + \hat\rho_0 k}$$

and the gain $k > 0$ represents the design parameter of the lowpass filter, while $\hat{\rho}_0 = \hat{\rho}(0)$ is the initial guess of ρ.

3.3 Adding a Command Governor

The idea of making a virtual command signal seems to have originally been introduced in (Bemporad and Mosca, 1995). Recently, the papers by (Yucelen and Johnson, 2012a) and (Schatz et al., 2013) discuss a novel command governor algorithm to improve both transient and steady state tracking of a reference signal for the model reference adaptive control algorithm. However, the command governor in (Yucelen and Johnson, 2012a) is not directly applicable to nonlinear controllers. Hence, we propose the following dynamics for the command signal $\boldsymbol{\eta}_i$ as

$$\dot{\boldsymbol{\eta}}_i \triangleq \dot{\boldsymbol{\eta}}_d - \mathbf{K}_a(\boldsymbol{\eta} - \boldsymbol{\eta}_i) + \mathbf{K}_b(\boldsymbol{\eta}_d - \boldsymbol{\eta}_i), \tag{35}$$

and

$$\ddot{\boldsymbol{\eta}}_i = \ddot{\boldsymbol{\eta}}_d - \mathbf{K}_a(\dot{\boldsymbol{\eta}} - \dot{\boldsymbol{\eta}}_i) + \mathbf{K}_b(\dot{\boldsymbol{\eta}}_d - \dot{\boldsymbol{\eta}}_i), \tag{36}$$

where $\mathbf{K}_b > \mathbf{K}_a > 0$ and the initial condition of the command governor is $\boldsymbol{\eta}_{i,0} = \boldsymbol{\eta}_0$.

Using the command governor means that

$$\mathbf{z}_1 \triangleq \mathbf{R}^\top(\boldsymbol{\eta} - \boldsymbol{\eta}_i), \tag{37}$$

which means that the vessel tracks an intermediate pose $\boldsymbol{\eta}_i$, which tracks the desired pose $\boldsymbol{\eta}_d$, in order to improve transient control performance.

By choosing the CLF

$$V_0 = \frac{1}{2}\mathbf{z}_0^\top \mathbf{z}_0, \tag{38}$$

where

$$\mathbf{z}_0 = \boldsymbol{\eta}_i - \boldsymbol{\eta}_d, \tag{39}$$

the derivative of V_0 will be

$$\begin{aligned}\dot{V}_0 &= \mathbf{z}_0^\top(-\mathbf{K}_a(\boldsymbol{\eta} - \boldsymbol{\eta}_i) - \mathbf{K}_b(\boldsymbol{\eta}_i - \boldsymbol{\eta}_d))\\ &= \mathbf{z}_0^\top(-\mathbf{K}_a(\boldsymbol{\eta} - \boldsymbol{\eta}_i) - \mathbf{K}_b\mathbf{z}_0)\\ &= \mathbf{z}_0^\top(-\mathbf{K}_a\mathbf{R}\mathbf{z}_1 - \mathbf{K}_b\mathbf{z}_0)\\ &= -\mathbf{z}_0^\top\mathbf{K}_a\mathbf{R}\mathbf{z}_1 - \mathbf{z}_0^\top\mathbf{K}_b\mathbf{z}_0 \end{aligned} \tag{40}$$

To cancel the term $-\mathbf{z}_0^\top\mathbf{K}_a\mathbf{R}\mathbf{z}_1$, the stabilising function $\boldsymbol{\alpha}$ is altered to be

$$\boldsymbol{\alpha} = \mathbf{R}^\top\dot{\boldsymbol{\eta}}_i + \mathbf{R}^\top\mathbf{K}_a\mathbf{z}_0 - \mathbf{K}_1\mathbf{z}_1, \tag{41}$$

which means that

$$\dot{\boldsymbol{\alpha}} = \mathbf{R}^\top\ddot{\boldsymbol{\eta}}_i + \mathbf{S}^\top\mathbf{R}^\top\dot{\boldsymbol{\eta}}_i + \mathbf{R}^\top\mathbf{K}_a\dot{\mathbf{z}}_0 + \mathbf{S}^\top\mathbf{R}^\top\mathbf{K}_a\mathbf{z}_0 - \mathbf{K}_1\dot{\mathbf{z}}_1 \tag{42}$$

Hence, introduction of the command governor does not change the stability of the closed-loop system. A general schematic of the proposed adaptive controller scheme with command governor is displayed in Fig. 1.

4. SIMULATION RESULTS AND PERFORMANCE EVALUATION

This section starts with the structure and parameters of the vessel model, followed by the initial states and control parameters used in the simulations. Subsequently, the metrics used to evaluate the performance are stated. Finally, the results associated with the different controllers are presented and discussed. For simulation purposes, the controllers are implemented in Matlab.

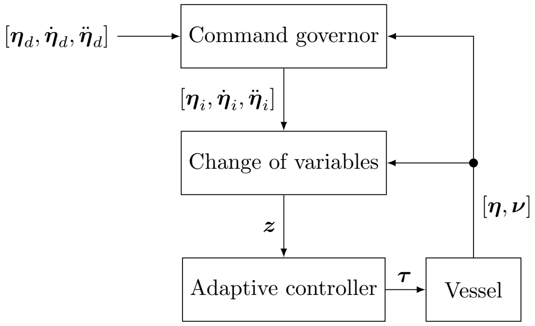

Fig. 1. Schematic of the command governor principle

4.1 Simulation Setup

Vessel Model Parameters

The model ship CyberShip II from (Skjetne et al., 2004) will be used to verify the performance of the proposed adaptive control methods. CyberShip II is a 1:70 scale replica of a supply ship, with a length of $L = 1.255$ (m). It is fully actuated and can maximum produce 2 (N) in surge and sway.

The inertia matrix is given as

$$\mathbf{M}^* \triangleq \mathbf{M}_{RB} + \mathbf{M}_A,$$

where

$$\mathbf{M}_{RB} = \begin{bmatrix} m & 0 & 0 \\ 0 & m & mx_g \\ 0 & mx_g & I_z \end{bmatrix}, \quad \mathbf{M}_A = \begin{bmatrix} -X_{\dot{u}} & 0 & 0 \\ 0 & -Y_{\dot{v}} & -Y_{\dot{r}} \\ 0 & -N_{\dot{v}} & -N_{\dot{r}} \end{bmatrix},$$

and m represent the mass of the ship, while x_g is the distance along the x-axis in the body from the centre of gravity. As displayed in (5), the real Coriolis matrix has the same uncertainty as (4) since

$$\mathbf{C}^*(\boldsymbol{\nu}) \triangleq \mathbf{C}_{RB}(\boldsymbol{\nu}) + \mathbf{C}_A(\boldsymbol{\nu}),$$

with

$$\mathbf{C}_{RB}(\boldsymbol{\nu}) = \begin{bmatrix} 0 & 0 & -m(x_g r + v) \\ 0 & 0 & mu \\ m(x_g r + v) & -mu & 0 \end{bmatrix},$$

$$\mathbf{C}_A(\boldsymbol{\nu}) = \begin{bmatrix} 0 & 0 & c_{13}(\boldsymbol{\nu}) \\ 0 & 0 & c_{23}(\boldsymbol{\nu}) \\ -c_{13}(\boldsymbol{\nu}) & -c_{23}(\boldsymbol{\nu}) & 0 \end{bmatrix},$$

where $c_{13}(\boldsymbol{\nu}) = Y_{\dot{v}}v + \frac{1}{2}(N_{\dot{v}} + Y_{\dot{r}})r$ and $c_{23}(\boldsymbol{\nu}) = -X_{\dot{u}}u$. Finally, the damping matrix $\mathbf{D}^*(\boldsymbol{\nu})$ is given as

$$\mathbf{D}^*(\boldsymbol{\nu}) \triangleq \mathbf{D}_L + \mathbf{D}_{NL}(\boldsymbol{\nu}),$$

where

$$\mathbf{D}_L = \begin{bmatrix} -X_u & 0 & 0 \\ 0 & -Y_v & -Y_r \\ 0 & -N_v & -N_r \end{bmatrix},$$

$$\mathbf{D}_{NL}(\boldsymbol{\nu}) = \begin{bmatrix} -d_{11}(\boldsymbol{\nu}) & 0 & 0 \\ 0 & -d_{22}(\boldsymbol{\nu}) & -d_{23}(\boldsymbol{\nu}) \\ 0 & -d_{32}(\boldsymbol{\nu}) & -d_{33}(\boldsymbol{\nu}) \end{bmatrix},$$

where $d_{11}(\boldsymbol{\nu}) = X_{|u|u}|u| + X_{uuu}u^2$, $d_{22}(\boldsymbol{\nu}) = Y_{|v|v}|v| + Y_{|r|v}|r|$, $d_{23}(\boldsymbol{\nu}) = Y_{|v|r}|v| + Y_{|r|r}|r|$, $d_{32}(\boldsymbol{\nu}) = N_{|v|v}|v| + N_{|r|v}|r|$ and $d_{33}(\boldsymbol{\nu}) = N_{|v|r}|v| + N_{|r|r}|r|$. The parameter values are listed in Table 1.

m	23.8	$X_{\dot{u}}$	-2	$N_{\dot{v}}$	0
I_z	1.760	$Y_{\dot{v}}$	-10	$N_{\dot{r}}$	-1
x_g	0.046	$Y_{\dot{r}}$	0		

X_u	-0.72253	Y_v	-0.88965
$X_{\lvert u \rvert u}$	-1.32742	$Y_{\lvert v \rvert v}$	-36.47287
X_{uuu}	-5.86643	N_v	0.03130
		$N_{\lvert v \rvert v}$	3.95645
$Y_{\lvert r \rvert v}$	-0.805	$N_{\lvert r \rvert v}$	0.130
Y_r	-7.250	N_r	-1.900
$Y_{\lvert v \rvert r}$	-0.845	$Y_{\lvert v \rvert r}$	0.080
$Y_{\lvert r \rvert r}$	-3.450	$N_{\lvert r \rvert r}$	-0.750

Table 1. Parameters for CyberShip II from (Skjetne et al., 2004)

Reference Signal, Initial States and Control Parameters
For a straight-line path, the reference pose $\boldsymbol{\eta}_d(t)$ is derived from

$$\boldsymbol{\eta}_d(t) = \left[x_d(t), y_d(t), \varphi\right]^\top, \tag{43}$$

where

$$\begin{aligned} x_d(t) &= 1 + \omega t \cos(\varphi) \\ \dot{x}_d(t) &= \omega \cos(\varphi) \\ \ddot{x}_d(t) &= 0 \\ \dot{\omega} &= 0, \end{aligned}$$

and

$$\begin{aligned} y_d(t) &= \omega t \sin(\varphi) \\ \dot{y}_d(t) &= \omega \sin(\varphi) \\ \ddot{y}_d(t) &= 0. \end{aligned}$$

It is assumed that the reference target has a constant speed $\omega = 0.15$ (m/s). For the full scale vessel, this corresponds to 1.255 m/s using the Bis scale (Fossen, 2011). It is desired to have a constant orientation of the path relative to the x-axis $\varphi = 0.9273$ (rad), which is equivalent to 53 (deg). The initial condition of the reference signal is chosen to be $\boldsymbol{\eta}_d(0) = [1\ (m), 0\ (m),\ 0.9273\ (rad)]^\top$.

The initial vessel states are chosen to be $\boldsymbol{\eta}_0 = [0.5\ (m), 0\ (m), \pi/4\ (rad)]^\top$ and $\boldsymbol{\nu}_0 = [0\ (m/s), 0\ (m/s), 0\ (rad/s)]^\top$.

The uncertainties for the system are chosen to be $\delta = 2$, $\sigma = 2$, $\rho = 0.7$ and $\boldsymbol{w}^* = [-0.3536\ (N), 0.3536\ (N), 0\ (Nm)]^\top$, which becomes active at $t = 150$ sec. Hence, the disturbance $\boldsymbol{w}^*$ has a magnitude of 0.5 (N) and direction of 135 (deg). The initial values for the estimated uncertainties are $\delta_0 = 1$, $\sigma_0 = 1$, $\rho_0 = 1$ and $\boldsymbol{w}_0 = [0, 0, 0]^\top$.

The adaptive backstepping control parameters are chosen as $\mathbf{K}_1 = diag([0.05,\ 0.05,\ 0.02])$, $\mathbf{K}_2 = diag([5,\ 7,\ 15])$, $\gamma_{\delta_\rho} = \gamma_{\sigma_\rho} = 40$ and $\gamma_{w_\rho} = 6$.

The $\mathcal{L}_1$ adaptive backstepping method has a lowpass filter integrated in the control law to reject high frequency oscillations in the estimation of the uncertainties. Utilising this benefit, the $\mathcal{L}_1$ adaptive backstepping control parameters are chosen as $\mathbf{K}_1 = diag([0.05,\ 0.05,\ 0.02])$, $\mathbf{K}_2 = diag([5,\ 7,\ 15])$, $\mathbf{L}_1 = \mathbf{L}_2 = 100\mathbf{I}$, $k = 100$, $\gamma_{\rho_\delta} = \gamma_{\sigma_\delta} = 40$ and $\gamma_{w_\delta} = 500$. Notice that the $\mathcal{L}_1$ adaptive backstepping method has higher adaptation gains than the adaptive backstepping method.

The command governor uses the gains $\mathbf{K}_a = [0.01,\ 0.01,\ 0.005]$ and $\mathbf{K}_b = [0.05,\ 0.05,\ 0.01]$.

Since it was assumed that there are no magnitude or rate saturations for the control input $\boldsymbol{\tau}^*$, the control parameters and adaptation gains were obtained after iterative tuning.

Performance Metrics
To evaluate and compare the performance of the different control algorithms, performance metrics must be used. These include the integral of the absolute error (IAE), integral of the square of the error (ISE) and integral of the absolute error multiplied by time (ITAE) for the cross-track error. The cross-track error e will be used, which can be calculated by

$$e = -\sin(\psi)(x - x_d) + \cos(\psi)(y - y_d). \tag{44}$$

The formula for the IAE is then given as

$$IAE(e) = \int_0^t |e| dt, \tag{45}$$

which simply describes the temporal evolution of the absolute value of the error without adding any weight to the error. The ISE is defined as

$$ISE(e) = \int_0^t e^2 dt \tag{46}$$

and penalises large errors more than smaller ones, indicating how good the particular algorithm is at eliminating large errors. The calculation of ITAE is given as

$$ITAE(e) = \int_0^t t|e| dt, \tag{47}$$

which penalises errors which have been present for a long time more heavily than those present at the beginning. ITAE will show if there is a stationary error present in the system.

Finally, a new evaluation criterion is proposed, namely the integral of the absolute error multiplied by the energy consumption (IAEW), which can be computed by

$$IAEW(e) = \int_0^t |e| dt \int_0^t P dt, \tag{48}$$

where

$$P = ||\boldsymbol{\nu}^\top \boldsymbol{\tau}|| \tag{49}$$

represents the mechanical power. IAEW thus indicates which control algorithm has the best tracking performance versus energy consumption, in one single metric.

4.2 Results for Straight-line Motion

In the following, AB, AB-CG, L1-AB and L1-AB-CG refer to adaptive backstepping, adaptive backstepping with command governor, $\mathcal{L}_1$ adaptive backstepping and $\mathcal{L}_1$ adaptive backstepping with command governor, respectively.

Fig. 2 displays the desired path and the actual trajectory of the vessel in a North-East plot.

Fig. 3 illustrates the cross-track error of the methods scaled by the vessel length. The results of this figure show that all the methods have good tracking performance both with and without the presence of a disturbance. However, the $\mathcal{L}_1$ adaptive backstepping methods are faster to track the predefined trajectory and compensate for the disturbance, but overshoot the trajectory somewhat.

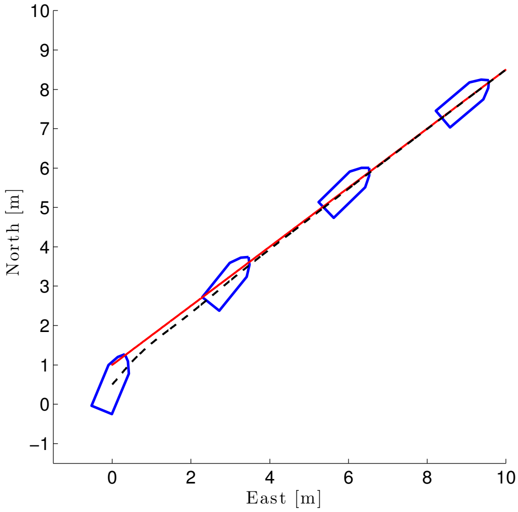

Fig. 2. Vessel tracing the desired straight-line path

A particular reason to why the $\mathcal{L}_1$ adaptive backstepping methods have a faster tracking performance is due to the choice of adaptation gains. The $\mathcal{L}_1$ adaptive backstepping then gets a tracking performance which is similar to the performance of a backstepping implemented to the vessel without the uncertainties and the disturbance.

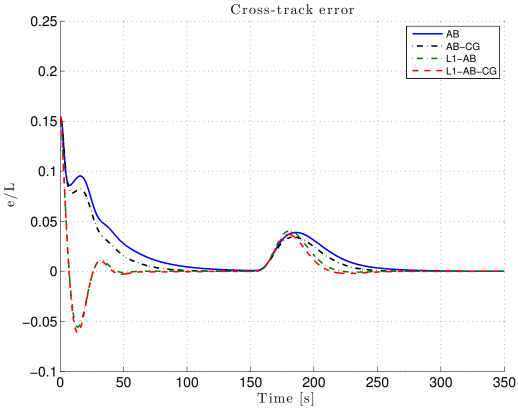

Fig. 3. The cross-track error scaled by the vessel length, in the straight-line motion scenario

The control signals are shown in Fig. 4. From this figure it is not possible to differentiate between the method with and without the command governor. However, there is a small difference between adaptive backstepping control and $\mathcal{L}_1$ adaptive backstepping control at the beginning.

Fig. 5 and 6 display the curves of IAE, ISE, ITAE and IAEW for the cross-track error. Both Fig 5 and 6 indicate that the $\mathcal{L}_1$ adaptive backstepping control methods have a better performance than the adaptive backstepping counterparts. Both IAE and ISE indicate that a command-governor improves the performance when the disturbance is introduced.

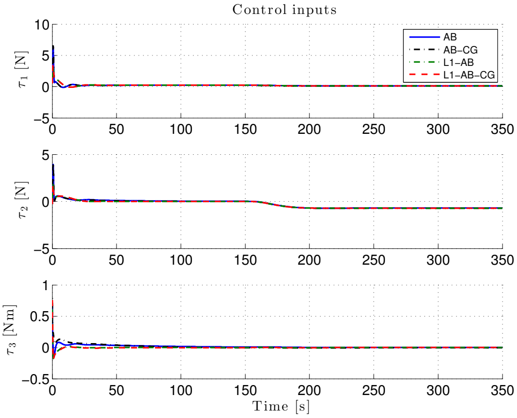

Fig. 4. The control inputs in the straight-line motion scenario

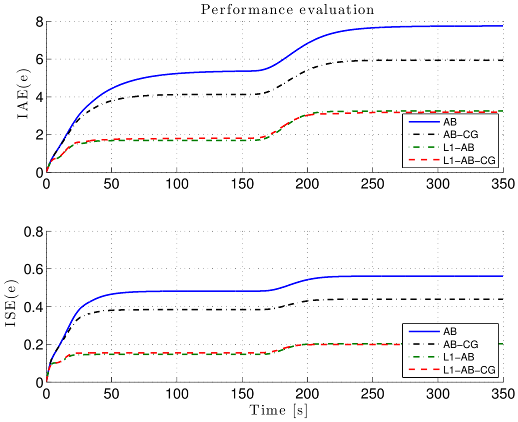

Fig. 5. The IAE and ISE of the cross-track error in the straight-line motion scenario

The ITAE displayed in Fig. 6a indicates that all the methods yield convergence of the cross-track error to zero. The plots of the IAEW illustrate that introducing the command governor improves the tracking performance versus energy consumption when a disturbance is affecting the system.

4.3 Results for Circular Motion

Here, motion control for a circular trajectory is considered. Note that this scenario does not satisfy the assumption about the uncertainty dynamics from Section 2, since the disturbance will get similar dynamics as the manoeuvring vessel.

For the circular motion, the reference pose $\boldsymbol{\eta}_d(t)$ is derived from

$$\boldsymbol{\eta}_p(t) = [x_p(t), y_p(t), \mathrm{atan2}\,(\dot{y}_p(t), \dot{x}_p(t))]^\top,$$

where

$$x_p(t) = r_c \cos\left(\frac{\omega t}{r_c}\right), \quad y_p(t) = r_c \sin\left(\frac{\omega t}{r_c}\right),$$

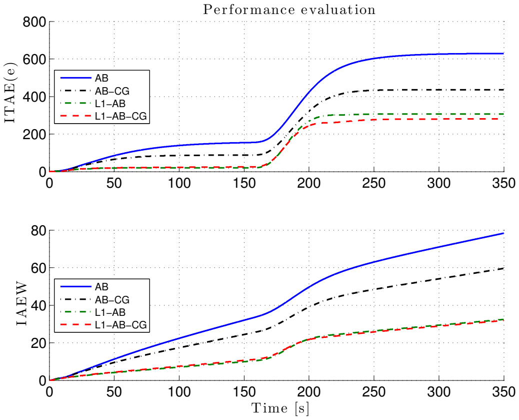

Fig. 6. The ITAE and IAEW of the cross-track error in the straight-line motion scenario

with speed $\omega = 0.15$ (m/s) and circle radius $r_c = 6$ (m). By applying $\boldsymbol{\eta}_p(t)$ to a third-order lowpass filter, we get $\boldsymbol{\eta}_d(t) \in \mathcal{C}^2$. The initial condition of the reference signal is chosen to be $\boldsymbol{\eta}_d(0) = [6\ (m), 0\ (m),\ 1.5708\ (rad)]^\top$, while the initial vessel states are chosen as $\boldsymbol{\eta}_0 = [5.5\ (m), 0\ (m),\ 1.5708\ (rad)]^\top$ and $\boldsymbol{\nu}_0 = [0\ (m/s), 0\ (m/s), 0\ (rad/s)]^\top$. The rest of the parameters are equivalent to those in Section 4.1.

Fig. 7 illustrates the desired and real trajectory of the vessel. The performance metrics are used to evaluate the performance of the different methods. Results are displayed in figures 8-11.

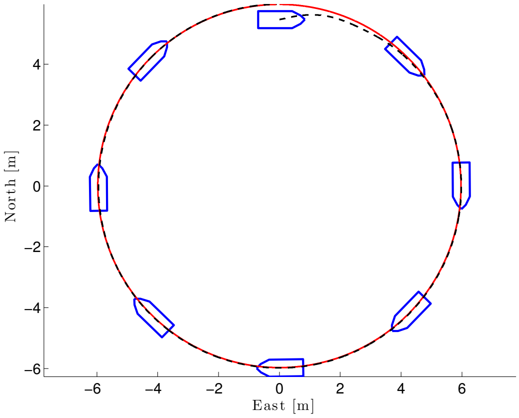

Fig. 7. Vessel tracing the desired circular path

The performance metrics give the same conclusion as they did for straight-line motion, which is that the $\mathcal{L}_1$ adaptive backstepping method is better than the adaptive backstepping methods, and that the transient is improved by combining the adaptive control method with a command governor. The growing ITAE indicates that there is a stationary error in performance of all the controllers, which is because of the assumption about the external disturbance is not satisfied for circular motion.

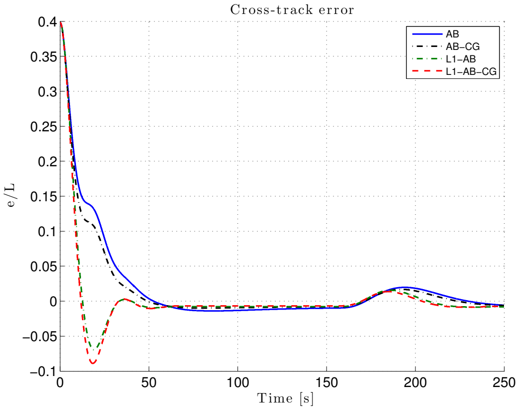

Fig. 8. The cross-track error scaled by the vessel length, in the circular motion scenario

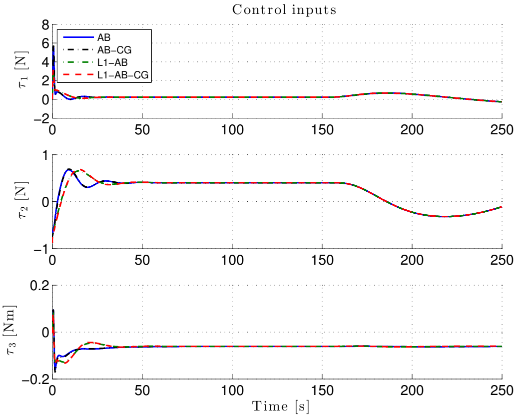

Fig. 9. The control inputs in the circular motion scenario

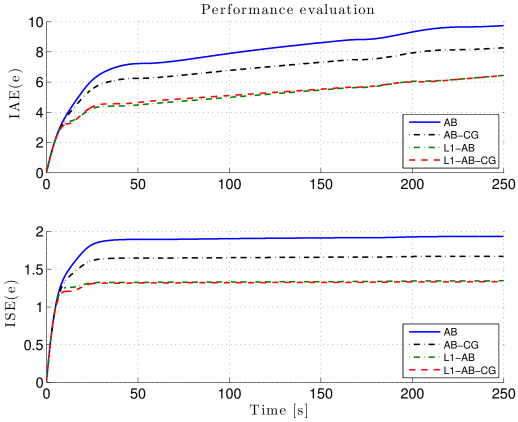

Fig. 10. The IAE and and ISE of the cross-track error in the circular motion scenario

5. CONCLUSION

We have presented the design of four control laws based on adaptive backstepping, $\mathcal{L}_1$ adaptive backstepping and the

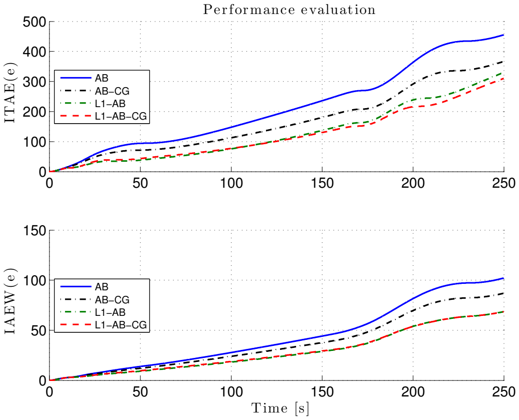

Fig. 11. The ITAE and IAEW of the cross-track error in the circular motion scenario

command governor concept, with the purpose of controlling the motion of a nonlinear 3 DOF model of a marine surface vessel. A comparative analysis of the methods have been made in order to find out which controller has the best performance. The simulation results have shown that all the considered controllers have good tracking performance and ability to compensate for internal and external uncertainties. However, utilising the benefit which $\mathcal{L}_1$ adaptive control gives, we are able to choose higher adaptation rates without encountering the problem of high-frequency oscillations in the control signal and therefore get a better tracking performance than for adaptive backstepping. Through the simulations, we have also observed that by combining an adaptive controller with a command governor, it is possible to improve transient performance.

Future work includes proving stability and robustness of the closed-loop adaptive systems. Additionally, it is desirable to experimentally verify the results by implementing the methods on a model-scale test vessel in a controlled environment.

ACKNOWLEDGEMENTS

This work was supported by the Research Council of Norway through the Centres of Excellence funding scheme, project number 223254.

REFERENCES

Bemporad, A. and Mosca, E. (1995). Nonlinear predictive reference governor for constrained control systems. *Proceedings of 34th IEEE Conference on Decision and Control, New Orleans, USA.*

Breu, D.A. and Fossen, T.I. (2011). $\mathcal{L}_1$ adaptive and extremum seeking control applied to roll parametric resonance in ships. *Proceedings of 9th IEEE International Conference on Control and Automation, Santiago, Chile.*

Fossen, T.I. (2011). *Handbook of Marine Craft Hydrodynamics and Motion Control.* Wiley.

Fossen, T.I. and Strand, J.P. (1999). Tutorial on nonlinear backstepping: Applications to ship control. *Modeling, Identification and Control*, vol. 20 (No. 2), pp. 83–135.

Hovakimyan, N. and Cao, C. (2010). *$\mathcal{L}1$ adaptive control theory: Guaranteed robustness with fast adaptation.* SIAM.

Krstic, M., Kanellakopoulos, I., and Kokotovic, P.V. (1995). *Nonlinear and adaptive control design.* Wiley.

Lee, C.H., Tahk, M.J., and Jun, B.E. (2012). Autopilot design for an agile missile using $\mathcal{L}_1$ adaptive backstepping control. *Proceedings of 28th Congress of the International Council of the Aeronautical Sciences, Brisbane, Australia.*

Patel, V.V., Wise, K.A., Hovakimyan, N., Cao, C., and Lavretsky, E. (2007). $\mathcal{L}_1$ adaptive controller for tailless unstable aircraft in the presence of unknown actuator failures. *Proceedings of AIAA Guidance, Navigation, and Control Conf., Hilton Head, South Carolina, USA.*

Ren, R., Zou, Z., and Wang, X. (2014). $\mathcal{L}_1$ adaptive control used in path following of surface ships. *Proceedings of 33rd Chinese Control Conference, Nanjing, China.*

Schatz, P., Yucelen, T., and Johnson, E.N. (2013). Constrained adaptive control with transient and steady-state performance guarantees. *Proceedings of CEAS EuroGNC, Delft, Netherlands.*

Skjetne, R., Smogeli, Ø.N., and Fossen, T.I. (2004). Nonlinear ship manoeuvering model: Identification and adaptive control with experiments for a model ship. *Modeling, Identification and Control*, vol. 25 (No. 1), pp. 3–27.

Svendsen, C.H., Holck, N.O., Galeazzi, R., and Blanke, M. (2012). $\mathcal{L}_1$ adaptive manoeuvring control of unmanned high-speed water craft. *Proceedings of 9th IFAC Conference on Manoeuvring and Control of Marine Craft, Arenzano, Italy.*

Theisen, L.R.S., Galeazzi, R., and Blanke, M. (2013). Unmanned water craft identification and adaptive control in low-speed and reversing regions. *Proceedings of 9th IFAC Conference on Control Applications in Marine Systems, Osaka, Japan.*

Yucelen, T. and Johnson, E. (2012a). Command governor-based adaptive control. *Proceedings of AIAA Guidance, Navigation, and Control Conference, Minneapolis, USA.*

Yucelen, T. and Johnson, E. (2012b). Design and analysis of a novel command governor architecture for shaping the transient response of nonlinear uncertain dynamical systems. *Proceedings of 51st IEEE Conference on Decision and Control, Maui, USA.*

A.4 Comparing Combinations of Linear and Nonlinear Feedback Terms for Motion Control of Marine Surface Vessels

M. E. N. Sørensen and M. Breivik, Comparing combinations of linear and nonlinear feedback terms for motion control of marine surface vessels, *in Proceedings of the 10th IFAC Conference on Control Applications in Marine Systems, Trondheim, Norway*, 2016.

Comparing Combinations of Linear and Nonlinear Feedback Terms for Motion Control of Marine Surface Vessels

Mikkel Eske Nørgaard Sørensen* **Morten Breivik***

** Centre for Autonomous Marine Operations and Systems, Department of Engineering Cybernetics, Norwegian University of Science and Technology (NTNU), NO-7491 Trondheim, Norway*
E-mail: mikkel.sorensen@itk.ntnu.no, morten.breivik@ieee.org

Abstract: Nonlinear control algorithms are often designed with linear feedback terms. Such linear feedback typically gives rise to nice exponential stability properties, but are not physically realistic since all actuators have magnitude constraints. One way to address such constraints can be to introduce nonlinear feedback terms. Hence, this paper investigates combinations of linear and nonlinear feedback terms for pose and velocity control of marine surface vessels. Three cascaded controllers are developed and compared through three simulation scenarios and one model-scale experiment. The comparisons are made using performance metrics which consider both control accuracy and energy use.

Keywords: Marine surface vessel, Cascaded control, Nonlinear feedback control, Target tracking, Constant bearing guidance, Performance metrics

1. INTRODUCTION

Automatic motion control of marine surface vessels has been a research topic since the early 20th century. In recent years, the research has expanded from control of manned vessels to also include unmanned vessels. However, many motion control algorithms found in the literature do not inherently consider physical saturation constraints for the actuators. For example, the nonlinear control algorithms in (Fossen and Strand, 1999),(Fossen, 2000), (Refsnes et al., 2008), (Fossen, 2011) and (Chen et al., 2013) are all designed with linear feedback terms.

This paper therefore investigates combinations of linear and nonlinear feedback terms for pose and velocity control of marine surface vessels. In particular, the nonlinear feedback terms are developed based on constant bearing (CB) guidance principles, inspired by the guided dynamic positioning approach originally suggested in (Breivik et al., 2006). Further inspiration has been found in (Breivik and Fossen, 2007) on the concept of guided motion control, as well as in (Breivik and Fossen, 2009). Also, the concept of CB guided motion control was employed in (Breivik and Loberg, 2011) for a virtual target-based underway docking control system, achieving docking of an unmanned surface vehicle with a mother ship moving in transit at sea. Similarly, a CB guided heading controller was designed in (Skejic et al., 2011) in order to maneuver a ship around a floating object in deep and calm water under the influence of a uniform current.

Specifically, three cascaded controllers are developed in the paper, where the feedback connection between pose and velocity which is traditionally found in backstepping control design has been removed. The controllers respectively employ linear feedback for both the pose and velocity control errors (LP-LV), nonlinear feedback for the pose control error and linear feedback for the velocity control error (NP-LV), as well as nonlinear feedback for both the pose and velocity control errors (NP-NV). The performance of the controllers are compared through three simulation scenarios and one model-scale experiment, where the comparisons are made using performance metrics which consider both control accuracy and energy use.

The structure of the paper is as follows: A mathematical vessel model and assumptions are presented in Section 2; Section 3 presents the design of three different cascaded control laws inspired by backstepping and CB guidance; Section 4 includes simulation results, experimental results and a performance evaluation; while Section 5 concludes the paper.

2. MARINE SURFACE VESSEL MODEL

The motion of a surface vessel can be represented by the pose vector $\boldsymbol{\eta} = [x, y, \psi]^\top \in \mathbb{R}^2 \times \mathbb{S}$ and the velocity vector $\boldsymbol{\nu} = [u, v, r]^\top \in \mathbb{R}^3$, where $\mathbb{S} \in [-\pi, \pi]$. Here, (x, y) represents the Cartesian position in the local earth-fixed reference frame, ψ is the yaw angle, (u, v) represents the body-fixed linear velocities and r is the yaw rate. The 3 degrees-of-freedom dynamics of a surface vessel can then be stated as (Fossen, 2011):

$$\dot{\boldsymbol{\eta}} = \mathbf{R}(\psi)\boldsymbol{\nu} \tag{1}$$

$$\boldsymbol{M}\dot{\boldsymbol{\nu}} + \boldsymbol{C}(\boldsymbol{\nu})\boldsymbol{\nu} + \boldsymbol{D}(\boldsymbol{\nu})\boldsymbol{\nu} = \boldsymbol{\tau}, \tag{2}$$

where

$$\mathbf{R}(\psi) = \begin{bmatrix} \cos(\psi) & -\sin(\psi) & 0 \\ \sin(\psi) & \cos(\psi) & 0 \\ 0 & 0 & 1 \end{bmatrix} \tag{3}$$

is a rotation matrix $\mathbf{R} \in SO(3)$, and where $\mathbf{M}$, $\boldsymbol{C(\nu)}$, $\boldsymbol{D(\nu)}$ and $\boldsymbol{\tau}$ represent the inertia matrix, Coriolis and centripetal matrix, damping matrix and control input vector, respectively. Here, the system matrices are assumed to satisfy the properties $\mathbf{M} = \mathbf{M}^\top > 0$, $\mathbf{C}(\boldsymbol{\nu}) = -\mathbf{C}(\boldsymbol{\nu})^\top$ and $\mathbf{D}(\boldsymbol{\nu}) > 0$.

Since this paper focuses on fundamental motion control aspects, it is assumed that both the pose vector $\boldsymbol{\eta}$ and velocity vector $\boldsymbol{\nu}$ can be measured, and that no disturbances and uncertainties are affecting the system. Such assumptions will be relaxed and investigated elsewhere.

3. FEEDBACK CONTROL DESIGN

The control objective is to make $\tilde{\boldsymbol{\eta}}(t) \triangleq \boldsymbol{\eta}(t) - \boldsymbol{\eta}_t(t) \rightarrow \mathbf{0}$ as $t \rightarrow \infty$, where $\boldsymbol{\eta}_t(t) = [x_t(t), y_t(t), \psi_t(t)]^\top \in \mathbb{R}^2 \times \mathbb{S}$ represents the pose associated with a target point which is $\mathcal{C}^2$ and bounded. The motion of the target is typically defined by a human or generated by a guidance system.

The control design is divided into two stages, including definition of new state variables and deriving the control laws through control Lyapunov functions (CLFs). The design is similar to the backstepping method, which has been applied in e.g. (Fossen and Strand, 1999) and (Sørensen and Breivik, 2015), but omits the coupling between the pose and velocity control loops, resulting in a cascade system. This cascade system represents a classical inner-outer loop guidance and control structure, where the outer loop handles the kinematics and the inner loop handles the vessel kinetics. The total system can then be analysed by cascade theory (Lamnabhi-Lagarrigue et al., 2005).

In particular, it is desirable to investigate the effect of using nonlinear feedback terms, inspired by CB guidance (Breivik and Fossen, 2009), compared to standard linear feedback terms. Consequently, we investigate three combinations of linear and nonlinear feedback terms.

For notational simplicity, the time t is omitted in the rest of this section.

3.1 Linear Pose and Velocity Feedbacks

Start by defining the error variables $\mathbf{z}_1$ and $\mathbf{z}_2$:

$$\mathbf{z}_1 \triangleq \mathbf{R}^\top(\psi)(\boldsymbol{\eta} - \boldsymbol{\eta}_t) \tag{4}$$

$$\mathbf{z}_2 \triangleq \boldsymbol{\nu} - \boldsymbol{\alpha}, \tag{5}$$

where $\boldsymbol{\alpha} \in \mathbb{R}^3$ is a vector of stabilising functions, which can be interpreted as a desired velocity and which is to be designed later.

Kinematic Control
Choosing the positive definite CLF

$$V_1 \triangleq \frac{1}{2}\mathbf{z}_1^\top \mathbf{z}_1, \tag{6}$$

the derivative of V_1 with respect to time along the $\mathbf{z}_1$-dynamics gives

$$\begin{aligned} \dot{V}_1 &= \mathbf{z}_1^\top \dot{\mathbf{z}}_1 \\ &= \mathbf{z}_1^\top(\mathbf{S}(r)^\top \mathbf{R}^\top(\psi)(\boldsymbol{\eta} - \boldsymbol{\eta}_t) + \mathbf{R}^\top(\psi)(\dot{\boldsymbol{\eta}} - \dot{\boldsymbol{\eta}}_t)) \\ &= \mathbf{z}_1^\top(\mathbf{S}(r)^\top \mathbf{z}_1 + \mathbf{R}^\top(\psi)(\dot{\boldsymbol{\eta}} - \dot{\boldsymbol{\eta}}_t)), \end{aligned} \tag{7}$$

where

$$\mathbf{S}(r) = \begin{bmatrix} 0 & -r & 0 \\ r & 0 & 0 \\ 0 & 0 & 0 \end{bmatrix} \tag{8}$$

is a skew-symmetric matrix satisfying $\mathbf{z}_1^\top \mathbf{S}(r)^\top \mathbf{z}_1 = 0$, which gives

$$\dot{V}_1 = \mathbf{z}_1^\top(\boldsymbol{\nu} - \mathbf{R}^\top(\psi)\dot{\boldsymbol{\eta}}_t). \tag{9}$$

Using (5), the CLF becomes

$$\begin{aligned} \dot{V}_1 &= \mathbf{z}_1^\top(\mathbf{z}_2 + \boldsymbol{\alpha} - \mathbf{R}^\top(\psi)\dot{\boldsymbol{\eta}}_t) \\ &= \mathbf{z}_1^\top \mathbf{z}_2 + \mathbf{z}_1^\top(\boldsymbol{\alpha} - \mathbf{R}^\top(\psi)\dot{\boldsymbol{\eta}}_t), \end{aligned} \tag{10}$$

where the stabilising function can be chosen as

$$\boldsymbol{\alpha} = \mathbf{R}^\top(\psi)\dot{\boldsymbol{\eta}}_t - \mathbf{K}_1 \mathbf{z}_1 \tag{11}$$

with $\mathbf{K}_1 > 0$, which results in

$$\dot{V}_1 = -\mathbf{z}_1^\top \mathbf{K}_1 \mathbf{z}_1 + \mathbf{z}_1^\top \mathbf{z}_2. \tag{12}$$

It can be concluded that the origin of $\mathbf{z}_1$ is uniformly globally exponentially stable (UGES) when seeing $\mathbf{z}_2$ as an input with $\mathbf{z}_2 = \mathbf{0}$. Consequently, it can be concluded by Lemma 4.6 from (Khalil, 2002) that the subsystem

$$\dot{\mathbf{z}}_1 = \mathbf{S}(r)^\top \mathbf{z}_1 - \mathbf{K}_1 \mathbf{z}_1 + \mathbf{z}_2 \tag{13}$$

is input-to-state stable (ISS). Note that (12) shows that $\mathbf{S}(r)$ in (13) does not affect the ISS property.

Kinetic Control
The $\mathbf{z}_2$-dynamics can be written as

$$\begin{aligned} \mathbf{M}\dot{\mathbf{z}}_2 =& \mathbf{M}(\dot{\boldsymbol{\nu}} - \dot{\boldsymbol{\alpha}}) \\ =& \boldsymbol{\tau} - \mathbf{C}(\boldsymbol{\nu})\boldsymbol{\nu} - \mathbf{D}(\boldsymbol{\nu})\boldsymbol{\nu} - \mathbf{M}\dot{\boldsymbol{\alpha}}, \end{aligned} \tag{14}$$

where the time derivative of (11) becomes

$$\dot{\boldsymbol{\alpha}} = \mathbf{R}^\top(\psi)\ddot{\boldsymbol{\eta}}_t + \mathbf{S}(r)^\top \mathbf{R}^\top(\psi)\dot{\boldsymbol{\eta}}_t - \mathbf{K}_1 \dot{\mathbf{z}}_1 \tag{15}$$

where $\boldsymbol{\eta}_t$ is the pose of the target point and $\dot{\mathbf{z}}_1$ given by (13). The CLF for $\mathbf{z}_2$ is then defined as

$$V_2 \triangleq \frac{1}{2}\mathbf{z}_2^\top \mathbf{M}\mathbf{z}_2. \tag{16}$$

Simplifying $\mathbf{C}(\boldsymbol{\nu}) = \mathbf{C}$, $\mathbf{D}(\boldsymbol{\nu}) = \mathbf{D}$, $\mathbf{R}(\psi) = \mathbf{R}$ and $\mathbf{S}(r) = \mathbf{S}$ for notational brevity, the derivative of (16) becomes

$$\begin{aligned} \dot{V}_2 =& \mathbf{z}_2^\top \mathbf{M}\dot{\mathbf{z}}_2 \\ =& \mathbf{z}_2^\top(\boldsymbol{\tau} - \mathbf{C}\boldsymbol{\nu} - \mathbf{D}\boldsymbol{\nu} - \mathbf{M}\dot{\boldsymbol{\alpha}}). \end{aligned} \tag{17}$$

The control input can be chosen as

$$\boldsymbol{\tau} = \mathbf{M}\dot{\boldsymbol{\alpha}} + \mathbf{C}\boldsymbol{\nu} + \mathbf{D}\boldsymbol{\nu} - \mathbf{K}_2 \mathbf{z}_2, \tag{18}$$

where $\mathbf{K}_2 > 0$, which results in

$$\dot{V}_2 = -\mathbf{z}_2^\top \mathbf{K}_2 \mathbf{z}_2 < 0, \tag{19}$$

which makes the origin of the $\mathbf{z}_2$-dynamics

$$\dot{\mathbf{z}}_2 = -\mathbf{M}^{-1}\mathbf{K}_2 \mathbf{z}_2 \tag{20}$$

UGES.

It should be noted that it is possible to choose $\boldsymbol{\tau}$ in (18) as e.g.

$$\boldsymbol{\tau} = \mathbf{M}\dot{\boldsymbol{\alpha}} + \mathbf{C}\boldsymbol{\alpha} + \mathbf{D}\boldsymbol{\alpha} - \mathbf{K}_2 \mathbf{z}_2, \tag{21}$$

but this choice is not desirable since it changes (20) to

$$\dot{\mathbf{z}}_2 = -\mathbf{M}^{-1}(\mathbf{C}+\mathbf{D}+\mathbf{K}_2)\mathbf{z}_2, \tag{22}$$

where the convergence rate of the $\mathbf{z}_2$-dynamics becomes influenced by the vessel $\mathbf{C}$ and $\mathbf{D}$ matrices.

Stability Analysis

The total closed-loop dynamics become

$$\dot{\mathbf{z}}_1 = \mathbf{S}^\top\mathbf{z}_1 - \mathbf{K}_1\mathbf{z}_1 + \mathbf{z}_2 \tag{23}$$

$$\dot{\mathbf{z}}_2 = -\mathbf{M}^{-1}\mathbf{K}_2\mathbf{z}_2. \tag{24}$$

Since the origins of both subsystems are UGES if the $\mathbf{z}_1$-dynamics in (23) is unperturbed ($\mathbf{z}_2 = \mathbf{0}$), and the kinematic control loop has linear growth in the perturbation term $\mathbf{z}_2$, all the conditions of Theorem 2.1 and Proposition 2.3 from (Lamnabhi-Lagarrigue et al., 2005) are satisfied, and therefore the origin of the overall system $(\mathbf{z}_1, \mathbf{z}_2) = (\mathbf{0}, \mathbf{0})$ is UGES.

3.2 Nonlinear Pose Feedback and Linear Velocity Feedback

We now introduce nonlinear pose feedback inspired by constant bearing (CB) guidance, which was originally used for vessel control in (Breivik et al., 2006). CB guidance is a so-called two-point guidance scheme developed for interceptor missiles, where the interceptor is supposed to align the relative interceptor-target velocity along the line-of-sight (LOS) vector between the interceptor and the target.

The most common method of implementing CB guidance is to make the rotation rate of the interceptor velocity directly proportional to the rotation rate of the interceptor-target LOS, which is widely known as proportional navigation. However, CB guidance can also be implemented through the direct velocity assignment

$$\mathbf{v}_d = \mathbf{v}_t - \boldsymbol{\kappa}\frac{\tilde{\mathbf{p}}}{||\tilde{\mathbf{p}}||}, \tag{25}$$

where $\mathbf{v}_t \in \mathbb{R}^2$ is the target velocity and

$$\tilde{\mathbf{p}} \stackrel{\triangle}{=} \mathbf{p} - \mathbf{p}_t \tag{26}$$

is the LOS vector between the interceptor position $\mathbf{p} = [x, y]^\top$ and the target position $\mathbf{p}_t = [x_t, y_t]^\top$, such that

$$||\tilde{\mathbf{p}}|| \stackrel{\triangle}{=} \sqrt{\tilde{\mathbf{p}}^\top\tilde{\mathbf{p}}} \geq 0, \tag{27}$$

is the Euclidean length of $\tilde{\mathbf{p}}$. Additionally, $\boldsymbol{\kappa} \geq 0$, which can be chosen as

$$\boldsymbol{\kappa} = U_{a,max}\frac{||\tilde{\mathbf{p}}||}{\sqrt{\tilde{\mathbf{p}}^\top\tilde{\mathbf{p}} + \Delta_{\tilde{p}}^2}}, \tag{28}$$

where $U_{a,max} > 0$ represents the maximum approach speed toward the target and $\Delta_{\tilde{p}} > 0$ is a tuning parameter which affects the transient convergence behavior between the interceptor and target. The concept of using such nonlinear feedback is shown in Fig. 1.

By introducing nonlinear feedback based on CB guidance to the controller, the stabilising function can now be chosen as

$$\boldsymbol{\alpha} = \mathbf{R}^\top\dot{\boldsymbol{\eta}}_t - \mathbf{K}_1(\mathbf{z}_1, \Delta_i)\mathbf{z}_1, \tag{29}$$

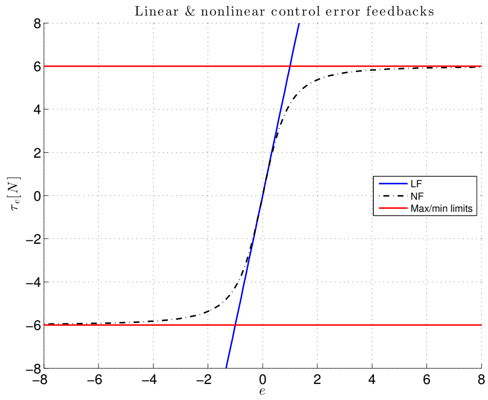

Fig. 1. LF is a linear feedback term as a function of the control error e, while NF is a nonlinear feedback term based on a sigmoid function of e

where

$$\mathbf{K}_1(\mathbf{z}_1, \Delta_i) = \mathbf{K}_1 \begin{bmatrix} \frac{1}{\sqrt{\mathbf{z}_{1,\tilde{p}}^\top\mathbf{z}_{1,\tilde{p}} + \Delta_{\tilde{p}}^2}}\mathbf{I}_{2\times2} & \mathbf{0}_{2\times1} \\ \mathbf{0}_{1\times2} & \frac{1}{\sqrt{z_{1,\tilde{\psi}}^2 + \Delta_{\tilde{\psi}}^2}} \end{bmatrix} \tag{30}$$

and $\mathbf{K}_1 > 0$ as before, $\mathbf{z}_{1,\tilde{p}} \stackrel{\triangle}{=} [z_{1,1}, z_{1,2}]^\top$, $z_{1,\tilde{\psi}} \stackrel{\triangle}{=} z_{1,3}$, $\Delta_{\tilde{p}} > 0$ and $\Delta_{\tilde{\psi}} > 0$. However, it is also possible to choose

$$\mathbf{K}_1(\mathbf{z}_1, \Delta_i) = \mathbf{K}_1\left[\frac{1}{\sqrt{\mathbf{z}_1^\top\mathbf{z}_1 + \Delta^2}}\mathbf{I}_{3\times3}\right], \tag{31}$$

if $\Delta_{\tilde{p}} = \Delta_{\tilde{\psi}} = \Delta > 0$, but then it is not possible to define a different transient behavior for the position and heading.

Choosing (30) leads to

$$\dot{\boldsymbol{\alpha}} = \mathbf{R}^\top\ddot{\boldsymbol{\eta}}_t + \mathbf{S}^\top\mathbf{R}^\top\dot{\boldsymbol{\eta}}_t - \dot{\mathbf{K}}_1(\mathbf{z}_1, \Delta_i)\mathbf{z}_1 - \mathbf{K}_1(\mathbf{z}_1, \Delta_i)\dot{\mathbf{z}}_1, \tag{32}$$

where

$$\dot{\mathbf{K}}_1(\mathbf{z}_1, \Delta_i) = -\mathbf{K}_1 \begin{bmatrix} \frac{\mathbf{z}_{1,\tilde{p}}^\top\dot{\mathbf{z}}_{1,\tilde{p}}\mathbf{I}_{2\times2}}{(\mathbf{z}_{1,\tilde{p}}^\top\mathbf{z}_{1,\tilde{p}} + \Delta_{\tilde{p}}^2)^{\frac{3}{2}}} & \mathbf{0}_{2\times1} \\ \mathbf{0}_{1\times2} & \frac{z_{1,\tilde{\psi}}\dot{z}_{1,\tilde{\psi}}}{(z_{1,\tilde{\psi}}^2 + \Delta_{\tilde{\psi}}^2)^{\frac{3}{2}}} \end{bmatrix}. \tag{33}$$

Stability Analysis

The total closed-loop dynamics now changes to

$$\dot{\mathbf{z}}_1 = \mathbf{S}^\top\mathbf{z}_1 - \mathbf{K}_1(\mathbf{z}_1, \Delta_i)\mathbf{z}_1 + \mathbf{z}_2 \tag{34}$$

$$\dot{\mathbf{z}}_2 = -\mathbf{M}^{-1}\mathbf{K}_2\mathbf{z}_2. \tag{35}$$

Here, we can see that

$$||\mathbf{z}_1|| \gg 1 \Rightarrow \dot{\mathbf{z}}_1 = \mathbf{S}^\top\mathbf{z}_1 - \mathbf{K}_1\mathrm{sign}(\mathbf{z}_1) + \mathbf{z}_2 \tag{36}$$

and

$$||\mathbf{z}_1|| \approx 0 \Rightarrow \dot{\mathbf{z}}_1 = \mathbf{S}^\top\mathbf{z}_1 - \mathbf{K}_1 \begin{bmatrix} \frac{1}{\Delta_{\tilde{p}}}\mathbf{I}_{2\times2} & \mathbf{0}_{2\times1} \\ \mathbf{0}_{1\times2} & \frac{1}{\Delta_{\tilde{\psi}}} \end{bmatrix} \mathbf{z}_1 + \mathbf{z}_2. \tag{37}$$

Hence, by introducing nonlinear pose feedback, the stability of the origin of the unperturbed $\mathbf{z}_1$ subsystem is changed to uniform semiglobal exponential stability (USGES), since the values Δ_i in (30) can be chosen arbitrarily large, see also Theorem 1 in (Fossen and Pettersen, 2014). This also changes the stability of the origin of the total system to USGES.

3.3 Nonlinear Pose and Velocity Feedbacks

We now also introduce nonlinear velocity feedback, which changes the control law (18) to

$$\boldsymbol{\tau} = \mathbf{M}\dot{\boldsymbol{\alpha}} + \mathbf{C}\boldsymbol{\nu} + \mathbf{D}\boldsymbol{\nu} - \mathbf{K}_2(\mathbf{z}_2, \Delta_i)\mathbf{z}_2, \tag{38}$$

where

$$\mathbf{K}_2(\mathbf{z}_2, \Delta_i) = \mathbf{K}_2 \begin{bmatrix} \frac{1}{\sqrt{\mathbf{z}_{2,\tilde{v}}^\top \mathbf{z}_{2,\tilde{v}} + \Delta_{\tilde{v}}^2}} \mathbf{I}_{2\times 2} & \mathbf{0}_{2\times 1} \\ \mathbf{0}_{1\times 2} & \frac{1}{\sqrt{z_{2,\tilde{r}}^2 + \Delta_{\tilde{r}}^2}} \end{bmatrix} \tag{39}$$

with $\mathbf{K}_2 > 0$ as before, and where $\mathbf{z}_{2,\tilde{v}}$ and $z_{2,\tilde{r}}$ are defined as $\mathbf{z}_{2,\tilde{v}} \triangleq [z_{2,1}, z_{2,2}]^\top$, $z_{2,\tilde{r}} \triangleq z_{2,3}$, $\Delta_{\tilde{v}} > 0$ and $\Delta_{\tilde{r}} > 0$.

Stability Analysis
The total closed-loop dynamics become

$$\dot{\mathbf{z}}_1 = \mathbf{S}^\top \mathbf{z}_1 - \mathbf{K}_1(\mathbf{z}_1, \Delta_i)\mathbf{z}_1 + \mathbf{z}_2 \tag{40}$$

$$\dot{\mathbf{z}}_2 = -\mathbf{M}^{-1}\mathbf{K}_2(\mathbf{z}_2, \Delta_i)\mathbf{z}_2. \tag{41}$$

The stability of the origin of the $\mathbf{z}_2$ subsystem is now also changed to USGES, and utilizing Theorem 2.1 and Proposition 2.3 from (Lamnabhi-Lagarrigue et al., 2005), it can be concluded that the origin of the total system is USGES.

4. SIMULATION AND EXPERIMENTAL RESULTS

The model-scale ship Cybership Enterprise I, with parameters from (Sandved, 2015), will be used to test the performance of the proposed motion controllers through both numerical simulations in Matlab and model-scale experiments in an ocean basin. Cybership Enterprise I is a 1:70 scale replica of a supply ship, with a length of $L = 1.105$ (m). It is fully actuated with two Voith-Schneider propellers aft and one bow thruster. We have limited the output of the actuators such that they can only produce a maximum of 2.0 (N) in surge and sway and 1.5 (Nm) in yaw. Hence, the commanded control input with saturation $\boldsymbol{\tau}_s$ is bounded as follows

$$\tau_{s,i}(\tau_i) = \begin{cases} \tau_{i,min} & \text{if } \tau_i \leq \tau_{i,min} \\ \tau_i & \text{if } \tau_{i,min} < \tau_i < \tau_{i,max} \\ \tau_{i,max} & \text{if } \tau_i \geq \tau_{i,max} \end{cases}, \quad \forall i \in \{1, 2, 3\} \tag{42}$$

where $\boldsymbol{\tau}$ is the commanded control input without saturation, such as in (18) and (38), while $\boldsymbol{\tau}_{min} = [\tau_{1,min},\ \tau_{2,min},\ \tau_{3,min}]^\top$ with negative and bounded elements and $\boldsymbol{\tau}_{max} = [\tau_{1,max},\ \tau_{2,max},\ \tau_{3,max}]^\top$ with positive and bounded elements, which represent the magnitude saturation limits. Details about the ship are given in (Sandved, 2015). The experiment is conducted in the Marine Cybernetics Laboratory (MCLab) at NTNU, where it is possible to get accurate pose measurement through a Qualisys motion capture system.

In this section, the abbreviation LP-LV refers to linear feedback for both the pose and velocity control errors, NP-LV refers to nonlinear feedback for the pose control error and linear feedback for the velocity control error, while NP-NV refers to nonlinear feedback for both the pose and velocity control errors.

Performance Metrics
To evaluate and compare the performance of the different controllers, some performance metrics must be used.
For this, we will use the norm of the pose error e, which can be calculated by

$$e(t) \triangleq \sqrt{\tilde{\boldsymbol{\eta}}(t)^\top \tilde{\boldsymbol{\eta}}(t)}. \tag{43}$$

The performance metric IAE (integral of the absolute error) is then

$$IAE(t) \triangleq \int_0^t |e(\tau)| d\tau, \tag{44}$$

which simply integrates the temporal evolution of the absolute value of the error without adding any weight to the error. We will also use the integral of the absolute error multiplied by the energy consumption (IAEW), which was proposed earlier in (Sørensen and Breivik, 2015). The IAEW can be computed as

$$IAEW(t) \triangleq \int_0^t |e(\tau)| d\tau \int_0^t P(\tau) d\tau, \tag{45}$$

where

$$P(t) = |\boldsymbol{\nu}(t)^\top \boldsymbol{\tau}(t)| \tag{46}$$

represents the mechanical power. IAEW thus indicates which controller has the best combined control accuracy and energy use through one single metric.

4.1 Simulation Results for Straight-Line Motion Control

For a straight-line target motion, the target pose $\boldsymbol{\eta}_t(t)$ is derived from

$$\boldsymbol{\eta}_t(t) = [x_t(t), y_t(t), \psi_t]^\top, \tag{47}$$

where

$$x_t(t) = 1 + v_t t \cos(\psi_t) \tag{48}$$

$$\dot{x}_t(t) = v_t \cos(\psi_t), \tag{49}$$

and

$$y_t(t) = v_t t \sin(\psi_t) \tag{50}$$

$$\dot{y}_t(t) = v_t \sin(\psi_t), \tag{51}$$

where ψ_t is a constant.

The reference target has a constant speed $v_t = 0.15$ (m/s) and $\dot{v}_t = 0$. Hence, the acceleration of the target point is $\ddot{x}_t(t) = 0$ and $\ddot{y}_t(t) = 0$. For the full-scale vessel, this corresponds to 1.275 m/s using the Bis scale (Fossen, 2011). Also, the straight-line trajectory has a constant orientation relative to the x-axis $\psi_t = 0.9273$ (rad), which is equivalent to 53 (deg).

The initial condition of the target pose is chosen to be $\boldsymbol{\eta}_t(0) = [1\ (m), 0\ (m),\ 0.9273\ (rad)]^\top$ and $\dot{\boldsymbol{\eta}}_t(0) = [0.09$

$(m/s), 0.12\ (m/s), 0\ (rad/s)]^\top$.

In the following, we consider three simulation scenarios to compare and evaluate the different controllers.

Scenario 1: Non-Saturated Control Inputs
The initial vessel states are chosen to be $\boldsymbol{\eta}(0) = [0.5\ (m), 0\ (m), \pi/8\ (rad)]^\top$ and $\boldsymbol{\nu}(0) = [0\ (m/s), 0\ (m/s), 0\ (rad/s)]^\top$, which leads to $||\mathbf{z}_1(0)|| = 0.7320$, $||\mathbf{z}_2(0)|| = 0.1961$ for LP-LV and $||\mathbf{z}_2(0)|| = 0.2262$ for NP-LV and NP-NV. Notice that $\boldsymbol{\alpha}$ is changed when nonlinear feedback terms are introduced, which also affects $||\mathbf{z}_2(0)||$. The normed pose error starts at $e(0) = 0.7320$. The constant gain matrices $\mathbf{K}_1$ and $\mathbf{K}_2$ are chosen such that the LP-LV controller does not saturate, and hence neither the NP-LV nor NP-NV controllers, see Table 1.

	LP-LV	**NP-LV**	**NP-NV**
$\mathbf{K}_1$	$diag([0.13, 0.13, 0.01])$	$-\|\|-$	$-\|\|-$
$\mathbf{K}_2$	$diag([7, 8, 6])$	$-\|\|-$	$-\|\|-$
$\Delta_{\tilde{p},\tilde{\psi}}$	-	[0.4 , 0.2]	[0.4 , 0.2]
$\Delta_{\tilde{v},\tilde{r}}$	-	-	[0.97 , 0.2]

Table 1. Control gains for scenarios 1 and 2

In Fig. 2, the vessel and target pose outlines are plotted to show the transient convergence behavior. Here, the blue outline represents the LP-LV-controlled vessel, the dash-dotted black outline represents the NP-LV-controlled vessel, the dashed green outline represents the NP-NV-controlled vessel, while the red outline represents the target.

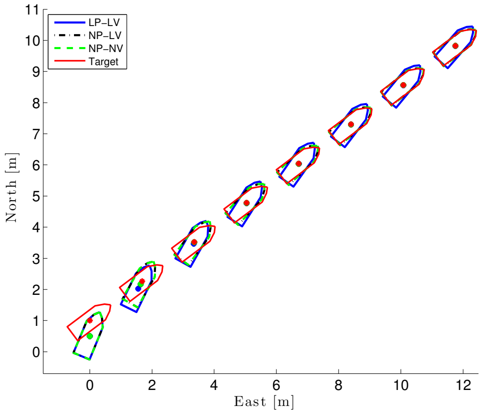

Fig. 2. Scenario 1: The vessel tracking the target moving in a straight-line motion

Fig. 3a illustrates the normed pose error e scaled by the vessel length L, showing that all the controllers are able to track the target. It is worth noting that the introduction of nonlinear feedback control terms lead to significantly faster convergence despite identical gain matrices $\mathbf{K}_1$ and $\mathbf{K}_2$ for all the controllers.

The phase-portrait relation between the normed error variables $\mathbf{z}_1$ and $\mathbf{z}_2$ is shown in Fig. 3b. Here, we can see that the controllers with nonlinear feedback terms are able to reduce the initial increase in $\mathbf{z}_1$ faster than the pure linear feedback controller, and achieve a sharper trajectory toward the origin of the $\mathbf{z}$-dynamics.

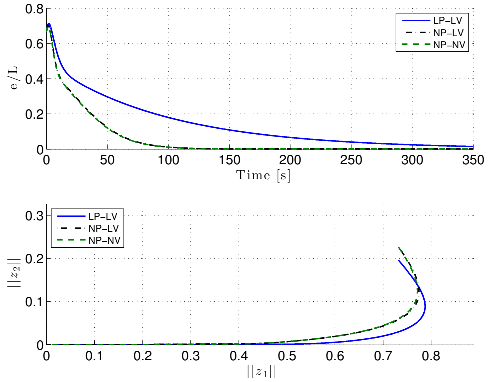

Fig. 3. Scenario 1: The normed pose error scaled by the vessel length (top) and the phase portrait of the normed $\mathbf{z}$-dynamics (bottom)

The commanded control inputs in Fig. 4 show that all the controllers stay below the saturation limits of 2.0 (N) in surge and sway and 1.5 (Nm) in yaw, which was the criterium when choosing the gain matrices $\mathbf{K}_1$ and $\mathbf{K}_2$.

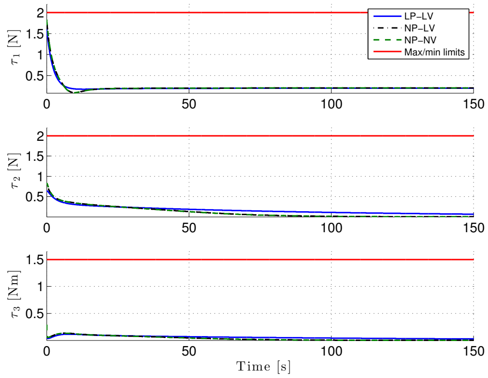

Fig. 4. Scenario 1: The commanded control inputs and force/moment saturation limits

Fig. 5 shows the performance metrics IAE and IAEW for Scenario 1. In particular, Fig. 5a confirms the fact that the nonlinear feedback controllers have the fastest transient response since they quickly establish the smallest IAE value. In addition, Fig. 5b shows that these controllers have the significantly smallest value for combined control accuracy and energy use, thus achieving the best overall control performance for this scenario.

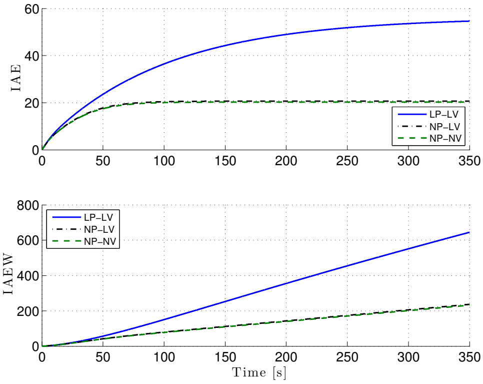

Fig. 5. Scenario 1: IAE and IAEW performance metrics

Scenario 2: Large Initial Errors

By increasing the initial pose error, we can see how sensitive the controllers are to variations in this error. For this scenario, the initial pose of the vessel is therefore changed to $\boldsymbol{\eta}(0) = [-3\ (m), -1.4\ (m),\ 0.6\pi\ (rad)]^\top$, which changes the initial errors to $e(0) = 4.3448$, $||\mathbf{z}_1(0)|| = 4.3448$, $||\mathbf{z}_2(0)|| = 0.6807$ for LP-LV and $||\mathbf{z}_2(0)|| = 0.2675$ for NP-LV and NP-NV. The control gains remain unchanged, as in Table 1.

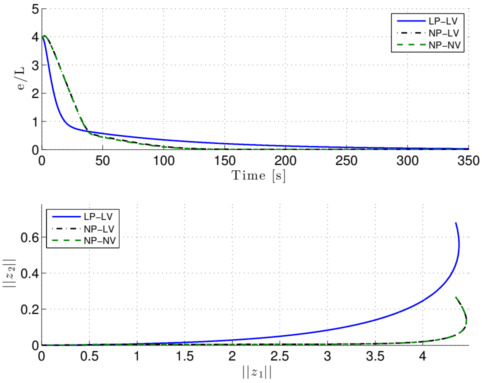

Fig. 6. Scenario 2: The normed pose error scaled by the vessel length (top) and the phase portrait of the normed **z**-dynamics (bottom)

Fig. 6a shows that the LP-LV-controlled vessel has the fastest convergence of the normed pose error until about 40 s. However, as seen in Fig. 7, this can be explained by the fact that the LP-LV controller significantly exceeds the saturation limits, which makes it more sensitive to changes in the control errors than its nonlinear counterparts. Fig. 8 is particularly interesting since the IAEW metric shows that the nonlinear feedback controllers achieve a smaller value even from the start, thus achieving the best overall control performance also for this scenario, while staying within the saturation bounds.

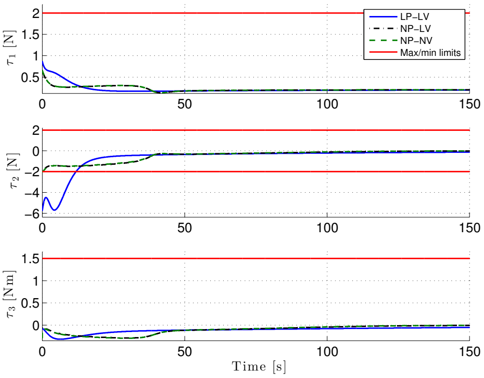

Fig. 7. Scenario 2: The commanded control inputs and force/moment saturation limits

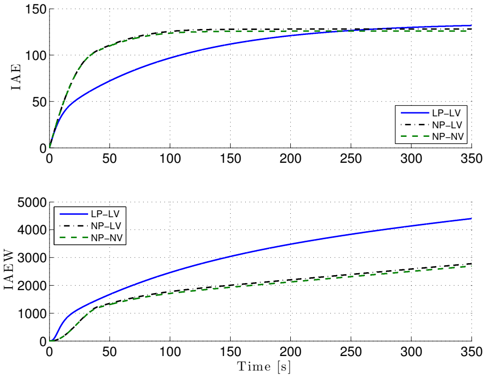

Fig. 8. Scenario 2: IAE and IAEW performance metrics

Scenario 3: Adjusted Nonlinear Gain Parameters

The control parameter Δ is usually known as the lookahead distance in LOS-based control (Breivik and Fossen, 2009). In (Pavlov et al., 2009) it is shown that a small Δ-value corresponds to fast convergence to the path, but with a large overshoot. At the same time, a large Δ-value reduces overshoot and results in smooth but slow convergence. In this scenario, we will investigate the effects of changing the Δ_i parameters for the nonlinear feedback controllers. The initial pose of the vessel is the same as in Scenario 1, with $\boldsymbol{\eta}(0) = [0.5\ (m), 0\ (m),\ \pi/8\ (rad)]^\top$, which means that the initial errors become $e(0) = 0.7320$, $||\mathbf{z}_1(0)|| = 0.7320$, $||\mathbf{z}_2(0)|| = 0.1961$ for LP-LV and $||\mathbf{z}_2(0)|| = 0.2305$ for NP-LV and NP-NV. The updated control gains can be seen in Table 2.

	LP-LV	**NP-LV**	**NP-NV**
$\mathbf{K}_1$	$diag([0.13, 0.13, 0.01])$	$-\|\|-$	$-\|\|-$
$\mathbf{K}_2$	$diag([7, 8, 6])$	$-\|\|-$	$-\|\|-$
$\Delta_{\tilde{p},\tilde{\psi}}$	-	[0.35 , 0.01]	[0.4 , 0.2]
$\Delta_{\tilde{v},\tilde{r}}$	-	-	[0.8 , 0.02]

Table 2. Control gains for Scenario 3

Comparing tables 1 and 2, the parameters $\Delta_{\tilde{p}}$ and $\Delta_{\tilde{\psi}}$ have been decreased for the NP-LV controller, which means that the region of exponential convergence is decreased. This can be seen in Fig. 9a where the convergence behavior becomes almost discontinuous, which would be unrealistic for a vessel with actuator rate constraints. By not changing the $\Delta_{\tilde{p},\tilde{\psi}}$ parameters and decreasing the $\Delta_{\tilde{v},\tilde{r}}$ parameters for the NP-NV controller, Fig. 10 shows a slight violation of the saturation limit of τ_1. However, both nonlinear feedback controllers continue to perform significantly better than their linear counterpart, as shown in Fig. 11.

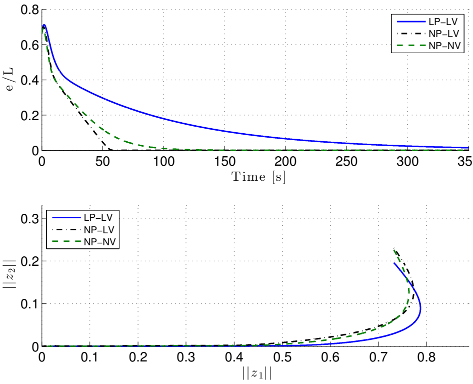

Fig. 9. Scenario 3: The normed pose error scaled by the vessel length (top) and the phase portrait of the normed **z**-dynamics (bottom)

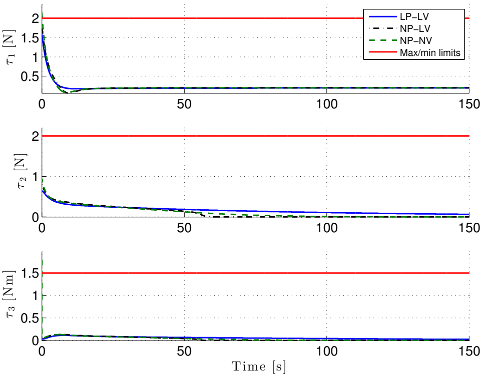

Fig. 10. Scenario 3: The commanded control inputs and force/moment saturation limits

4.2 *Experimental Result for Point Stabilisation*

The LP-LV and NP-NV controllers have been implemented and experimentally tested for the model-scale ship Cybership Enterprise I in the Marine Cybernetics Laboratory at NTNU, for a scenario concerning point stabilisation toward a stationary target, where the initial vessel states are $\boldsymbol{\eta}(0) = [0\ (m), 0\ (m),\ 0\ (rad)]^\top$ and $\boldsymbol{\nu}(0) = [0\ (m/s), 0\ (m/s), 0\ (rad/s)]^\top$, while the initial target pose is $\boldsymbol{\eta}_t(0) = [2\ (m), 2\ (m),\ 1.6\ (rad)]^\top$. The control parameters are given in Table 3.

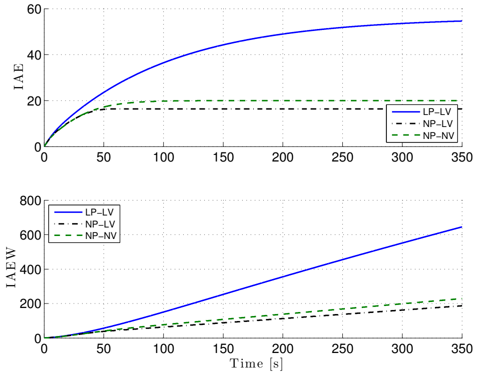

Fig. 11. Scenario 3: IAE and IAEW performance metrics

	LP-LV	NP-NV
$\mathbf{K}_1$	$diag([0.2, 0.2, 0.04])$	$-\|\|-$
$\mathbf{K}_2$	$diag([7, 8, 6])$	$-\|\|-$
$\Delta_{\tilde{p},\tilde{\psi}}$	-	[0.4 , 0.2]
$\Delta_{\tilde{v},\tilde{r}}$	-	[0.97 , 0.9]

Table 3. Control gains for the experiment

Fig. 12 shows the transient convergence behavior of the LP-LV-controlled vessel outlined in blue, and the NP-NV-controlled vessel outlined in dashed green, where the dots indicate the final position. For easier viewing, the size of the plotted vessel outline has been made smaller than the real one. As can be seen, the nonlinear feedback controller gives a smooth and energy-efficient motion toward the target, while its linear counterpart moves almost sideways in the beginning, only changing heading toward the end. The final steady-state error is due to a poorly designed control allocation, which means that the actual output from the actuators is zero even though the controllers command a non-zero output, which can be seen in Fig. 13. This figure also shows that the LP-LV controller's commands exceed the saturation limits in the beginning, resulting in a rapid-as-possible convergence toward the target, which can also be observed through the IAE metric in Fig. 14a. However, the NP-NV controller still has the best overall performance as shown by the IAEW metric in Fig. 14b, and the NP-NV-controlled ship is seen to be located closer to the target at the end.

5. CONCLUSION

This paper has investigated combinations of linear and nonlinear feedback terms for pose and velocity control of marine surface vessels. Three cascaded controllers were developed and compared through numerical simulations and a model-scale experiment. Two performance metrics were used to compare the behavior of the controllers. Interestingly, the nonlinear feedback controllers outperformed their linear counterpart in all scenarios, concerning both the handling of actuator saturation limits and the combined performance of control accuracy and energy use. Another lesson is that the nonlinear gain parameters should not be chosen too small. Future work includes introducing model uncertainties and unknown disturbances to the vessel system. It is also relevant to consider actuator

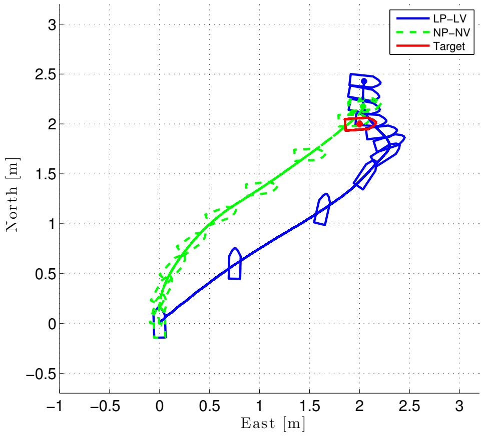

Fig. 12. Experiment: Vessel point stabilisation

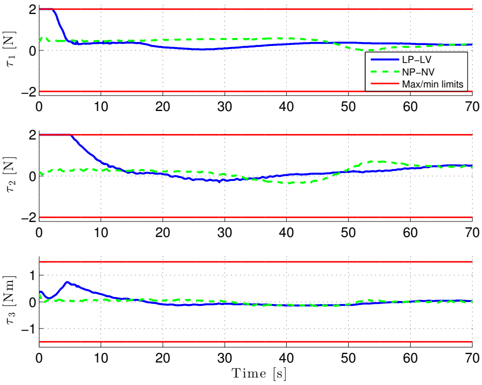

Fig. 13. Experiment: The commanded control inputs and force/moment saturation limits

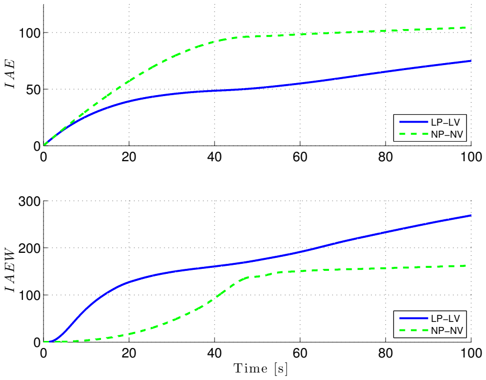

Fig. 14. Experiment: IAE and IAEW performance metrics

rate saturation in addition to magnitude saturation, and thus investigate the effect of time-varying Δ_i-parameters.

ACKNOWLEDGEMENTS

This work was supported by the Research Council of Norway through the Centres of Excellence funding scheme, project number 223254.

REFERENCES

Breivik, M. and Fossen, T.I. (2007). Applying missile guidance concepts to motion control of marine craft. *in Proceedings of the 7th IFAC Conference on Control Applications in Marine Systems, Bol, Croatia.*

Breivik, M. and Fossen, T.I. (2009). *Guidance laws for autonomous underwater vehicles.* in A. V. Inzartsev, *Underwater Vehicles*, IN-TECH Education and Publishing, 51-76.

Breivik, M. and Loberg, J.E. (2011). A virtual target-based underway docking procedure for unmanned surface vehicles. *in Proceedings of the 18th IFAC World Congress, Milano, Italy.*

Breivik, M., Strand, J.P., and Fossen, T.I. (2006). Guided dynamic positioning for fully actuated marine surface vessels. *in Proceedings of the 7th IFAC Conference on Manoeuvring and Control of Marine Craft, Lisbon, Portugal.*

Chen, M., Ge, S., How, B., and Choo, Y. (2013). Robust adaptive position mooring control for marine vessels. *IEEE Transactions on Control Systems Technology*, 21(2), 395–409.

Fossen, T.I. (2000). Nonlinear passive control and observer design for ships. *Modeling, Identification and Control*, 21(3), 129–184.

Fossen, T.I. (2011). *Handbook of Marine Craft Hydrodynamics and Motion Control.* Wiley.

Fossen, T.I. and Pettersen, K.Y. (2014). On uniform semiglobal exponential stability (USGES) of proportional line-of-sight guidance laws. *Automatica*, 50(11), 2912–2917.

Fossen, T.I. and Strand, J.P. (1999). Tutorial on nonlinear backstepping: Applications to ship control. *Modeling, Identification and Control*, 20(2), 83–135.

Khalil, H.K. (2002). *Nonlinear Systems.* Prentice Hall.

Lamnabhi-Lagarrigue, F., Panteley, E., Lefeber, E., and Loria, A. (2005). *Advanced Topics in Control Systems Theory: Lecture Notes from FAP 2004.* Springer.

Pavlov, A., Nordahl, H., and Breivik, M. (2009). MPC-based optimal path following for underactuated vessels. *in Proceedings of the 8th IFAC Conference on Manoeuvring and Control of Marine Craft, Guarujá, Brazil.*

Refsnes, J.E., Sørensen, A.J., and Pettersen, K.Y. (2008). Model-based output feedback control of slender-body underactuated AUVs: Theory and experiments. *IEEE Transactions on Control Systems Technology*, 16(5), 930–946.

Sandved, F. (2015). *Remote Control and Automatic Path-following for C/S Enterprise I and ROV Neptunus.* MSc thesis. Dept. of Marine Technology, Norwegian University of Science and Technology, Trondheim, Norway.

Skejic, R., Breivik, M., and Berg, T.E. (2011). Investigating ship maneuvers around a floating structure under the influence of a uniform current in deep and calm water. *in Proceedings of the 2nd International Conference on Ship Manoeuvring in Shallow and Confined Water: Ship to Ship Interaction, Trondheim, Norway.*

Sørensen, M.E.N. and Breivik, M. (2015). Comparing nonlinear adaptive motion controllers for marine surface vessels. *in Proceedings of the 10th IFAC Conference on Manoeuvring and Control of Marine Craft, Copenhagen, Denmark.*

A.5 Performance Comparison of Backstepping-based Adaptive Controllers for Marine Surface Vessels

M. E. N. Sørensen, E. S. Bjørne and M. Breivik, Performance comparison of backstepping-based adaptive controllers for marine surface vessels, *in Proceedings of the IEEE Multi-Conference on Systems and Control, Buenos Aires, Argentina*, 2016.

Performance Comparison of Backstepping-Based Adaptive Controllers for Marine Surface Vessels

Mikkel Eske Nørgaard Sørensen* Elias S. Bjørne* Morten Breivik*

Abstract— **This paper deals with the design and evaluation of three controllers based on backstepping and different adaptive control schemes, which are applied to the motion control of a nonlinear 3 degrees-of-freedom model of a marine surface vessel. The goal is to make a comparative analysis of the controllers in order to find out which one has the best performance. The considered controllers are: Adaptive backstepping, backstepping with composite concurrent learning and backstepping with cascaded concurrent learning. Numerical simulations are performed for target tracking along an elliptic path, with uncertain vessel model parameters. Motion control performance is evaluated by performance metrics such as IAE and a novel metric named IAEW-WT which combines control accuracy, energy use and actuator wear and tear in one single metric.**

Index Terms— **Marine surface vessel, Nonlinear motion control, Adaptive backstepping, Concurrent learning, Composite adaptation, Cascaded adaptation, Performance metrics**

I. INTRODUCTION

Automated motion control of marine surface vessels has been a research topic since the early 20th century. In recent years, the research has expanded from control of manned vessels to also include unmanned vessels. Challenges include uncertain nonlinear hydrodynamics and external disturbances, since the ocean is an unreliable environment with nonlinearities and unpredictable events. The hydrodynamic forces are often modelled with hydrodynamical coefficients. However, it is typically only a few of these coefficients that can be found. External disturbances such as waves, wind and current are also difficult to measure. Hence, it is important to develop adaptive and robust control algorithms, which can deal with these model uncertainties and external disturbances in a precise and energy-efficient manner.

An overview of some of the recent developments of state-of-the-art adaptive control methods are given in [1], [2], [3] and [4]. In [5], a comparative analysis of various adaptive controllers is made in order to investigate which one has the best control performance by using performance metrics.

An adaptation method which has received attention in recent years is concurrent learning (CL). In [6], it is shown that for an adaptive controller which uses both recorded and instantaneous data concurrently for adaptation, a verifiable condition on linear independence of the recorded data is sufficient to guarantee exponential convergence of the tracking and parameter errors. Concurrent learning is combined with a model reference adaptive control (MRAC) algorithm to improve the trajectory tracking performance of a quadrotor in [7]. The tracking performance is compared against a traditional MRAC algorithm and a standard PID controller using the root mean square error. In [8], a concurrent learning MRAC method is developed for handling linear uncertain dynamical systems, where the sign of the control signal and parameters of the control allocation matrix are unknown.

This paper is based on the work in [9]. Here, we suggest new adaptivce control approaches by combining the concurrent learning concept from [6] with a traditional backstepping controller. The tracking performance is compared against the standard adaptive backstepping controller [10] as a benchmark controller. Simulation results are made using a fully actuated 3 degrees-of-freedom model of a marine surface vessel [11]. The results show that the adaptive controller based on concurrent learning achieves better and more energy-efficient tracking performance than the benchmark controller. However, the CL controllers require acceleration measurements which the benchmark controller does not.

The structure of this paper is as follows: A mathematical vessel model and assumptions are presented in Section II; Section III presents the design of the considered adaptive controllers for a vessel with model uncertainties; Section IV includes simulation results and performance evaluation; while Section V concludes the paper.

II. MARINE SURFACE VESSEL MODEL

The motion of a surface vessel can be represented by the pose vector $\boldsymbol{\eta} = [x, y, \psi]^\top \in \mathbb{R}^2 \times \mathbb{S}$ and the velocity vector $\boldsymbol{\nu} = [u, v, r]^\top \in \mathbb{R}^3$, where $\mathbb{S} \in [-\pi, \pi]$. Here, (x, y) represents the Cartesian position in the local reference frame, ψ is the yaw angle, (u, v) represents the body-fixed linear velocities and r is the yaw rate. The 3 degrees-of-freedom dynamics of a surface vessel can be stated as [12]:

$$\dot{\boldsymbol{\eta}} = \mathbf{R}(\psi)\boldsymbol{\nu} \tag{1}$$

$$\boldsymbol{M}\dot{\boldsymbol{\nu}} + \boldsymbol{C}(\boldsymbol{\nu})\boldsymbol{\nu} + \boldsymbol{D}(\boldsymbol{\nu})\boldsymbol{\nu} = \boldsymbol{\tau}, \tag{2}$$

where

$$\mathbf{R}(\psi) = \begin{bmatrix} \cos(\psi) & -\sin(\psi) & 0 \\ \sin(\psi) & \cos(\psi) & 0 \\ 0 & 0 & 1 \end{bmatrix}, \tag{3}$$

is a rotation matrix $\mathbf{R} \in SO(3)$, and where $\boldsymbol{M}$, $\boldsymbol{C}(\boldsymbol{\nu})$, $\boldsymbol{D}(\boldsymbol{\nu})$ and $\boldsymbol{\tau}$ represent the inertia matrix, Coriolis and centripetal matrix, damping matrix and control input vector, respectively. The system matrices are assumed to satisfy

---

*M. E. N. Sørensen, E. S. Bjørne and M. Breivik are with the Department of Engineering Cybernetics, Norwegian University of Science and Technology (NTNU), NO-7491 Trondheim, Norway. (Email: `mikkel.sorensen@itk.ntnu.no`, `eliasbjorne@gmail.com`, `morten.breivik@ieee.org`)

Additionally, M. E. N. Sørensen and M. Breivik are associated with the NTNU Centre for Autonomous Marine Operations and Systems.

the properties $\boldsymbol{M} = \boldsymbol{M}^\top > 0$, $\boldsymbol{C}(\boldsymbol{\nu}) = -\boldsymbol{C}^\top(\boldsymbol{\nu})$ and $\boldsymbol{D}(\boldsymbol{\nu}) > 0$.

However, there are uncertainties associated with these system matrices. This paper will base the relationship between the real and considered system matrices upon the assumption made in [13], where all the inertia coefficients and some of the hydrodynamic coefficients are assumed to be known, which changes (2) to

$$\boldsymbol{M}\dot{\boldsymbol{\nu}} + \boldsymbol{C}(\boldsymbol{\nu})\boldsymbol{\nu} - \boldsymbol{g}(\boldsymbol{\nu}) - \boldsymbol{\Phi}(\boldsymbol{\nu})\boldsymbol{\varphi}^* = \boldsymbol{\tau}. \tag{4}$$

Here,

$$\boldsymbol{g}(\boldsymbol{\nu}) = \begin{bmatrix} X_u u, & Y_v v, & N_v v \end{bmatrix}^\top, \tag{5}$$

is the known part of $\boldsymbol{D}(\boldsymbol{\nu})\boldsymbol{\nu}$, while

$$\boldsymbol{\Phi}(\boldsymbol{\nu}) \triangleq \begin{bmatrix} u^3 & |u|u & 0 & 0 & 0 & 0 & 0 & 0 & 0 & 0 & 0 & 0 \\ 0 & 0 & |v|v & |r|v & r & |v|r & |r|r & 0 & 0 & 0 & 0 & 0 \\ 0 & 0 & 0 & 0 & 0 & 0 & 0 & |v|v & |r|v & r & |v|r & |r|r \end{bmatrix}, \tag{6}$$

$$\boldsymbol{\varphi}^* \triangleq [X^*_{uuu}, X^*_{|u|u}, Y^*_{|v|v}, Y^*_{|r|v}, Y^*_{r}, Y^*_{|v|r}, Y^*_{|r|r}, \\ N^*_{|v|v}, N^*_{|r|v}, N^*_{r}, N^*_{|v|r}, N^*_{|r|r}]^\top \tag{7}$$

are the regressor matrix and the vector of unknown parameters, respectively, such that

$$\boldsymbol{g}(\boldsymbol{\nu}) + \boldsymbol{\Phi}(\boldsymbol{\nu})\boldsymbol{\varphi}^* = -\boldsymbol{D}(\boldsymbol{\nu})\boldsymbol{\nu}. \tag{8}$$

Additionally, it is assumed that $\dot{\boldsymbol{\varphi}}^* = \mathbf{0}$, i.e., the uncertainties are constant or slowly varying relative to the vessel dynamics.

It is furthermore assumed that the pose vector $\boldsymbol{\eta}$ and velocity vector $\boldsymbol{\nu}$ can be measured. Finally, it is assumed that there are no magnitude or rate saturation constraints for the control input $\boldsymbol{\tau}$.

III. CONTROLLER DESIGN

The control objective is to make $\tilde{\boldsymbol{\eta}}(t) \triangleq \boldsymbol{\eta}(t) - \boldsymbol{\eta}_t(t) \to \mathbf{0}$ as $t \to \infty$, where $\boldsymbol{\eta}_t(t) = [x_t(t), y_t(t), \psi_t(t)]^\top \in \mathbb{R}^2 \times \mathbb{S}$ represents the pose associated with a target point, which is $\mathcal{C}^2$ and bounded. The motion of the target is typically defined by a human or generated by a guidance system.

In this section, we will start by designing a benchmark controller based on a standard adaptive backstepping controller, and subsequently extend and change it by incorporating the concurrent learning concept in two different ways.

The backstepping controller design is divided into two stages, including the definition of state variables and deriving the control laws through control Lyapunov functions (CLFs). The design is based on the backstepping method, which has been applied in e.g. [5] and [14].

For notational simplicity, the time t is omitted in the following.

A. Adaptive Backstepping Control

Start by defining the error variables $\mathbf{z}_1$ and $\mathbf{z}_2$:

$$\mathbf{z}_1 \triangleq \mathbf{R}^\top(\psi)(\boldsymbol{\eta} - \boldsymbol{\eta}_t) \tag{9}$$

$$\mathbf{z}_2 \triangleq \boldsymbol{\nu} - \boldsymbol{\alpha}, \tag{10}$$

where $\boldsymbol{\alpha} \in \mathbb{R}^3$ is a so-called stabilising function, which can be interpreted as a desired velocity and which is to be designed later.

1) Step 1:

Choosing the positive definite CLF

$$V_1 \triangleq \frac{1}{2}\mathbf{z}_1^\top \mathbf{z}_1, \tag{11}$$

the derivative of V_1 with respect to time along the $\mathbf{z}_1$-dynamics gives

$$\begin{aligned} \dot{V}_1 &= \mathbf{z}_1^\top \dot{\mathbf{z}}_1 \\ &= \mathbf{z}_1^\top(\mathbf{S}^\top(r)\mathbf{R}^\top(\psi)(\boldsymbol{\eta} - \boldsymbol{\eta}_t) + \mathbf{R}^\top(\psi)(\dot{\boldsymbol{\eta}} - \dot{\boldsymbol{\eta}}_t)) \\ &= \mathbf{z}_1^\top(\mathbf{S}^\top(r)\mathbf{z}_1 + \mathbf{R}^\top(\psi)(\dot{\boldsymbol{\eta}} - \dot{\boldsymbol{\eta}}_t)), \end{aligned} \tag{12}$$

where

$$\mathbf{S}(r) = \begin{bmatrix} 0 & -r & 0 \\ r & 0 & 0 \\ 0 & 0 & 0 \end{bmatrix} \tag{13}$$

is a skew-symmetric matrix satisfying $\mathbf{z}_1^\top \mathbf{S}^\top(r)\mathbf{z}_1 = 0$, which gives

$$\dot{V}_1 = \mathbf{z}_1^\top(\boldsymbol{\nu} - \mathbf{R}^\top(\psi)\dot{\boldsymbol{\eta}}_t). \tag{14}$$

Using (10), the CLF becomes

$$\begin{aligned} \dot{V}_1 &= \mathbf{z}_1^\top(\mathbf{z}_2 + \boldsymbol{\alpha} - \mathbf{R}^\top(\psi)\dot{\boldsymbol{\eta}}_t) \\ &= \mathbf{z}_1^\top \mathbf{z}_2 + \mathbf{z}_1^\top(\boldsymbol{\alpha} - \mathbf{R}^\top(\psi)\dot{\boldsymbol{\eta}}_t), \end{aligned} \tag{15}$$

where the stabilising function can be chosen as

$$\boldsymbol{\alpha} = \mathbf{R}^\top(\psi)\dot{\boldsymbol{\eta}}_t - \mathbf{K}_1\mathbf{z}_1 \tag{16}$$

with $\mathbf{K}_1 > 0$, which results in

$$\dot{V}_1 = -\mathbf{z}_1^\top \mathbf{K}_1 \mathbf{z}_1 + \mathbf{z}_1^\top \mathbf{z}_2, \tag{17}$$

and the $\mathbf{z}_1$-dynamics becomes

$$\dot{\mathbf{z}}_1 = \mathbf{S}^\top(r)\mathbf{z}_1 - \mathbf{K}_1\mathbf{z}_1 + \mathbf{z}_2. \tag{18}$$

2) Step 2:

The $\mathbf{z}_2$-dynamics can be written as

$$\begin{aligned} \mathbf{M}\dot{\mathbf{z}}_2 =& \mathbf{M}(\dot{\boldsymbol{\nu}} - \dot{\boldsymbol{\alpha}}) \\ =& \boldsymbol{\tau} - \mathbf{C}(\boldsymbol{\nu})\boldsymbol{\nu} + \boldsymbol{g}(\boldsymbol{\nu}) + \boldsymbol{\Phi}(\boldsymbol{\nu})\boldsymbol{\varphi}^* - \mathbf{M}\dot{\boldsymbol{\alpha}}, \end{aligned} \tag{19}$$

where the time derivative of (16) becomes

$$\dot{\boldsymbol{\alpha}} = \mathbf{R}^\top(\psi)\ddot{\boldsymbol{\eta}}_t + \mathbf{S}(r)^\top \mathbf{R}^\top(\psi)\dot{\boldsymbol{\eta}}_t - \mathbf{K}_1\dot{\mathbf{z}}_1. \tag{20}$$

The CLF for both $\mathbf{z}_1$ and $\mathbf{z}_2$ is then defined as

$$V_2 \triangleq \frac{1}{2}\mathbf{z}_2^\top \mathbf{M}\mathbf{z}_2 + V_1. \tag{21}$$

Simplifying $\mathbf{C}(\boldsymbol{\nu}) = \mathbf{C}$, $\boldsymbol{g}(\boldsymbol{\nu}) = \boldsymbol{g}$, $\boldsymbol{\Phi}(\boldsymbol{\nu}) = \boldsymbol{\Phi}$, $\mathbf{R}(\psi) = \mathbf{R}$ and $\mathbf{S}(r) = \mathbf{S}$ for notational brevity, the derivative of (21) becomes

$$\begin{aligned}\dot{V}_2 =& \mathbf{z}_2^\top \mathbf{M}\dot{\mathbf{z}}_2 + \dot{V}_1 \\ =& \mathbf{z}_2^\top (\boldsymbol{\tau} - \mathbf{C}\boldsymbol{\nu} + \boldsymbol{g} + \boldsymbol{\Phi}\boldsymbol{\varphi}^* - \mathbf{M}\dot{\boldsymbol{\alpha}}) \\ & - \mathbf{z}_1^\top \mathbf{K}_1 \mathbf{z}_1 + \mathbf{z}_1^\top \mathbf{z}_2. \end{aligned} \tag{22}$$

The control input can be chosen as

$$\boldsymbol{\tau} = \mathbf{M}\dot{\boldsymbol{\alpha}} + \mathbf{C}\boldsymbol{\nu} - \boldsymbol{g} - \boldsymbol{\Phi}\boldsymbol{\varphi}^* - \mathbf{z}_1 - \mathbf{K}_2\mathbf{z}_2, \tag{23}$$

where $\mathbf{K}_2 > 0$, which results in

$$\dot{V}_2 = -\mathbf{z}_1^\top \mathbf{K}_1 \mathbf{z}_1 - \mathbf{z}_2^\top \mathbf{K}_2 \mathbf{z}_2 < 0, \tag{24}$$

which makes the origin of the $\mathbf{z}$-dynamics

$$\dot{\mathbf{z}}_1 = \mathbf{S}^\top \mathbf{z}_1 - \mathbf{K}_1 \mathbf{z}_1 + \mathbf{z}_2 \tag{25}$$

$$\dot{\mathbf{z}}_2 = -\mathbf{M}^{-1}(\mathbf{z}_1 + \mathbf{K}_2 \mathbf{z}_2) \tag{26}$$

uniformly globally exponentially stable (UGES).

3) Step 3:
The parameter $\boldsymbol{\varphi}^*$ is however unknown and must be estimated as $\hat{\boldsymbol{\varphi}}$. The CLF is therefore expanded to

$$V_3 \triangleq \tilde{\boldsymbol{\varphi}}^\top \boldsymbol{\Gamma}_\varphi^{-1} \tilde{\boldsymbol{\varphi}} + V_2, \tag{27}$$

where $\boldsymbol{\Gamma}_\varphi > 0$ is the adaptation gain and $\tilde{\boldsymbol{\varphi}} \triangleq \boldsymbol{\varphi}^* - \hat{\boldsymbol{\varphi}}$. Hence, the control law in (23) is modified to

$$\boldsymbol{\tau} = \mathbf{M}\dot{\boldsymbol{\alpha}} + \mathbf{C}\boldsymbol{\nu} - \boldsymbol{g} - \boldsymbol{\Phi}\hat{\boldsymbol{\varphi}} - \mathbf{z}_1 - \mathbf{K}_2\mathbf{z}_2 \tag{28}$$

such that it uses the estimated parameter $\hat{\boldsymbol{\varphi}}$ instead of the real parameter, which changes the derivative of (21) to

$$\dot{V}_2 = -\mathbf{z}_1^\top \mathbf{K}_1 \mathbf{z}_1 - \mathbf{z}_2^\top \mathbf{K}_2 \mathbf{z}_2 + \tilde{\boldsymbol{\varphi}}^\top \boldsymbol{\Phi}^\top \mathbf{z}_2. \tag{29}$$

The derivative of (27) then becomes

$$\dot{V}_3 = -\mathbf{z}_1^\top \mathbf{K}_1 \mathbf{z}_1 - \mathbf{z}_2^\top \mathbf{K}_2 \mathbf{z}_2 + \tilde{\boldsymbol{\varphi}}^\top (\boldsymbol{\Phi}^\top \mathbf{z}_2 - \boldsymbol{\Gamma}_\varphi^{-1} \dot{\hat{\boldsymbol{\varphi}}}), \tag{30}$$

where the assumption that $\boldsymbol{\varphi}^*$ is constant or slowly varying relative to the vessel dynamics, has been applied. Hence, the adaptation law

$$\dot{\hat{\boldsymbol{\varphi}}} = \boldsymbol{\Gamma}_\varphi \boldsymbol{\Phi}^\top \mathbf{z}_2 \tag{31}$$

is chosen, which results in

$$\dot{V}_3 = -\mathbf{z}_1^\top \mathbf{K}_1 \mathbf{z}_1 - \mathbf{z}_2^\top \mathbf{K}_2 \mathbf{z}_2 \leq 0 \quad \forall\ \mathbf{z}_1, \mathbf{z}_2.$$

4) Stability Analysis:
The total closed-loop dynamics become

$$\dot{\mathbf{z}}_1 = \mathbf{S}^\top \mathbf{z}_1 - \mathbf{K}_1 \mathbf{z}_1 + \mathbf{z}_2 \tag{32}$$

$$\dot{\mathbf{z}}_2 = -\mathbf{M}^{-1}(\mathbf{z}_1 + \mathbf{K}_2 \mathbf{z}_2 - \boldsymbol{\Phi}\tilde{\boldsymbol{\varphi}}) \tag{33}$$

$$\dot{\tilde{\boldsymbol{\varphi}}} = -\boldsymbol{\Gamma}_\varphi \boldsymbol{\Phi}^\top \mathbf{z}_2. \tag{34}$$

It can hence be concluded that the origin of the error system $(\mathbf{z}_1, \mathbf{z}_2, \tilde{\boldsymbol{\varphi}})$ is uniformly globally asymptotically stable (UGAS) by utilising Theorem A.6 from [12].

B. Concurrent Learning Backstepping

Concurrent learning is an adaptation concept based on the intuition that if the recorded data is sufficiently rich, i.e., there is a linear independence in the data, concurrent learning adaptation can be used to estimate true values without the need for persistency of excitation in the instantaneous data. However, Condition 1 from [6] needs to be fulfilled:

Condition 1: The recorded data has as many linearly independent elements as the dimension of the regressor matrix $\boldsymbol{\Omega}(\boldsymbol{x}(t)) \in \mathbb{R}^{l \times m}$. That is if $\mathbf{Z} = [\boldsymbol{\Omega}(\boldsymbol{x}(t_1))^\top, \boldsymbol{\Omega}(\boldsymbol{x}(t_2))^\top, ..., \boldsymbol{\Omega}(\boldsymbol{x}(t_p))^\top]$, then $rank(\mathbf{Z}) = m$.

1) Composite Adaptation Law:
If Condition 1 is satisfied for the regressor matrix $\boldsymbol{\Phi}$, the adaptation law (31) can be changed to

$$\dot{\hat{\boldsymbol{\varphi}}} = \boldsymbol{\Gamma}_\varphi \left(\boldsymbol{\Phi}^\top \mathbf{z}_2 + \sum_{j=1}^{p} \boldsymbol{\Phi}_j^\top \boldsymbol{\epsilon}_j \right), \tag{35}$$

where $j \in \{1, 2, ...p\}$ denotes the index of a recorded data point $\boldsymbol{x}_j = [\boldsymbol{\eta}_j^\top, \boldsymbol{\nu}_j^\top]^\top$ and $\boldsymbol{\Phi}_j$ is the regressor matrix evaluated at point $\boldsymbol{x}_j$, while $\boldsymbol{\epsilon}$ is an approximation error defined as

$$\boldsymbol{\epsilon} \triangleq \boldsymbol{y} - \hat{\boldsymbol{y}} \tag{36}$$

where

$$\begin{aligned} \boldsymbol{y} &= \boldsymbol{\Phi}\boldsymbol{\varphi}^* \\ &= \boldsymbol{M}\dot{\boldsymbol{\nu}} - \boldsymbol{\tau} + \boldsymbol{C}(\boldsymbol{\nu})\boldsymbol{\nu} - \boldsymbol{g}(\boldsymbol{\nu}) \end{aligned} \tag{37}$$

$$\hat{\boldsymbol{y}} = \boldsymbol{\Phi}\hat{\boldsymbol{\varphi}}, \tag{38}$$

and it is assumed that the acceleration vector $\dot{\boldsymbol{\nu}}$ can be measured. Hence,(35) is a composite adaptation law since it both uses the control error $\mathbf{z}_2$ and the approximation error $\boldsymbol{\epsilon}$ to update the estimate of the uncertainties, see [15]. By combining the control law (28) and the new adaptation law (35), the derivative of (27) becomes

$$\begin{aligned} \dot{V}_3 =& - \mathbf{z}_1^\top \mathbf{K}_1 \mathbf{z}_1 - \mathbf{z}_2^\top \mathbf{K}_2 \mathbf{z}_2 - \tilde{\boldsymbol{\varphi}}^\top \sum_{j=1}^{p} \boldsymbol{\Phi}_j^\top \boldsymbol{\epsilon}_j \\ =& - \mathbf{z}_1^\top \mathbf{K}_1 \mathbf{z}_1 - \mathbf{z}_2^\top \mathbf{K}_2 \mathbf{z}_2 - \tilde{\boldsymbol{\varphi}}^\top \sum_{j=1}^{p} \boldsymbol{\Phi}_j^\top (\boldsymbol{\Phi}_j \tilde{\boldsymbol{\varphi}}). \end{aligned} \tag{39}$$

Note that $\sum_{j=1}^{p} \boldsymbol{\Phi}_j^\top \boldsymbol{\Phi}_j > 0$ due to Condition 1. Hence, it can be shown that the origin of the error system $(\mathbf{z}_1, \mathbf{z}_2, \tilde{\boldsymbol{\varphi}})$ is UGES by utilising Theorem 4.10 from [16].

2) Cascaded Adaptation Law:
We can also change (35) to

$$\dot{\hat{\boldsymbol{\varphi}}} = \boldsymbol{\Gamma}_\varphi \left(\boldsymbol{\Phi}^\top \boldsymbol{\epsilon} + \sum_{j=1}^{p} \boldsymbol{\Phi}_j^\top \boldsymbol{\epsilon}_j \right), \tag{40}$$

such that the adaptation dynamics are in cascade with the controller and only uses the approximation error to calculate the estimate of the model uncertainties. Hence, (40) is no longer a composite adaptation law since the control error $\mathbf{z}_2$ has been replaced by the approximation error $\boldsymbol{\epsilon}$.

In this case, it can be concluded that the origin of $\mathbf{z}_1$ and $\mathbf{z}_2$ is UGES when seeing $\tilde{\boldsymbol{\varphi}}$ as an input with $\tilde{\boldsymbol{\varphi}} = \mathbf{0}$. Consequently, it can be concluded by Lemma 4.6 from [16] that the subsystem (32) and (33) is input-to-state stable (ISS).

Using the CLF

$$V_4 \overset{\triangle}{=} \tilde{\boldsymbol{\varphi}}^\top \boldsymbol{\Gamma}_\varphi^{-1} \tilde{\boldsymbol{\varphi}}, \tag{41}$$

it can be shown that the origin of the adaptation error dynamics $\tilde{\boldsymbol{\varphi}}$ becomes UGES when using (40).

The total closed-loop dynamics now become

$$\dot{\mathbf{z}}_1 = \mathbf{S}^\top \mathbf{z}_1 - \mathbf{K}_1 \mathbf{z}_1 + \mathbf{z}_2 \tag{42}$$

$$\dot{\mathbf{z}}_2 = -\mathbf{M}^{-1}(\mathbf{z}_1 + \mathbf{K}_2 \mathbf{z}_2 - \boldsymbol{\Phi} \tilde{\boldsymbol{\varphi}}) \tag{43}$$

$$\dot{\tilde{\boldsymbol{\varphi}}} = -\boldsymbol{\Gamma}_\varphi \left(\boldsymbol{\Phi}^\top \boldsymbol{\epsilon} + \sum_{j=1}^{p} \boldsymbol{\Phi}_j^\top \boldsymbol{\epsilon}_j \right). \tag{44}$$

Since the stability of the origin of the $\mathbf{z}_1$ and $\mathbf{z}_2$ subsystem in (42) and (43)is UGES for $\tilde{\boldsymbol{\varphi}} = 0$, and utilising Theorem 2.1 from [17], it can be concluded that the origin of the total system $(\mathbf{z}_1, \mathbf{z}_2, \tilde{\boldsymbol{\varphi}})$ is UGES.

3) Data Storage Algorithm:

From (40), the convergence rate is related to the summation of the stored data. The concurrent learning gives the option of choosing which data to store for this summation. An algorithm is therefore chosen such that the data stored is diverse, which ensures full rank of the matrix $\mathbf{Z}$ from Condition 1.

The data window algorithm, described in Algorithm 1, works like a queue with a constant number of matrices, such that if a new measurement is sufficiently different from the previous one, then the new regression matrix is stored and the oldest regression matrix is rejected.

Algorithm 1 Pseudocode for the data window choosing algorithm

```
$end \leftarrow SM$ {% number of stored matrices in the queue}
$[m, n] \leftarrow$ size($\boldsymbol{\Phi}(\boldsymbol{\nu}_0)$)
$\boldsymbol{\Phi_M} \leftarrow$ zeros($SM, m, n$) {% Initializing the storage matrix}
$\boldsymbol{\Upsilon_M} \leftarrow$ zeros($SM, m, 1$) {% Initializing the error storage matrix}
for $i = 1$ to $endTime$ do
    $\boldsymbol{\Phi}_{temp} \leftarrow \boldsymbol{\Phi}(\boldsymbol{\nu}_i)$
    $\boldsymbol{\Phi}_p \leftarrow \boldsymbol{\Phi_M}[1]$
    if norm($\boldsymbol{\Phi}_{temp} - \boldsymbol{\Phi}_p$) $< \delta$ then
        $\boldsymbol{\Phi_M}[2 : end] \leftarrow \boldsymbol{\Phi_M}[1 : end - 1]$
        $\boldsymbol{\Phi_M}[1] \leftarrow \boldsymbol{\Phi}_{temp}$ { % Queuing the regression matrices}
        $\boldsymbol{\Upsilon_M}[2 : end] \leftarrow \boldsymbol{\Upsilon_M}[1 : end - 1]$
        $\boldsymbol{\Upsilon_M}[1] \leftarrow \boldsymbol{y_i}$ { % Queuing the $y$ error vectors}
        $\boldsymbol{\mathcal{E}} = \Upsilon_M - \boldsymbol{\Phi}_M * \hat{\boldsymbol{\varphi}}_{\boldsymbol{i}}$
        $\boldsymbol{\Sigma} = \boldsymbol{\Phi}_M * \boldsymbol{\mathcal{E}}$ { % Multiplication like the sum in (40)}
    end if
end for
```

X^*_{uuu}	-3.787	$X^*_{\lvert u \rvert u}$	0.3545
$Y^*_{\lvert v \rvert v}$	-2.776	$Y^*_{\lvert r \rvert v}$	-0.805
Y^*_r	-7250	$Y^*_{\lvert v \rvert r}$	-0.845
$Y^*_{\lvert r \rvert r}$	-3.450	$N^*_{\lvert v \rvert v}$	-0.2088
$N^*_{\lvert r \rvert v}$	0.130	N^*_r	-1.900
$N^*_{\lvert v \rvert r}$	0.080	$N^*_{\lvert r \rvert r}$	-0.750

TABLE I: Model parameters

IV. SIMULATION RESULTS AND PERFORMANCE EVALUATION

This section starts with describing the vessel model, followed by the target motion, initial states and control parameters used in the simulations. Subsequently, performance metrics used to evaluate the the control performance are defined. Finally, the simulation results are presented and discussed.

A. Simulation Setup

1) Vessel Model Parameters:

The model-scale ship Cybership Enterprise I, with parameters from [11], will be used to test the performance of the adaptive controllers through numerical simulations in Matlab. Cybership Enterprise I is a 1:70 scale replica of a supply ship, with a length of $L = 1.105$ (m). It is fully actuated with two Voith-Schneider propellers aft and one bow thruster.

The model parameters for the vessel are chosen as shown in Table I.

2) Target Motion, Initial States and Control Parameters:

For an elliptic target motion, the target pose $\boldsymbol{\eta}_t(t)$ is derived from

$$\boldsymbol{\eta}_t(t) = \left[x_t(t), y_t(t), \tfrac{\pi}{2} - \arctan\left(\tfrac{\dot{y}_t(t)}{\dot{x}_t(t)} \right) \right]^\top, \tag{45}$$

where

$$x_t(t) = 5 + \sin\left(\frac{\pi}{180} \theta(t) \right) \tag{46}$$

$$y_t(t) = 0.5 + 1.5 \cos\left(\frac{\pi}{180} \theta(t) \right), \tag{47}$$

and

$$\dot{\theta}(t) = \frac{v_t}{\frac{\pi}{180} \sqrt{\left(\cos\left(\frac{\pi}{180} \theta(t) \right) \right)^2 + \left(1.5 \sin\left(\frac{\pi}{180} \theta(t) \right) \right)^2}}. \tag{48}$$

The reference target has a constant speed $v_t = 0.15$ (m/s). For the full-scale vessel, this corresponds to 1.275 m/s using the Bis scale [12]. By taking the time derivative, $\dot{\boldsymbol{\eta}}_t(t)$ and $\ddot{\boldsymbol{\eta}}_t(t)$ can be found.

The initial condition of the target trajectory is chosen to be $\theta(0) = 0$ and $\boldsymbol{\eta}_t(0) = [5\ (m), 2\ (m),\ 0\ (rad)]^\top$.

The initial vessel states are chosen to be $\boldsymbol{\eta}(0) = [5.5\ (m), 2.5\ (m), \frac{1}{4}\pi\ (rad)]^\top$ and $\boldsymbol{\nu}(0) = [0\ (m/s), 0\ (m/s), 0\ (rad/s)]^\top$. The control and adaptation gains in Table II are obtained after iterative tuning, since it is assumed that there are no magnitude or rate saturation constraints for the control input $\boldsymbol{\tau}$. It should be noted that all of the adaptive controllers use the same gain matrices. The data window was chosen to have a size of 10 such that it both uses recorded and instantaneous data and at the same time does not require a large amount of computational power.

$\mathbf{K}_1$	$diag([0.4, 0.4, 0.1])$
$\mathbf{K}_2$	$diag([5, 8, 6])$
$\mathbf{\Gamma}_\varphi$	$diag([8, 8, 8, 8, 4, 8, 8, 8, 8, 4, 8, 8])$

TABLE II: Control and adaptation gains

The initial values for the estimated model parameters are $\hat{\boldsymbol{\varphi}}(0) = \mathbf{0}_{12\times 1}$.

3) Performance Metrics:
To evaluate and compare the performance of the control algorithms, performance metrics must be defined and used. These include the integral of the absolute error (IAE) for a chosen error metric. For this, we will use the norm of the pose error e, which can be calculated by

$$e(t) = \sqrt{\tilde{\boldsymbol{\eta}}(t)^\top \tilde{\boldsymbol{\eta}}(t)}. \tag{49}$$

The IAE is then calculated as

$$IAE(t) = \int_0^t |e(\sigma)| d\sigma, \tag{50}$$

which simply describes the temporal evolution of the absolute value of the error without adding any weight to the error.

Finally, we will use combination of the integral of the absolute error multiplied by the energy consumption (IAEW), which was proposed in [5] and evaluate the property of how smooth the controller is by how fast $\boldsymbol{\tau}$ is changing, thus including $\dot{\boldsymbol{\tau}}$. If the control input is smooth, it is more realistic that "wear and tear" of the actuator is reduced. Multiplying all these effects together gives the metric integral of the absolute error with work, wear and tear (IAEW-WT), which was proposed in [9] and is defined as

$$IAEW\text{-}WT(t) = \int_0^t |e(\sigma)| d\sigma \int_0^t P(\sigma) d\sigma \int_0^t ||\dot{\boldsymbol{\tau}}(\sigma)|| d\sigma, \tag{51}$$

where

$$P(t) = |\boldsymbol{\nu}(t)^\top \boldsymbol{\tau}(t)| \tag{52}$$

represents the mechanical power. We compute the change of control input as

$$\dot{\boldsymbol{\tau}}(t) = \frac{\boldsymbol{\tau}(t) - \boldsymbol{\tau}(t-h)}{h}, \tag{53}$$

where h is the sample time.

B. Simulation Results

In the following plots, AB refers to the adaptive backstepping controller, CL-CO refers to the concurrent learning backstepping controller with the composite adaptation law, while CL-CA refers to the concurrent learning backstepping controller with the cascaded adaptation law.

In Fig. 1, the vessel and target pose outlines are plotted to show the transient convergence behavior. Here, the blue outline represents the AB-controlled vessel, the dash-dotted black outline represents the CL-CO-controlled vessel, the dash-dotted green outline represents the CL-CA-controlled vessel, while the red solid outline represents the target. It should be noted that the outlined vessels have been scaled down for increased readability of the figure. Here, it can easily been seen that CL-CA controller has a better control performance than the two others.

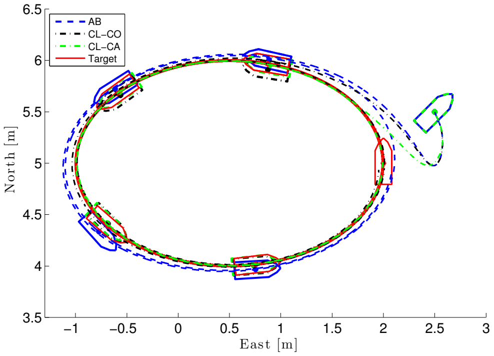

Fig. 1: The vessel tracking the target which is moving along an elliptic path

Fig. 2 illustrates the normed pose error e scaled by the vessel length L, showing that all controllers are able to converge to a neighbourhood of the target, which is due to the fact that the assumption $\dot{\boldsymbol{\varphi}}^* = \mathbf{0}$ is not satisfied. It is worth noting that the introduction of cascaded concurrent learning leads to faster convergence despite identical gain matrices $\mathbf{K}_1$, $\mathbf{K}_2$ and $\mathbf{\Gamma}_\varphi$ for all the controllers.

The phase-portrait relation between the normed error variables $\mathbf{z}_1$ and $\mathbf{z}_2$ is shown in Fig. 2b. Here, we can see that the controller with cascaded concurrent learning is able to reduce the initial increase in $\mathbf{z}_1$ marginally faster than the standard adaptive backstepping controller and the composite concurrent learning, and achieve a sharper trajectory toward the origin of the $\mathbf{z}$-dynamics. In Fig. 3a, the normed control input of the controllers is shown. In addition, the feedforward, feedback and adaptive parts of the normed control input are plotted separately in Fig 3b, 3c and 3d, where

$$\boldsymbol{\tau}_{FF} = \mathbf{M}\dot{\boldsymbol{\alpha}} + \mathbf{C}(\boldsymbol{\nu})\boldsymbol{\nu} - \boldsymbol{g}(\boldsymbol{\nu}) \tag{54}$$

$$\boldsymbol{\tau}_{FB} = -\mathbf{z}_1 - \mathbf{K}_2\mathbf{z}_2 \tag{55}$$

$$\boldsymbol{\tau}_{AD} = -\boldsymbol{\Phi}(\boldsymbol{\nu})\hat{\boldsymbol{\varphi}}. \tag{56}$$

Note that Fig. 3a-d only show the first 100 seconds of the simulation. It is hard to distinguish the normed control input of the controllers in Fig. 3a. However, by splitting the signal into its components (54)-(56), it can be seen that the adaptive backstepping controller uses most energy in the feedback part of the control law, while the concurrent learning backstepping controllers use most energy in the feedforward part. In addition, Fig. 3d shows that the CL-CA controller also uses significant energy in the adaptive

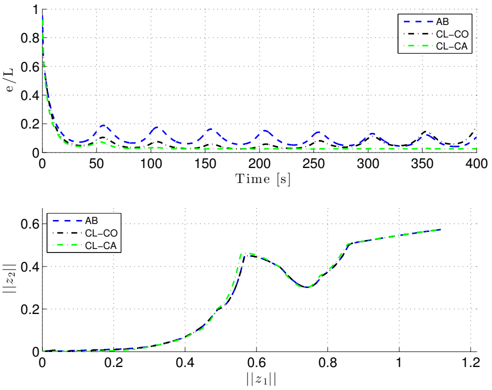

Fig. 2: The normed pose error scaled by the vessel length (top) and the phase portrait of the normed $\mathbf{z}$-dynamics (bottom)

part of the control input.

In Fig. 4, the normed error between the real and the estimated damping forces is shown, where

$$\boldsymbol{\omega} \triangleq \boldsymbol{g}(\boldsymbol{\nu}) + \boldsymbol{\Phi}(\boldsymbol{\nu})\hat{\boldsymbol{\varphi}} + \boldsymbol{D}(\boldsymbol{\nu})\boldsymbol{\nu}. \tag{57}$$

Here, the CL-CA controller has the fastest convergence rate. However, the CL-CO controller has a good convergence rate in the beginning, but after some time it starts to diverge from zero, which affects the pose error, see also Fig. 2a. We have yet to find out why this happens.

Fig. 5 display the curves of the performance metrics IAE and IAEW-WT for the normed pose error. The figure indicates that the cascaded concurrent learning concept improves the tracking performance. In particular, Fig. 5a shows that the CL-CA controller has the fastest transient response since it quickly establishes the smallest IAE value. In addition, Fig. 5b shows that this controller has a significantly smaller value for the combined control accuracy, energy use and actuator wear and tear, thus achieving the best overall performance for this scenario.

V. CONCLUSION

This paper uses the adaptive backstepping controller as a benchmark controller to evaluate the control performance of two different combinations of the concurrent learning concept with the traditional backstepping controller: A concurrent learning backstepping controller with a composite adaptation law and a concurrent learning backstepping controller with a cascaded adaptation law. Simulations are conducted with a nonlinear 3 degrees-of-freedom model of a marine surface vessel, showing the considered controllers have a good tracking performance and the ability to adapt for model uncertainties. The simulations also show that the concurrent learning backstepping controller with cascaded adaptation has the best control performance and is better at handling uncertainties than the other two controllers.

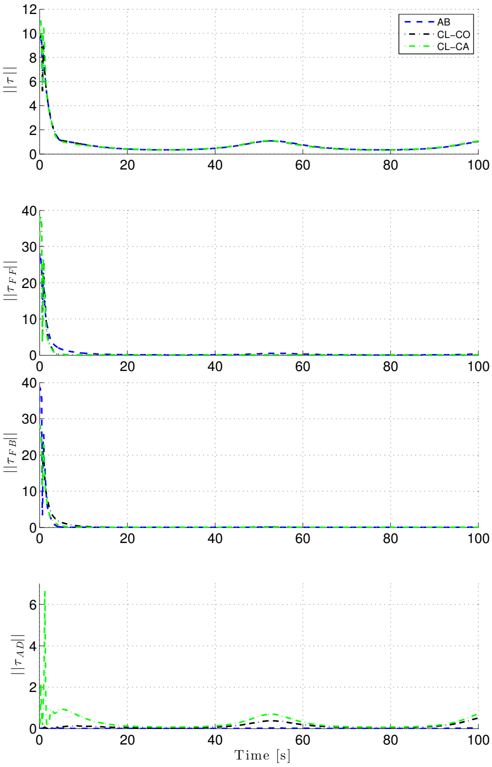

Fig. 3: The normed control input (top), the feedforward part of the normed control input (upper middle), the feedback part of the normed control input (lower middle) and the adaptive part of the normed control input (bottom)

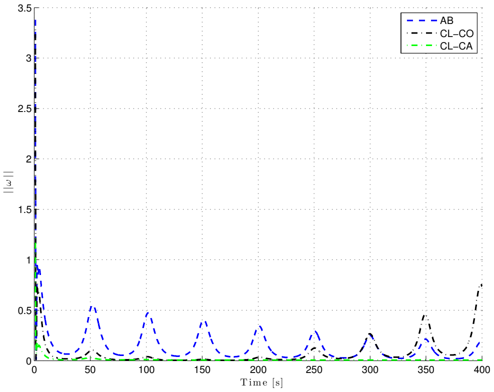

Fig. 4: The normed error between the real and the estimated damping forces

Future work includes improving the concurrent learning

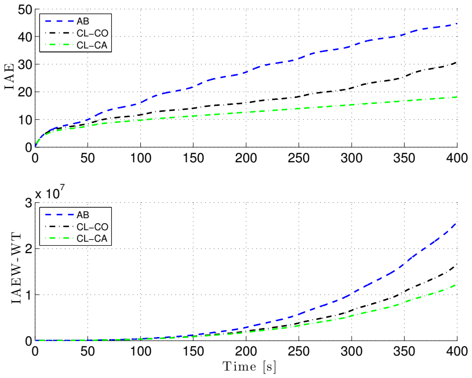

Fig. 5: The IAE and IAEW-WT performance metrics

adaptation algorithm such that it does not require acceleration measurements. Also, it is desirable to investigate why the composite concurrent learning starts to go into a limit cycle and try other concurrent learning adaptation algorithms which might further improve performance. Finally, it is desirable to verify the results experimentally by implementing and testing the controllers on a model-scale vessel.

ACKNOWLEDGEMENT

This work was supported by the Research Council of Norway through the Centres of Excellence funding scheme, project number 223254.

REFERENCES

[1] E. Lavretsky and K. A. Wise, *Robust and Adaptive Control with Aerospace Applications*. Springer, 2012.

[2] N. Hovakimyan and C. Cao, $\mathcal{L}_1$ *Adaptive Control Theory: Guaranteed Robustness with Fast Adaptation*. SIAM, 2010.

[3] A. Astolfi, D. Karagiannis, and R. Ortega, *Nonlinear and Adaptive Control with Applications*. Springer, 2008.

[4] T. Yucelen and E. Johnson, "Command governor-based adaptive control," *In Proceedings of AIAA Guidance, Navigation, and Control Conference, Minneapolis, USA*, 2012.

[5] M. E. N. Sørensen and M. Breivik, "Comparing nonlinear adaptive motion controllers for marine surface vessels," *in Proceedings of the 10th IFAC Conference on Manoeuvring and Control of Marine Craft, Copenhagen, Denmark*, 2015.

[6] G. Chowdhary and E. Johnson, "Concurrent learning for convergence in adaptive control without persistency of excitation," *in Proceedings of the 49th IEEE Conference on Decision and Control. Atlanta, USA*, 2010.

[7] G. Chowdhary, M. Culterz, N. K. Üre, and J. P. How, "Experimental results of concurrent learning adaptive controllers," *in Proceedings of the AIAA Guidance, Navigation, and Control Conference, Minneapolis, USA*, 2012.

[8] B. Reish and G. Chowdhary, "Concurrent learning adaptive control for systems with unknown sign of control effectiveness," *in Proceedings of the 53rd IEEE Conference on Decision and Control, Los Angeles, USA*, 2014.

[9] E. S. Bjørne, *Nonlinear Adaptive Motion Control and Model-Error Analysis for Ships*. MSc thesis. Dept. of Engineering Cybernetics, Norwegian University of Science and Technology, Trondheim, Norway, 2016.

[10] M. Krstic, I. Kanellakopoulos, and P. V. Kokotovic, *Nonlinear and Adaptive Control Design*. Wiley, 1995.

[11] F. Sandved, *Remote Control and Automatic Path-following for C/S Enterprise I and ROV Neptunus*. MSc thesis. Dept. of Marine Technology, Norwegian University of Science and Technology, Trondheim, Norway, 2015.

[12] T. I. Fossen, *Handbook of Marine Craft Hydrodynamics and Motion Control*. Wiley, 2011.

[13] R. Skjetne, Ø. N. Smogeli, and T. I. Fossen, "Nonlinear Ship Manoeuvering Model: Identification and Adaptive Control with Experiments for a Model Ship," *Modeling, Identification and Control*, vol. 25 , no. 1, pp. 3–27, 2004.

[14] T. I. Fossen and J. P. Strand, "Tutorial on Nonlinear Backstepping: Applications to Ship Control," *Modeling, Identification and Control*, vol. 20 , no. 2, pp. 83–135, 1999.

[15] J.-J. E. Slotine and W. Li, *Applied Nonlinear Control*. Prentice Hall, 1991.

[16] H. K. Khalil, *Nonlinear Systems*. Prentice Hall, 2002.

[17] F. Lamnabhi-Lagarrigue, E. Panteley, E. Lefeber, and A. Loria, *Advanced Topics in Control Systems Theory: Lecture Notes from FAP 2004*. Springer, 2005.

A.6 A Ship Heading and Speed Control Concept Inherently Satisfying Actuator Constraints

M. E. N. Sørensen, M. Breivik, and B.-O. H. Eriksen, A ship heading and speed control concept inherently satisfying actuator constraints, *in Proceedings of the 1st IEEE Conference on Control Technology and Applications, Hawai'i, USA*, 2017.

A Ship Heading and Speed Control Concept Inherently Satisfying Actuator Constraints

Mikkel Eske Nørgaard Sørensen, Morten Breivik and Bjørn-Olav H. Eriksen

***Abstract*— Satisfying actuator constraints is often not considered in the academic literature on the design of ship heading and speed controllers. This paper considers the use of a simplified dynamic window algorithm as a way to ensure that actuator constraints are satisfied. To accomplish this, we use the simplified dynamic window algorithm as a dynamic window-based controller (DWC) to guarantee that the velocities remain within a set of feasible boundaries, while simultaneously respecting the actuator constraints. We also develop a modified nonlinear ship model on which to test the proposed concept. The DWC is compared with a more traditional ship heading and speed controller, using performance metrics which consider both control accuracy and energy use.**

I. INTRODUCTION

When a ship sails the sea, its autopilot system usually leads the ship along the desired heading. Numerous motion controllers and autopilots have been proposed over the years. However, many control algorithms found in the literature do not consider saturation constraints for the actuators. Examples of traditional control designs for ship autopilot systems are given in [1]. Not considering actuator constraints may lead to unsatisfying performance or stability issues. In [2], a gain-scheduled control law is developed and tested for handling actuator constraints for a rudder-roll model of a ship.

In [3], the dynamic window (DW) algorithm is suggested as a method to perform collision avoidance and deal with constraints imposed by limited velocities and accelerations for mobile robots. This algorithm first generates a set of possible trajectories. Based on these trajectories, a search space of possible velocities can be approximated. The acceleration constrains are considered by limiting the search space to reachable velocities within a next time interval. To reduce the search space even further, all non-admissible velocities are removed to make the vehicle stop safely before it reaches the closest obstacle on the corresponding trajectory.

The DW algorithm is modified for AUVs in [4] and shows promising results for handling magnitude and rate constraints for the actuators. In this paper, we consider a simplification of the DW algorithm in [4], by removing the collision avoidance part of the algorithm. In particular, this DW-based controller (DWC) will be combined with a heading controller based on the design in [5].

The contribution of this paperis the proposal of the DWC, which inherently satisfies actuator constraints. Furthermore, necessary modifications to a 3 degrees-of-freedom nonlinear ship model based on [6] are done, in order to achieve a more physically realistic behavior. The DWC is compared with a traditional controller (TC) from [5], and the performance of the controllers are compared through simulations, where the comparison is made using performance metrics which consider both control accuracy and energy use.

The structure of the paper is as follows: A mathematical ship model and assumptions are presented in Section II; Section III describes the assumptions and control objective; Section IV presents the design of a traditional control inspired by backstepping and constant-bearing guidance; Section V presents the proposed DWC concept; Section VI presents simulation results; while Section VII concludes the paper.

II. SHIP MODEL

The motion of a ship can be represented by the pose vector $\boldsymbol{\eta} = [x, y, \psi]^\top \in \mathbb{R}^2 \times \mathbb{S}$ and the velocity vector $\boldsymbol{\nu} = [u, v, r]^\top \in \mathbb{R}^3$. Here, (x, y) represents the Cartesian position in the local earth-fixed reference frame, ψ is the yaw angle, (u, v) represents the body-fixed linear velocities and r is the yaw rate. The 3 degrees-of-freedom dynamics of a ship can then be stated as [1]:

$$\dot{\boldsymbol{\eta}} = \boldsymbol{R}(\psi)\boldsymbol{\nu} \tag{1}$$

$$\boldsymbol{M}\dot{\boldsymbol{\nu}} + \boldsymbol{C}(\boldsymbol{\nu})\boldsymbol{\nu} + \boldsymbol{D}(\boldsymbol{\nu})\boldsymbol{\nu} = \boldsymbol{\tau}, \tag{2}$$

where $\boldsymbol{M} \in \mathbb{R}^{3\times3}$, $\boldsymbol{C}(\boldsymbol{\nu}) \in \mathbb{R}^{3\times3}$, $\boldsymbol{D}(\boldsymbol{\nu}) \in \mathbb{R}^{3\times3}$ and $\boldsymbol{\tau} = [\tau_1, \tau_2, \tau_3]^\top$ represent the inertia matrix, Coriolis and centripetal matrix, damping matrix and control input vector, respectively. The rotation matrix $\boldsymbol{R}(\psi) \in SO(3)$ is given by

$$\boldsymbol{R}(\psi) = \begin{bmatrix} \cos(\psi) & -\sin(\psi) & 0 \\ \sin(\psi) & \cos(\psi) & 0 \\ 0 & 0 & 1 \end{bmatrix}. \tag{3}$$

The system matrices are assumed to satisfy the properties $\boldsymbol{M} = \boldsymbol{M}^\top > 0$, $\boldsymbol{C}(\boldsymbol{\nu}) = -\boldsymbol{C}(\boldsymbol{\nu})^\top$ and $\boldsymbol{D}(\boldsymbol{\nu}) > 0$.

A. Nominal Model

The model and parameters of the model-scale ship CyberShip II [6] will be used for control design and evaluation through numerical simulations in this paper. CyberShip II is a 1:70 scale replica of a supply ship, with a length of $L = 1.255$ m. The inertia matrix is given as

$$\boldsymbol{M} = \boldsymbol{M}_{RB} + \boldsymbol{M}_A, \tag{4}$$

M. E. N. Sørensen, M. Breivik and B.-O. H. Eriksen are with the Centre for Autonomous Marine Operations and Systems, Department of Engineering Cybernetics, Norwegian University of Science and Technology (NTNU), NO-7491 Trondheim, Norway. Email: {`Mikkel.E.N.Sorensen`, `morten.breivik`, `bjorn-olav.h.eriksen`}`@ieee.org`

where

$$\boldsymbol{M}_{RB} = \begin{bmatrix} m & 0 & 0 \\ 0 & m & mx_g \\ 0 & mx_g & I_z \end{bmatrix} \tag{5}$$

$$\boldsymbol{M}_{A} = \begin{bmatrix} -X_{\dot{u}} & 0 & 0 \\ 0 & -Y_{\dot{v}} & -Y_{\dot{r}} \\ 0 & -N_{\dot{v}} & -N_{\dot{r}} \end{bmatrix}. \tag{6}$$

The mass of CyberShip II is $m = 23.8$ kg, while $x_g = 0.046$ m is the distance along the x-axis in the body frame from the centre of gravity, and $I_z = 1.760\ \mathrm{kg\,m^2}$ is the the moment of inertia about the z-axis in the body frame. Other parameter values are listed in Table I. The Coriolis and centripetal matrix is

$$\boldsymbol{C}(\boldsymbol{\nu}) = \boldsymbol{C}_{RB}(\boldsymbol{\nu}) + \boldsymbol{C}_{A}(\boldsymbol{\nu}), \tag{7}$$

with

$$\boldsymbol{C}_{RB}(\boldsymbol{\nu}) = \begin{bmatrix} 0 & 0 & -m(x_g r + v) \\ 0 & 0 & mu \\ m(x_g r + v) & -mu & 0 \end{bmatrix} \tag{8}$$

$$\boldsymbol{C}_{A}(\boldsymbol{\nu}) = \begin{bmatrix} 0 & 0 & -c_{A,13}(\boldsymbol{\nu}) \\ 0 & 0 & c_{A,23}(\boldsymbol{\nu}) \\ c_{A,13}(\boldsymbol{\nu}) & -c_{A,23}(\boldsymbol{\nu}) & 0 \end{bmatrix}, \tag{9}$$

where

$$c_{A,13}(\boldsymbol{\nu}) = -Y_{\dot{v}} v - \frac{1}{2}(N_{\dot{v}} + Y_{\dot{r}})r \tag{10}$$

$$c_{A,23}(\boldsymbol{\nu}) = -X_{\dot{u}} u. \tag{11}$$

Finally, the damping matrix $\boldsymbol{D}(\boldsymbol{\nu})$ is given as

$$\boldsymbol{D}(\boldsymbol{\nu}) = \boldsymbol{D}_L + \boldsymbol{D}_{NL}(\boldsymbol{\nu}), \tag{12}$$

where

$$\boldsymbol{D}_{L} = \begin{bmatrix} -X_{u} & 0 & 0 \\ 0 & -Y_{v} & -Y_{r} \\ 0 & -N_{v} & -N_{r} \end{bmatrix} \tag{13}$$

$$\boldsymbol{D}_{NL}(\boldsymbol{\nu}) = \begin{bmatrix} d_{NL,11}(\boldsymbol{\nu}) & 0 & 0 \\ 0 & d_{NL,22}(\boldsymbol{\nu}) & d_{NL,23}(\boldsymbol{\nu}) \\ 0 & d_{NL,32}(\boldsymbol{\nu}) & d_{NL,33}(\boldsymbol{\nu}) \end{bmatrix}, \tag{14}$$

and

$$d_{NL,11}(\boldsymbol{\nu}) = -X_{|u|u}|u| - X_{uuu}u^2 \tag{15}$$

$$d_{NL,22}(\boldsymbol{\nu}) = -Y_{|v|v}|v| - Y_{|r|v}|r| \tag{16}$$

$$d_{NL,23}(\boldsymbol{\nu}) = -Y_{|v|r}|v| - Y_{|r|r}|r| \tag{17}$$

$$d_{NL,32}(\boldsymbol{\nu}) = -N_{|v|v}|v| - N_{|r|v}|r| \tag{18}$$

$$d_{NL,33}(\boldsymbol{\nu}) = -N_{|v|r}|v| - N_{|r|r}|r|. \tag{19}$$

TABLE I: Parameters for CyberShip II [6]

Parameter	**Value**	**Parameter**	**Value**
$X_{\dot{u}}$	-2	N_v	0.03130
$Y_{\dot{v}}$	-10	$N_{\|v\|v}$	3.95645
$Y_{\dot{r}}$	0	$Y_{\|r\|v}$	-0.805
$N_{\dot{v}}$	0	Y_r	-7.250
$N_{\dot{r}}$	-1	$Y_{\|v\|r}$	-0.845
X_u	-0.72253	$Y_{\|r\|r}$	-3.450
$X_{\|u\|u}$	-1.32742	$Y_{\|v\|r}$	0.080
X_{uuu}	-5.86643	$N_{\|r\|v}$	0.130
Y_v	-0.88965	N_r	-1.900
$Y_{\|v\|v}$	-36.47287	$N_{\|r\|r}$	-0.750

The considered model describes a fully actuated ship. However, heading and speed controllers are typically used at higher speeds, where the ship is underactuated. We have therefore excluded the bow thruster from the actuator model since it loses its effectiveness at high speeds. Inspired by [6], the modified ship actuator forces and moments can be modelled using two thrusters $\boldsymbol{n} = [n_1, n_2]^\top \in \mathbb{R}^2$ with revolutions per second (rps) and two rudder angles $\boldsymbol{\delta} = [\delta_1, \delta_2]^\top \in \mathbb{S}^2$. These are related to the input vector $\boldsymbol{\tau}$ through the actuator model

$$\boldsymbol{\tau}(\boldsymbol{\nu}, \boldsymbol{n}, \boldsymbol{\delta}) = \boldsymbol{B}\boldsymbol{\tau}_{act}(\boldsymbol{\nu}, \boldsymbol{n}, \boldsymbol{\delta}), \tag{20}$$

where $\boldsymbol{B} \in \mathbb{R}^{3\times 4}$ is an actuator configuration matrix. The function $\boldsymbol{\tau}_{act} : \mathbb{R}^3 \times \mathbb{R}^2 \times \mathbb{S}^2 \to \mathbb{R}^4$ relates the actuator variables $\boldsymbol{n}$ and $\boldsymbol{\delta}$ to the input vector $\boldsymbol{\tau}$ for a given velocity $\boldsymbol{\nu}$. The actuator configuration matrix and actuator force vector is

$$\boldsymbol{B} = \begin{bmatrix} 1 & 1 & 0 & 0 \\ 0 & 0 & 1 & 1 \\ |l_{yT_1}| & -|l_{yT_2}| & -|l_{xR_1}| & -|l_{xR_2}| \end{bmatrix}. \tag{21}$$

Moreover, $\boldsymbol{\tau}_{act}$ is given by

$$\boldsymbol{\tau}_{act} = [T_1, T_2, L_1, L_2]^\top, \tag{22}$$

with

$$T_i \triangleq T_{|n|n}|n_i|n_i - T_{|n|u}|n_i|u, \quad \text{for } i = 1, 2 \tag{23}$$

$$L_i \triangleq (L_\delta \delta_i - L_{|\delta|\delta}|\delta_i|\delta_i)|u|u, \quad \text{for } i = 1, 2, \tag{24}$$

where T_i is the thrust force from the preceding propeller and L_i is the lift force from the preceding rudder. The constants $l_{yT_1}, l_{yT_2}, l_{xR_1}, l_{xR_2}$ represent physical placements of the actuators, and the parameters $T_{|n|n}, T_{|n|u}, L_\delta, L_{|\delta|\delta}$ are positive coefficients. It should be noted that (24) is dependent on the surge speed, which leads to a saturation constraint of the yaw moment having a nonlinear behavior, which is 0 if the surge speed is 0. In [6], the actuator variable limitations are stated as $n_i \in [0, 33.33]$ rps and $\delta_i \in [-35, 35]$ deg. Based on (20)-(24), infinitely many combinations of the actuator variables $\boldsymbol{n}$ and $\boldsymbol{\delta}$ can generate the input vector $\boldsymbol{\tau}$. Here, we assume that $n_1 = n_2$ and $\delta_1 = \delta_2$. We will only consider the control of the surge and yaw motion, since our model is underactuated.

Using this ship model, we can map the steady-state solution of (2) associated with a given control input. In particular, the blue asterisks in Fig. 1 represent the steady-state solutions for a set of uniformly distributed control inputs. Analysing the model from [6], it is concluded that the modelled Munk moment, which is a destabilizing factor, give rise to physically impossible motion. In this model, the equilibrium point at $r = 0$ is unstable, which is not consistent with the actual behavior of CyberShip II.

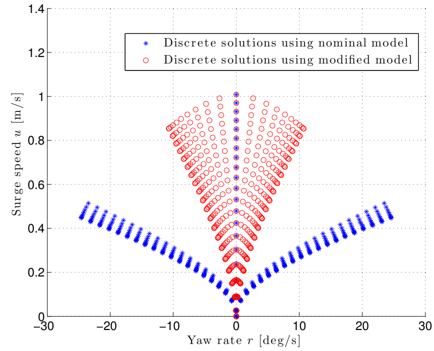

Fig. 1: Possible combinations of surge speed and yaw rate using the same control inputs for the nominal model [6] (blue) and the modified model based on [7] (red).

B. Modified Model

In [7], an analysis on how to accommodate for the Munk moment on an AUV is made. It is suggested to add damping terms to the damping matrix that are linearly increasing with the forward speed. Based on the observation in [7], we change (17)-(19) to

$$d_{NL,23}(\boldsymbol{\nu}) = -Y_{|v|r}|v| - Y_{|r|r}|r| - Y_{ur}u \tag{25}$$
$$d_{NL,32}(\boldsymbol{\nu}) = -N_{|v|v}|v| - N_{|r|v}|r| - N_{uv}u \tag{26}$$
$$d_{NL,33}(\boldsymbol{\nu}) = -N_{|v|r}|v| - N_{|r|r}|r| - N_{ur}u, \tag{27}$$

where

$$Y_{ur} = X_{\dot{u}} \tag{28}$$
$$N_{uv} = -(Y_{\dot{u}} - X_{\dot{u}}) \tag{29}$$
$$N_{ur} = Y_{\dot{r}}, \tag{30}$$

to get a more physically realistic model behavior. The red circles in Fig. 1 show the steady-state solutions for the combined [6] and [7] model using the same set of control inputs as previously. The steady-state response of this modified model qualitatively corresponds to the experimentally derived response of a high-speed boat in [8].

III. ASSUMPTIONS AND CONTROL OBJECTIVE

It is assumed that both the pose vector $\boldsymbol{\eta}(t)$ and velocity vector $\boldsymbol{\nu}(t)$ can be measured, and that no disturbances and uncertainties affect the system.

The control objective is to make $\tilde{\psi}(t) \triangleq \psi(t) - \psi_t(t) \to 0$ as $t \to \infty$ and $\tilde{u}(t) \triangleq u(t) - u_t(t) \to 0$ as $t \to \infty$, where $\psi_t(t) \in \mathbb{S}$ represents the heading associated with a target ship and u_t is the target surge speed. Furthermore, $\psi_t(t)$ is $\mathcal{C}^2$ and bounded. The motion of the target ship is typically defined by a human or generated by a guidance system.

For notational simplicity, the time t is omitted in most of this paper.

IV. TRADITIONAL CONTROL DESIGN

Using a combination of a cascaded feedback controller [5] and a dynamic feedback controller where the dynamics of the uncontrolled sway mode enters the yaw control law [9], the control input can be chosen as

$$\boldsymbol{\tau} = \boldsymbol{M}\dot{\boldsymbol{\alpha}} + \boldsymbol{C}(\boldsymbol{\nu})\boldsymbol{\alpha} + \boldsymbol{D}(\boldsymbol{\nu})\boldsymbol{\alpha} - \boldsymbol{K}_2(\cdot)\boldsymbol{z}_2. \tag{31}$$

The error variables z_1 and $\boldsymbol{z}_2 = [z_{2,u}, z_{2,v}, z_{2,r}]^\top$ are defined as

$$z_1 \triangleq \psi - \psi_t \tag{32}$$
$$\boldsymbol{z}_2 \triangleq \boldsymbol{\nu} - \boldsymbol{\alpha}, \tag{33}$$

where $\boldsymbol{\alpha} = [\alpha_u, \alpha_v, \alpha_r] \in \mathbb{R}^3$ is a vector of stabilising functions, which can be interpreted as a desired velocity

$$\alpha_u = u_t \tag{34}$$
$$\alpha_r = \dot{\psi}_t - K_1(\cdot)z_1, \tag{35}$$

where

$$K_1(\cdot) = \Gamma_1 \frac{1}{\sqrt{z_1^2 + \Delta_{\tilde{\psi}}^2}}, \tag{36}$$

represents a nonlinear control gain with $\Gamma_1 > 0$ and $\Delta_{\tilde{\psi}} > 0$. The nonlinear feedback term in (31) is given as

$$\boldsymbol{K}_2(\cdot) = \boldsymbol{\Gamma}_2 \begin{bmatrix} \frac{1}{\sqrt{\boldsymbol{z}_{2,\tilde{v}}^\top \boldsymbol{z}_{2,\tilde{v}} + \Delta_{\tilde{v}}^2}} \boldsymbol{I}_{2\times 2} & \boldsymbol{0}_{2\times 1} \\ \boldsymbol{0}_{1\times 2} & \frac{1}{\sqrt{z_{2,\tilde{r}}^2 + \Delta_{\tilde{r}}^2}} \end{bmatrix}, \tag{37}$$

with the control gain $\boldsymbol{\Gamma}_2 > 0$, where $\boldsymbol{z}_{2,\tilde{v}}$ is defined as $\boldsymbol{z}_{2,\tilde{v}} \triangleq [z_{2,u}, z_{2,v}]^\top$, $\Delta_{\tilde{v}} > 0$ and $\Delta_{\tilde{r}} > 0$. The time derivative of the vector of stabilising functions then becomes

$$\dot{\boldsymbol{\alpha}} = [\dot{u}_t, \dot{\alpha}_v, \dot{\alpha}_r]^\top, \tag{38}$$

where $\dot{u}_t$ is the target surge acceleration and

$$\dot{\alpha}_r = \ddot{\psi}_t - \dot{K}_1(z_1, \Delta_i)z_1 - K_1(z_1, \Delta_i)\dot{z}_1, \tag{39}$$

with

$$\dot{z}_1 = -K_1(\cdot)z_1 + z_{2,\tilde{r}}, \tag{40}$$

and

$$\dot{K}_1(\cdot) = \Gamma_1 \frac{z_1 \dot{z}_1}{(z_1^2 + \Delta_{\tilde{\psi}}^2)^{\frac{3}{2}}}. \tag{41}$$

Based on design of the dynamics of the uncontrolled sway mode in [9], the variable α_v is a dynamic state of the controller, and is given by

$$m_{22}\dot{\alpha}_v = -d_{22}(\boldsymbol{\nu})\alpha_v + \gamma(\alpha_r, \dot{\alpha}_r, \boldsymbol{z}_2), \tag{42}$$

where

$$\gamma(\alpha_r, \dot{\alpha}_r, \boldsymbol{z}_2) = K_{2,22}(\cdot)z_{2,v} - m_{23}\dot{\alpha}_r - d_{23}(\boldsymbol{\nu})\alpha_r - c_{23}(\boldsymbol{\nu})\alpha_r, \tag{43}$$

and m_{ij}, $c_{ij}(\boldsymbol{\nu})$, $d_{ij}(\boldsymbol{\nu})$ and $K_{2,ij}(\cdot)$ are components at the ith row and jth column of the matrices $\boldsymbol{M}$, $\boldsymbol{C}(\boldsymbol{\nu})$, $\boldsymbol{D}(\boldsymbol{\nu})$ and $\boldsymbol{K}_2(\cdot)$, while

$$\alpha_v = \int_0^t \dot{\alpha}_v(\sigma)\mathrm{d}\sigma, \quad \alpha_v(0) = v(0). \tag{44}$$

V. DYNAMIC WINDOW-BASED CONTROL DESIGN

A. Simplified Dynamic Window Algorithm

Here, we describe a step-by-step design procedure for a simplified version of the dynamic window (DW) algorithm presented in [4] by removing the collision avoidance part of the algorithm.

Based on the modified ship model and its actuator magnitude constraints, a set of possible velocities can be found. This set contains all velocities the ship can achieve, with respect to the actuator constraints. The possible velocities can be found by computing the steady-state solution of the kinetics (2) for all possible control inputs:

$$\boldsymbol{\tau}(\boldsymbol{\nu}_{ss}, \boldsymbol{n}, \boldsymbol{\delta}) = \boldsymbol{C}(\boldsymbol{\nu}_{ss})\boldsymbol{\nu}_{ss} + \boldsymbol{D}(\boldsymbol{\nu}_{ss})\boldsymbol{\nu}_{ss}, \tag{45}$$

within the actuator magnitude constraints

$$n_i \in [0, 33.33] \text{ rps} \tag{46}$$

$$\delta_i \in [-30, 30] \text{ deg.} \tag{47}$$

The steady-state solutions of (45)-(47) for a uniformly distributed set of the control inputs is shown in Fig. 2. By designing an approximation of the boundaries, the set of possible velocities can be defined as:

$$V_p = \{(u, r) \in \mathbb{R} \times \mathbb{R} | g(u, r) \geq 0\}, \tag{48}$$

where $g(u, r)$ is greater than or equal to zero for valid solutions of (45)-(47), and negative otherwise. Given m approximated boundaries, defined by the functions $h_a(u, r) = 0$, $a \in \{1, 2, ..., m\}$ where $\nabla h_a(u, r)$ is required to be pointing inwards to the valid solutions, the approximated $g(u, r)$ is given as:

$$g(u, r) = \min(h_1(u, r), h_2(u, r), ..., h_m(u, r)). \tag{49}$$

In Fig. 3, a plot of the function $g(u, r)$ is shown.

Next, the space of reachable points within a time step T needs to be defined. This is done by finding acceleration limits, and based on these, the set of reachable velocities can be computed. The possible ship accelerations can be found by evaluating

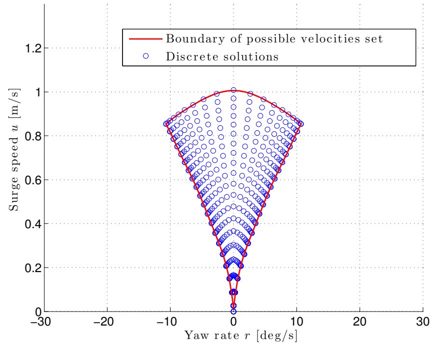

Fig. 2: Possible combinations of surge speed and yaw rate, with respect to actuator magnitude limits. The approximated boundary of V_p is shown as the red line.

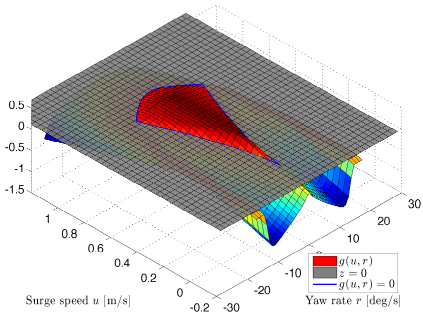

Fig. 3: Function to find possible velocities.

$$\dot{\boldsymbol{\nu}} = \boldsymbol{M}^{-1}(\boldsymbol{\tau}(\boldsymbol{\nu}^*, \boldsymbol{n}, \boldsymbol{\delta}) - \boldsymbol{C}(\boldsymbol{\nu}^*)\boldsymbol{\nu}^* - \boldsymbol{D}(\boldsymbol{\nu}^*)\boldsymbol{\nu}^*), \tag{50}$$

for the current velocity $\boldsymbol{\nu}^* = \boldsymbol{\nu}(t)$ and boundaries of the control input vector. The acceleration limits at the current time step can be computed as:

$$\begin{aligned}\dot{\boldsymbol{\nu}}_{min} = \boldsymbol{M}^{-1}(\boldsymbol{\tau}(\boldsymbol{\nu}^*, \boldsymbol{n}_{min}, \boldsymbol{\delta}_{max}) - \boldsymbol{C}(\boldsymbol{\nu}^*)\boldsymbol{\nu}^* \\ - \boldsymbol{D}(\boldsymbol{\nu}^*)\boldsymbol{\nu}^*)\end{aligned} \tag{51}$$

$$\begin{aligned}\dot{\boldsymbol{\nu}}_{max} = \boldsymbol{M}^{-1}(\boldsymbol{\tau}(\boldsymbol{\nu}^*, \boldsymbol{n}_{max}, \boldsymbol{\delta}_{min}) - \boldsymbol{C}(\boldsymbol{\nu}^*)\boldsymbol{\nu}^* \\ - \boldsymbol{D}(\boldsymbol{\nu}^*)\boldsymbol{\nu}^*).\end{aligned} \tag{52}$$

It should be noted that this method does not consider actuator rate saturations. However, by introducing dynamics to the control input vector $\boldsymbol{\tau}$, the algorithm can also be further developed to handle rate constraints. Additionally, it is worth noticing that a positive rudder deflection results in a negative yaw moment.

Using T as the time allowed for acceleration during the next time step, the dynamic velocity window is then defined using the acceleration limits from (51) and (52) as

$$\begin{aligned}V_w = \{(u, r) \in \mathbb{R} \times \mathbb{R} | u \in [u^* + \dot{u}_{min}T, u^* + \dot{u}_{max}T] \\ \wedge r \in [r^* + \dot{r}_{min}T, r^* + \dot{r}_{max}T]\}.\end{aligned} \tag{53}$$

The set of dynamically feasible velocities is defined as

$$V_f \triangleq V_p \cap V_w. \tag{54}$$

Next, the set of dynamically feasible velocities V_f is discretized uniformly to obtain a discrete set of dynamically feasible velocity pairs.

The desired velocity is defined as

$$\boldsymbol{\nu}_{1d} \triangleq [u_d, r_d]^\top, \tag{55}$$

since the focus is on controlling the surge and yaw rate. Given $\boldsymbol{\nu}_{1t}$, the optimal velocity pair $\boldsymbol{\nu}_{1f} = [u_f, r_f]^\top$ can be selected as

$$\boldsymbol{\nu}_{1f} = \underset{(u,r)\in V_f}{\arg\max}\; G(u, u_d, r, r_d), \tag{56}$$

where $G(u, u_d, r, r_d)$ is an objective function, which is defined as

$$G(u, u_d, r, r_d) \overset{\triangle}{=} \text{surge}(u, u_d) + \text{yawrate}(r, r_d), \tag{57}$$

with

$$\text{surge}(u, u_d) = 1 - \frac{|u_d - u|}{\max\limits_{u'\in V_f}(|u_d - u'|)} \in [0, 1] \tag{58}$$

$$\text{yawrate}(r, r_d) = 1 - \frac{|r_d - r|}{\max\limits_{r'\in V_f}(|r_d - r'|)} \in [0, 1]. \tag{59}$$

Notice that by using this objective function, we minimise the scaled 1-norm of the entire discrete set of dynamically feasible velocity pairs. In [3], [4] and [10], a distance function and tuningparameters are used to achieve collision avoidance, but this function is removed here since we only focus on handling actuator constraints. As a result, the tuning parameters also become redundant since the remaining two functions are orthogonal to each other. Fig. 4 illustrates V_p, V_w, V_f and $\boldsymbol{\nu}_{1d} = [0.79 \text{ m/s } 4.0107 \text{ deg/s}]$ given a current velocity pair of $[0.76 \text{ m/s } 5.6723 \text{ deg/s}]$.

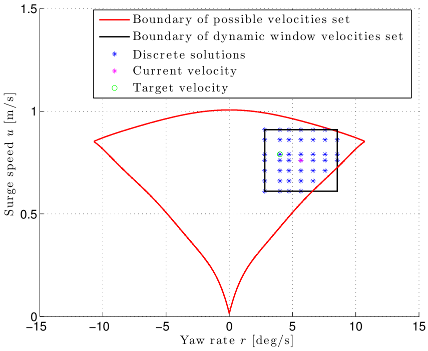

Fig. 4: The dynamically feasible velocity set, surrounded by the boundaries of the dynamic velocity window and the possible velocity set.

B. Dynamic Window-based Controller

We now combine the traditional control design with the simplified DW algorithm in order to develop a dynamic window-based controller (DWC).

In this setup, the simplified DW algorithm will use $\boldsymbol{\alpha}_1 = [\alpha_u, \alpha_r]^\top$ as an input such that $\boldsymbol{\nu}_{1d} = \boldsymbol{\alpha}_1$. In the case where $\boldsymbol{\alpha}_1$ is an infeasible velocity, the simplified DW algorithm will modify $\boldsymbol{\alpha}_1$ to a feasible velocity $\boldsymbol{\alpha}_{1f} = [\alpha_{f,u}, \alpha_{f,r}]^\top$, otherwise $\boldsymbol{\alpha}_{1f} = \boldsymbol{\alpha}_1$. A pseudocode of the simplified DW algorithm is shown in Algorithm 1.

Algorithm 1 Pseudocode of the simplified DW algorithm

```
$V_w$ is calculated using (51) to (53) and discretized uniformly
if the desired velocity vector $\alpha_1 \in V_f$ then
    The closest reachable velocity row and column to $\alpha_1$ is shifted such that $\alpha_1$ is one of the reachable velocity pairs in $V_w$
end if
Remove all the reachable velocity pairs in $V_w$ which are outside of the $g(u, r)$ boundaries to describe the set of dynamically feasible velocities $V_f$.
Select the optimal velocity pair $\alpha_{1f}$ through maximizing the objective function (57) over the discrete feasible search space $V_f = V_p \cap V_w$
```

After the optimal velocity pair $\boldsymbol{\alpha}_{1f}$ is found, the vector of stabilising functions is given as

$$\boldsymbol{\alpha}_f = [\alpha_{f,u}, \alpha_{f,v}, \alpha_{f,r}]^\top, \tag{60}$$

where $\alpha_{f,v}$ is given as

$$\alpha_{f,v} = \int_0^t \dot{\alpha}_{f,v}(\sigma)\mathrm{d}\sigma, \quad \alpha_{f,v}(0) = v(0), \tag{61}$$

where

$$m_{22}\dot{\alpha}_{f,v} = -d_{22}(\boldsymbol{\nu})\alpha_{f,v} + \gamma(\alpha_r, \dot{\alpha}_r) \tag{62}$$

$$\gamma(\alpha_r, \dot{\alpha}_r) = -m_{23}\dot{\alpha}_r - d_{23}(\boldsymbol{\nu})\alpha_r - c_{23}(\boldsymbol{\nu})\alpha_r. \tag{63}$$

We want the ship to reach $\boldsymbol{\alpha}_f$ after time T, hence the desired acceleration is chosen to be

$$\dot{\boldsymbol{\alpha}}_{DWC} = \frac{\boldsymbol{\alpha}_f - \boldsymbol{\nu}}{T}, \tag{64}$$

which means that

$$\boldsymbol{\alpha}_{DWC} = \int_0^t \dot{\boldsymbol{\alpha}}_{DWC} d\sigma. \tag{65}$$

Both $\boldsymbol{\alpha}_{DWC}$ and $\dot{\boldsymbol{\alpha}}_{DWC}$ are used in the kinetic controller which is modified to

$$\boldsymbol{\tau} = \boldsymbol{M}\dot{\boldsymbol{\alpha}}_{DWC} + \boldsymbol{C}(\boldsymbol{\nu})\boldsymbol{\alpha}_{DWC} + \boldsymbol{D}(\boldsymbol{\nu})\boldsymbol{\alpha}_{DWC}. \tag{66}$$

The DWC uses the heading controller given in (35) together with the target speed u_t as inputs to the simplified DW algorithm, which is described in Algorithm 1, in order to determine the vector of stabilizing functions given in (60)-(63). Based on (60), the desired acceleration and velocity vectors are found using (64)-(65), which are used to construct the control input (66).

A block diagram of the new dynamic window-based controller is shown in Fig. 5.

C. Discussion

When comparing the control law in (66) against (31), it can be seen that the feedback term $-\boldsymbol{K}_2(\cdot)\boldsymbol{z}_2$ in (31) is not included in (66) since the DWC makes the optimal velocity pair track the target velocity by using (64)-(65). However, (66) can only fulfil the control objective when the

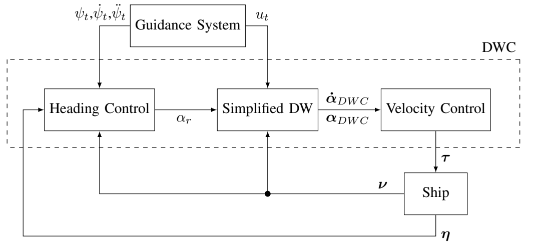

Fig. 5: Schematic structure of the dynamic window-based controller.

model is correct. In practice, when the model is not perfectly known, the control law (66) should also include a feedback term. This feedback term will also accommodate for internal uncertainties and external disturbances, instead of just controlling the surge speed and yaw rate. When the system is affected by internal uncertainties and external disturbances, the DWC will attempt to compensate for them since the DWC tries to find the optimal velocity pair. However, the performance in terms of robustness for the DWC is limited by the actuator constraints, which give a maximum bound on the uncertainties and disturbances which the controller can compensate for. This is similar to many robust controllers.

VI. SIMULATION AND EVALUATION

In this section, we present numerical simulation results of the considered heading and speed controllers using the model and actuator constraints of CyberShip II presented in Section II. In addition, performance metrics are used to evaluate the controller behavior.

The control target is defined as a constant heading $\psi_t = 30$ deg and a constant surge speed $u_t = 0.9$ m/s. Furthermore, the initial ship states are chosen to be $\boldsymbol{\eta}(0) = \mathbf{0}$ and $\boldsymbol{\nu}(0) = \mathbf{0}$. The chosen control gains are listed in Table II.

TABLE II: Control gains

	TC	**DWC**
Γ_1	0.0873	0.0873
$\boldsymbol{\Gamma}_2$	diag$([4, 4, 0.1745])\boldsymbol{M}$	–
$\Delta_{\tilde\psi}$	0.3	0.3
$\Delta_{\tilde v}$	10	–
$\Delta_{\tilde r}$	4	–

A. Performance Metrics

To evaluate and compare the performance of the two controllers, performance metrics are used. We define

$$e_1(t) \triangleq \sqrt{\tilde\psi^2} \tag{67}$$

$$e_2(t) \triangleq \sqrt{\tilde u_n^2 + \tilde r_n^2}, \tag{68}$$

as the error inputs for the performance metrics, with $\tilde u_n \triangleq u_n - u_{t,n}$ and $\tilde r_n \triangleq r_n - r_{t,n}$. Here, since the surge speed and yaw rate have different units, we define the normalized signals u_n, $u_{t,n}$, r_n and $r_{t,n}$ in the intervals $[0, 1]$ and $[-0.5, 0.5]$ in the expected operational space of the ship [8]. In addition, these signals represent the instantaneous control errors, while we would like to consider the accumulated errors over time. Hence, we use the performance metric IAE (integral of the absolute error)

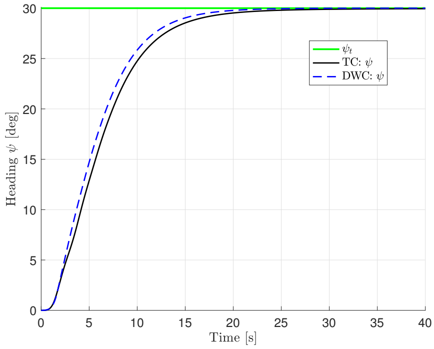

Fig. 6: Tracking the target heading.

$$IAE(e_i, t) \triangleq \int_0^t |e_i(\sigma)| d\sigma, \tag{69}$$

which integrates the temporal evolution of the absolute error. We also consider the integral of the absolute error multiplied by the energy consumption (IAEW), which was proposed earlier in [11] as

$$IAEW(e_i, t) \triangleq \int_0^t |e_i(\sigma)| d\sigma \int_0^t P(\sigma) d\sigma, \tag{70}$$

where

$$P(t) = |\boldsymbol{\nu}(t)^\top \boldsymbol{\tau}(t)| \tag{71}$$

represents the mechanical power. IAEW thus indicates which controller has the best combined control accuracy and energy use in one single metric.

B. Simulation Results

In Fig. 6, the ship and target heading is plotted to show the transient convergence behavior. It can be seen that both control laws manage to converge the target heading in about 25 seconds, but the DWC gives a slightly faster convergence.

Fig. 7 shows the surge speed and yaw rate of the ship together with the target surge speed and yaw rate. It can be seen that both control laws are able to track the target speed and yaw rate even though the DWC does not have a traditional velocity feedback term. Additionally, it can be seen that there is a difference in how fast the controllers are able to make the surge speed and yaw rate converge to the target since the DWC makes the surge speed converge in less than 5 seconds but it takes about 10 seconds for the surge speed to converge using the TC. Notice that the trajectory

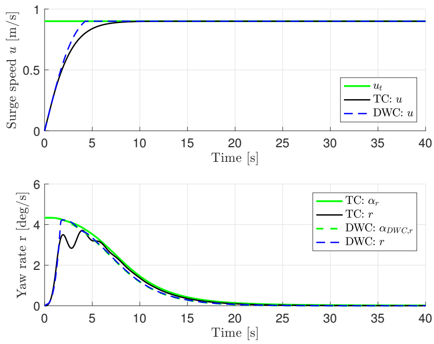

Fig. 7: Tracking of the surge speed (top) and yaw rate (bottom).

of α_r is different for the two controllers since it depends on the tracking performance of the heading.

Fig. 8 shows that the DWC commands the control inputs to stay at the maximum magnitude constraints of the actuators for a longer time than the control inputs from TC. These constraints (red lines) are calculated by using (20)-(24) and the limits of n_i and δ_i given in (46)-(47). The DWC keeps the control inputs at the maximum magnitude constraints of the actuators as long as possible, since the DWC tracks the optimal velocity pair $\boldsymbol{\alpha}_{1f}$ which is on the boundaries for the window unless the target velocity pair $\boldsymbol{\alpha}_1$ is inside the velocity window, while the control inputs from TC have a more conservative behavior. The oscillations in the yaw moment control input of the TC is a side-effect the TC is because it tries to compensate for the nonlinear magnitude constraint in the yaw moment.

Fig. 9 illustrates how the surge speed and yaw rate moves in the velocity space in order to track the target heading and surge speed. Note that the considered controllers move along two different trajectories inside V_p in order to solve the same control problem.

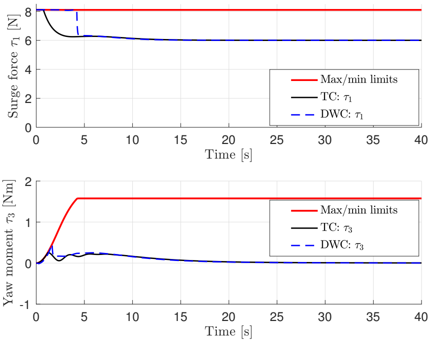

Fig. 8: The commanded surge force and yaw moment with magnitude limits.

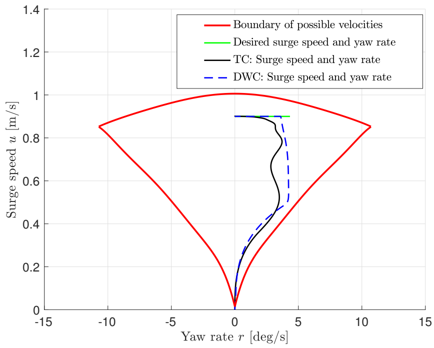

Fig. 9: Velocity trajectories in the set of possible velocities V_p, where the target heading and target speed are $\psi_t = 30$ deg and $u_t = 0.9$ m/s.

In Fig. 10, the performance metrics IAE and IAEW with e_1 as the error input are shown. In particular, the IAE trajectory in the top of Fig. 10 confirms that the DWC has a faster transient response since it converges faster to a stationary value. The IAEW trajectory in the bottom of Fig. 10 shows that the DWC uses a larger amount of energy to fulfil the control objective. However, the DWC has a faster transient response, which makes the DWC have a better overall performance.

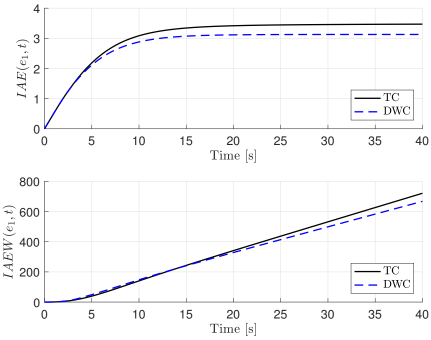

Fig. 10: IAE and IAEW performance metrics with $e_1 = \sqrt{\tilde{\psi}^2}$ as the error input.

Fig. 11 displays the performance metrics IAE and IAEW with e_2 as the error input, where a similar result as in Fig. 10 can be seen. Based on Fig. 10 and Fig. 11, it can be concluded that DWC has the better overall control performance for this scenario.

The presented results show that both the TC and the DWC stay within the boundaries in Fig. 9 and the tracking performance of the DWC is slightly faster, even though the DWC has fewer tuning parameters than the TC. It should be stated that the TC has been extensively tuned to get the optimal performance for this scenario and remain inside

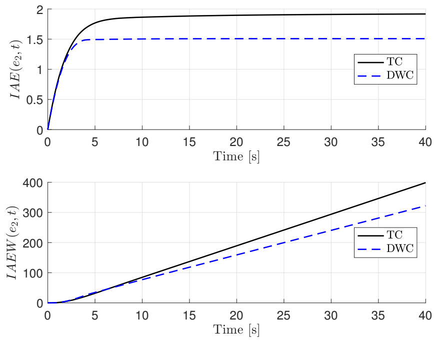

Fig. 11: IAE and IAEW performance metrics with $e_2 = \sqrt{\tilde{u}_n^2 + \tilde{r}_n^2}$ as the error input.

velocity boundaries, but it still falls short. For experimental purposes, it is suggested to add a feedback term to (66) in order to accommodate for model uncertainties and external disturbances.

One of the advantages of using DWC can be shown by changing the target heading and target speed to $\psi_t = 90$ deg and $u_t = 0.6$ m/s, but keeping the control gains unchanged. Fig. 12 shows the velocity trajectories for this scenario, where it can be seen that the TC yields velocities outside the boundaries, which means that the TC does not inherently satisfy the actuator constraints, while the DWC continues to stay inside the boundaries. Additionally, the TC also has some unwanted oscillations.

VII. CONCLUSION

This paper has proposed the use of a simplified dynamic window algorithm as a way to ensure that the actuator constraints of a ship are satisfied. This algorithm has been used as a dynamic window-based controller (DWC) to guarantee that that ship velocities remain within a feasible set. An existing nonlinear dynamic model of a ship was modified to make it more physically realistic. Additionally, a DWC was evaluated against a heading and speed controller using a traditional design approach. Both methods were compared through numerical simulations. Two performance metrics were used to compare the behaviour of the controllers. The simulation results showed good tracking performance of the considered controllers, and that the dynamic window-based controller was able to inherently handle actuator magnitude constraints.

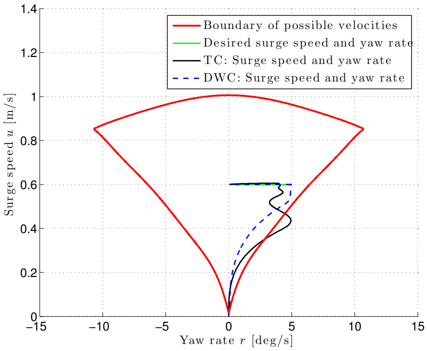

Fig. 12: Velocity trajectories in the set of possible velocities V_p, where the target heading and target speed are changed to $\psi_t = 90$ deg and $u_t = 0.6$ m/s while keeping the control gains unchanged..

Future work will include introducing model uncertainties and unknown disturbances. It is also relevant to consider actuator rate constraints in addition to magnitude constraints.

ACKNOWLEDGEMENT

This work was supported by the Research Council of Norway through the Centres of Excellence funding scheme, project number 223254.

REFERENCES

[1] T. I. Fossen, *Handbook of Marine Craft Hydrodynamics and Motion Control*. Wiley, 2011.

[2] T. Lauvdal, *Stabilization of Linear Systems with Input Magnitude and Rate Saturations*. PhD thesis, Department of Engineering Cybernetics, Norwegian University of Science and Technology, Trondheim, Norway, 1998.

[3] D. Fox, W. Burgard, and S. Thrun, “The dynamic window approach to collision avoidance,” *IEEE Robotics & Automation Magazine*, vol. 4, no. 1, pp. 23–33, 1997.

[4] B.-O. H. Eriksen, M. Breivik, K. Y. Pettersen, and M. S. Wiig, “A modified dynamic window algorithm for horizontal collision avoidance for AUVs,” *in Proceedings of the IEEE Multi-Conference on Systems and Control, Buenos Aires, Argentina*, 2016.

[5] M. E. N. Sørensen and M. Breivik, “Comparing combinations of linear and nonlinear feedback terms for motion control of marine surface vessels,” *in Proceedings of the 10th IFAC Conference on Control Applications in Marine Systems, Trondheim, Norway*, 2016.

[6] R. Skjetne, *The Maneuvering Problem*. PhD thesis, Department of Engineering Cybernetics, Norwegian University of Science and Technology, Trondheim, Norway, 2005.

[7] J. E. Refsnes, *Nonlinear Model-Based Control of Slender Body AUVs*. PhD thesis, Department of Marine Technology, Norwegian University of Science and Technology, Trondheim, Norway, 2008.

[8] B.-O. H. Eriksen and M. Breivik, *Modeling, Identification and Control of High-Speed ASVs: Theory and Experiments*, pp. 407–431. Cham: Sensing and Control for Autonomous Vehicles: Applications to Land, Water and Air Vehicles, Springer International Publishing, 2017.

[9] T. I. Fossen, M. Breivik, and R. Skjetne, “Line-of-sight path following of underactuated marine craft,” *in Proceedings of the 6th IFAC Conference on Manoeuvring and Control of Marine Craft, Girona, Spain*, 2003.

[10] P. Ögren and N. E. Leonard, “A convergent dynamic window approach to obstacle avoidance,” *IEEE Transactions on Robotics*, vol. 21, no. 2, pp. 188–195, 2005.

[11] M. E. N. Sørensen and M. Breivik, “Comparing nonlinear adaptive motion controllers for marine surface vessels,” *in Proceedings of the 10th IFAC Conference on Manoeuvring and Control of Marine Craft, Copenhagen, Denmark*, 2015.

A.7 AMOS DP Research Cruise 2016: Academic Full-scale Testing of Experimental Dynamic Positioning Control Algorithms Onboard R/V Gunnerus

R. Skjetne, M. E. N. Sørensen, M. Breivik, S. A. T. Værnø, A. H. Brodtkorb, A. J. Sørensen, Ø. K. Kjerstad, V. Calabrò and B. O. Vinje, AMOS DP research cruise 2016: Academic full-scale testing of experimental dynamic positioning control algorithms onboard R/V Gunnerus, *in Proceedings of the 36th International Conference on Ocean, Offshore and Arctic Engineering,Trondheim, Norway*, 2017.

AMOS DP RESEARCH CRUISE 2016: ACADEMIC FULL-SCALE TESTING OF EXPERIMENTAL DYNAMIC POSITIONING CONTROL ALGORITHMS ONBOARD R/V GUNNERUS

Roger Skjetne[*]
Department of Marine Technology
Norwegian Univ. Science & Technology
NO-7491 Trondheim, Norway
Email: roger.skjetne@ntnu.no

Mikkel E. N. Sørensen
Morten Breivik
Department of Engineering Cybernetics
Norwegian Univ. Science & Technology
NO-7491 Trondheim, Norway
Emails: mikkel.e.n.sorensen@ieee.org
morten.breivik@ieee.org

Svenn A. T. Værnø
Astrid H. Brodtkorb
Asgeir J. Sørensen
Department of Marine Technology
Norwegian Univ. Science & Technology
NO-7491 Trondheim, Norway
Emails: svenn.are.varno@ntnu.no
astrid.h.brodtkorb@ntnu.no
asgeir.sorensen@ntnu.no

Øivind K. Kjerstad
Arctic Technology Department
The University Centre in Svalbard
Norwegian Univ. Science & Technology
NO-9171 Longyearbyen, Norway
Email: oivind.kjerstad@unis.no

Vincenzo Calabrò
Bjørn Ole Vinje
Kongsberg Maritime
NO-3601 Kongsberg, Norway
Emails: v.calabro@ieee.org
bjorn.ole.vinje@km.kongsberg.com

ABSTRACT

In order to validate relevant dynamic positioning (DP) control algorithms in a realistic environment, a full-scale DP test campaign, the AMOS DP Research Cruise 2016 (ADPRC'16), was organized in a collaboration between the NTNU Centre for Autonomous Marine Operations and Systems (NTNU AMOS) and the company Kongsberg Maritime onboard the research vessel (R/V) Gunnerus. To the authors' best knowledge, closed-loop DP feedback control algorithms have never been tested full-scale on a ship in an academic research experiment before. However, we have now achieved this by coding our algorithms into a test-module of the DP system, as prepared by Kongsberg Maritime. Among the tested algorithms is an output feedback control law with both good transient and steady-state performance. In another experiment, different adaptive backstepping control laws for DP were tested to compare and contrast their performance and properties. A hybrid state observer with a performance monitoring function proposed to switch between two observers, choosing the best one at any time instant, was also part of the test scope. For this, necessary measurements (including acceleration measurements) were logged to be able to rerun and validate the observer algorithms in post-processing. Finally, several experiments were done to test a pseudo-derivative feedback control law for DP. The feedback mechanism was tested with and without a feedforward disturbance rejection term, called acceleration feedforward. This paper reports the experimental setup, test program, and an overview of results from the ADPRC'16 campaign.

INTRODUCTION

After 55 years of dynamic positioning (DP) technology for ships [1], a group of students and researchers at the Norwegian University of Science and Technology (NTNU) and the Centre for Autonomous Marine Operations and Systems (NTNU AMOS) has enabled full-scale testing of real-time DP-related control and monitoring algorithms, using the NTNU-owned R/V Gunnerus as an experimental marine technology platform.

According to IMO [2], a *dynamically positioned* vessel (DP-

---

[*] Address all correspondence to this author.

vessel) means "a unit or a vessel which automatically maintains its position (fixed location or predetermined track) exclusively by means of thruster force." To realize this function, a DP system consists of a power system, a thruster system, and a DP control system that includes sensors (position reference systems, heading reference systems, motion sensors, wind sensors, etc.), control computers, operator stations, networks, and signal cabling. For further information of such control system topologies, including DP control systems, see [3]. In the core of the DP control computers we find a set of algorithms for state estimation and feedback/feedforward control, performing the software instructions to safely and automatically make the vessel maintain its station in presence of wind, currents, and ocean waves. For an overview of conventional DP algorithms, see [4].

Suppliers of DP control systems perform their own DP testing trials on the vessel when installing and configuring a new DP control system. However, the hardware and, especially, the software of such control systems, are proprietary to each vendor company. The DP software makes out, in such a business, the major intellectual asset of a DP vendor company. Hence, it has traditionally been impossible for academic researchers to get access to test research code and technology within a commercial DP control system. A solution for the academic researcher to go around this could be to develop a complete experimental DP control system on his own, for the objective of academic experimentation. However, due to the extensiveness of such a system, including necessity to interface with many different vendor subsystems for power, propulsion, and various sensors, this has never been a feasible solution within limited academic budgets of time and money. As a consequence, academic testing of DP-related control algorithms has been limited to model-scale vessels equipped with thrusters, battery power, lowcost real-time computer boards, and necessary sensors and instrumentation to perform testing, typically in a model basin.

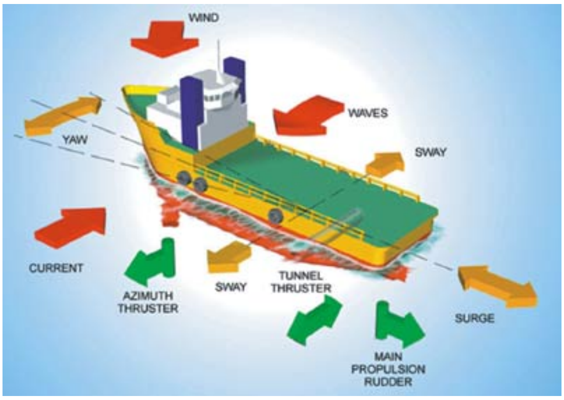

FIGURE 1. DP principle sketch. Courtesy: Kongsberg Maritime.

At NTNU, the Cybership series of model ships started with the Guidance, Navigation, and Control Laboratory (GNC-Lab) at the Department of Engineering Cybernetics, and Cybership I (with four azimuth thrusters); see [5]. This was later replaced by the Cybership II (with a tunnel thruster and two main propellers with rudders) [6–8] and then the larger Cybership III (with two main azimuth thrusters aft and an azimuth and a tunnel thruster fore) [9], which were operated in the Marine Cybernetics Laboratory (MC-Lab) at the Marine Technology Centre. In 2010, the smaller supply model ship, C/S Enterprise I (where C/S stands for Cyber Ship) was built [10], having two main Voith Schneider propellers aft and a tunnel truster fore. The latest and grandest model ship in the C/S series is provided by the work of Bjørnø [11] for a newly developed Arctic drillship in scale 1:90, having 6 azimuth thrusters, a turret, and capability of both DP and thruster-assisted position mooring (TAPM) experiments in the MC-Lab.

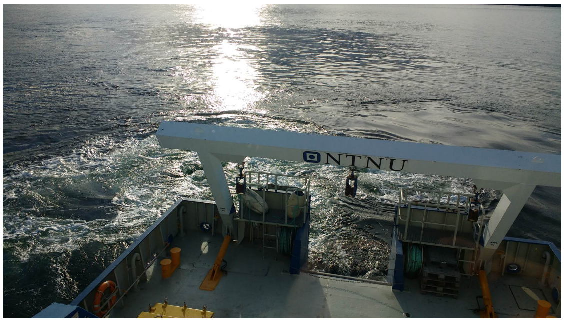

FIGURE 2. Dynamic positioning operation by R/V Gunnerus in calm conditions. Photo: Astrid H. Brodtkorb, 2016.

It has been a long-sought goal to be able to validate such research control algorithms in full-scale trials, in order to fulfill our range of assessment studies. These start with offline simulation, before conducting real-time hardware-in-the-loop simulation [3], then real-time model-scale testing in a basin, and now finally validation by full-scale testing. To come to this end, an initiative was made in 2016 within the NTNU AMOS research centre together with the company Kongsberg Maritime to enable full-scale testing of relevant DP control and monitoring algorithms developed by PhD students. Kongsberg Maritime has been the dominant supplier of DP control systems on the world market for several decades and the supplier of the DP control system onboard R/V Gunnerus. They also have a "collaborator" status in the NTNU AMOS centre, which indicates common research interests towards our full-scale test goals. Thus, by establishing contact within the DP Development & Cybernetics department in Kongsberg Maritime, a technical solution to safely implement external control algorithms was soon found. A project and a project team were established to realize the full-scale AMOS DP Research Cruise 2016 (ADPRC'16).

In this paper we will present the test system and methodologies used in the full-scale DP trials in weeks 42 and 46, during the ADPRC'16. We will give an overview of the test program and briefly discuss the results of testing.

THE AMOS DP RESEARCH CRUISE 2016

In NTNU AMOS there is a research activity on advanced stationkeeping operations, where cybernetic algorithms are developed related to DP and TAPM stationkeeping operations in normal and extreme conditions. Examples are DP and TAPM in extreme environments such as stationkeeping in high concentration Arctic sea-ice [12], impact with large wave trains in open sea, being exposed to highly fluctuating wind and current conditions, or DP during external load transfers such as jackup bottom landing and take-off, well intervention (e.g. by coiled tubing), gangway connections, and so on. A much used experimental platform for NTNU AMOS in other domains of research is the NTNU research vessel R/V Gunnerus. This ship is fitted with 2 main azimuth thrusters by Rolls-Royce, a Brunvoll tunnel thruster, and a K-Pos DP-11 system by Kongsberg Maritime.

Marine control algorithms developed at NTNU are traditionally tested in the MC-Lab at the Marine Technology Centre, on model-scaled vessels [5–11]. To the authors' best knowledge, academic experimental DP feedback control algorithms have never before been tested full-scale on a ship in an academic technology experiment. However, this has changed in the NTNU AMOS collaboration with Kongsberg Maritime, and for the first time we have performed full-scale experiments on new DP algorithms resulting from our research. The testing was done in the fall 2016, during the weeks of 42 and 46.

Objectives

The objectives of the ADPRC'16 campaign were to:

1. Establish a test interface and a method for the academic researchers to test their control-related algorithms on the industrial DP control system onboard R/V Gunnerus.
2. Test relevant DP state observer algorithms in full-scale.
3. Test relevant DP feedback control algorithms in full-scale.
4. Test experimental adaptive autopilot control algorithms in full-scale.
5. Evaluate the test methodology and results from testing, and learn from both successes and failures.

Especially the last "learn from failures" effect was important. It was decided to give the students the opportunity to test many variations of the proposed algorithms, for them to get experience with the small details in their algorithms, understand why some methods fail in real practice, and being positively surprised when some worked better than anticipated. This motivated enthusiasm and creativity.

Experimental Setup

FIGURE 3. The NTNU-owned R/V Gunnerus that was used in the DP trials. Photo: Helge Sunde/Samfoto.

Vessel The university-owned and -operated research vessel R/V Gunnerus was launched to sea in 2006, and since then it has operated as an experimental platform within marine biology, marine archeology, oceanography, subsea geology, fisheries, and marine technology. It is a diesel-electric ship of 31.25 m length overall and powered by two 500 kW gensets. Originally it was equipped with two main propellers, shaftlines, rudders, and steering gear for conventional propulsion and steering, in addition to a tunnel thruster from Brunvoll. However, as Gunnerus is also a platform for testing innovative marine technology, it was retrofitted in spring 2015, where the conventional propulsion and steering were replaced by two new main azimuth permanent magnet rim drive thrusters in a prototype development project by Rolls-Royce [13]. The new thruster system makes the vessel highly maneuverable and capable of DP in a wide range of sea-states. Then later the same year, Kongsberg Maritime donated a new DP control system to Gunnerus, where the older Kongsberg SDP-11 system was replaced by a new K-Pos DP-11 system [14]. This makes use of the thrusters and ensures that the vessel can keep its position with high accuracy.

DP Control System and Test Interface The onboard DP control system is a K-Pos DP-11, satisfying IMO DP Class 1 [2]. However, the DP computer software (and necessary hardware) was for the campaign replaced by the next generation DP software development by Kongsberg Maritime. Here, they have provided an API, or test module, where the students have access to all relevant DP library and header files. In this way, the students were able to develop and implement their own DP algorithms into the full-scale DP system without accessing Kongsberg source code. Since the architecture of the next generation DP system is modular, with a well-defined interface between the modules, this is now feasible and makes such testing possible.

A topology drawing is shown in Figure 4 to illustrate the setup. Here we see that the NTNU test module is a new layer within the core DP software, where this module gets access to sensor signals from the signal processing modules, guidance signals (reference filter, the “carrot”, etc.), and estimated states from the KM Kalman filter. Then the module can command force/moment control actions using the KM built-in thrust allocation module that computes individual thruster setpoints.

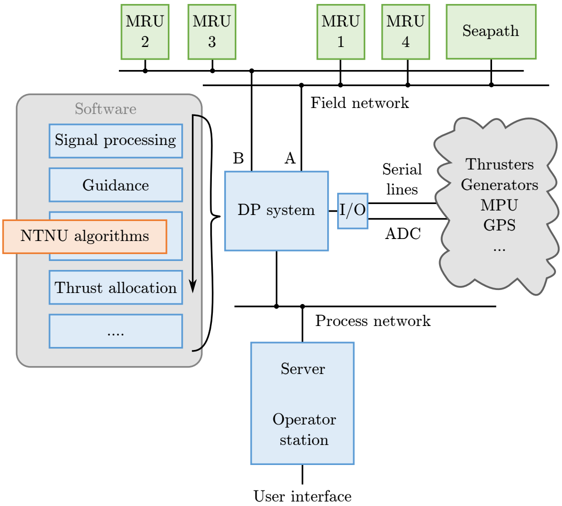

FIGURE 4. Topology drawing of the DP test interface that made the academic algorithms possible to test on the full-scale DP control system.

In particular, the vessel was equipped with four Kongsberg Seatex MRU 5+ motion sensors. These were interfaced to the DP control system so that acceleration measurements could be used.

The setup also included an external computer with a customized Software-In-the-Loop (SIL) simulator of Gunnerus and the DP control software, so that testing and tuning of control parameters could be done on this simulator for those that did not test on the real DP system. This proved instrumental for efficient debugging and preparations before the actual experiment.

Test Program

Among the algorithms planned for testing, was a model-based output feedback controller. The hypothesis was to achieve good transient as well as steady-state performance, to handle the combined DP operation of steady conditions mixed with rapid transient events. This is done by two changes from the traditional design. In the observer a flexible injection gain is used in the bias force estimation, and in the controller the bias force estimate is lowpass-filtered and then used to compensate the disturbances. See Værnø et al. in [15] for details.

In another planned experiment, different DP feedback mechanisms, such as adaptive backstepping [8] with a nonlinear update law and an adaptive nonlinear cascaded feedback controller, were in the test scope. The objectives here were to understand their behavior in full-scale operations and to compare their differences with respect to robustness and performance, where the metrics used for comparison consider both control accuracy and energy consumption. These control algorithms are presented in more detail below, while Sørensen and Breivik in [16] and [17] provide in-depth insight.

An observer (or state estimator) is an important part of a DP control system. An experiment was planned to test two main types. A model-based observer is used in steady conditions due to its ability to attenuate first order wave-induced motions and perform dead-reckoning in the case of signal loss. The other is a kinematic observer (referred to as a signal-based observer), which by hypothesis has superior performance during transients. A hybrid observer mechanism with a performance monitoring function is proposed to switch between these two observers, choosing the one that provides the best estimate of the vessel position and heading. This allows for improved transient response while also maintaining good steady-state performance. The test setup and data collection for this hybrid observer is presented below, while the reader is referred to Brodtkorb et al. in [18] for in-depth details of the algorithm.

Lastly, an experiment was planned to test a newly proposed type of feedback control law for DP, called pseudo-derivative feedback (PDF) control [19], for which a nonlinear extension was presented by Kjerstad et al. in [20]. This nonlinear feedback mechanism would be tested with and without a feedforward disturbance rejection term, called acceleration feedforward (AFF). This is a control mechanism, presented by Kjerstad and Skjetne in [21], to more rapidly compensate the exogenous disturbances, by measuring the full 6DOF acceleration vector of the vessel and from that deduce the external loads that act on it. Two different observers, corresponding to choice of feedback/feedforward used, were planned to be included in the test, including a wave peak frequency observer to estimate the wave frequency in each case.

The 4-corner DP Test During the DP testing, the 4-corner test seen in Figure 5, was used. Typically the vessel is first initialized in DP to point straight North at heading 0° (unless weather conditions dictates another favorable initial heading). Then the following setpoint changes are commanded:

1. Position change 40 m straight North: tests a pure surge movement ahead.
2. Position change 40 m straight West: tests a pure sway movement in port direction.
3. Heading change 45° counterclockwise: tests a pure yaw motion while keeping position steady.
4. Position change 40 m straight South: tests a combined surge-sway movement while keeping heading steady.
5. Position change 40 m straight East and heading change 45°

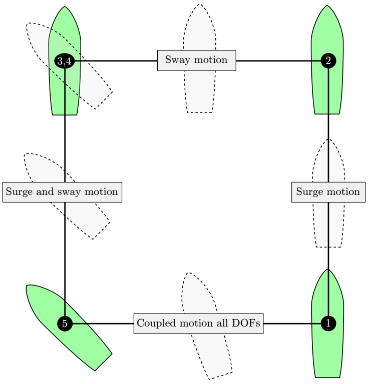

FIGURE 5. The 4-corner DP test.

clockwise: tests combined surge-sway-yaw movement.

When the test is completed, the vessel will have returned accurately to its initial position and heading, ready for a new test at the same spot and along the same track.

Project Timeline

The project was started within summer 2016, with the goal to perform the full-scale DP testing in collaboration between NTNU AMOS and Kongsberg Maritime. An interfacing workshop was organized in Kongsberg for the involved research team in August to implement the test interface. After that the process continued with selection of algorithms and preparations of a draft Scope of Work (SoW) document. Then a month of implementation, code testing, and planning was conducted until code freeze early October, for code review internally and by Kongsberg Maritime, approximately one week before the first week of sea trials. Figure 6 shows the overall timeline, from early preparations to post-analysis and evaluation of the experiments.

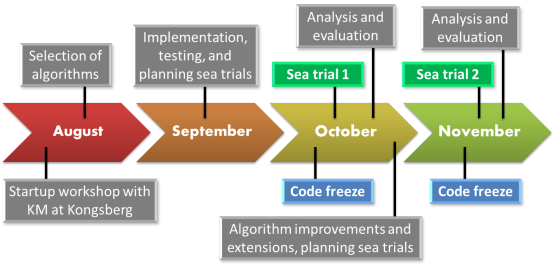

FIGURE 6. Project timeline leading up to the two weeks of the DP trials in weeks 42 and 46, 2016.

In Week 42, the first week of DP sea trials was conducted in the Trondheimsfjord. Two days were spent in the fjord outside Trondheim, then 2 days outside Brekstad where the fjord opens up to the Norwegian Sea, and then return to Trondheim on the last day. During transits, autopilot algorithms were tested, while DP algorithms were the focus during most of the stationary periods. One of the reasons going to the Brekstad area, was to find areas of larger waves that would better challenge the algorithms than calm sea. Unfortunately, weather was extremely nice during all week, and the best environmental loading condition we could find was a specific area with large eddies and rotational flows due to strong tidal currents. This proved, however, to cause adequate loading and challenges to our control algorithms to obtain sufficiently good tests.

After the first sea trial week, the experiences were evaluated, algorithms and test methodology were improved, new algorithms were implemented, until a new code freeze. Then we conducted another 5 days of sea trials in Week 46, repeating the same organization of time and place as in Week 42. Again, weather was better than planned for, except for some few hours of large waves during transit to Brekstad on Wednesday Nov. 16th and also during return on Friday Nov. 18th.

During the sea trials, a large amount of data was collected in addition to experiences and learnings. This is currently being studied, and several papers are in review with more expected in the near future.

ALGORITHMS AND RESULTS

The experiments can be categorized between some robust control algorithms performing DP with improved transient performance, and some algorithms performing adaptive DP control for adaptation to varying loads and uncertain vessel parameterization. In addition, some tests targeted alternative observer algorithms, that is, a nonlinear model-based DP observer, a signal-based kinematic observer algorithm, and a hybrid observer with the objective to switch between these two.

In the following we will present some of these control algorithms, and some resulting responses from the experiments. For further details on the models, gains, parameters, etc., the reader is referred to contact the respective authors of this paper.

The typical DP model of a marine vessel is on the form

$$\dot{\eta} = R(\psi)\nu \tag{1a}$$

$$M\dot{\nu} = -D\nu + R(\psi)^{\top} b(t) + \tau, \tag{1b}$$

where $\eta = \mathrm{col}\,(\eta_N, \eta_E, \psi) \in \mathbb{R}^2 \times \mathbb{S}$ contains the North/East position and heading angle of the vessel, and $\nu = \mathrm{col}\,(u, v, r) \in \mathbb{R}^3$ contains the surge/sway velocity and yaw rate in the body frame of the vessel. The vector $\tau \in \mathbb{R}^3$ is the thruster load used as control input, and $b \in \mathbb{R}^3$ is a load disturbance vector. The matrices M and D are the inertia and damping matrices, respectively, and

$R(\psi)$ is the rotation matrix between the Body and NED coordinate systems, satisfying

$$\dot{R} = R(\psi)S(r), \qquad R(\psi)^{\top}R(\psi) = R(\psi)R(\psi)^{\top} = I$$

$$R(\psi) = \begin{bmatrix} \cos\psi & -\sin\psi & 0 \\ \sin\psi & \cos\psi & 0 \\ 0 & 0 & 1 \end{bmatrix}, \quad S(r) = \begin{bmatrix} 0 & -r & 0 \\ r & 0 & 0 \\ 0 & 0 & 0 \end{bmatrix} = -S(r)^{\top}.$$

DP Observer Algorithms

The observer that was intended for testing in closed-loop feedback DP control, was a hybrid observer structure that would switch between a model-based observer, for superior steady-state performance, and a signal-based observer, for superior performance during transients. The structure is shown in Figure 7, based on the work by Brodtkorb et al. in [18]. The observer algorithm is formulated in a hybrid dynamical systems framework [22]. During time-continuous (flows), the signal-based observer and model-based observer estimate the states of the control system in parallel. The monitoring function then measures the position estimation error for both observers over a period of time. During discrete jumps, the observer performance is evaluated, and the better performing observer is selected for closed-loop control.

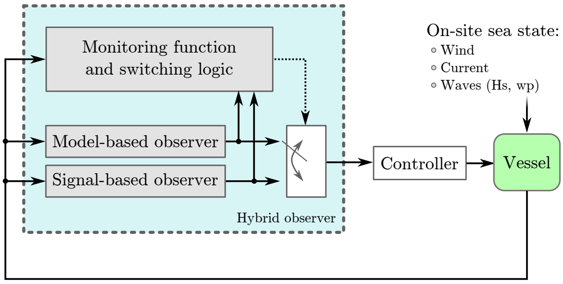

FIGURE 7. Hybrid observer structure [18].

Unfortunately, there was an issue with the MRU acceleration feedback signals available for the signal-based observer algorithm onboard R/V Gunnerus, in particular gravity compensation conducted within the proprietary layers of the sensors, that rendered the signal-based observer infeasible to run in real-time and closed-loop with the feedback control laws. Hence, the selected state estimates used for most of the testing were the available estimates (position, velocity, and bias) provided by the commercial DP control system. Instead we installed an alternative IMU data acquisition system, as seen in Figure 8, where 3 IMUs were placed close to the existing two MRU5+ motion sensors in the instrument room of the ship. The IMU data acquisition was time synchronized with the DP system measurements (by the Seapath NTP server) and stored on a network attached storage. Then the real vessel states can be reconstructed and the observer algorithms validated after the cruise.

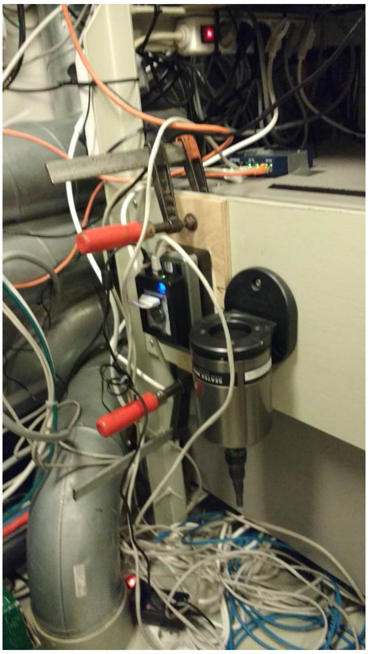

FIGURE 8. Alternative IMUs clamped to ship construction in the instrument room, close to the permanent MRU 5+ located in the same room. Photo: Astrid H. Brodtkorb, 2016.

Improved Transient Performance DP Control

Improved transient control has been a focus in recent DP research. This is motivated by challenges related to safe DP operation in extreme conditions, such as DP in heavy Arctic sea-ice, improved response when the vessel suddenly encounters large wave trains in open heavy seas, or when the DP vessel experiences large and rapidly varying external loads due to connection with some other structure. A few algorithms are presented next.

Model-Based Output Feedback Controller with Improved Transient Response This algorithm was proposed by Værnø et al. in [15] and tested on R/V Gunnerus for full-scale verification. The output feedback controller has two contributions compared to traditional design. The first one is in the observer. Here, a time-varying injection gain for the bias estimation is included. This gives a more flexible bias estimation that is fast in transients and slow (and calm) in steady-state, providing more accurate estimates in transients as well as less oscillatory estimates in steady-state.

The second contribution is the control law, given by

$$
\begin{aligned}
\tau &= \tau_{FB} + \tau_{FF} \qquad (2)\\
\tau_{FB} &= -K_p R(\psi)^\top (\hat{\eta} - \eta_d(t)) - K_d(\hat{\nu} - \nu_d(t)) - R(\psi)^\top \hat{b}_f\\
\tau_{FF} &= M\dot{\nu}_d(t) + D\nu_d(t),
\end{aligned}
$$

where $\eta_d(t)$, $\nu_d(t)$, and $\dot{\nu}_d(t)$ are desired references generated by a guidance system, and $\hat{\eta}$, $\hat{\nu}$, and $\hat{b}_f$ are state estimates from the observer. This is a typical nonlinear PID control law, with the variation that the filtered bias estimate from the observer is used in feedback instead of traditional integral action. The bias estimate from the observer is made fast in transients and calm in steady state. Hence, we have proposed to filter the bias state before it enters the feedback control. A detailed derivation is provided in [15], including simulation results.

Experimental Results Several DP 4-corner tests were performed for the output feedback transient controller algorithm. In Figure 9 the position footprint of one of them is shown. The environmental conditions for this test were: Current of 0.6 m/s at 170° and wind of 5 m/s at 150° degrees. The waves were negligible. As seen in Figure 9, the algorithm gives satisfactory, though not yet excellent, performance. The box-maneuver is almost square with the exception of some small oscillations.

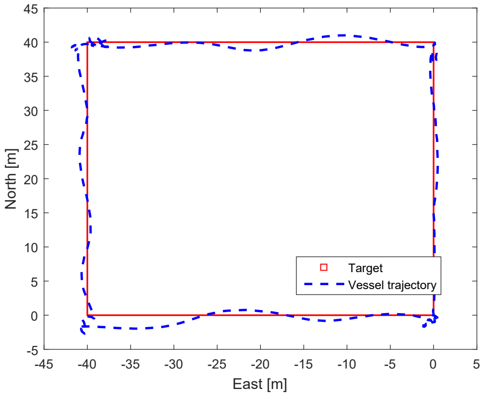

FIGURE 9. Trajectory of the DP 4-corner test of the model-based output feedback with improved transient response control algorithm.

Pseudo-Derivative Feedback Control with Acceleration Feedforward The structural design of the pseudo-derivative feedback (PDF) control law for marine vessels is similar to nonlinear PID methods [20]. The proposed control design differs from conventional methods in two ways. The first difference is the removal of the position setpoint in the proportional error term and injection of the velocity setpoint in the integral state, that is,

$$
\begin{aligned}
\dot{\xi} &= K_i(\eta_d - \eta) + K_p\vartheta_d \qquad (3a)\\
\tau &= M(\tau_{FF} + \tau_{FB}) - \Delta \qquad (3b)\\
\tau_{FB} &= R(\psi)^\top (\xi - K_p\eta) - K_{D1}\nu + K_{D2}\nu_d \qquad (3c)\\
\tau_{FF} &= R(\psi)^\top \dot{\vartheta}_d, \qquad (3d)
\end{aligned}
$$

where $K_{D1} = R(\psi)^\top K_d R(\psi) - M^{-1}D + S(r)$, $K_{D2} = R(\psi)^\top K_d R(\psi)$, and $\vartheta_d = R(\psi)\nu_d$. This effectively creates an internal reference point in the control law without affecting steady-state tracking performance. It is shown that this improves the transient convergence and mitigates overshoots caused by significant setpoint offsets while offering global exponential stability. Improved transient control can be further achieved, without compromising stability, by introducing a saturation function on the position error term in (3a).

The second difference is the introduction of the dynamic reference-less disturbance feedforward compensation term Δ in (3b), formed by the acceleration signal of the vessel. This term is generated by

$$\dot{\Delta} = \mu\left(-\Delta + Ma(t) - \tau + D\nu\right) \qquad (4)$$

where $\mu > 0$ is a gain, and $a(t)$ is the reconstructed acceleration measurement from the MRUs. This is termed Acceleration FeedForward (AFF); see [21] for details. AFF enables fast and direct compensation of external loads and unmodeled dynamics with low time lag.

The control law provides the same functionality as conventional tracking control laws, but with improved disturbance rejection and convergence transients. Although PDF is as simple as PID, and has demonstrated feasible experimental performance by [23] and [24], it has received little attention in marine applications. To the authors' best knowledge, only [25] considers the method for autopilot design prior to Kjerstad et al. in [20].

Experimental Results In general the PDF, with and without AFF, control law showed very promising performance, as seen in Figure 10 and Figure 11. The reason for the difference between the two plots are due to different days of testing, with different environmental conditions and lower speed when testing the PDF control without AFF. Due to practical reasons, only one MRU was used for the AFF tests, implying no AFF control in yaw.

Nonlinear Adaptive DP Control Laws

Adaptive DP control laws were proposed for testing by Sørensen and Breivik, based on their works in [16] and [17].

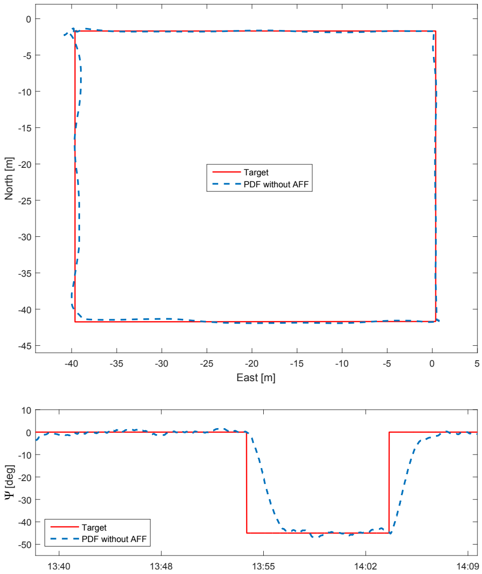

FIGURE 10. PDF control without AFF.

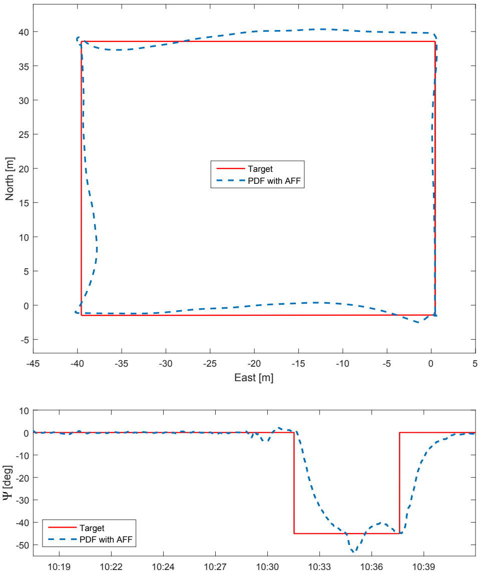

FIGURE 11. PDF control with AFF.

The control objective was to make $\eta(t) \to \eta_t(t)$ as $t \to \infty$, where $\eta_t(t) = [x_t(t), y_t(t), \psi_t(t)]^\top \in \mathbb{R}^2 \times \mathbb{S}$ represents the pose associated with a target point. Additionally, $\eta_t(t)$ is twice continuously differentiable and bounded. The motion of the target is typically defined by a human or generated by a guidance system.

Adaptive Nonlinear Cascaded Feedback Controller

The design of this control algorithm is similar to the backstepping method, for instance seen in [26] and [16], but it omits the coupling between the pose and velocity control loops, resulting in a cascaded system. Additionally, nonlinear pose and velocity feedback is introduced, inspired by constant bearing guidance, which was originally used for vessel control in [27]. By definition of new state variables, the recursive backstepping design results in the following control law,

$$\tau = M\dot{\alpha} + D\nu + \xi(\dot{\alpha})\hat{\theta} + \Phi(\nu)\hat{\sigma} - R(\psi)^\top\hat{\omega} - L_2(z_2, \Delta_i)z_2, \tag{5}$$

where $z_1 = R(\psi)^\top(\eta - \eta_t)$, $z_2 = \nu - \alpha$, $\alpha = -L_1(z_1, \Delta_i)z_1 + R(\psi)^\top\dot{\eta}_t$, $\xi(\dot{\alpha}) = \mathrm{diag}(\dot{\alpha}_u, \dot{\alpha}_v, \dot{\alpha}_r)$, and

$$L_1(z_1, \Delta_i) = K_1 \begin{bmatrix} \frac{I_{2\times2}}{\sqrt{z_{1,\tilde{p}}^\top z_{1,\tilde{p}} + \Delta_{\tilde{p}}^2}} & 0_{2\times1} \\ 0_{1\times2} & \frac{1}{\sqrt{z_{1,\tilde{\psi}}^2 + \Delta_{\tilde{\psi}}^2}} \end{bmatrix} \tag{6}$$

with $K_1 > 0$, $z_{1,\tilde{p}} = [z_{1,1}, z_{1,2}]^\top$, $z_{1,\tilde{\psi}} = z_{1,3}$, $\Delta_{\tilde{p}} > 0$, $\Delta_{\tilde{\psi}} > 0$, and

$$L_2(z_2, \Delta_i) = K_2 \begin{bmatrix} \frac{I_{2\times2}}{\sqrt{z_{2,\tilde{v}}^\top z_{2,\tilde{v}} + \Delta_{\tilde{v}}^2}} & 0_{2\times1} \\ 0_{1\times2} & \frac{1}{\sqrt{z_{2,\tilde{r}}^2 + \Delta_{\tilde{r}}^2}} \end{bmatrix} \tag{7}$$

with $K_2 > 0$ and $z_{2,\tilde{v}} = [z_{2,1}, z_{2,2}]^\top$, $z_{2,\tilde{r}} = z_{2,3}$, $\Delta_{\tilde{v}} > 0$, and $\Delta_{\tilde{r}} > 0$.

In (5), $\theta = [\theta_1,\ \theta_2,\ \theta_3]^\top$ is the uncertainty associated with the inertia matrix, $\sigma = [\sigma_1,\ \sigma_2,\ \sigma_3,\ \sigma_4,\ \sigma_5]^\top$ is the uncertainty associated with the damping matrix, and $\omega = [\omega_1,\ \omega_2,\ \omega_3]^\top$ is the disturbance vector. Additionally, it is assumed that $\dot{\theta} = 0$, $\dot{\sigma} = 0$, and $\dot{\omega} = 0$. Three update laws of the uncertainties are

$$\dot{\hat{\theta}} = -\Gamma_1\xi(\dot{\alpha})z_2, \tag{8a}$$

$$\dot{\hat{\sigma}} = -\Gamma_2\Phi(\nu)^\top z_2, \qquad \Phi(\nu) = \begin{bmatrix} u & 0 & 0 & 0 & 0 \\ 0 & v & r & 0 & 0 \\ 0 & 0 & 0 & v & r \end{bmatrix}, \tag{8b}$$

$$\dot{\hat{\omega}} = \Gamma_3 R z_2. \tag{8c}$$

Adaptive Backstepping with Nonlinear Update Laws Inspired by the previous controller, a question was raised on improving the traditional adaptive backstepping controller by introducing sigmoid functions to the adaptive update laws. This gave

$$\tau = M\dot{\alpha} + D\nu + \xi(\dot{\alpha})\hat{\theta} + \Phi(\nu)\hat{\sigma} - R^\top\hat{\omega} - K_2 z_2 - z_1 \tag{9a}$$

$$\dot{\hat{\theta}} = -\Gamma_1 \frac{1}{\sqrt{z_2^\top \xi(\dot{\alpha})^2 z_2 + \Delta_1^2}} \xi(\dot{\alpha}) z_2 \tag{9b}$$

$$\dot{\hat{\sigma}} = -\Gamma_2 \frac{1}{\sqrt{z_2^\top \Phi(\nu)\Phi(\nu)^\top z_2 + \Delta_2^2}} \Phi(\nu)^\top z_2 \tag{9c}$$

$$\dot{\hat{\omega}} = \Gamma_3 \frac{1}{\sqrt{z_2^\top z_2 + \Delta_3^2}} R z_2, \tag{9d}$$

with z_1 and z_2 as before, $\Delta_{1,2,3} > 0$, and $\alpha = -K_1 z_1 + R^\top \dot{\eta}_t$. The derivation and stability analysis are given in [16] and [17].

Experimental Results The abbreviation ANCF refers in this section to adaptive nonlinear cascaded feedback controller, AB refers to adaptive backstepping, while AB-NLU refers to adaptive backstepping with nonlinear update laws.

A modified 4-corner test was used as the desired trajectory for the vessel to track. This test was made in calm sea with insignificant current and wind. The results shown in figures 12 and 13 were conducted on October 20th, 2016.

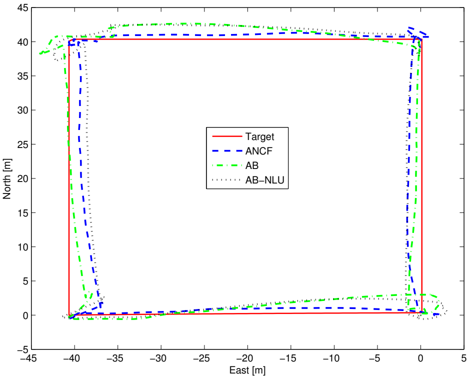

FIGURE 12. The vessel tracking the target moving in the modified 4-corner test.

It can be seen from Figure 12 and Figure 13 that the adaptive controllers have a similar behavior in terms of tracking the target trajectory. It can also be seen that the largest problem occurs during the combined backwards surge and sway motion. The ANCF has the best overall performance of the test.

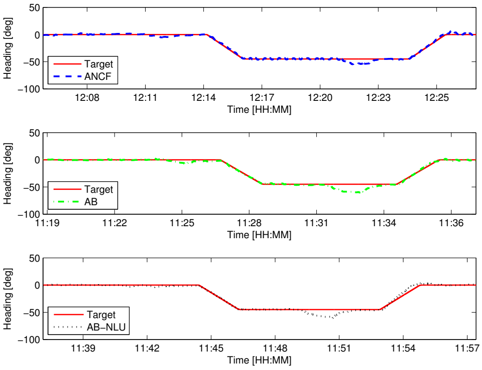

FIGURE 13. The vessel tracking the heading of the 4-corner test.

CONCLUSION

We have reported the planning, preparations, and given an overview of results from the full-scale testing of academic DP control algorithms, developed at NTNU AMOS, on the AMOS DP Research Cruise 2016 with R/V Gunnerus. This full-scale DP trials of academic control research was made possible by a collaboration with Kongsberg Maritime, whereby a test interface was established to allow our researchers to implement their algorithms into an external test module that was plugged into the newest generation DP software onboard R/V Gunnerus. During two weeks of testing in the Trondheimsfjord, in the weeks 42 and 46 of 2016, a total of 17 control and observer algorithms were tested, and within each of these many variations we tested, resulting in more than 100 tests. Many of these resulted in some kind of failure or weaknesses to learn from, while others performed very well. During the entire cruise, we experienced no system failures of the DP control system as a platform for testing. Only failures in some specific algorithms occurred, and then we could just switch to the commercial DP control system to regain steady DP behavior before commencing the next test.

In overall we are left with a lot of good experiences, where learning has been generated from both from failures and success. Based on these experiences, we have concluded that such testing is important, innovative, and up for repetition.

ACKNOWLEDGMENT

This work was supported by the Research Council of Norway, partly through the Centre of Excellence NTNU AMOS, project no. 223254 and partly through the Centre for Research-based Innovation SAMCoT, project no. 203471. We would like to thank the engineers from Kongsberg Maritime supporting the preparations and execution of the DP trials, in particular Vincenzo Calabrò, Rune Skullestad, and Øystein Lurås. We would also like to thank MSc student Alexander Mykland for joining the mission and taking responsibility for the handwritten test log.

REFERENCES

[1] Breivik, M., Kvaal, S., and Østby, P., 2015. "From Eureka to K-Pos: Dynamic Positioning as a highly successful and important marine control technology". In Proc. IFAC Conf. Manoeuvering and Contr. Marine Crafts, Vol. 10, IFAC.

[2] Int. Maritime Org., 1994. Guidelines for vessels with dynamic positioning systems. Standard MSC/Circ. 645, IMO, London, England, June 6. Ref. T4/3.03.

[3] Skjetne, R., and Egeland, O., 2006. "Hardware-in-the-loop testing of marine control systems". *Modeling, Identification and Control,* ***27***(4), pp. 239–258.

[4] Sørensen, A. J., 2011. "A survey of dynamic positioning control systems". *Annual Rev. Control,* ***35***, pp. 123–136.

[5] Strand, J. P., 1999. "Nonlinear position control systems design for marine vessels". PhD thesis, Norwegian Univ. Sci. & Tech., Dept. Eng. Cybernetics, Trondheim, Norway.

[6] Lindegaard, K.-P., 2003. "Acceleration feedback in dynamic positioning". PhD thesis, Norwegian Univ. Sci. & Tech., Dept. Eng. Cybernetics, Trondheim, Norway, Oct.

[7] Skjetne, R., Smogeli, Ø. N., and Fossen, T. I., 2004. "A nonlinear ship maneuvering model: Identification and adaptive control with experiments for a model ship". *Modeling, Identification and Control,* ***25***(1), pp. 3–27.

[8] Skjetne, R., Fossen, T. I., and Kokotović, P. V., 2005. "Adaptive maneuvering, with experiments, for a model ship in a marine control laboratory". *Automatica,* ***41***(2), pp. 289–298.

[9] Ruth, E., 2008. "Propulsion control and thrust allocation on marine vessels". PhD thesis, Norwegian Univ. Sci. & Tech., Dept. Marine Tech., Trondheim, Norway. NTNU 2008:203.

[10] Skåtun, H. N., 2011. "Development of a DP system for CS Enterprise I with Voith Schneider thrusters". MSc thesis, Norwegian Univ. Sci. & Tech., Trondheim, Norway, June.

[11] Bjørnø, J., 2016. "Thruster-assisted position mooring of C/S Inocean Cat I Drillship". MSc thesis, Norwegian Univ. Sci. & Tech., Trondheim, Norway, July 8.

[12] Skjetne, R., Imsland, L., and Løset, S., 2014. "The Arctic DP research project: Effective stationkeeping in ice". *Modeling, Identification and Control,* ***35***(4), pp. 191–210.

[13] Rolls-Royce, 2016. New: Azimuthing permanent magnet thruster. Tech. rep., Rolls-Royce, Aug. 19.

[14] Adresseavisen, 2015. Gunnerus utstyrt til å ligge helt i ro, April. Accessed: 2017-03-20.

[15] Værnø, S. A. T., Brodtkorb, A. H., Skjetne, R., and Sørensen, A. J., 2016. "An output feedback controller with improved transient response of marine vessels in dynamic positioning". In Proc. IFAC Conf. Contr. Appl. Marine Systems, Vol. 49, IFAC, pp. 133 – 138.

[16] Sørensen, M. E. N., and Breivik, M., 2015. "Comparing nonlinear adaptive motion controllers for marine surface vessels". In Proc. IFAC Conf. Manoeuvering and Contr. Marine Crafts, Vol. 48, IFAC, pp. 291–298. IFAC-PapersOnLine.

[17] Sørensen, M. E. N., and Breivik, M., 2016. "Comparing combinations of linear and nonlinear feedback terms for motion control of marine surface vessels". In Proc. IFAC Conf. Contr. Appl. Marine Systems, Vol. 49, IFAC, pp. 303–310.

[18] Brodtkorb, A. H., Værnø, S. A. T., Teel, A. R., Sørensen, A. J., and Skjetne, R., 2016. "Hybrid observer for improved transient performance of a marine vessel in dynamic positioning". In Proc. IFAC Symp. Nonlinear Control Systems Design, Vol. 49, IFAC, pp. 345–350.

[19] Phelan, R. M., 1977. *Automatic Control Systems*. Cornell University Press.

[20] Kjerstad, Ø. K., Værnø, S. A. T., and Skjetne, R., 2016. "A robust dynamic positioning tracking control law mitigating integral windup". In Proc. IFAC Conf. Contr. Appl. Marine Systems, Vol. 49, IFAC, pp. 239 – 244.

[21] Kjerstad, Ø. K., and Skjetne, R., 2016. "Disturbance rejection by acceleration feedforward for marine surface vessels". *IEEE Access,* ***4***, pp. 2656–2669.

[22] Goebel, R., Sanfelice, R. G., and Teel, A. R., 2012. *Hybrid Dynamical Systems: Modeling, Stability, and Robustness*. Princeton Univ. Press, New Jersey, USA.

[23] Nikolic, I. Z., and Milivojevic, I., 1998. "Application of pseudo-derivative feedback in industrial robot controllers". *Facta Universitatis, Automatic Control and Robotics*.

[24] Setiawan, A., Albright, L. D., and Phelan, R. M., 2000. "Application of pseudo-derivative-feedback algorithm in greenhouse air temperature control". *Computers and Electronics in Agriculture,* ***26***(3), pp. 283–302.

[25] Vahedipour, A., and Bobis, J., 1993. "Cascade pseudo derivative feedback control algorithm and its application to design of autopilots". In Proc. IECON.

[26] Fossen, T. I., and Strand, J. P., 1999. "Tutorial on nonlinear backstepping: Applications to ship control". *Modeling, Identification and Control,* ***20***(2), pp. 83–135.

[27] Breivik, M., Strand, J. P., and Fossen, T. I., 2006. "Guided dynamic positioning for fully actuated marine surface vessels". In Proc. IFAC Conf. Manoeuvering and Contr. Marine Crafts, Vol. 7, IFAC.

A.8 Improvement of Ship Motion Control Using a Magnitude-rate Saturation Model

O. N. Lyngstadaas, T. E. Sæterdal, M. E. N. Sørensen and M. Breivik, Improvement of ship motion control using a magnitude-rate saturation model, *in Proceedings of the 2nd IEEE Conference on Control Technology and Applications, Copenhagen, Denmark*, 2018.

Improvement of Ship Motion Control Using a Magnitude-Rate Saturation Model

Ole Nikolai Lyngstadaas, Tore Egil Sæterdal, Mikkel Eske Nørgaard Sørensen, Morten Breivik

***Abstract*— Motion control concepts for ships have traditionally not focused on handling actuator constraints. This paper investigates the effects on performance of a pair of nonlinear control schemes by developing and implementing a magnitude-rate saturation (MRS) model. The effects of using the MRS model is tested in experiments with a model ship in an ocean basin. Performance metrics are used to evaluate performance in terms of control error, energy efficiency, and actuator wear and tear.**

***Index Terms*— Ship motion control, Magnitude-rate saturation model, Constraint handling, Nonlinear control, Model-scale experiments, Wear and tear**

I. INTRODUCTION

In traditional control theory, an ideal controller might achieve perfect reference tracking in simulations, having no or non-sufficient limitations on the control input. However, in real-life applications it would not be feasible due to limitations in physical output and wear and tear of the actuators.

Several ways of handling actuator constraints have been investigated throughout the years. In [1], model predictive control for systems with actuator magnitude and rate constraints is presented. A solution using a modified dynamic window approach to handle actuator constraints is investigated in [2], and further expanded in [3].

To easily include magnitude and rate saturation (MRS) effects into a control system, a possible low-level approach is to limit the output of the control signal within the limits of the actuators. However, this may lead to an under-damped closed-loop system. To avoid this, effort has been put into implementing a model for combining MRS to smoothen the control output within allowed actuator limits. In [4], an MRS model is derived to address the issue of anti-windup, and the MRS model used in this paper is based on this approach.

In particular, the magnitude and rate saturations in this paper are set at lower limits than the actual actuator constraints. The main purpose is to investigate how limiting the actuator's magnitude and rate outputs will impact the overall performance of the motion control system. The MRS model, depending on how it is tuned, can be implemented in a simulation scenario, where the purpose is to mimic the actual constraints of the system, or be used to limit actuator outputs in laboratory experiments and on-board actual vessels.

The main contribution of this paper are the experimental results from scale testing on a 1:90 ship model. The MRS model from [4] is adapted to a three degrees of freedom (DOF) ship model and experimentally tested at the Marine Cybernetics Laboratory (MC-Lab) at the Norwegian University of Science and Technology (NTNU) in Trondheim, Norway. Furthermore, the positive effects of employing MRS to a pair of nonlinear feedback control schemes from [5] have been investigated.

The rest of this paper is organized as follows: Section II presents a mathematical ship model; Section III defines the control objective and the 4-corner test, derivation of the MRS model, and also presents a pair of nonlinear controllers from [5]; Section IV presents the experimental results from model-scale testing in the MC-Lab, while Section V concludes the paper.

II. SHIP MODEL

The motion of a ship can be represented by the pose vector $\boldsymbol{\eta} = [x, y, \psi]^\top \in \mathbb{R}^2 \times \mathbb{S}$ and the velocity vector $\boldsymbol{\nu} = [u, v, r]^\top \in \mathbb{R}^3$. Here, (x, y) represents the Cartesian position in the local earth-fixed reference frame, ψ is the yaw angle, (u, v) represents the body-fixed linear velocities and r is the yaw rate. The 3-DOF dynamics of a ship can then be stated as in [6]:

$$\dot{\boldsymbol{\eta}} = \boldsymbol{R}(\psi)\boldsymbol{\nu} \tag{1}$$

$$\boldsymbol{M}\dot{\boldsymbol{\nu}} + \boldsymbol{C}(\boldsymbol{\nu})\boldsymbol{\nu} + \boldsymbol{D}(\boldsymbol{\nu})\boldsymbol{\nu} = \boldsymbol{\tau}, \tag{2}$$

where $\boldsymbol{M} \in \mathbb{R}^{3\times3}$, $\boldsymbol{C}(\boldsymbol{\nu}) \in \mathbb{R}^{3\times3}$, $\boldsymbol{D}(\boldsymbol{\nu}) \in \mathbb{R}^{3\times3}$ and $\boldsymbol{\tau} = [\tau_1, \tau_2, \tau_3]^\top$ represent the inertia matrix, Coriolis and centripetal matrix, damping matrix and control input vector, respectively. The rotation matrix $\boldsymbol{R}(\psi) \in SO(3)$ is given by

$$\boldsymbol{R}(\psi) = \begin{bmatrix} \cos(\psi) & -\sin(\psi) & 0 \\ \sin(\psi) & \cos(\psi) & 0 \\ 0 & 0 & 1 \end{bmatrix}. \tag{3}$$

The system matrices are assumed to satisfy the properties $\boldsymbol{M} = \boldsymbol{M}^\top > 0$, $\boldsymbol{C}(\boldsymbol{\nu}) = -\boldsymbol{C}(\boldsymbol{\nu})^\top$ and $\boldsymbol{D}(\boldsymbol{\nu}) > 0$.

A. Nominal model

The model and parameters of the model-scale ship C/S Inocean Cat I Drillship (CSAD) [7], as shown in Fig. 1, will be used in this paper. CSAD is a 1:90 scale replica of a supply ship, with a length of $L = 2.578$ m. The inertia matrix is given as

$$\boldsymbol{M} = \boldsymbol{M}_{RB} + \boldsymbol{M}_A, \tag{4}$$

O. N. Lyngstadaas and T. E. Sæterdal are M.Sc. students at the Department of Engineering Cybernetics, Norwegian University of Science and Technology (NTNU), NO-7491 Trondheim, Norway. M. E. N. Sørensen and M. Breivik are with the Centre for Autonomous Marine Operations and Systems, Department of Engineering Cybernetics, Norwegian University of Science and Technology (NTNU), NO-7491 Trondheim, Norway. Email: `{mikkel.e.n.sorensen, morten.breivik}@ieee.org`

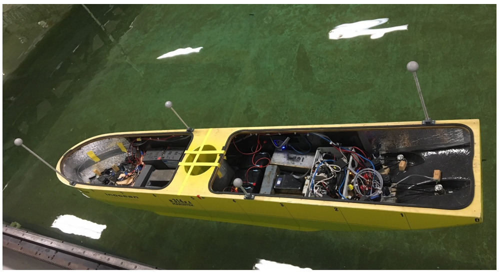

Fig. 1: C/S Inocean Cat I Drillship in the MC-lab.

where

$$\boldsymbol{M}_{RB} = \begin{bmatrix} m & 0 & 0 \\ 0 & m & mx_g \\ 0 & mx_g & I_z \end{bmatrix} \tag{5}$$

$$\boldsymbol{M}_A = \begin{bmatrix} -X_{\dot{u}} & 0 & 0 \\ 0 & -Y_{\dot{v}} & -Y_{\dot{r}} \\ 0 & -N_{\dot{v}} & -N_{\dot{r}} \end{bmatrix}. \tag{6}$$

The mass of CSAD is $m = 127.92$ kg, while $x_g = 0.00375\ \mathrm{m}$ is the distance along the x-axis in the body frame from the centre of gravity, and $I_z = 61.987\ \mathrm{kg\,m^2}$ is the moment of inertia about the z-axis in the body frame. Other parameter values are listed in Table I, which are updated values from [7], where a few changes to the numerical values and signs have been done to better fit the actual laboratory performance of CSAD.

CSAD has six azimuth thrusters, which in the experiments presented here are fixed to the angles $\boldsymbol{\delta} = [\pi, \pi/4, -\pi/4, 0, 5\pi/4, 3\pi/4]^\top$ rad, in the body-fixed coordinate system, giving a fully actuated vessel [3].

The Coriolis and centripetal matrix is

$$\boldsymbol{C}(\boldsymbol{\nu}) = \boldsymbol{C}_{RB}(\boldsymbol{\nu}) + \boldsymbol{C}_A(\boldsymbol{\nu}), \tag{7}$$

with

$$\boldsymbol{C}_{RB}(\boldsymbol{\nu}) = \begin{bmatrix} 0 & 0 & -m(x_g r + v) \\ 0 & 0 & mu \\ m(x_g r + v) & -mu & 0 \end{bmatrix} \tag{8}$$

$$\boldsymbol{C}_A(\boldsymbol{\nu}) = \begin{bmatrix} 0 & 0 & -c_{A,13}(\boldsymbol{\nu}) \\ 0 & 0 & c_{A,23}(\boldsymbol{\nu}) \\ c_{A,13}(\boldsymbol{\nu}) & -c_{A,23}(\boldsymbol{\nu}) & 0 \end{bmatrix}, \tag{9}$$

where

$$c_{A,13}(\boldsymbol{\nu}) = -Y_{\dot{r}} r - Y_{\dot{v}} v \tag{10}$$

$$c_{A,23}(\boldsymbol{\nu}) = -X_{\dot{u}} u. \tag{11}$$

Finally, the damping matrix $\boldsymbol{D}(\boldsymbol{\nu})$ is given as

$$\boldsymbol{D}(\boldsymbol{\nu}) = \boldsymbol{D}_L + \boldsymbol{D}_{NL}(\boldsymbol{\nu}), \tag{12}$$

where

$$\boldsymbol{D}_L = \begin{bmatrix} -X_u & 0 & 0 \\ 0 & -Y_v & -Y_r \\ 0 & -N_v & -N_r \end{bmatrix} \tag{13}$$

TABLE I: Parameters for CSAD, updated from [7].

Parameter	**Value**
$X_{\dot{u}}$	−3.262
$Y_{\dot{v}}$	−28.890
$Y_{\dot{r}}$	−0.525
$N_{\dot{v}}$	−0.157
$N_{\dot{r}}$	−13.980
X_u	−2.332
$X_{\lvert u \rvert u}$	0
X_{uuu}	−8.557
Y_v	−4.673
$Y_{\lvert v \rvert v}$	−0.398
Y_{vvv}	−313.300
Y_r	−7.250
$Y_{\lvert r \rvert r}$	−3.450
Y_{rrr}	0
N_r	−6.916
$N_{\lvert r \rvert r}$	−4.734
N_{rrr}	−0.147
N_v	0
$N_{\lvert v \rvert v}$	−0.209
N_{vvv}	0
$N_{\lvert r \rvert v}$	0.080
$N_{\lvert v \rvert r}$	0.080
$Y_{\lvert r \rvert v}$	−0.805
$Y_{\lvert v \rvert r}$	−0.845

$$\boldsymbol{D}_{NL}(\boldsymbol{\nu}) = \begin{bmatrix} d_{NL,11}(\boldsymbol{\nu}) & 0 & 0 \\ 0 & d_{NL,22}(\boldsymbol{\nu}) & d_{NL,23}(\boldsymbol{\nu}) \\ 0 & d_{NL,32}(\boldsymbol{\nu}) & d_{NL,33}(\boldsymbol{\nu}) \end{bmatrix}, \tag{14}$$

with

$$d_{NL,11}(\boldsymbol{\nu}) = -X_{|u|u}|u| - X_{uuu}u^2 \tag{15}$$

$$d_{NL,22}(\boldsymbol{\nu}) = -Y_{|v|v}|v| - Y_{|r|v}|v| - Y_{vvv}v^2 \tag{16}$$

$$d_{NL,23}(\boldsymbol{\nu}) = -Y_{|r|r}|r| - Y_{|v|r}|v| - Y_{rrr}v^2 - Y_{ur}u \tag{17}$$

$$d_{NL,32}(\boldsymbol{\nu}) = -N_{|v|v}|v| - N_{|r|v}|r| - N_{vvv}v^2 - N_{uv}u \tag{18}$$

$$d_{NL,33}(\boldsymbol{\nu}) = -N_{|r|r}|v| - N_{|v|r}|v| - N_{rrr}r^2 - N_{ur}u, \tag{19}$$

where

$$Y_{ur} = X_{\dot{u}} \tag{20}$$

$$N_{uv} = -(Y_{\dot{v}} - X_{\dot{u}}) \tag{21}$$

$$N_{ur} = Y_{\dot{r}}, \tag{22}$$

which are damping terms which are linearly increasing with the forward speed. These are added to compensate for the Munk moment, and to get a more physically realistic model behavior [2], [8].

III. CONTROL DESIGN

A. Control objective and 4-corner test

The main control objective is to make $\tilde{\boldsymbol{\eta}}(t) \triangleq \boldsymbol{\eta}(t) - \boldsymbol{\eta}_t(t) \to \mathbf{0}\ t \to \infty$, where $\boldsymbol{\eta}_t(t) = [x_t(t), y_t(t), \psi_t(t)]^\top \in \mathbb{R}^2 \times \mathbb{S}$ represents the pose associated with a target point. The motion of the target is typically defined by a human or generated by a guidance system. For notational simplicity, time t will mostly be omitted for the rest of the paper.

It is desirable to investigate the effect of the magnitude-rate saturation model during different ship maneuvers. For this reason, a 4-corner maneuvering test is used, as shown in Fig. 2. For comparison, the experiments will be conducted with and without using the MRS model to identify notable effects on performance.

The 4-corner maneuvering test is proposed in [9] as a way to compare ship performance of dynamic positioning control algorithms. The ship is first initialized in dynamic positioning to point straight North at heading $0\,(deg)$. Then the following setpoint changes are commanded:

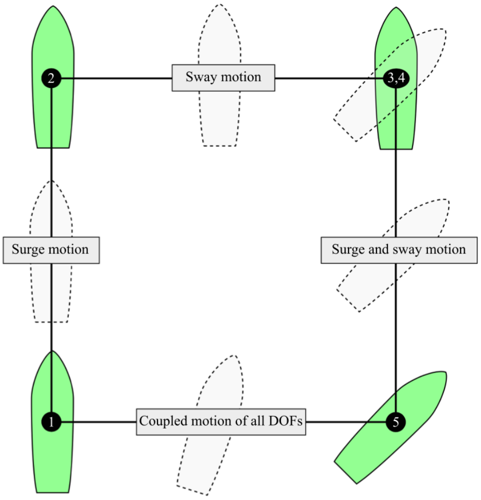

Fig. 2: The 4-corner dynamic positioning test. Modified from [9].

- Position change $2\,(m)$ straight North: tests a pure surge movement ahead.
- Position change $2\,(m)$ straight East: tests a pure sway movement in the starboard direction.
- Heading change $45\,(deg)$ clockwise: tests a pure yaw motion while keeping position steady.
- Position change $2\,(m)$ straight South: tests a combined surge-sway movement while keeping heading steady.
- Position change $2\,(m)$ straight West and heading change $45\,(deg)$ counterclockwise: tests a combined surge-sway-yaw movement.

B. Magnitude-rate saturation model design

Modelling the vessel's actuator constraints is important to ensure that the controller output remains inside a feasible range of values. Both magnitude and rate constraints will impact a vessel's ability to maneuver, and should be handled in the control system.

1) Saturation modeling: A generalized saturation block for an actuator can be modeled as

$$\tau_{s,i}(\tau_i) = \begin{cases} \tau_{i,min} & \text{if } \tau_i \leq \tau_{i,min} \\ \tau_i & \text{if } \tau_{i,min} < \tau_i < \tau_{i,max}, \\ \tau_{i,max} & \text{if } \tau_i \geq \tau_{i,max} \end{cases} \quad \forall i \in \{1,2,3\}, \tag{23}$$

where τ_i is the commanded control input without saturation with $i \in \{1,2,3\}$ to control surge, sway and yaw forces and moment, respectively. The saturation limits are represented by $\boldsymbol{\tau}_{min} = [\tau_{1,min}, \tau_{2,min}, \tau_{3,min}]^\top$ and $\boldsymbol{\tau}_{max} = [\tau_{1,max}, \tau_{2,max}, \tau_{3,max}]^\top$ with negative and positive bounded elements, respectively.

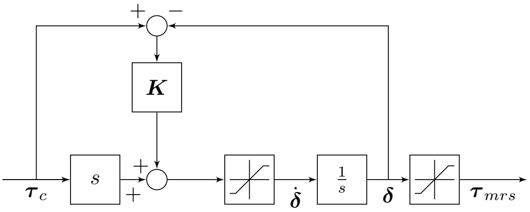

Fig. 3: Block diagram for the MRS model (24).

2) Magnitude-rate saturation model: An approach to model the MRS effects is given by

$$\dot{\boldsymbol{\delta}} = sat_{\boldsymbol{r}}(\dot{\boldsymbol{\tau}}_c + \boldsymbol{K}(\boldsymbol{\tau_c} - \boldsymbol{\delta})) \tag{24}$$

$$\boldsymbol{\tau}_{mrs} = sat_{\boldsymbol{m}}(\boldsymbol{\delta}), \tag{25}$$

where $\boldsymbol{\tau}_c$, $\boldsymbol{\delta}$ and $\boldsymbol{\tau}_{mrs}$ are the input, state and output of the MRS model, respectively, and where $\boldsymbol{K} > 0$ is a diagonal tuning matrix. The matrix is introduced in order to avoid an unstable cancellation between the derivative operator s and the integrator in Fig. 3, where the block diagram for the MRS model is shown. Because of this, an important observation is that neither of the elements of the matrix $\boldsymbol{K}$ can be equal to 1, and thus also $\boldsymbol{K} \neq \boldsymbol{I}$. The gain matrix $\boldsymbol{K}$ affects the speed of the inner-loop in the MRS model, and should be chosen based on the desired tracking performance. The derivative of the input, $\dot{\boldsymbol{\tau}}_c$, is supposed to exist and can be calculated using numerical derivation. The saturation limits $sat_{\boldsymbol{r}}$ and $sat_{\boldsymbol{m}}$ are modeled as the saturation block above, and contain the vessel's rate and magnitude constraints, respectively. See [4] for further details.

In this setup, the rate is limited first and the magnitude next, meaning that the MRS model state $\boldsymbol{\delta}$ can exceed the magnitude-bounds vector $\boldsymbol{m}$, although the output $\boldsymbol{\tau}_{mrs}$ never does. It should also be noted that this model can be further extended to effectively solve anti-windup problems, should such effects be needed to be accounted for.

C. Nonlinear control design

The MRS model will be tested with two types of feedback controllers in order to investigate the impact on performance for both linear and nonlinear feedback terms.

1) Nonlinear pose and linear velocity feedbacks: Using a control scheme based on a combination of nonlinear feedback of pose and linear feedback of velocity from [5], the control input can be chosen as

$$\boldsymbol{\tau} = \boldsymbol{M}\dot{\boldsymbol{\alpha}} + \boldsymbol{C}(\boldsymbol{\nu})\boldsymbol{\alpha} + \boldsymbol{D}(\boldsymbol{\nu})\boldsymbol{\alpha} - \boldsymbol{\Gamma}_2\boldsymbol{z}_2, \tag{26}$$

where

$$\dot{\boldsymbol{\alpha}} = \boldsymbol{R}^\top(\psi)\ddot{\boldsymbol{\eta}}_t + \boldsymbol{S}(r)^\top\boldsymbol{R}^\top(\psi)\dot{\boldsymbol{\eta}}_t - \dot{\boldsymbol{K}}_1(\cdot)\boldsymbol{z}_1 - \boldsymbol{K}_1(\cdot)\dot{\boldsymbol{z}}_1, \tag{27}$$

with $\boldsymbol{\Gamma}_2 > 0$ and where

$$\boldsymbol{S}(r) = \begin{bmatrix} 0 & -r & 0 \\ r & 0 & 0 \\ 0 & 0 & 0 \end{bmatrix}. \tag{28}$$

Here, the error variables $\boldsymbol{z}_1 = [z_{1,x}, z_{1,y}, z_{1,\psi}]^\top$ and $\boldsymbol{z}_2 = [z_{2,u}, z_{2,v}, z_{2,r}]^\top$ are defined as

$$\boldsymbol{z}_1 \overset{\triangle}{=} \boldsymbol{R}(\psi)(\boldsymbol{\eta} - \boldsymbol{\eta}_t) \tag{29}$$

$$\boldsymbol{z}_2 \overset{\triangle}{=} \boldsymbol{\nu} - \boldsymbol{\alpha}, \tag{30}$$

where $\boldsymbol{\alpha} \in \mathbb{R}^3$ is a vector of stabilizing functions, which can be interpreted as a desired velocity. As in [5], $\boldsymbol{\alpha}$ can be chosen as

$$\boldsymbol{\alpha} = \boldsymbol{R}^\top(\psi)\dot{\boldsymbol{\eta}}_{\boldsymbol{t}} - \boldsymbol{K}_1(\cdot)\boldsymbol{z}_1, \tag{31}$$

with the nonlinear feedback term $\boldsymbol{K}_1(\cdot)$ chosen as

$$\boldsymbol{K_1}(\cdot) = \boldsymbol{\Gamma}_1 \begin{bmatrix} \frac{1}{\sqrt{\boldsymbol{z}_{1,\tilde{p}}^\top \boldsymbol{z}_{1,\tilde{p}} + \Delta_{\tilde{p}}^2}} \boldsymbol{I}_{2\times 2} & \boldsymbol{0}_{2\times 1} \\ \boldsymbol{0}_{1\times 2} & \frac{1}{\sqrt{z_{1,\tilde{\psi}}^2 + \Delta_{\tilde{\psi}}^2}} \end{bmatrix}, \tag{32}$$

where $\boldsymbol{z}_{1,\tilde{p}} = [z_{1,x}, z_{1,y}]^\top$, $\boldsymbol{\Gamma}_1 > 0$ and $\Delta_i > 0$ are tuning parameters. Furthermore, $\dot{\boldsymbol{K}}_1(\cdot)$ is given by

$$\dot{\boldsymbol{K}}_1(\cdot) = -\boldsymbol{\Gamma}_1 \begin{bmatrix} \frac{\boldsymbol{z}_{1,\tilde{p}}^\top \dot{\boldsymbol{z}}_{1,\tilde{p}}}{(\boldsymbol{z}_{1,\tilde{p}}^\top \boldsymbol{z}_{1,\tilde{p}} + \Delta_{\tilde{p}}^2)^{\frac{3}{2}}} \boldsymbol{I}_{2\times 2} & \boldsymbol{0}_{2\times 1} \\ \boldsymbol{0}_{1\times 2} & \frac{z_{1,\tilde{\psi}} \dot{z}_{1,\tilde{\psi}}}{(z_{1,\tilde{\psi}}^2 + \Delta_{\tilde{\psi}}^2)^{\frac{3}{2}}} \end{bmatrix}. \tag{33}$$

2) Nonlinear pose and velocity feedbacks: The other control scheme from [5] augments (26) with a nonlinear velocity feedback term, giving the control input

$$\boldsymbol{\tau} = \boldsymbol{M}\dot{\boldsymbol{\alpha}} + \boldsymbol{C}(\boldsymbol{\nu})\boldsymbol{\alpha} + \boldsymbol{D}(\boldsymbol{\nu})\boldsymbol{\alpha} - \boldsymbol{K}_2(\cdot)\boldsymbol{z}_2, \tag{34}$$

where $\dot{\boldsymbol{\alpha}}$ and $\boldsymbol{\alpha}$ are given by (27) and (31), respectively, and with the nonlinear feedback term $\boldsymbol{K}_2(\cdot)$ chosen as

$$\boldsymbol{K_2}(\cdot) = \boldsymbol{\Gamma}_2 \begin{bmatrix} \frac{1}{\sqrt{\boldsymbol{z}_{2,\tilde{v}^\top} \boldsymbol{z}_{2,\tilde{v}} + \Delta_{\tilde{v}}^2}} \boldsymbol{I}_{2\times 2} & \boldsymbol{0}_{2\times 1} \\ \boldsymbol{0}_{1\times 2} & \frac{1}{\sqrt{z_{2,\tilde{r}^2} + \Delta_{\tilde{r}}^2}} \end{bmatrix}, \tag{35}$$

where $\boldsymbol{z}_{2,\tilde{v}} = [z_{2,u}, z_{2,v}]^\top$ and $\Delta_i > 0$ are tuning parameters. The feedback gain $\boldsymbol{\Gamma}_2$ is the same matrix as in (26).

The nonlinear pose and linear velocity feedback controller and the nonlinear pose and velocity feedback controller will be abbreviated NP-LV and NP-NV, respectively, throughout the rest of this paper.

TABLE II: Control gains.

	NP-LV	**NP-NV**
$\boldsymbol{\Gamma}_1$	$\mathrm{diag}([0.08, 0.08, 0.0698])$	$-\vert\vert-$
$\boldsymbol{\Gamma}_2$	$\mathrm{diag}([0.2, 0.2, 0.1745])\boldsymbol{M}$	$-\vert\vert-$
$\Delta_{\tilde{p}}$	0.5	$-\vert\vert-$
$\Delta_{\tilde{\psi}}$	0.5	$-\vert\vert-$
$\Delta_{\tilde{v}}$	$-$	0.7
$\Delta_{\tilde{r}}$	$-$	1
$\boldsymbol{K}$	$\mathrm{diag}([4, 3, 2])$	$-\vert\vert-$

3) Stability: Based on the theorems and stability proofs in [10], we can conclude that the two controllers have the following stability properties: The origin $(\boldsymbol{z}_1, \boldsymbol{z}_2) = (\boldsymbol{0}, \boldsymbol{0})$ is uniformly globally asymptotically stable (UGAS) and on each compact set $B \subset \mathbb{R}^6$ containing the origin, it is uniformly exponentially stable (UES) [10]. The MRS model is a nonlinear filter, and it is proven in [4] that the output will be an $\mathcal{L}_2$ signal if the input is an $\mathcal{L}_2$ signal, so it can be concluded that the MRS model does not alter the stability properties of the system.

4) Parameter tuning: The experiments are conducted with the gain parameters shown in Table II. The choice of the gain parameters for the two controllers are based on the tuning rules described in [10]. Here, the goal is to make the kinetic subsystem faster than the kinematic subsystem, which means that the kinetic subsystem needs to have smaller time constants than the kinematic subsystem in the linear region. The Δ-values scale the linear feedback gains and therefore the resulting time constants of the linear region, and must therefore be chosen such that they do not make the kinematic subsystem faster than the kinetic subsystem.

The actuator saturation limits are chosen by the following set of suggested tuning rules as well [11]. Here, the magnitude saturation limits are set lower than the actual limitations in order to save energy, and chosen as $\boldsymbol{m} = [2, 1.5, 1]$. The rate saturation limits are chosen by $\boldsymbol{r} = [m_1/t_{mrs,1}, m_2/t_{mrs,2}, m_3/t_{mrs,3}]^\top$, where m_1, m_2 and m_3 are the magnitude saturation limits given by $\boldsymbol{m}$, and where $t_{mrs,1}$, $t_{mrs,2}$ and $t_{mrs,3}$ are the desired transition times for the actuators to go from zero to max thrust in surge, sway and yaw, respectively. Here, suitable values for the rate saturation limits were found to be $\boldsymbol{r} = [1.9, 1.1, 0.8]$. Then, the gain matrix $\boldsymbol{K}$ can be chosen by $\boldsymbol{K} = \mathrm{diag}([K_{1,1}, \frac{m_2}{m_1}K_{1,1}, \frac{m_3}{m_1}K_{1,1}])$, where under normal operations it is desired to have all the diagonal elements $\boldsymbol{K}_{i,i} > 1$, $\forall i \in \{1, 2, 3\}$. Here, $K_{1,1} = 4$ to ensure a fast tracking of the target signal in all three degrees of freedom. The block diagram for the full control system is shown in Fig. 4.

IV. EXPERIMENTAL RESULTS AND PERFORMANCE EVALUATION

A. Marine Cybernetics Laboratory

As already mentioned, the MC-Lab is a small ocean basin at NTNU. Due to its relatively small size and advanced instrumentation package, the facility is especially suited for

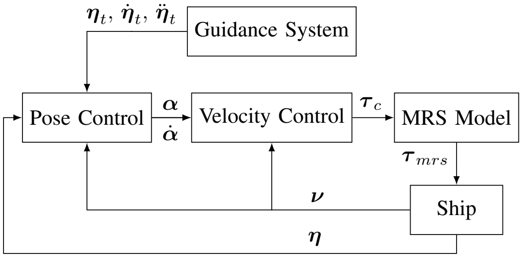

Fig. 4: Block diagram for the ship control system.

tests of motion control systems for marine vessel models, but is also suitable for more specialized hydrodynamic tests due to the advanced towing carriage, which has capability for precise movement of models up to six degrees of freedom [12].

The experiments will be conducted under the following conditions: In the experiments, the actual model ship's $\boldsymbol{M}$, $\boldsymbol{C}$ and $\boldsymbol{D}$ matrices will differ somewhat from those used in the controllers. Also, measurement noise is present in the Qualisys motion tracking system used in the laboratory.

B. Performance metrics

Performance metrics are used to objectively compare the performance of different control schemes. In this paper, the error variable is defined as the scaled norm of the pose control error $\boldsymbol{z}_1$, such that

$$e = \sqrt{\bar{\boldsymbol{z}}_1^\top \bar{\boldsymbol{z}}_1}, \tag{36}$$

where

$$\bar{\boldsymbol{z}}_1 = [\frac{z_{1,x}}{4}, \frac{z_{1,y}}{4}, \frac{z_{1,\psi}}{\pi/2}]^\top. \tag{37}$$

Since the position and yaw angle in pose have different units, we have defined the normalized pose error signals $\bar{z}_{1,x}$, $\bar{z}_{1,y}$ and $\bar{z}_{1,\psi}$ on the intervals $[-0.5, 0.5]$ in the expected operational space of the ship [13]. To get this interval, the position errors are divided by 4 and the yaw error is divided by $\frac{\pi}{2}$, since the position errors are in the intervals $[-2, 2]$ and the yaw error is in the interval $[-\frac{\pi}{4}, \frac{\pi}{4}]$, resulting in the normalized control error e.

Three different performance metrics are used in this paper, namely IAE, IAEW and IADC. The IAE (integral of the absolute error) metric is defined as an unweighted integral over time:

$$IAE(t) = \int_0^t |e(\gamma)|\, d\gamma. \tag{38}$$

The IAEW (integral of the absolute error multiplied by energy consumption) metric scales IAE by the energy consumption

$$IAEW(t) = \int_0^t |e(\gamma)|\, d\gamma \int_0^t P(\gamma) d\gamma, \tag{39}$$

where $P = |\boldsymbol{\nu}^\top \boldsymbol{\tau}|$, thus yielding a measure of energy efficiency.

Since the aim of the MRS model is also to reduce actuator wear and tear, it is interesting to investigate the dynamic behavior of the control signal. The IADC (integral of absolute differentiated control) metric is defined as in [13]:

$$IADC(t) = \int_{t_0}^t |\dot{\bar{\tau}}(\gamma)|\, d\gamma, \tag{40}$$

with $\bar{\tau}(t) = \sqrt{\boldsymbol{\tau}^\top \boldsymbol{\tau}}$, and where $\dot{\bar{\tau}}$ is computed using numerical derivation.

C. Experimental results

In the experiments, the target pose changes between setpoints for the 4-corner test. The system is implemented such that the target will automatically change to the next setpoint when the ship is within 0.003 m from the target in both x and y direction and 0.2 deg from the target heading. When the 4-corner test is completed, the ship will have returned accurately to its initial position and heading, ready for a new test at the same pose and along the same track.

While CSAD has a length of $L = 2.578$ m, its outline has been scaled by 1:6 in the 4-corner plots in Fig. 5 and 8, to better display the ship behaviour. By the plotted values of the performance metrics in Fig. 6 and 9, the effects of the MRS model on control performance can be examined. Fig. 5 shows the 4-corner track and the actual trajectory for the CSAD with and without the MRS model applied to the NP-LV controller. The results show no remarkable difference in the trajectory.

The performance metrics are plotted in Fig. 6. The metrics show that the while MRS does not reduce the overall tracking error by the IAE metric, both energy consumption (IAEW) and actuator wear and tear (IADC) are reduced by 6.8% and 38.8%, respectively.

In Fig. 7, the commanded thrust signals are shown for the 4-corner test. It can be seen that the MRS contributes to a smoother and amplitude-wise smaller control signal, while achieving approximately the same tracking performance. The spikes that can be seen in the control signal, especially during transients, are caused by noise related to the velocity estimation.

Fig. 8 displays the 4-corner trajectory for the NP-NV controller. Even though the NP-NV-controlled vessel with MRS effects takes a wider arch in the coupled motion ($5 \rightarrow 1$) in Fig. 2, the overall tracking error is not increased, as seen in Table III.

Furthermore, Fig. 9 shows improvement in energy efficiency, shown by the IAEW metric, and lower actuator wear and tear through the IADC metric. The reduction is greater for the NP-NV controller than the NP-LV controller, which is due to the fact the NP-NV is inherently a more aggressive controller, and thus benefits more from using an MRS model. For the NP-NV controller, the reduction is 12.2% and 46.4% for IAEW and IADC, respectively.

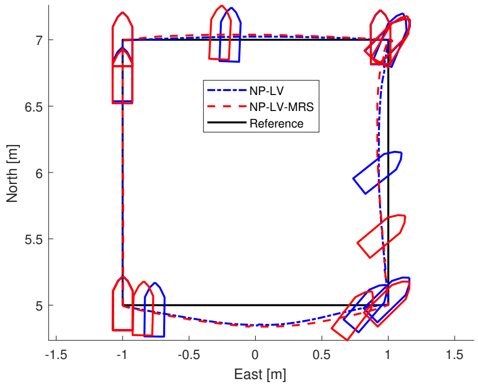

Fig. 5: Vessel performing the 4-corner manoeuver using the NP-LV controller.

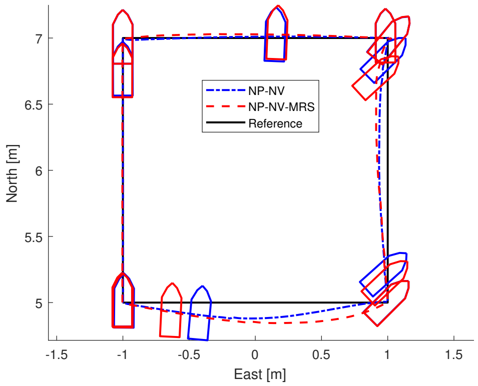

Fig. 8: Vessel performing the 4-corner maneuver using the NP-NV controller.

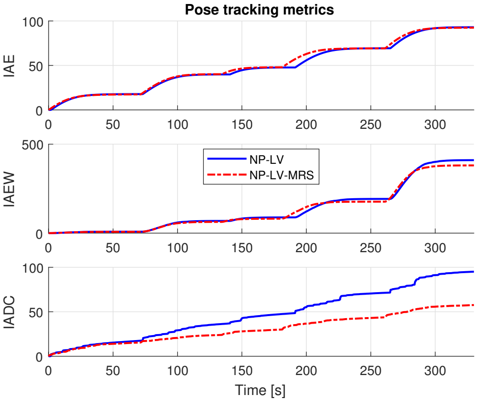

Fig. 6: Performance metrics for NP-LV.

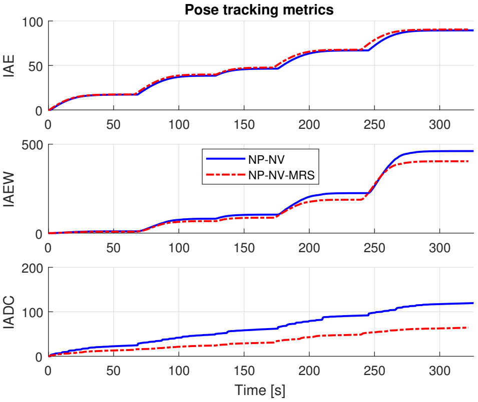

Fig. 9: Performance metrics for NP-NV.

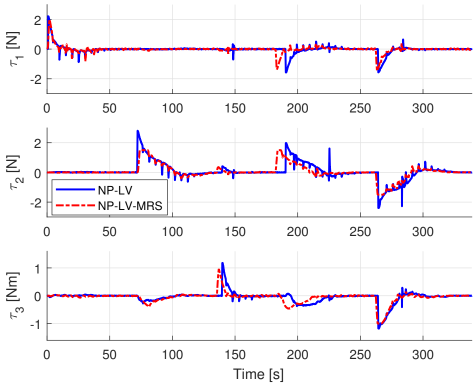

Fig. 7: Commanded control input for NP-LV.

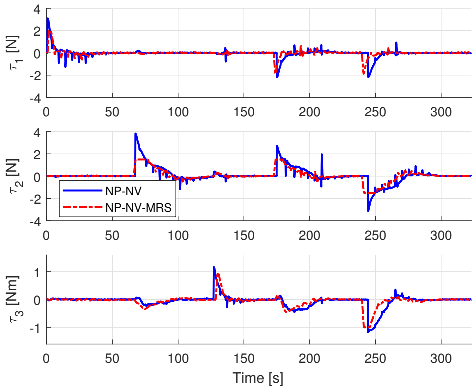

Fig. 10: Commanded control input for NP-NV.

TABLE III: Performance metrics final values.

	NP-LV	NP-LV MRS	NP-NV	NP-NV MRS
IAE final	92.99	**92.85**	**89.49**	90.38
IAEW final	410.12	**382.23**	460.08	**403.79**
IADC final	95.99	**58.73**	118.26	**63.34**

Fig. 10 shows the commanded control inputs for the NP-NV controller. Similar to NP-LV, a smoothing effect can be observed, although less significant. This is likely due to the nature of the pure nonlinear feedback, giving overall better tracking performance, which has previously been discussed in [5].

A significant effect of the MRS model, which can be seen in the performance metrics in Fig. 6 and 9, is that it results in a significantly reduced rate of change in the commanded control input.

The final values for the performance metrics are displayed in Table III, where the best performing controller for the different metrics is noted in bold.

V. CONCLUSION

Depending on the type of controller that is being used, including an MRS model to limit the actuator magnitude and rate outputs can contribute positively in several ways. As seen in both cases presented, an MRS model can effectively reduce actuator twitching, and thus wear and tear, without the degradation of performance in ship control. In addition, it has the potential to improve overall energy efficiency and pose tracking abilities, as can be seen from the performance metrics and trajectory plots, and can thus have positive effects on ship performance in setpoint navigation. These effects are especially important for vessels which must operate for long times at sea, and can be particularly useful for ships in DP operations, effectively contributing to the longevity of the operation with a reduced need for maintenance and repairs.

Future work includes optimizing the MRS model to further improve performance. This includes, through experimental tests in a laboratory, further tuning of the gain matrix $\boldsymbol{K}$ and the desired magnitude and rate saturation effects to obtain optimal ship control for the wanted ship operational environment.

ACKNOWLEDGEMENTS

This work was supported by the Research Council of Norway through the Centres of Excellence funding scheme, project number 223254. The authors gratefully acknowledge senior engineer Torgeir Wahl and Ph.D. candidate Andreas R. Dahl at NTNU's Department of Marine Technology for valuable support during the experiments.

REFERENCES

[1] V. Kapila and S. Valluri, "Model predictive control of systems with actuator amplitude and rate saturation," *in Proceedings of the 37th IEEE Conference on Decision and Control, pp. 1396-1401*, 1998.

[2] M. E. N. Sørensen, M. Breivik, and B.-O. H. Eriksen, "A ship heading and speed control concept inherently satisfying actuator constraints," *in Proceedings of the 1st IEEE Conference on Control Technology and Applications, HI, USA*, 2017.

[3] M. E. N. Sørensen, O. N. Lyngstadaas, B.-O. H. Eriksen, and M. Breivik, "A dynamic window-based controller for dynamic positioning satisfying actuator magnitude constraints," *in Proceedings of the 11th IFAC Conference on Control Applications in Marine Systems, Robotics, and Vehicles, Opatija, Croatia*, 2018.

[4] S. Galeani, S. Onori, A. R. Teel, and L. Zaccarian, "A magnitude and rate saturation model and its use in the soluton of a static anti-windup problem," *Systems & Control Letters, Volume 57, Issue 1, pp. 1-9*, 2008.

[5] M. E. N. Sørensen and M. Breivik, "Comparing combinations of linear and nonlinear feedback terms for motion control of marine surface vessels," *in Proceedings of the 10th IFAC Conference on Control Applications in Marine Systems, Trondheim, Norway*, 2016.

[6] T. I. Fossen, *Handbook of Marine Craft Hydrodynamics and Motion Control*. Wiley, 2011.

[7] J. Bjørnø, *Thruster-Assisted Position Mooring of C/S Inocean Cat I Drillship*. Master thesis, Norwegian University of Science and Technology, Trondheim, Norway, 2016.

[8] J. E. Refsnes, *Nonlinear Model-Based Control of Slender Body AUVs*. PhD thesis, Norwegian University of Science and Technology, Trondheim, Norway, 2008.

[9] R. Skjetne, M. E. N. Sørensen, M. Breivik, S. A. T. Værnø, A. H. Brodtkorb, A. J. Sørensen, Ø. K. Kjerstad, V. Calabrò, and B. O. Vinje, "AMOS DP research cruise 2016: Academic full-scale testing of experimental dynamic positioning control algorithms onboard R/V Gunnerus," *in Proceedings of the 36th International Conference on Ocean, Offshore and Arctic Engineering*, 2017.

[10] M. E. N. Sørensen, M. Breivik, and R. Skjetne, "Comparing combinations of linear and nonlinear feedback terms for ship motion control," *submitted to IEEE Transactions on Control Systems Technology*, 2018.

[11] O. N. Lyngstadaas, *Ship Motion Control Concepts Considering Actuator Constraints*. Master thesis, Norwegian University of Science and Technology, Trondheim, Norway, 2018.

[12] "Marine cybernetics laboratory." https://www.ntnu.edu/imt/lab/cybernetics. Accessed: 2018-01-30.

[13] B.-O. H. Eriksen and M. Breivik, *Modeling, Identification and Control of High-Speed ASVs: Theory and Experiments*, pp. 407–431. Sensing and Control for Autonomous Vehicles: Applications to Land, Water and Air Vehicles, Springer International Publishing, 2017.

A.9 A Dynamic Window-based Controller for Dynamic Positioning Satisfying Actuator Magnitude Constraints

M. E. N. Sørensen, O. N. Lyngstadaas, B.-O. H. Eriksen and M. Breivik, A dynamic window-based controller for dynamic positioning satisfying actuator magnitude constraints, *in Proceedings of the 11th IFAC Conference on Control Applications in Marine Systems, Opatija, Croatia*, 2018.

A Dynamic Window-Based Controller for Dynamic Positioning Satisfying Actuator Magnitude Constraints

Mikkel Eske Nørgaard Sørensen, Ole Nikolai Lyngstadaas,
Bjørn-Olav H. Eriksen and Morten Breivik

Centre for Autonomous Marine Operations and Systems, Department
of Engineering Cybernetics, Norwegian University of Science and
Technology (NTNU), NO-7491 Trondheim, Norway
E-mail: {mikkel.e.n.sorensen, bjorn-olav.h.eriksen,
morten.breivik}@ieee.org, olenl@stud.ntnu.no

Abstract: This paper considers the use of a simplified dynamic window (DW) algorithm to handle actuator magnitude constraints for a 3 degrees-of-freedom dynamic positioning controller for ships. To accomplish this, we use the simplified DW algorithm to design a dynamic window-based controller (DWC) which guarantees that the velocities remain within a feasible set, while simultaneously respecting the actuator magnitude constraints. The DWC is compared with a benchmark motion controller which uses nonlinear position and velocity feedback terms. The comparison is made using performance metrics which consider both control accuracy and energy efficiency.

Keywords: Dynamic positioning, Dynamic window, Actuator magnitude constraints

---

1. INTRODUCTION

Numerous ship motion controllers and autopilots have been proposed over the years. However, many control algorithms found in the literature do not explicitly consider saturation constraints for the actuators. Examples of traditional motion control designs for ships are given in (Fossen, 2011). Not considering actuator constraints may lead to unsatisfying performance or stability issues.

In (Fox et al., 1997), the dynamic window (DW) algorithm is suggested as a method to achieve collision avoidance and deal with actuator constraints imposed by limited velocities and accelerations for mobile robots. The DW algorithm is modified for AUVs in (Eriksen et al., 2016), and shows promising results for handling actuator magnitude and rate constraints. In (Sørensen et al., 2017), a simplification of this algorithm is proposed for a 2 degrees-of-freedom (DOF) heading and speed controller, by removing the collision avoidance part of the algorithm. This DW-based controller (DWC) is combined with a motion controller based on the design in (Sørensen and Breivik, 2016).

The contribution of this paper is the extension of the 2 DOF DWC presented in (Sørensen et al., 2017) to a 3 DOF DWC suitable for dynamic positioning (DP). The 3 DOF DWC is compared with a benchmark controller (BC) from (Sørensen and Breivik, 2016), where the comparison is made using performance metrics which consider both control accuracy and energy efficiency.

The rest of the paper is organized as follows: A mathematical ship model is presented in Section 2; Section 3 describes the assumptions and control objective; Section 4 presents the design of a benchmark controller inspired by backstepping and constant-bearing guidance; Section 5 presents the proposed DWC concept; Section 6 presents simulation results, while Section 7 concludes the paper.

2. SHIP MODEL

The motion of a ship can be represented by the pose vector $\boldsymbol{\eta} = [x, y, \psi]^\top \in \mathbb{R}^2 \times \mathbb{S}$ and the velocity vector $\boldsymbol{\nu} = [u, v, r]^\top \in \mathbb{R}^3$. Here, (x, y) represents the Cartesian position in a local earth-fixed reference frame, while ψ is the yaw angle. The body-fixed linear velocities are represented by (u, v), and the yaw rate is given by r. The 3 DOF dynamics of a ship can then be stated as (Fossen, 2011):

$$\dot{\boldsymbol{\eta}} = \boldsymbol{R}(\psi)\boldsymbol{\nu} \tag{1}$$

$$\boldsymbol{M}\dot{\boldsymbol{\nu}} + \boldsymbol{C}(\boldsymbol{\nu})\boldsymbol{\nu} + \boldsymbol{D}(\boldsymbol{\nu})\boldsymbol{\nu} = \boldsymbol{\tau}, \tag{2}$$

where $\boldsymbol{M} \in \mathbb{R}^{3\times3}$, $\boldsymbol{C}(\boldsymbol{\nu}) \in \mathbb{R}^{3\times3}$, $\boldsymbol{D}(\boldsymbol{\nu}) \in \mathbb{R}^{3\times3}$ and $\boldsymbol{\tau} = [\tau_1, \tau_2, \tau_3]^\top$ represent the inertia matrix, Coriolis and centripetal matrix, damping matrix and control input vector, respectively. The rotation matrix $\boldsymbol{R}(\psi) \in SO(3)$ is given as

$$\boldsymbol{R}(\psi) = \begin{bmatrix} \cos(\psi) & -\sin(\psi) & 0 \\ \sin(\psi) & \cos(\psi) & 0 \\ 0 & 0 & 1 \end{bmatrix}. \tag{3}$$

The system matrices are assumed to satisfy the properties $\boldsymbol{M} = \boldsymbol{M}^\top > 0$, $\boldsymbol{C}(\boldsymbol{\nu}) = -\boldsymbol{C}(\boldsymbol{\nu})^\top$ and $\boldsymbol{D}(\boldsymbol{\nu}) > 0$. In this paper, we use the model and parameters of the model-scale ship CyberShip Inocean CAT I Arctic Drillship (CSAD) (Bjørnø et al., 2017) for control design and evaluation through numerical simulations. CSAD is a 1:90 scale replica of the full-scale Statoil CAT I Arctic Drillship, with a length of $L = 2.578$ m, and is shown in Fig 1. The inertia matrix is given as

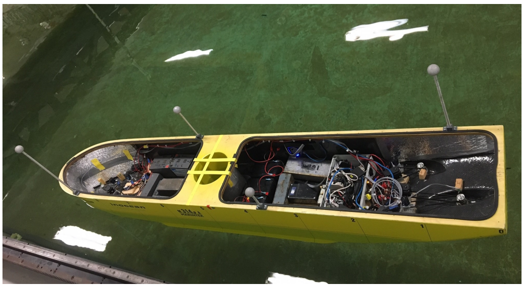

Fig. 1. CyberShip Inocean CAT I Arctic Drillship in the Marine Cybernetics Laboratory at NTNU.

$$\boldsymbol{M} = \boldsymbol{M}_{RB} + \boldsymbol{M}_A, \tag{4}$$

where

$$\boldsymbol{M}_{RB} = \begin{bmatrix} m & 0 & 0 \\ 0 & m & mx_g \\ 0 & mx_g & I_z \end{bmatrix} \tag{5}$$

$$\boldsymbol{M}_A = \begin{bmatrix} -X_{\dot{u}} & 0 & 0 \\ 0 & -Y_{\dot{v}} & -Y_{\dot{r}} \\ 0 & -N_{\dot{v}} & -N_{\dot{r}} \end{bmatrix}. \tag{6}$$

The mass of CSAD is $m = 127.92$ kg, while $x_g = 0.00375$ m is the distance along the x-axis in the body frame from the center of gravity. The moment of inertia about the z-axis in the body frame is $I_z = 61.987\ \text{kg}\,\text{m}^2$. Other parameter values are listed in Table 1. Note that N_r, which is marked in bold, has been changed to correspond better with the actual physical behavior of CSAD. The Coriolis and centripetal matrix is

$$\boldsymbol{C}(\boldsymbol{\nu}) = \boldsymbol{C}_{RB}(\boldsymbol{\nu}) + \boldsymbol{C}_A(\boldsymbol{\nu}), \tag{7}$$

with

$$\boldsymbol{C}_{RB}(\boldsymbol{\nu}) = \begin{bmatrix} 0 & 0 & -m(x_g r + v) \\ 0 & 0 & mu \\ m(x_g r + v) & -mu & 0 \end{bmatrix} \tag{8}$$

$$\boldsymbol{C}_A(\boldsymbol{\nu}) = \begin{bmatrix} 0 & 0 & -c_{A,13}(\boldsymbol{\nu}) \\ 0 & 0 & c_{A,23}(\boldsymbol{\nu}) \\ c_{A,13}(\boldsymbol{\nu}) & -c_{A,23}(\boldsymbol{\nu}) & 0 \end{bmatrix}, \tag{9}$$

where

$$c_{A,13}(\boldsymbol{\nu}) = -Y_{\dot{v}} v - \frac{1}{2}(N_{\dot{v}} + Y_{\dot{r}}) r \tag{10}$$

$$c_{A,23}(\boldsymbol{\nu}) = -X_{\dot{u}} u. \tag{11}$$

Finally, the damping matrix $\boldsymbol{D}(\boldsymbol{\nu})$ is given as

$$\boldsymbol{D}(\boldsymbol{\nu}) = \boldsymbol{D}_L + \boldsymbol{D}_{NL}(\boldsymbol{\nu}), \tag{12}$$

where

$$\boldsymbol{D}_L = \begin{bmatrix} -X_u & 0 & 0 \\ 0 & -Y_v & 0 \\ 0 & 0 & -N_r \end{bmatrix} \tag{13}$$

$$\boldsymbol{D}_{NL}(\boldsymbol{\nu}) = \begin{bmatrix} d_{NL,11}(\boldsymbol{\nu}) & 0 & 0 \\ 0 & d_{NL,22}(\boldsymbol{\nu}) & 0 \\ 0 & 0 & d_{NL,33}(\boldsymbol{\nu}) \end{bmatrix}, \tag{14}$$

and

$$d_{NL,11}(\boldsymbol{\nu}) = -X_{|u|u}|u| - X_{uuu}u^2 \tag{15}$$

$$d_{NL,22}(\boldsymbol{\nu}) = -Y_{|v|v}|v| - Y_{|r|v}|r| \tag{16}$$

$$d_{NL,33}(\boldsymbol{\nu}) = -N_{|v|r}|v| - N_{|r|r}|r|. \tag{17}$$

Table 1. Parameters for CSAD (Bjørnø et al., 2017).

Parameter	Value	Parameter	Value
$X_{\dot{u}}$	−3.262	X_{uuu}	−8.557
$Y_{\dot{v}}$	−28.89	Y_v	−4.673
$Y_{\dot{r}}$	−0.525	$Y_{\|v\|v}$	0.398
$N_{\dot{v}}$	−0.157	$Y_{\|r\|v}$	−0.805
$N_{\dot{r}}$	−13.98	$N_{\|v\|r}$	0.080
X_u	−2.332	N_r	**-6.900**
$X_{\|u\|u}$	0	$N_{\|r\|r}$	−0.0115

The considered model describes a fully actuated ship, where the actuator forces and moments are modeled using the six mounted thrusters $\boldsymbol{u} = [u_1, u_2, u_3, u_4, u_5, u_6]^\top \in \mathbb{R}^6$ (Bjørnø et al., 2017). These are related to the input vector $\boldsymbol{\tau}$ through the actuator model

$$\boldsymbol{\tau}(\boldsymbol{u}) = \boldsymbol{T}\boldsymbol{K}_T\boldsymbol{u}, \tag{18}$$

where $\boldsymbol{T} \in \mathbb{R}^{3\times 6}$ is an actuator configuration matrix, while $\boldsymbol{K}_T \in \mathbb{R}^{6\times 6}$ is an actuator force matrix. The actuator configuration matrix is

$$\boldsymbol{T} = \begin{bmatrix} c(\delta_1) & c(\delta_2) & c(\delta_3) & c(\delta_4) & c(\delta_5) & c(\delta_6) \\ s(\delta_1) & s(\delta_2) & s(\delta_3) & s(\delta_4) & s(\delta_5) & s(\delta_6) \\ \phi_1 & \phi_2 & \phi_3 & \phi_4 & \phi_5 & \phi_6 \end{bmatrix}, \tag{19}$$

where $c(\delta_i) = \cos(\delta_i)$, $s(\delta_i) = \sin(\delta_i)$. The constant $\phi_i = L_i \cos(\beta_i)\sin(\delta_i)$ with $L_i = \sqrt{L_{x,i}^2 + L_{y,i}^2}$, where $L_{x,i}$ and $L_{y,i}$ represent the physical placements of the ith actuator and $\beta_i = \operatorname{atan}(L_{y,i}/L_{x,i})$ for $i \in [1, 6]$. The actuator force matrix is given as

$$\boldsymbol{K}_T = \operatorname{diag}([K_{T,1}, K_{T,2}, K_{T,3}, K_{T,4}, K_{T,5}, K_{T,6}]), \tag{20}$$

where $K_{T,i} > 0$ is the thrust force from the ith propeller. In (Bjørnø et al., 2017), the actuator magnitude constraints are stated as

$$u_i \in [-0.5, 0.5]. \tag{21}$$

In this work, we fix the actuators to the following angles $\boldsymbol{\delta} = [\pi, \pi/4, -\pi/4, 0, 5\pi/4, 3\pi/4]$.

The considered ship has to move at low speeds in order to be fully actuated for DP operations. Assuming low-speed maneuvers, the kinetic model in (2) can be simplified to

$$\boldsymbol{M}\dot{\boldsymbol{\nu}} + \boldsymbol{D}_L\boldsymbol{\nu} = \boldsymbol{\tau}, \tag{22}$$

since for low-speed maneuvers the linear damping will dominate over both the nonlinear damping and the Coriolis and centripetal forces (Fossen, 2011). The model (22) will be used in the control designs in the following sections.

3. ASSUMPTIONS AND CONTROL OBJECTIVE

It is assumed that both the pose vector $\boldsymbol{\eta}(t)$ and velocity vector $\boldsymbol{\nu}(t)$ can be measured, and that no disturbances and uncertainties affect the system.

The control objective is to make $\tilde{\boldsymbol{\eta}}(t) \triangleq \boldsymbol{\eta}(t) - \boldsymbol{\eta}_t(t) \to \boldsymbol{0}$ as $t \to \infty$, where $\boldsymbol{\eta}_t(t) \in \mathbb{R}^2 \times \mathbb{S}$ represents the pose associated with a virtual target ship. The motion of the target ship is typically defined by a human or generated by a guidance system.

For notational simplicity, the time t is omitted in the rest of this paper.

4. BENCHMARK CONTROLLER

In (Sørensen and Breivik, 2016), a cascaded motion controller with nonlinear pose and velocity feedback is suggested. Through its nonlinear feedback terms, this controller can partly handle actuator magnitude constraints. In this paper, this controller is modified to a low-speed DP version where the control input can be chosen as

$$\boldsymbol{\tau} = \boldsymbol{M}\dot{\boldsymbol{\alpha}} + \boldsymbol{D}_L\boldsymbol{\alpha} - \boldsymbol{K}_2(\boldsymbol{z}_2)\boldsymbol{z}_2. \tag{23}$$

The error variables $\boldsymbol{z}_1 = [z_{1,x}, z_{1,y}, z_{1,\psi}]^\top$ and $\boldsymbol{z}_2 = [z_{2,u}, z_{2,v}, z_{2,r}]^\top$ are defined as

$$\boldsymbol{z}_1 \triangleq \boldsymbol{R}^\top(\psi)(\boldsymbol{\eta} - \boldsymbol{\eta}_t) \tag{24}$$

$$\boldsymbol{z}_2 \triangleq \boldsymbol{\nu} - \boldsymbol{\alpha}, \tag{25}$$

where $\boldsymbol{\alpha} = [\alpha_u, \alpha_v, \alpha_r] \in \mathbb{R}^3$ is a vector of stabilising functions that can be interpreted as a desired velocity

$$\boldsymbol{\alpha} = \boldsymbol{R}^\top\dot{\boldsymbol{\eta}}_t - \boldsymbol{K}_1(\boldsymbol{z}_1)\boldsymbol{z}_1, \tag{26}$$

where

$$\boldsymbol{K}_1(\boldsymbol{z}_1) \triangleq \boldsymbol{\Gamma}_1 \begin{bmatrix} \frac{1}{\sqrt{\boldsymbol{z}_{1,\tilde{p}}^\top\boldsymbol{z}_{1,\tilde{p}}+\Delta_{\tilde{p}}^2}}\mathbf{I}_{2\times 2} & \mathbf{0}_{2\times 1} \\ \mathbf{0}_{1\times 2} & \frac{1}{\sqrt{z_{1,\tilde{\psi}}^2+\Delta_{\tilde{\psi}}^2}} \end{bmatrix}, \tag{27}$$

represents a nonlinear control gain with $\boldsymbol{\Gamma}_1 > 0$, $\mathbf{z}_{1,\tilde{p}} \triangleq [z_{1,x}, z_{1,y}]^\top$, $\Delta_{\tilde{p}} > 0$ and $\Delta_{\tilde{\psi}} > 0$. The nonlinear feedback term in (23) is given as

$$\boldsymbol{K}_2(\boldsymbol{z}_2) \triangleq \boldsymbol{\Gamma}_2 \begin{bmatrix} \frac{1}{\sqrt{\boldsymbol{z}_{2,\tilde{v}}^\top\boldsymbol{z}_{2,\tilde{v}}+\Delta_{\tilde{v}}^2}}\boldsymbol{I}_{2\times 2} & \mathbf{0}_{2\times 1} \\ \mathbf{0}_{1\times 2} & \frac{1}{\sqrt{z_{2,\tilde{r}}^2+\Delta_{\tilde{r}}^2}} \end{bmatrix}, \tag{28}$$

with the control gain $\boldsymbol{\Gamma}_2 > 0$, where $\boldsymbol{z}_{2,\tilde{v}} \triangleq [z_{2,u}, z_{2,v}]^\top$, $\Delta_{\tilde{v}} > 0$ and $\Delta_{\tilde{r}} > 0$. The time derivative of $\boldsymbol{\alpha}$ is

$$\dot{\boldsymbol{\alpha}} = \boldsymbol{R}^\top\ddot{\boldsymbol{\eta}}_t + \boldsymbol{S}^\top\boldsymbol{R}^\top\dot{\boldsymbol{\eta}}_t - \dot{\boldsymbol{K}}_1(\boldsymbol{z}_1)\boldsymbol{z}_1 - \boldsymbol{K}_1(\boldsymbol{z}_1)\dot{\boldsymbol{z}}_1, \tag{29}$$

where

$$\dot{\boldsymbol{K}}_1(\boldsymbol{z}_1) = -\boldsymbol{\Gamma}_1 \begin{bmatrix} \frac{\boldsymbol{z}_{1,\tilde{p}}^\top\dot{\boldsymbol{z}}_{1,\tilde{p}}}{(\boldsymbol{z}_{1,\tilde{p}}^\top\boldsymbol{z}_{1,\tilde{p}}+\Delta_{\tilde{p}}^2)^{\frac{3}{2}}}\boldsymbol{I}_{2\times 2} & \mathbf{0}_{2\times 1} \\ \mathbf{0}_{1\times 2} & \frac{z_{1,\tilde{\psi}}\dot{z}_{1,\tilde{\psi}}}{(z_{1,\tilde{\psi}}^2+\Delta_{\tilde{\psi}}^2)^{\frac{3}{2}}} \end{bmatrix}, \tag{30}$$

with

$$\dot{\boldsymbol{z}}_1 = \boldsymbol{S}^\top\boldsymbol{z}_1 - \boldsymbol{K}_1(\boldsymbol{z}_1)\boldsymbol{z}_1 + \boldsymbol{z}_2, \tag{31}$$

where

$$\mathbf{S}(r) = \begin{bmatrix} 0 & -r & 0 \\ r & 0 & 0 \\ 0 & 0 & 0 \end{bmatrix} \tag{32}$$

is a skew-symmetric matrix satisfying $\mathbf{z}_1^\top\mathbf{S}(r)^\top\mathbf{z}_1 = 0$.

5. DYNAMIC WINDOW-BASED CONTROL DESIGN

5.1 Simplified Dynamic Window Algorithm

Here, we present a 3 DOF extension to the 2 DOF DWC controller suggested in (Sørensen et al., 2017).

Based on the ship model (22) and its actuator magnitude constraints, a set of possible velocities can be found. This set contains all the velocities the ship can achieve with respect to the actuator magnitude constraints. The possible velocities can be found by computing the steady-state solutions of the kinetics of (22) for all possible control inputs:

$$\boldsymbol{\tau}(\boldsymbol{u}) = \boldsymbol{D}_L\boldsymbol{\nu}_{ss}, \tag{33}$$

within the actuator magnitude constraints given by (21). The steady-state solutions (33) for a uniformly distributed set of control inputs are shown in Fig. 2. The set of possible velocities is defined as

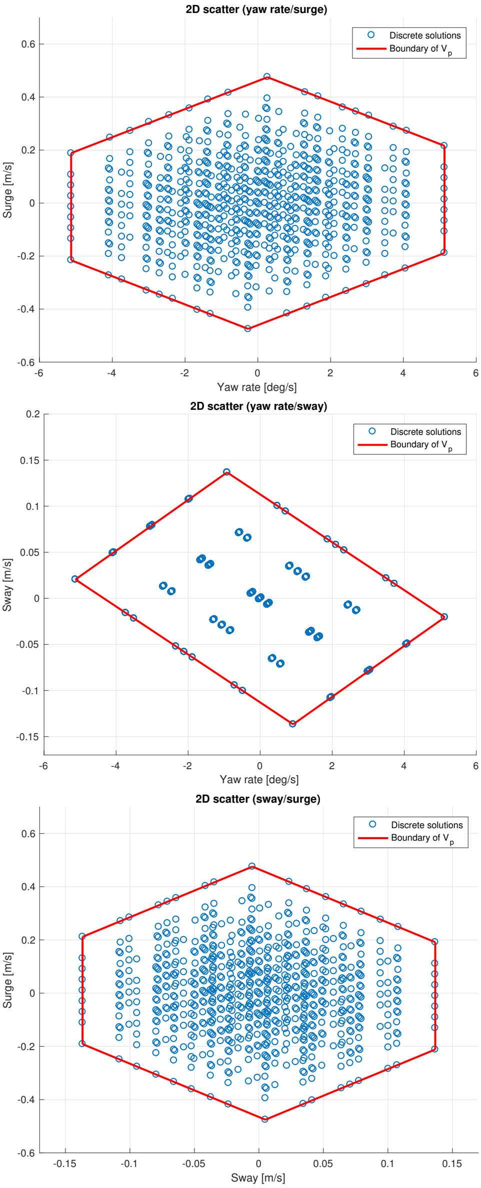

Fig. 2. Possible combinations of surge speed, sway speed and yaw rate, with respect to the actuator magnitude saturation limits.

$$V_p = \{(u, v, r) \in \mathbb{R} \times \mathbb{R} \times \mathbb{R} \mid g(u, v, r) \geq 0\}, \tag{34}$$

where $g(u, v, r)$ is a positive semidefinite function for feasible velocities with respect to the actuator constraints. An approximation of the 3 DOF set is done by projecting the set into three 2 DOF sets to simplify calculations. We justify this approximation by noting that each of the steady-state solution boundary faces are almost parallel with one axis, see Fig. 2. Following this, faces that are parallel with one axis can be parameterized by the remaining two variables. Notice, however, that we lose information where all three variables are correlated, and can therefore not model faces which are not parallel with one of the axes. The result of the approximation is the following three sets of possible velocities:

$$V_{p,(u,r)} = \{(u,r) \in \mathbb{R}\times\mathbb{R} \mid g_{(u,r)}(u,r) \geq 0\} \tag{35}$$
$$V_{p,(v,r)} = \{(v,r) \in \mathbb{R}\times\mathbb{R} \mid g_{(v,r)}(v,r) \geq 0\} \tag{36}$$
$$V_{p,(u,v)} = \{(u,v) \in \mathbb{R}\times\mathbb{R} \mid g_{(u,v)}(u,v) \geq 0\}, \tag{37}$$

where $g_{(u,r)}(u,r)$, $g_{(v,r)}(v,r)$ and $g_{(u,v)}(u,v)$ are positive semidefinite for velocities inside the corresponding boundaries. Given m, n and k approximated boundaries, defined by the functions $h_{a,(u,r)}(u,r) = h_{b,(v,r)}(v,r) = h_{c,(u,v)}(u,v) = 0$, $a \in \{1,2,...,m\}$, $b \in \{1,2,...,n\}$ and $c \in \{1,2,...,k\}$, the approximated functions are given as:

$$\begin{aligned} g_{(u,r)}(u,r) = \min(h_{1,(u,r)}(u,r),&h_{2,(u,r)}(u,r),\\ &..., h_{m,(u,r)}(u,r)) \end{aligned} \tag{38}$$
$$\begin{aligned} g_{(v,r)}(v,r) = \min(h_{1,(v,r)}(v,r),&h_{2,(v,r)}(v,r),\\ &..., h_{n,(v,r)}(v,r)) \end{aligned} \tag{39}$$
$$\begin{aligned} g_{(u,v)}(u,v) = \min(h_{1,(u,v)}(u,v),&h_{2,(u,v)}(u,v),\\ &,..., h_{k,(u,v)}(u,v)). \end{aligned} \tag{40}$$

Here, the functions $h_{a,(u,r)}(u,r) = h_{b,(v,r)}(v,r) = h_{c,(u,v)}(u,v) = 0$ are defined by using regression on the boundary of the sets $V_{p_{(u,r)}}$, $V_{p_{(v,r)}}$ and $V_{p_{(u,v)}}$, where $\nabla h_{a,(u,r)}(u,r)$, $\nabla h_{b,(v,r)}(v,r)$ and $\nabla h_{c,(u,v)}(u,v)$ are required to be pointing inwards to the valid solutions.

Next, the space of reachable points within one time step T needs to be defined. Using

$$\dot{\boldsymbol{\nu}}_{min} = [\dot{u}_{min}, \dot{v}_{min}, \dot{r}_{min}]^\top = \boldsymbol{M}^{-1}(\boldsymbol{\tau}_{min}(\boldsymbol{u}) - \boldsymbol{D}_L\boldsymbol{\nu}^*) \tag{41}$$
$$\dot{\boldsymbol{\nu}}_{max} = [\dot{u}_{max}, \dot{v}_{max}, \dot{r}_{max}]^\top = \boldsymbol{M}^{-1}(\boldsymbol{\tau}_{max}(\boldsymbol{u}) - \boldsymbol{D}_L\boldsymbol{\nu}^*), \tag{42}$$

where $\boldsymbol{\nu}^*$ is the current velocity of $\boldsymbol{\nu}(t)$, we find the acceleration limits and the reachable velocities for the current time step, resulting in the dynamic velocity window

$$\begin{aligned} V_w = \{(u,v,r) &\in \mathbb{R}\times\mathbb{R}\times\mathbb{R} \mid \\ u &\in [u^* + \dot{u}_{min}T, u^* + \dot{u}_{max}T] \\ &\wedge v \in [v^* + \dot{v}_{min}T, v^* + \dot{v}_{max}T] \\ &\wedge r \in [r^* + \dot{r}_{min}T, r^* + \dot{r}_{max}T]\}, \end{aligned} \tag{43}$$

which we project into the three cases

$$\begin{aligned} V_{w,(u,r)} =&\{(u,r) \in \mathbb{R}\times\mathbb{R} \mid u \in [u^* + \dot{u}_{min}T, u^* + \dot{u}_{max}T] \\ &\wedge r \in [r^* + \dot{r}_{min}T, r^* + \dot{r}_{max}T]\} \end{aligned} \tag{44}$$
$$\begin{aligned} V_{w,(v,r)} =&\{(v,r) \in \mathbb{R}\times\mathbb{R} \mid v \in [v^* + \dot{v}_{min}T, v^* + \dot{v}_{max}T] \\ &\wedge r \in [r^* + \dot{r}_{min}T, r^* + \dot{r}_{max}T]\} \end{aligned} \tag{45}$$
$$\begin{aligned} V_{w,(u,v)} =&\{(u,v) \in \mathbb{R}\times\mathbb{R} \mid u \in [u^* + \dot{u}_{min}T, u^* + \dot{u}_{max}T] \\ &\wedge v \in [v^* + \dot{v}_{min}T, v^* + \dot{v}_{max}T]\}. \end{aligned} \tag{46}$$

This defines the sets of dynamically feasible velocities as

$$V_{f,(u,r)} \triangleq V_{p,(u,r)} \cap V_{w,(u,r)} \tag{47}$$
$$V_{f,(v,r)} \triangleq V_{p,(v,r)} \cap V_{w,(v,r)} \tag{48}$$
$$V_{f,(u,v)} \triangleq V_{p,(u,v)} \cap V_{w,(u,v)}. \tag{49}$$

Next, the sets of dynamically feasible velocities are discretised uniformly to obtain discrete sets of dynamically feasible velocities.

For the 3 DOF case, the desired velocity is defined as

$$\boldsymbol{\nu}_d \triangleq [u_d, v_d, r_d]^\top. \tag{50}$$

Given $\boldsymbol{\nu}_d$, the optimal dynamically feasible velocity $\boldsymbol{\nu}_f \triangleq [u_f, v_f, r_f]^\top$ can be selected as

$$\boldsymbol{\nu}_f = \underset{(u,v,r)\in V_f}{\text{argmax}}\ G(\boldsymbol{\nu}, \boldsymbol{\nu}_d), \tag{51}$$

where V_f is the general 3 DOF set and $G(\boldsymbol{\nu}, \boldsymbol{\nu}_d)$ is an objective function which is defined as

$$\begin{aligned} G(\boldsymbol{\nu}, \boldsymbol{\nu}_d) \triangleq \text{surge}(u, u_d) &+ \text{sway}(v, v_d) \\ &+ \text{yawrate}(r, r_d), \end{aligned} \tag{52}$$

with

$$\text{surge}(u, u_d) = 1 - \frac{|u_d - u|}{\max\limits_{u'\in V_f}(|u_d - u'|)} \in [0,1] \tag{53}$$
$$\text{sway}(v, v_d) = 1 - \frac{|v_d - v|}{\max\limits_{v'\in V_f}(|v_d - v'|)} \in [0,1] \tag{54}$$
$$\text{yawrate}(r, r_d) = 1 - \frac{|r_d - r|}{\max\limits_{r'\in V_f}(|r_d - r'|)} \in [0,1]. \tag{55}$$

Notice that by using this objective function, we minimise the scaled 1-norm of the distance to the the desired velocity constrained by the set of dynamically feasible velocities.

For the three 2 DOF cases, this algorithm is modified to fit 2 DOF and run once for each velocity pair scenario; surge speed and yaw rate, sway speed and yaw rate, and surge and sway speed. Hence, it results in the three components of dynamically feasible velocities

$$\boldsymbol{\nu}_{f,(u,r)} = [\nu_{f,u}, 0, \nu_{f,r}]^\top \tag{56}$$
$$\boldsymbol{\nu}_{f,(v,r)} = [0, \nu_{f,v}, \nu_{f,r}]^\top \tag{57}$$
$$\boldsymbol{\nu}_{f,(u,v)} = [\nu_{f,u}, \nu_{f,v}, 0]^\top, \tag{58}$$

which combines into

$$\boldsymbol{\nu}_f = \frac{\boldsymbol{\nu}_{f,(u,r)} + \boldsymbol{\nu}_{f,(v,r)} + \boldsymbol{\nu}_{f,(u,v)}}{2} \tag{59}$$

for the full 3 DOF case. Fig. 3 illustrates V_p, V_w, V_f and $\boldsymbol{\nu}_d = [0.15 \text{ m/s}, -0.07 \text{ m/s}, -1.4324 \text{ deg/s}]$ given a current velocity $\boldsymbol{\nu}^* = [0.2 \text{ m/s}, -0.05 \text{ m/s} \ -1.1459 \text{ deg/s}]$.

5.2 Dynamic Window-based Controller

We now combine elements from the benchmark controller with the simplified DW algorithm in order to develop a dynamic window-based controller (DWC). In this setup, the simplified DW algorithm will use $\boldsymbol{\alpha} = [\alpha_u, \alpha_v, \alpha_r]^\top$ as an input such that $\boldsymbol{\nu}_d = \boldsymbol{\alpha}$. In the case where $\boldsymbol{\alpha}$ is an infeasible velocity, the simplified DW algorithm will modify $\boldsymbol{\alpha}$ to a feasible velocity $\boldsymbol{\alpha}_f = [\alpha_{f,u}, \alpha_{f,v}, \alpha_{f,r}]^\top$, otherwise $\boldsymbol{\alpha}_f = \boldsymbol{\alpha}$. Per definition, the ship will be able to achieve $\boldsymbol{\alpha}_f$ after time step T, hence the desired acceleration is chosen to be

$$\dot{\boldsymbol{\alpha}}_{DWC}(t) = \frac{\boldsymbol{\alpha}_f - \boldsymbol{\nu}}{T}, \tag{60}$$

and

$$\boldsymbol{\alpha}_{DWC} = \int_0^t \dot{\boldsymbol{\alpha}}_{DWC}(\sigma)d\sigma + \boldsymbol{\alpha}_{DWC}(0). \tag{61}$$

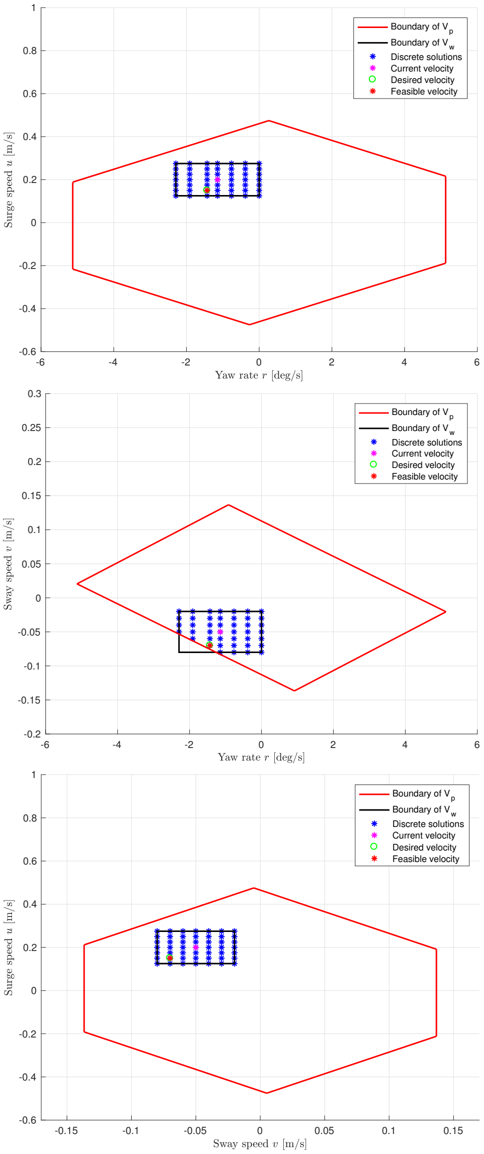

Fig. 3. The dynamically feasible velocity sets, surrounded by the boundaries of the dynamic velocity window and the set of possible velocities.

Both $\boldsymbol{\alpha}_{DWC}$ and $\dot{\boldsymbol{\alpha}}_{DWC}$ are used in the kinetic controller (23) which is modified to

$$\boldsymbol{\tau} = \boldsymbol{M}\dot{\boldsymbol{\alpha}}_{DWC} + \boldsymbol{D}_L\boldsymbol{\alpha}_{DWC}. \tag{62}$$

When comparing the control law (62) against (23), it can be seen that the explicit feedback term $-\boldsymbol{K}_2(\boldsymbol{z}_2)\boldsymbol{z}_2$ in (23) is not included in (62) since the DWC makes the feasible velocity track the derired velocity by using (60)-(61). Hence, (62) shows that the DWC is a feedforward-based control algorithm with implicit velocity feedback through α_{DWC}. However, augmenting the controller with explicit feedback terms and adaptive terms to robustify it against modeling uncertainties and unknown disturbances will not be done in this paper, but is considered future work.

6. SIMULATION RESULTS

In this section, we present numerical simulation results comparing the performance of the DWC against the benchmark controller using the full nonlinear ship model and actuator constraints of CSAD presented in Section 2. In particular, the performance is evaluated using two specific performance metrics which consider both control accuracy and energy efficiency.

The target to be tracked is defined as a changing setpoint in a 4-corner test(Skjetne et al., 2017). This test first tests the surge, sway and yaw motion individually and then increase the complexity of the task until the ship needs to do a combined surge, sway and yaw motion. In this test we use set-point tracking. Since the 4-corner test involves setpoint tracking, $\dot{\boldsymbol{\eta}}_t = \mathbf{0}$ and $\ddot{\boldsymbol{\eta}}_t = \mathbf{0}$ in (26) and (29). The initial ship states are chosen to be $\boldsymbol{\eta}(0) = [5, 1, 0]^\top$ and $\boldsymbol{\nu}(0) = \mathbf{0}$. The control gains are listed in Table 2, which are chosen such that the benchmark controller (BC) does not exceed the magnitude saturation constraints and follow the tuning rules suggested in (Sørensen et al., 2018).

Table 2. Control gains.

	BC	**DWC**
$\boldsymbol{\Gamma}_1$	$\mathrm{diag}([0.03, 0.03, 0.0349])$	$-\|\|-$
$\boldsymbol{\Gamma}_2$	$\mathrm{diag}([0.2, 0.12, 0.1745])\boldsymbol{M}$	N/A
$\Delta_{\tilde{p},\tilde{\psi}}$	$[0.5, 0.5]$	$-\|\|-$
$\Delta_{\tilde{v},\tilde{r}}$	$[0.7, 1]$	N/A

6.1 Performance Metrics

To evaluate and compare the performance of the controllers, two performance metrics are used. We define

$$e(t) \triangleq \sqrt{\bar{\boldsymbol{\eta}}(t)^\top \bar{\boldsymbol{\eta}}(t)}, \tag{63}$$

as the error input for the performance metrics, with $\bar{\boldsymbol{\eta}}$ being the normalized signal of $\tilde{\boldsymbol{\eta}} = [\tilde{x}, \tilde{y}, \tilde{\psi}]^\top \triangleq \boldsymbol{\eta} - \boldsymbol{\eta}_t$, where $\bar{x}$, $\bar{y}$ and $\bar{\psi}$ are in the intervals $[-0.5, 0.5]$ in the expected operational space of the ship (Eriksen and Breivik, 2017). These signals represent the instantaneous control errors, while we would like to consider the accumulated errors over time. Therefore, we use the performance metric integral of the absolute error (IAE)

$$IAE(t) \triangleq \int_0^t |e(\sigma)| d\sigma, \tag{64}$$

which integrates the temporal evolution of the absolute error. We also consider the integral of the absolute error multiplied by the energy consumption (IAEW) as (Sørensen and Breivik, 2015)

$$IAEW(t) \triangleq \int_0^t |e(\sigma)| d\sigma \int_0^t P(\sigma) d\sigma, \tag{65}$$

where

$$P(t) = |\boldsymbol{\nu}(t)^\top \boldsymbol{\tau}(t)| \tag{66}$$

represents the mechanical power. IAEW thus indicates which controller has the best combined control accuracy and energy use in one single metric.

6.2 Simulation Results

In Fig. 4, the outline of the ship pose is plotted to show the transient motion behavior associated with performing the 4-corner test using the two controllers.

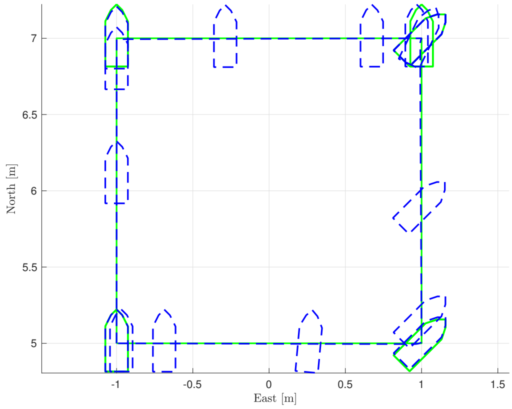

Using DWC.

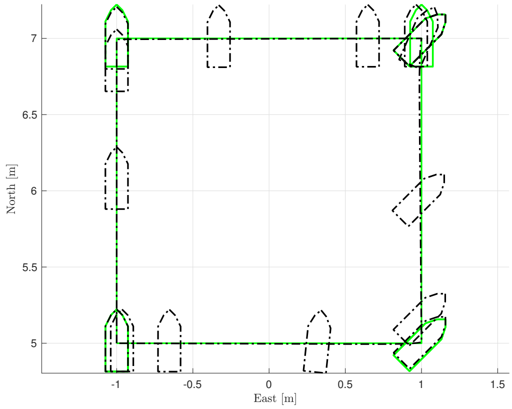

Using BC.

Fig. 4. The 4-corner test, where the dashed blue outline represents the DWC-controlled ship, the dash-dotted black outline represents the BC-controlled ship, while the green outline represents the setpoints of the 4-corner box.

Fig. 5 shows the pose of the ship together with the target pose. It can be seen that both control laws are able to track the target pose setpoints even though the DWC does not have a traditional velocity feedback term as in (23). Additionally, it can be seen that the DWC is slightly faster than the BC controller to track the target pose setpoints.

Fig. 6 shows that the DWC commands the control inputs to stay just below the maximum magnitude constraints of the actuators, while BC is tuned such that it does not exceed the magnitude constraints. The DWC keeps the control inputs high longer than the BC, since the DWC tracks the feasible velocity $\boldsymbol{\alpha}_f$ which is on the boundaries of the windows unless the desired velocity $\boldsymbol{\alpha}$ is inside the velocity window, while the control inputs from BC have a more conservative behavior.

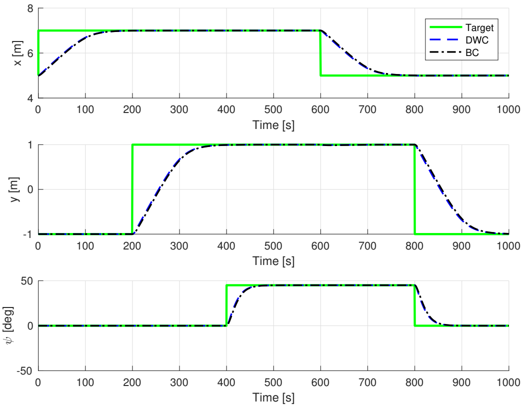

Fig. 5. Tracking the target pose.

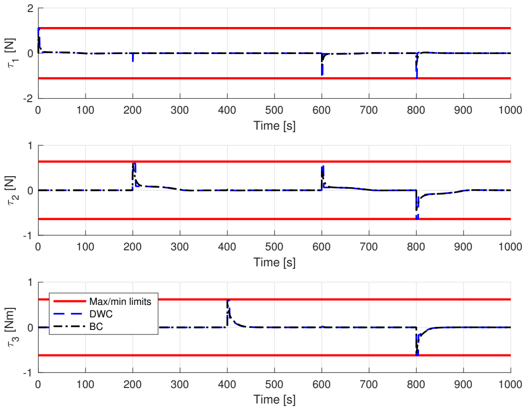

Fig. 6. The commanded control inputs with magnitude saturation limits.

Fig. 7 illustrates how the surge speed, sway speed and yaw rate moves in the velocity space in order to track α through the 4-corner test. The velocities of the ship are small in magnitude while performing the 4-corner test, constituting low-speed DP maneuvers satisfying the assumptions for using a linear ship model.

In Fig. 8, the performance metrics IAE and IAEW are shown. In particular, the IAE trajectory in the left of Fig. 8 confirms that the DWC has a slightly faster transient response since it converges faster to a stationary value. The IAEW trajectory in the right of Fig. 8 shows that the DWC has a slightly better overall performance than the benchmark controller when taking both control accuracy and energy use into account.

7. CONCLUSION

This paper has proposed an extension of a simplified dynamic window algorithm from 2 DOF to 3 DOF, as

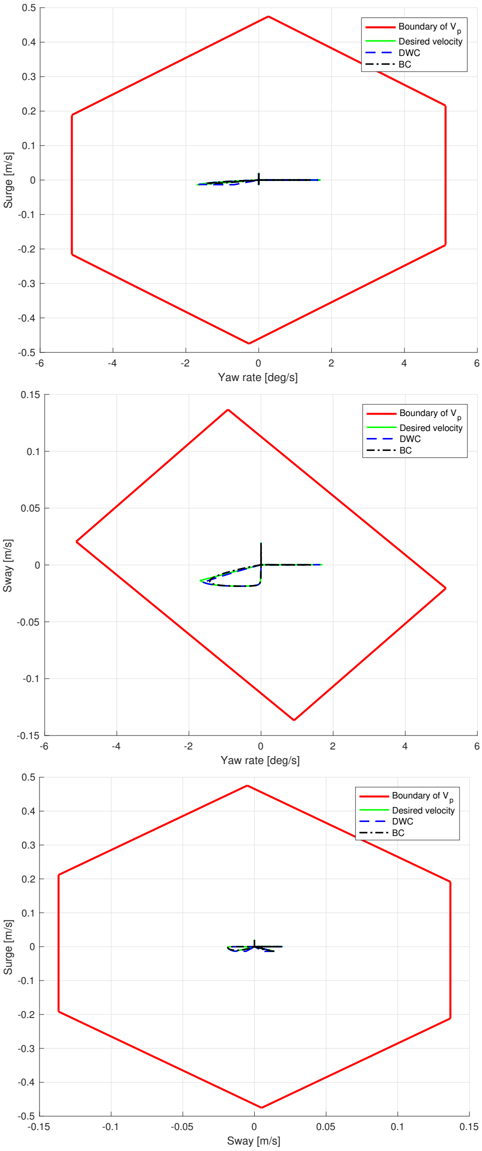

Fig. 7. Velocity trajectories in the set of possible velocities V_p.

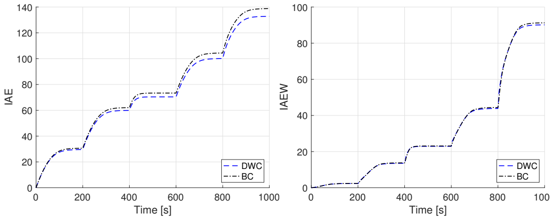

Fig. 8. IAE and IAEW performance metrics.

a way to ensure that the actuator magnitude constraints of a fully actuated ship are satisfied. This algorithm has been used in a dynamic window-based controller (DWC) to guarantee that ship velocities remain within a feasible set. The controllers are compared through numerical simulations with a fully actuated drillship performing a low-speed 4-corner dynamic positioning test, using two performance metrics to quantify the motion control behavior. The simulation results show that the proposed 3 DOF DWC controller has good tracking performance and is able to handle actuator magnitude constraints.

Future work includes exploring the robustness of the DWC controller to modeling uncertainties and unknown disturbances affecting the system. It is also relevant to consider the stability properties of the DWC controller. In addition, it is desirable to consider actuator rate constraints in addition to magnitude constraints. Finally, it is desirable to experimentally verify the results by testing the methods on a model-scale ship in an ocean basin.

ACKNOWLEDGEMENTS

This work was supported by the Research Council of Norway through the Centres of Excellence funding scheme, project number 223254.

REFERENCES

Bjørnø, J., Heyn, H.M., Skjetne, R., Dahl, A.R., and Frederich, P. (2017). Modeling, parameter identification and thruster-assisted position mooring of C/S Inocean CAT I Drillship. *in Proceedings of the 36th International Conference on Ocean, Offshore and Arctic Engineering, Trondheim, Norway.*

Eriksen, B.-O. H., Breivik, M., Pettersen, K.Y., and Wiig, M.S. (2016). A modified dynamic window algorithm for horizontal collision avoidance for AUVs. *in Proceedings of the IEEE Multi-Conference on Systems and Control, Buenos Aires, Argentina.*

Eriksen, B.-O. H. and Breivik, M. (2017). *Modeling, Identification and Control of High-Speed ASVs: Theory and Experiments*, 407–431. Sensing and Control for Autonomous Vehicles: Applications to Land, Water and Air Vehicles, Springer International Publishing.

Fossen, T.I. (2011). *Handbook of Marine Craft Hydrodynamics and Motion Control.* Wiley.

Fox, D., Burgard, W., and Thrun, S. (1997). The dynamic window approach to collision avoidance. *IEEE Robotics & Automation Magazine*, 4(1), 23–33.

Skjetne, R., Sørensen, M.E.N., Breivik, M., Værnø, S.A.T., Brodtkorb, A.H., Sørensen, A.J., Kjerstad, Ø.K., Calabrò, V., and Vinje, B.O. (2017). AMOS DP research cruise 2016: Academic full-scale testing of experimental dynamic positioning control algorithms onboard R/V Gunnerus. *in Proceedings of the 36th International Conference on Ocean, Offshore and Arctic Engineering, Trondheim, Norway.*

Sørensen, M.E.N. and Breivik, M. (2015). Comparing nonlinear adaptive motion controllers for marine surface vessels. *in Proceedings of the 10th IFAC Conference on Manoeuvring and Control of Marine Craft, Copenhagen, Denmark.*

Sørensen, M.E.N. and Breivik, M. (2016). Comparing combinations of linear and nonlinear feedback terms for motion control of marine surface vessels. *in Proceedings of the 10th IFAC Conference on Control Applications in Marine Systems, Trondheim, Norway.*

Sørensen, M.E.N., Breivik, M., and Skjetne, R. (2018). Comparing combinations of linear and nonlinear feedback terms for motion control of marine surface vessels. *submitted to IEEE Transactions on Control Systems Technology.*

Sørensen, M.E.N., Eriksen, B.-O. H., and Breivik, M. (2017). A ship heading and speed control concept inherently satisfying actuator constraints. *in Proceedings of the 1st IEEE Conference on Control Technology and Applications, Hawai'i, USA.*